THE CHEMISTRY OF HOT EXOPLANET ATMOSPHERES:

DEVELOPING AND APPLYING CHEMISTRY SCHEMES IN 1D AND 3D MODELS

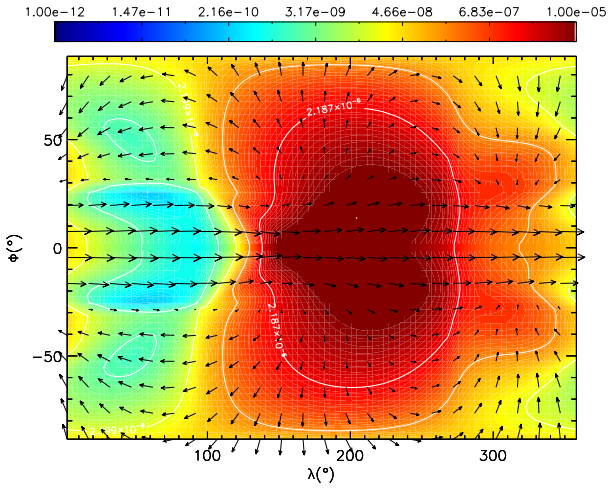

BENJAMIN DRUMMOND

SUBMITTED BY BENJAMIN DRUMMOND TO THE UNIVERSITY OF EXETER AS A THESIS FOR THE DEGREE OF DOCTOR OF PHILOSOPHY IN PHYSICS, MARCH 2017

SIGNED: .....

BENJAMIN DRUMMOND

DATE: .....

Front page figure (Fig. 5.7): The chemical equilibrium mole fraction of atomic hydrogen H (colour scale) and horizontal wind velocities (vector arrows) on a surface of constant pressure $P = 100$ Pa for a model of HD 209458b. See Chapter 5 for more details.

Abstract

The focus of this work is the development and improvement of chemistry schemes in both 1D and 3D atmosphere models, applied to exoplanets. With an ever increasing number of known exoplanets, planets orbiting stars other than the Sun, the diversity in the physical and chemical nature of planets and their atmospheres is becoming more apparent. One of the prime targets, and the focus of many observational and theoretical studies, are the subclass of exoplanets termed hot Jupiters, Jovian sized planets on very short period orbits around their host star.

Due to their close orbit, with orbital periods of just a few days, the atmospheres of such planets are heated to very high temperatures ($\sim 1000-2000$ K) by the intense irradiation from the star. In addition, it is expected that these planets should have synchronised their rotation with their orbital period, a phenomenon called tidal-locking, that leads to a permanently illuminated dayside and a perpetually dark nightside. This combination of intense heating and tidal-locking leads to an exotic type of atmosphere that is without analogue in our own Solar system.

Observational constraints suggest that some of these atmospheres may be clear whilst others may be cloudy or contain haze. Some hot Jupiters appear to be inflated with radii larger than is expected for their mass. For the warmest hot Jupiters optical absorbing species TiO and VO are expected to be present, due to the thermodynamical conditions, where they can strongly influence the thermal structure of the atmosphere, yet so far these species have remained elusive in observations. Theoretical simulations of these planets appear to provide poor matches to the observed emission flux from the nightside of the planet whilst providing a much better agreement with the observed dayside flux.

These outstanding questions can be tackled in two complimentary ways. Firstly, the number of exoplanets subject to intense observational scrutiny must be increased to improve the statistical significance of observed trends. Secondly, and in tandem, the suite of available theoretical models applied to such atmospheres must be improved to allow for a more comprehensive understanding of the potential physical and chemical processes that occur in these atmospheres, as well as for better comparison of model predictions with observations.

In this thesis we present the development and application of one-dimensional

(1D) and three-dimensional (3D) models to the atmospheres of hot exoplanets, with a focus on improving the representation of chemistry. One of the concerns of this work is to couple the radiative transfer and chemistry calculations in a one-dimensional model to allow for a self-consistent model that includes feedback between the chemical composition and the thermal structure. We apply this model to the atmospheres of two typical hot Jupiters to quantify this effect. Implications for previous models that do not include this consistency are discussed.

Another major focus is to improve the representation of chemistry in the Met Office Unified Model (UM) for exoplanet applications, a three-dimensional model with its heritage in modelling the Earth atmosphere that has recently been applied to exoplanets. We discuss the coupling of two new chemistry schemes that improve both the flexibility and capabilities of the UM applied to exoplanets. Ultimately these developments will allow for a consistent approach to calculate the 3D chemical composition of the atmosphere taking into account the effect of large scale advection, one of the processes currently hypothesised to cause the discrepancy between model predictions and observations of the nightside emission flux of many hot Jupiters.

Contents

List of Figures

List of Tables

Declarations

The majority of the research presented in this thesis was performed by myself, in collaboration with Isabelle Baraffe, Nathan Mayne, Pascal Tremblin and David S Amundsen. Here is a breakdown of contributions for each chapter:

Chapter Three

The foundations of the code ATMO were begun by Wolfgang Hayek, with major rewriting, restructuring and improvements by Pascal Tremblin and with contributions from myself and David S Amundsen. I wrote the section of code that calculates the photodissociation rate, the vertical mixing flux and modified the code to include the rainout phenomenon. I contributed to minor model improvements and testing. All benchmark tests of the ATMO chemistry calculations were performed and analysed by myself.

Chapter Four

All calculations were performed by myself, and analysed by myself with contributions from Isabelle Baraffe and Pascal Tremblin. The code that calculates the contribution function in ATMO was written by Jayesh Goyal.

Chapter Five

The coupling of both chemistry schemes to the UM were performed by myself, with contributions from James Manners for interfacing with the radiation modules of the UM, and with advice from Ian Boutle on using the free tracers. The testing of the coupled schemes was performed and analysed by myself with advice from Nathan Mayne.

Chapter Six

All calculations and analysis was performed by myself with guidance from Nathan Mayne. The validation of the k-coefficients via comparison with the Line-by-Line calculations was performed by myself with guidance from David S Amundsen, for

calculation of the flux and heating rates with SOCRATES and the overall methodology of the tests, and from Pascal Tremblin, for calculation of the Line-by-Line fluxes with ATMO. The ability of the UM to calculate and output the top-of-atmosphere flux as seen by an observer was implemented by James Manners.

Acknowledgements

First and foremost I thank my PhD supervisors, Isabelle and Nathan, who have given excellent guidance and advice from start to finish. Writing a PhD thesis, and performing all of the research that goes into it, requires two things. Firstly, lots of hard work and dedication, that only the student can provide. Secondly, it requires guidance, motivation and experience from the supervisors, and that is only down to the luck of having the right supervisors. I was very lucky.

I would also like to thank Pascal Tremblin who was always willing to spend the time to explain things clearly, especially in the early stages. Also, I thank David Amundsen who practically taught me how to use a computer.

Of course, I owe everything to my mum, Jill, who has always been supportive of what I have chosen to do and raised me to be who I am, through difficult circumstances. I am forever grateful to my stepdad, Pete, who has treated me like a son of his own. And to my nana, Elsie, who has always wanted a Doctor in the family. Unfortunately, not this kind of Doctor.

Last, and certainly not least, I thank Lucy, who I met during this PhD, introduced by a pinecone falling from the sky (and the subsequent call to the paramedic). You have been there to share the good times, and always been supportive through the tough times.

Benjamin Drummond
30 March 2017

Chapter 1

Introduction

The first extra-solar planet (exoplanet) orbiting a main-sequence star was discovered in 1995 [Mayor and Queloz, 1995], following the detection of two exoplanets orbiting a pulsar a few years earlier [Wolszczan and Frail, 1992]. Over the following two decades and more a large number of exoplanets have been discovered, totalling 3586 planets[1], following dedicated ground- and space-based detection surveys (e.g. SuperWASP [Pollacco et al., 2006] and Kepler [Borucki et al., 2010], amongst others) and with multiple future missions at various stages of proposal or preparation (e.g. TESS [Ricker et al., 2015], NGTS [McCormac et al., 2017] and the Terra Hunting Experiment[2]) this number is set to rise rapidly.

In addition to the advances in methods and instrumentation employed for exoplanet detection, the characterisation of exoplanetary atmospheres through a combination of detailed observations [e.g. Sing et al., 2016, Wong et al., 2016] and theoretical modelling [e.g. Showman et al., 2009, Moses et al., 2011, Venot et al., 2012, Amundsen et al., 2016] has led to a greater understanding of the diversity of the exoplanet population.

A significant focus of the community has been on the class of exoplanet termed hot Jupiters (Jovian-mass planets on very close-in orbits around their host stars) as these planets dominated the early exoplanet population (due to their relative ease of detection) and offer the best opportunity for follow-up observations to characterise their atmospheres. However, with more recent detections of lower mass and, potentially, more Earth-like planets [e.g. Berta-Thompson et al., 2015, Anglada-Escudé et al., 2016, Gillon et al., 2017] the focus is increasingly expanding to include terrestrial type objects, such as the recent climate simulations of a terrestrial planet orbiting the nearest star to the Sun [e.g. Turbet et al., 2016, Boutle et al., 2017].

The subject of this thesis is the development and application of numerical models to the atmospheres of close-in, highly-irradiated exoplanets. Particular focus

[1] http://exoplanets.eu/ - 06/03/2017
[2] http://www.terrahunting.org/ - 07/03/2017

is placed on modelling the chemical composition and how the composition can effect the dynamical and thermal structure of the atmosphere, as well as the subsequent predicted observable quantities. This work includes the development and application of both one-dimensional (1D) and three-dimensional (3D) models.

In this chapter we introduce the subject of exoplanetary science, beginning with a brief overview of the detection methods and the diversity of the current exoplanet population, as well as reviewing some particular observational highlights. We then introduce the different methods employed for the numerical modelling of exoplanet atmospheres, focusing on methods of representing the chemistry.

1.1 Detection methods and the exoplanet population

There are three primary methods employed for the detection of exoplanets: radial velocity measurements of the host star, observations of the transit of a planet in front of the disc of the host star and direct imaging of the planet itself. Each of these methods presents biases that favour the detection of planets with particular properties. However, it is clear that many exoplanets detected to date vary significantly from the physical and chemical characteristics typical of Solar system planets.

In this section, we introduce the three primary methods of exoplanet detection and the diversity of the current exoplanet population.

1.1.1 The transit method

The transit method infers the presence of a planet in orbit around a star through the observation of periodic reductions in the stellar brightness. This phenomenon can only be observed (from the Earth) if the orbital inclination of the planet is such that it will pass in front of the stellar disk. The first planet to be detected using the transit method was HD 209458b [Charbonneau et al., 2000] using a relatively small telescope. Since then dedicated ground-based (e.g. SuperWASP [Pollacco et al., 2006]) and space-based (Kepler [Borucki et al., 2010]) instruments have led to the discovery of ~ 2500 exoplanets[3,4] using the transit method, about 80% of the total exoplanet population.

The magnitude of the periodic dimming is related to the ratio of the apparent surface area of the transiting planet and the star R_p^2/R_s^2, where R_p and R_s are the planetary and stellar radii, respectively. Therefore, if the stellar radius can be accurately determined, the transit depth can be used to infer the radius of the planet.

[3]https://wasp-planets.net/ - 07/03/2017
[4]https://kepler.nasa.gov/ - 07/03/2017

In addition, from this we can infer that a larger transit depth will occur for either a larger planet or a smaller host star. This method therefore favours the detection of planets with large radii (i.e. hot Jupiters) around Sun-like stars, though has also yielded large numbers of smaller Neptune-size planets around smaller M-dwarf stars.

1.1.2 The radial velocity method

The radial velocity method relies on detecting the gravitational influence of an orbiting planet on its host star [e.g. Udry et al., 2007]. As the star orbits the barycentre of the system, any radial component of the velocity (into or out of the plane of the sky) will cause a Doppler shifting of the stellar radiation; blueshifted as the star moves radially towards the Earth and redshifted as the star moves radially away from the Earth.

From the period of this signal we can infer the period of the orbiting planet and the amplitude of the signal will depend on the mass of the planet M_p. The amplitude of the signal will yield the apparent planetary mass M_p^* that is related to the actual planetary mass by $M_p \sim M_p^* \sin i$, where i is the orbital inclination of the planet as seen from the Earth. If the orbital axis is parallel with the sky ($i = 90°$) then $M_p = M_p^*$. Due to the dependence of the amplitude of the signal on the planetary mass this technique favours the detection of massive planets.

The first exoplanet detection was achieved using the radial velocity method [Wolszczan and Frail, 1992], where two planets were discovered orbiting the pulsar PSR1257 + 12, and later the first detection of an exoplanet orbiting a main-sequence star [HD 209458b, Mayor and Queloz, 1995] was also achieved using this method. However, since then this method has largely been employed for the confirmation of planet candidates previously detected through the transit method [Bouchy et al., 2009]; planets initially detected through the radial velocity method amount to $\sim$ 18% of the total exoplanet population[5]. However, there are dedicated detection surveys that employ the radial velocity method such as the upcoming Terra Hunting Experiment[6] that will search for "Earth-like planets in Earth-like orbits around Solar-type stars"; a potential Earth analogue.

1.1.3 Determination of the planetary bulk density

By combining the inferred M_p from radial velocity measurements with the measured R_p from transit observations the bulk density $\rho \propto M_p/R_p^3$ can be determined. This first-order quantity can be useful in determining the composition of the planet in question [e.g. Pepe et al., 2013, Howard et al., 2013]; i.e. whether the planet is likely

[5]http://exoplanetarchive.ipac.caltech.edu/index.html - 07/03/2017
[6]http://www.terrahunting.org/ - 07/03/2017

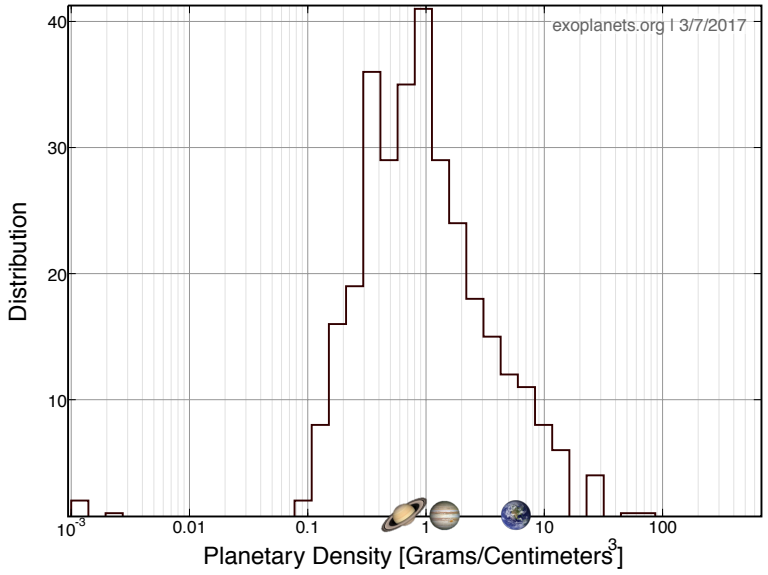

Figure 1.1: A figure showing the histogram distribution of bulk density for the exoplanets which have a measure of both mass M_p and radius R_p. On the x-axis we show the location of Saturn, Jupiter and Earth for reference. Figure initially generated using `https://exoplanets.org`.

to be "rocky", a terrestrial planet, or composed of gas, like the gas giants of our own Solar system.

Fig. 1.1 shows the distribution of bulk densities for all detected exoplanets that have a measure of both mass M_p and radius R_p. Overall, the exoplanet population extends to both smaller and larger densities than the range encapsulated by the Solar system planets ($\sim$0.7 g cm^{-3} for Saturn and $\sim$5.5 g cm^{-3} for Earth). However, the most common bulk densities lie in a range similar to the values for Jupiter and Saturn, indicating that the majority of detected exoplanets are composed mainly of hydrogen. There are, however, a significant number of detected planets with densities similar to or larger than that of Earth, indicating that these planets are more likely to be terrestrial in nature.

1.1.4 Direct imaging

In addition to indirect methods of detecting the presence of a planet (dimming of host star due to a transit or Doppler shifts of the stellar radiation) a small number ($\sim$1%) of planets have been detected by directly imaging the planet [e.g. Kalas et al., 2008, Macintosh et al., 2015]. Currently, the state-of-the-art instruments in this field are SPHERE [Beuzit et al., 2008, Vigan et al., 2016] at VLT and the Gemini Planet Imager [Macintosh et al., 2006, 2014] at the Gemini South Telescope.

The direct imaging method favours planets that are on very wide orbits (generally with a semi-major axis $a > 10$ AU) as they are more easily spatially-resolved

from the host star. In addition, the technique has a bias towards young giant planets that retain significant heat from their formation and therefore have a relatively large luminosity. This method holds great promise for future characterisation observations, demonstrated by early successes [e.g. Oppenheimer et al., 2013].

1.1.5 The exoplanet population

The exoplanet population discovered to date spans a large parameter space in terms of planetary mass, planetary radius, orbital separation and equilibrium temperature. Fig. 1.2 shows the population of currently detected exoplanets that have a measure of the planetary mass as a function of their semi-major axes; the radius of the planet is shown by the colour of the points, if available. It is quite clear that the population of known exoplanets is shaped by three to four subclasses.

At high masses ($M_p \gtrsim 0.5\ M_{p\mathrm{J}}$) and small semi-major axes ($a < 0.1$ AU) is the population of hot Jupiters, with radii typically similar to that of Jupiter ($R_p \sim R_\mathrm{J}$). This class of planet is the most extensively studied both observationally and theoretically [see Baraffe et al., 2010, Madhusudhan et al., 2014b, for a review]. While the majority of hot Jupiters have radii similar to that of Jupiter, there are a significant number with radii much larger than predicted by interior models based on their mass [see Baraffe et al., 2014, for a review]. These 'inflated' hot Jupiters have been the subject of great interest though the mechanism leading to their large radii remains uncertain; though possible explanations include the intense irradition delivering energy deep into the atmosphere [e.g. Showman and Guillot, 2002], ohmic heating due to interactions with the magnetic field [e.g. Batygin and Stevenson, 2010, Rauscher and Menou, 2012a] and delayed contraction of the planet [Burrows et al., 2007, Chabrier and Baraffe, 2007].

Towards larger orbital separations ($a \gtrsim 0.5$ AU) is another population of Jupiter mass planets. The vast majority of these planets are detected via the radial velocity method. As these planets generally do not transit their host star as seen from Earth the radii of these planets cannot be measured using current techniques. At even larger orbital separations lie the relatively small number of massive ($M_p \sim 10 M_\mathrm{J}$) planets detected via the direct imaging method.

A further significant population of planets are found with masses $0.001 < M_p < 0.1\ M_\mathrm{J}$ detected via the transit method and with measured radii $R_p < 0.5 R_\mathrm{J}$. This subclass of planets are termed the 'super Earths' and 'mini Neptunes' with masses typically less than that of Neptune but larger than that of Earth. The atmospheres of these planets have also been under intense scrutiny [e.g. Madhusudhan and Redfield, 2015] through observations [e.g. Knutson et al., 2014, Kreidberg et al., 2014] and modelling [e.g. Madhusudhan and Seager, 2011, Moses et al., 2013a, Kataria et al.,

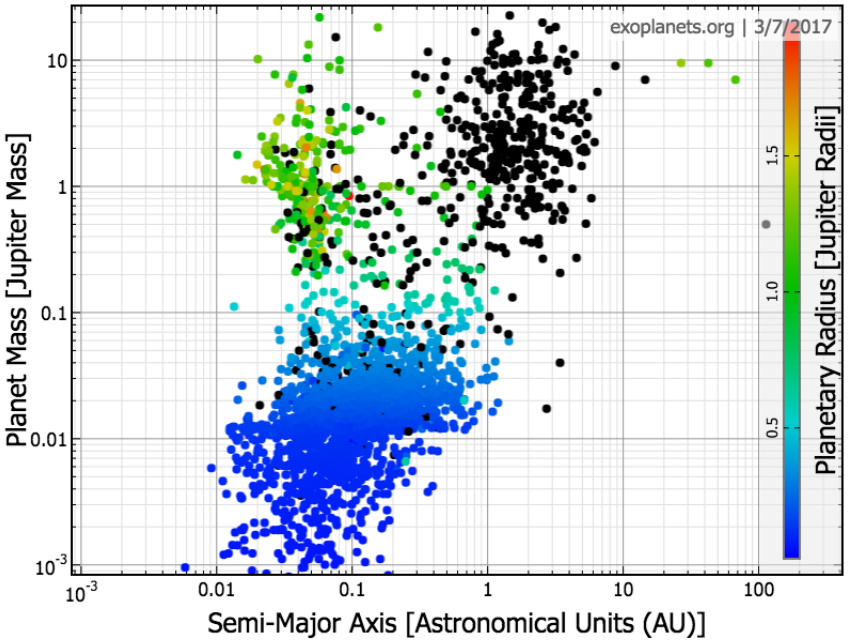

Figure 1.2: A figure showing the population of currently detected exoplanets that also have a measure of the planetary mass. The figure plots planetary mass against the semi-major axis. The colour of the points indicates the planetary radius; black signifies that there is no measured radius for that planet. Figure generated using `https://exoplanets.org`.

2014].

1.1.6 Summary

Through a series of dedicated detection programmes and instrumentation a significant population of exoplanets has been discovered, now totalling over 3500 confirmed planets. These planets have been detected primarily through three techniques: transit detection ($\sim$ 80%), radial velocity measurement ($\sim$ 18%) and direct imaging ($\sim$ 1%). The biases of these methods largely shapes the known population in parameter space.

1.2 Observational characterisation

In addition to detection of exoplanets, observational techniques are also applied to characterise their atmospheres. For transiting planets, this involves three primary methods: transmission spectroscopy, secondary eclipse emission spectroscopy and emission phase curves. In addition we also briefly introduce the methods of high-dispersion spectroscopy that is particularly useful for characterising non-transiting planets and high-contrast imaging that is used to observe exoplanets with wide orbital separations.

1.2.1 Transmission spectroscopy

Measuring the transit depth of a transiting exoplanet leads to a determination of the planetary radius. This apparent radius is a combination of a grey (spectrally invariant) contribution from the bulk planet and a spectrally varying contribution from the atmosphere. The contribution from the atmosphere is expected to vary with wavelength depending on the composition of the atmosphere; including the gas-phase composition and the presence of clouds or haze particles. Measuring the transit depth spectroscopically, therefore, allows for the opacity of the atmosphere to be measured as a function of wavelength. Ultimately, the identification of characteristic features such as molecular absorption features and scattering slopes constrain the composition of the atmosphere [e.g. Seager and Sasselov, 2000].

The first measured transmission spectrum of an exoplanet [Charbonneau et al., 2002] led to the first clear detection of an exoplanet atmosphere via the detection of the sodium doublet (589.3 nm), as predicted by earlier theoretical studies [Seager and Sasselov, 2000, Brown, 2001]. The detection suggests the presence of gas-phase atomic sodium in the atmosphere of HD 209458b.

There has subsequently been a wide range of campaigns employing both space-based and ground-based telescopes to characterise the atmospheres of exoplanets via transmission spectroscopy [e.g. Sing et al., 2008, Bean et al., 2011, Knutson et al., 2014, Nikolov et al., 2016] leading to: the detection of water [Knutson et al., 2007b, Barman, 2007, Madhusudhan et al., 2014a], the inference of hazes and/or clouds [e.g. Pont et al., 2008, Sing et al., 2013, Kreidberg et al., 2014] and the potential detection of titanium oxide (TiO) and vanadium oxide (VO) absorption [Evans et al., 2016]. Recently, Sing et al. [2016] performed the largest consistent transmission spectroscopy survey to date (see Fig. 1.3) with measured spectra of ten hot Jupiters, finding a large diversity in the cloudiness of the atmospheres.

The prime instrument used for transmission spectroscopy in recent years has been the Hubble Space Telescope (HST) Wide Field Camera 3 (WFC3) with a spectral coverage of 1.1–1.8 μm. This wavelength range covers a strong absorption band of H_2O which peaks at around 1.4 μm and observations with WFC3 have therefore lead to highly significant detections of H_2O in several hot Jupiter atmospheres [see Madhusudhan et al., 2016, for a review].

In combination with retrieval modelling (see Section 1.3) these observations have enabled constraints on the abundances of chemical species, in particular for H_2O, using transmission observations with WFC3. Assuming a clear atmosphere, lacking in clouds and hazes, the H_2O abundance was found to be significantly sub-solar in both HD 209458b (20–100× sub-solar) and HD 189733b (3–200× sub-solar) [Deming et al., 2013, Madhusudhan et al., 2014a], suggesting an atmosphere de-

pleted in oxygen and potentially a super-solar carbon-to-oxygen ratio. However, the lower than expected H_2O abundance can also be explained through the effects of clouds and hazes, which are currently poorly constrained. Therefore, without a good knowledge of the presence, composition and distribution of clouds in hot Jupiter atmospheres transmission spectroscopy in isolation is unlikely to be able to provide good contraints on the abundances of detected molecules [Madhusudhan et al., 2016].

Several lower mass and cooler planets (the warm Neptunes and super Earths) have been found to have flat transmission spectra [e.g. Kreidberg et al., 2014, Knutson et al., 2014] with high-precision WFC3 measurements. These highly significant observations of flat transmission spectra have been interpreted as being due to the presence of obscuring clouds or high mean molecular weight atmosphere that reduce the size of the absorption features.

1.2.2 Emission spectroscopy and phase curves

The thermal emission of the atmosphere of a transiting planet can be isolated from the planet-star system. Observing the system during secondary eclipse (when the planet passes behind the star) allows for the emission from the planet to be isolated, as the contribution of the planet to the total flux will temporarily be removed. This was first achieved for the hot Jupiter TrES-1 [Charbonneau et al., 2005] and comparison of the measured secondary eclipse depth with models gave an estimate for the effective temperature of the planet of $T = 1060 \pm 50$ K. The emission measured at secondary eclipse probes the emission resulting from the entire dayside of the planet. Similar secondary eclipse measurements have subsequently been performed for a range of planets [e.g. Deming et al., 2006, Knutson et al., 2008, Kammer et al., 2015].

In the early stages of these types of observation it was suggested that the emission from the daysides of several hot Jupiters were consistent with the presence of a thermal inversion [e.g. Knutson et al., 2008, Rogers et al., 2009, Haynes et al., 2015]: the temperature increases with increasing altitude. One of the prime candidates for forming such a thermal inversion is the presence of the strongly (optical) absorbing species TiO and VO [e.g. Fortney et al., 2008], due to thermochemical arguments. However, more recent re-analyses of these observations [Diamond-Lowe et al., 2014, Evans et al., 2015] have placed considerable doubt on the presence of such thermal structures. However, there remains tentative evidence of large optical absorption consistent with TiO/VO in the transmission spectrum of the very-hot atmosphere of WASP-121b [Evans et al., 2016].

Thermal emission spectroscopy, combined with the retrieval technique (Sec-

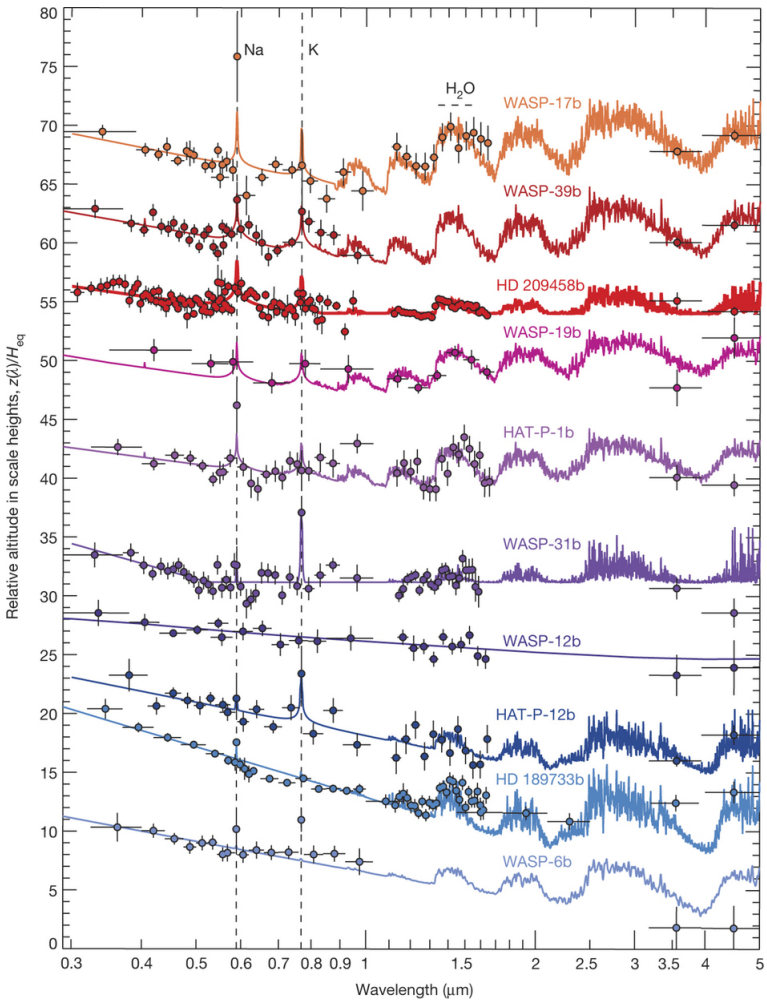

Figure 1.3: The measured transmission (data points) of ten hot Jupiters with best-fit models (coloured lines) from Sing et al. [2016]. The detection of Na and K as well as optical scattering slopes is seen for several planets at short wavelengths. The water absorption feature (around 1.4 μm) varies in its prominence and has been interpreted as being due to the varying cloudiness of these atmospheres.

tion 1.3), has lead to constraints on the abundances of some key chemical species in hot Jupiter atmospheres. For instance, Spitzer observations of the dayside of emission of WASP-12b suggested a H_2O abundance that is $\sim 100\times$ sub-solar [Madhusudhan et al., 2011b]. A sub-solar (0.3-3×) H_2O abundance was also found for WASP-43b [Kreidberg et al., 2014] and a sub-solar ($\sim 0.5\times$) H_2O abundance was found for WASP-33b [Haynes et al., 2015].

In addition to measuring the emission from the dayside during secondary eclipse the emission can be measured thoughout the orbit to yield a phase curve [Cowan and Agol, 2008]. For a tidally-locked planet the emission as a function of orbital phase is equivalent to the emission as a function of planetary longitude, for an observer from a fixed position. Such measurements have been performed for a series of hot Jupiters [e.g. Harrington et al., 2006, Knutson et al., 2009a, Zellem et al., 2014b, Wong et al., 2016] and allow for the temperature contrast between the hot, permanently irradiated dayside and the cooler, perpetually dark nightside to be estimated.

As well as measuring the horizontal temperature gradient the measured emission phase curve shows signatures of the dynamical structure of the atmosphere. For a tidally-locked planet the hottest region of the atmosphere would correspond to the substellar point, the region receiving the most intense irradiation, in the absence of the advection of heat. However, the measured phase curves of several hot Jupiter atmospheres show significant off-sets in the location of the peak emission by several tens of degrees longitude [e.g. Knutson et al., 2007a, Zellem et al., 2014b, Wong et al., 2016]. These observations of a longitudinally-shifted hot spot are consistent with the idea of heat being efficiently advected from the substellar point by a super-rotating equatorial jet, first predicted using theoretical models by Showman and Guillot [2002] and later supported by others [e.g. Showman et al., 2009, Amundsen et al., 2016].

Comparing the measured emission phase curves with those predicted by theoretical models shows generally a good agreement for the dayside flux [Zellem et al., 2014b, Wong et al., 2016]. However, the models regularly fail to accurately predict the nightside flux suggesting important physical and/or chemical processes are inaccurately captured or missing entirely from the models.

1.2.3 High-dispersion spectroscopy and high-contrast imaging

High-dispersion spectroscopy relies on ground-based telescopes that can achieve very high spectral resolution and has been used to infer the presence of chemical species (CO and H_2O) in the atmosphere and to constrain the orbital properties of the

planet [Snellen et al., 2010, Brogi et al., 2012, Rodler et al., 2012, Birkby et al., 2013, Lockwood et al., 2014, Schwarz et al., 2015, Brogi et al., 2016]. The planetary signal is obtained by exploiting the fact that the emission/absorption features are Doppler shifted due to the orbital motion of the planet.

The first observation using high-dispersion spectroscopy detected absorption due to CO in the atmosphere of HD 209458b [Snellen et al., 2010], with the Doppler shifting of the absorption features being consistent with strong zonal wind velocities, later supported by further observations of the same planet [Brogi et al., 2016]. The method has particular benefit in constraining the orbits of planets detected through radial velocity methods [e.g. Rodler et al., 2012, Brogi et al., 2012]. If the orbit is not known then radial velocity measurements can otherwise only provide minimum mass estimates of the planet. Precisely determining the orbit through high-dispersion spectroscopy can therefore lead to more accurate constraints on the masses of non-transiting planets.

In addition, the thermal structure of the atmosphere can also be constrained with detected absorption of CO in the atmosphere of τ Boo b [Brogi et al., 2012] and the non-detection of CO emission in the atmosphere of HD 209458b [Schwarz et al., 2015] both suggesting atmospheres with temperatures that decrease with altitude; i.e. these atmospheres likely do not possess thermal inversions.

Many of the observations to date have targeted the absorption or emission of CO at 2.3 μm [e.g. Snellen et al., 2010, Brogi et al., 2012, Rodler et al., 2012, Schwarz et al., 2015] due its relatively simple spectral features. However, H_2O has also been detected in HD 189733b [Birkby et al., 2013] and τ Boo b [Lockwood et al., 2014].

Snellen et al. [2013] suggest that ground-based high-dispersion spectroscopy using the next-generation Extremely Large Telescopes (ELTs will be capable of detecting signatures of oxygen in the atmospheres of Earth-like exoplanets. Meanwhile, the recent successes outlines above have demonstrated the ability of this method to constrain both the thermal and chemical properties of exoplanet atmospheres as well as the orbital configuration, and ultimately the mass, of non-transiting planets.

A further observational technique that is coming to the forefront in observational characterisation of exoplanets is the method of high-contrast imaging [e.g. Mizuki et al., 2016, Apai et al., 2016, Lovis et al., 2017]. The technique relies on large ground-based telescopes employing adaptive optics. Early works have placed constraints on the thermal and physical properties of the atmospheres of young, massive planets [Currie et al., 2011, Bonnefoy et al., 2013]. Snellen et al. [2015] explores the potential for combining the high-dispersion spectroscopy and high-contrast imaging techniques with the next generation ground based telescopes.

The emission spectra obtained for planets in the HR 8799 system has led to

the detection of several key molecules. H_2O, CH_4 and CO have each been detected in the atmosphere of HR 8799b [Barman et al., 2011, 2015] and H_2O and CO were detected in HR 8799c [Konopacky et al., 2013]. CH_4 has also been claimed to be present in the atmosphere of GJ 504b [Janson et al., 2013]. The high precision observations available for these directly imaged planets (in constrast to the close-in planets) provide great potential for detections of molecular species. However, since the physical properties of the planet (e.g. mass, radius, temperature, gravity) are not known, it is difficult to be place constraints on the abundances of such molecules based on the observed spectra [Madhusudhan et al., 2016].

1.2.4 Summary

By observing exoplanets via transmission spectroscopy, secondary eclipse emission spectroscopy and emission phase curves, as well as through high-contrast imaging, important constraints can be placed on the physical and chemical properties of the atmosphere, including: the composition, the presence of clouds/hazes, the thermal structure and the dynamical structure. However, important questions remain, including: why do some hot Jupiter atmospheres appear to be relatively clear while others are cloudy [Sing et al., 2016], and what is the cause for the model-observation discrepancy for the nightside emission flux of hot Jupiters [Zellem et al., 2014b, Wong et al., 2016]?

An important restriction of current observational techniques is the limitation of the available wavelength bands that can be measured. The majority of characterisation observations to date have been obtained using the Space Telescope Imaging Spectrograph (STIS) and Wide Field Camera 3 (WFC3) instruments [e.g. Sing et al., 2016], of the Hubble Space Telescope (HST), that cover spectral ranges of 0.3–1.01 μm and 1.1–1.7 μm, respectively. The former has been used to constrain the presence of optical scattering slopes and gas-phase sodium and potassium absorption whilst the spectral window of the latter is typically dominated by water absorption. In addition, two infrared channels of the Spitzer IRAC instrument at 3.6 and 4.5 μm have been widely to measure emission and transmission spectra [e.g. Zellem et al., 2014b, Knutson et al., 2011].

The limitations to the spectral windows presented by these instruments places a contraint on what can be inferred the observations. For instance, many of the absorption/emission features of the gas-phase molecules are found in the infrared wavelengths longer than 4.5 μm and are therefore currently inaccessible. The upcoming launch of the James Webb Space Telescope (JWST) should greatly improve this issue [e.g. Beichman et al., 2014, Greene et al., 2016] by providing a much greater

wavelength coverage (0.6–28.5 μm)[7] further into the infrared. The spectra obtained with JWST should provide much greater spectral resolution over a larger spectral region and with larger signal-to-noise ratio than current instruments, allowing for observations that will more greatly constrain the theoretical models. On the other hand, the eventual loss of HST will also mean the loss of our capability to observe the host stars of exoplanets at ultraviolet (UV) wavelengths, with significant consequences for constraining the level of photochemistry and habitability of exoplanets [e.g. Fossati et al., 2015].

To understand and interpret these observations requires the concurrent development and application of atmosphere models that incorporate the important physical and chemical processes. This is the main subject of this thesis.

1.3 Numerical modelling of exoplanet atmospheres

In this section we briefly review the current state of atmosphere models applied to exoplanets. Such models are required to both interpret the observations (transmission spectra, phase curves, etc) and to theoretically understand the physical and chemical processes that are important.

Currently there are two primary types of model that are applied to exoplanet atmospheres: "forward" models that attempt to include all of the important physical and chemical processes to represent the system and "retrieval" models that search for the set of parameters (e.g. temperature profile, chemical abundance profiles, etc) that best fit a set of observational data points, such as an emission or transmission spectrum.

The retrieval models [e.g. Irwin et al., 2008, Madhusudhan and Seager, 2009, Waldmann et al., 2015] determine the properties of the atmosphere (thermal structure, composition, presence of clouds, etc) by solving the inverse problem presented by a set of observations. In essence, the retrieval codes consist of a radiative transfer scheme and a number of free parameters that describe the physical and chemical properties. The method relies on calculating a large number of models that explore the parameter space to search for the set of parameters that best fit the observational data. Retrieval models are not the subject of the present work and we therefore do not consider them further, but we refer the reader to a detailed review of the technique in Madhusudhan et al. [2014b].

The main subject of this thesis is the development and application of models that fall into the forward modelling category. Presently, the literature shows many examples of forward models that take either one-dimensional (1D) or three-dimensional (3D) approaches and we consider each of these in turn. Note that there

[7] https://jwst.nasa.gov/facts.html - 24/05/17

is currently a lack of two-dimensional (2D) models for exoplanet atmospheres in the literature and such models may prove beneficial as intermediaries in the hierarchy of model complexity. We first introduce the 1D models that can be further classified into the radiative-convective equilibrium models and the chemical kinetics models. We then briefly overview the current 3D models applied to hot gas-giant exoplanets, focussing on the representation of chemistry.

1.3.1 One-dimensional models: radiative-convective equilibrium

An inherent aspect of 1D modelling of atmospheres is the assumption that the system can be well represented by a single column. Given the permanent dayside/nightside structure that is characteristic of the atmospheres of tidally-locked planets an obvious approach is to assume that the 1D atmosphere model represents some spatial average of the entire dayside or nightside. Generally a model that represents the dayside average is constructed by reducing the incoming irradiation flux by a factor f to account for redistribution of heat to the nightside [Burrows et al., 2004, Seager et al., 2005, Fortney et al., 2008].

Radiative-convective equilibrium models [e.g. Barman et al., 2005, Iro et al., 2005, Fortney et al., 2005, Madhusudhan et al., 2011a, Tremblin et al., 2015] solve for the temperature as a function pressure (often termed the "pressure–temperature" or P–T profile) that is consistent with the balance of energy, via both radiation and convection, for each level of the model atmosphere. For highly irradiated planets the atmosphere is generally dominated by a radiative zone and convection is not important for the typical pressures under consideration [Guillot et al., 1996].

The models generally combine 1D radiative transfer schemes with chemical equilibrium calculations and iterate over the P–T profile to find the profile that satisfies radiative-convective equilibrium. The input of energy into the model atmosphere, for a gas giant planet, includes irradiation from the host star as well as heating from the planetary interior.

The treatment of chemistry often assumes local chemical equilibrium using a Gibbs energy minimisation method, or similar, to compute the mole fractions of a set of chemical species for a given pressure and temperature [e.g. Burrows and Sharp, 1999, Lodders and Fegley, 2002, Gordon and McBride, 1994]. The Gibbs energy minimisation method solves for the chemical equilibrium composition by finding the set of chemical abundances that minimises the Gibbs energy of the system. The method is relatively efficient and simple as knowledge of the often complicated chemical reaction pathways is not required, only the chemical potential of each species is needed. However, inherent in the method is the limitation to the

assumption of local chemical equilibrium that is not generally valid for planetary atmospheres; we will expand on this in the next section.

The P–T profile that results from these models can be used to simulate observables (emission and transmission spectra, for example) to compare with observations [e.g. Burrows et al., 2006, Fortney et al., 2010].

1.3.2 One-dimensional models: Chemical kinetics

A further class of 1D models are the chemical kinetics codes that place a greater focus on detailed calculations of the chemical composition [e.g. Liang et al., 2003, Line et al., 2010, Moses et al., 2011, Venot et al., 2012, Zahnle and Marley, 2014, Tremblin et al., 2015, Tsai et al., 2017]; see Madhusudhan et al. [2016] for a review of chemical processes and their implications, with relation to exoplanet atmospheres. The kinetics models solve for the chemical composition by considering the net production and loss rate of each chemical species due to a number of chemical reactions. The method is therefore relatively complicated and not as flexible as the Gibbs energy minimisation (chemical equilibrium) methods that do not need to consider the precise chemical mechanisms that govern the conversion of one species to another. The method is also computationally expensive requiring the solution of a large number of stiff differential equations.

Non-equilibrium chemistry

A key benefit of the chemical kinetics method over the Gibbs energy minimisation method is the ability to include non-equilibrium processes, such as vertical mixing (transport) and photochemical dissociations, that lead to departures from chemical equilibrium. In cases where the mixing timescale is faster than the chemical timescale the chemical abundances become "quenched" and deviate from the abundances expected from chemical equilibrium. This has been shown to have important impacts on the abundances of species such as CH_4, CO and NH_3 [e.g. Moses et al., 2011, Zahnle and Marley, 2014]. In addition, photochemical dissociation of molecules driven by incident high energy photons may lead to the production of photochemical hazes [Zahnle et al., 2016] that could have significant impacts on the chemistry and radiative transfer in such atmospheres.

Fig. 1.4 demonstrates the effect of vertical mixing and photodissociation on the chemistry of a hot hydrogen-dominated atmosphere [Venot et al., 2014]. The abundance profiles of a number of key species are shown both assuming chemical equilibrium and with vertical mixing and photodissociations included.

In the deepest high pressure regions ($P > 1$ bar) the equilibrium and kinetics profiles converge and the chemistry is well described by chemical equilibrium. In

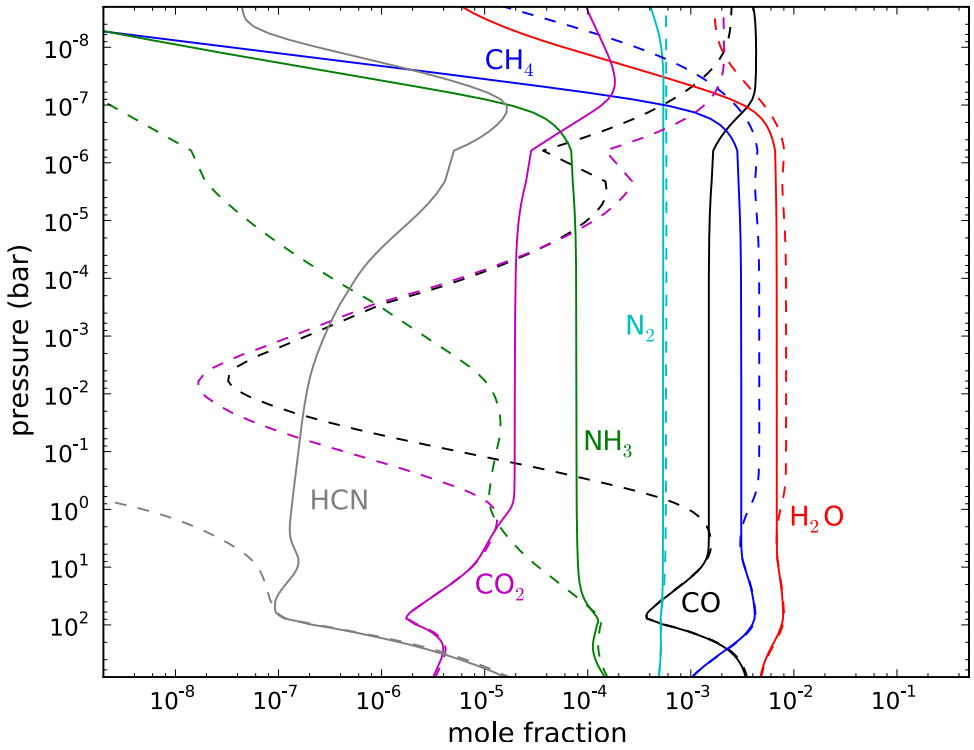

Figure 1.4: A figure showing the chemical equilibrium (dashed) and non-equilibrium (solid) abundances of the major chemical species for a model of GJ 3470b; taken from Venot et al. [2014]. The non-equilibrium profiles include the effects of vertical transport and photodissociations that lead to departures from chemical equilibrium.

this region the large pressure and temperature leads to fast chemical timescales that are able to maintain chemical equilibrium in the presence of vertical transport. However, the chemical timescale increases for decreasing pressure and temperature and at around $P \sim 1$ bar becomes larger than the mixing timescale. At this point the species are quenched as the chemistry is too slow to react to the mixing to lower pressures, leading to a region that is "well mixed" with abundance profiles that are near-constant in pressure. The quenched abundance of each species is determined by the abundance of that species at the "quench point", the pressure level at which the chemical and mixing timescales are equal.

The effect of transport-induced quenching is variable for each species. In this particular example (Fig. 1.4) the effect is to increase the mole fractions of CO, NH_3 and CO_2 by several orders of magnitude compared to their chemical equilibrium abundance profiles. In contrast, the mole fractions of H_2O and CH_4 show smaller decreases compared to chemical equilibrium. The significant changes in the abundance of these absorbing molecules could have significant impacts on the opacity of the atmosphere.

At lower pressures ($P \lesssim 10^{-6}$ bar) photodissociations become important as the availability of high energy photons incident from the host star increases. Photodissociations generally have the effect of reducing the mole fraction of molecular species (H_2O, CH_4, NH_3, etc) through dissociation, leading to the production of highly-reactive free-radicals (H, OH, CH_3, etc) [e.g. Line et al., 2010].

Overall we see that the chemistry of the atmosphere is well described by chemical equilibrium at high pressures, dominated by photochemical processes at low pressures and controlled by vertical mixing for pressures in between. Qualitatively, this is a common result from chemical kinetics models applied to highly irradiated exoplanets [e.g. Line et al., 2010, Moses et al., 2011, Kopparapu et al., 2012, Moses et al., 2013b, Venot et al., 2014, Agúndez et al., 2014a]. Of course, the 1D models can only capture non-equilibrium chemistry due to vertical mixing. We will consider the effect of horizontal mixing shortly.

Chemical networks

The chemical kinetics method solves for the steady-state solution of a chemical system taking into account the production and loss of each species in the system due to a large number of chemical reactions. The reactions that are included, as well as the rates at which they proceed, are provided in the form of a chemical network. The rates of the reactions are typically derived from empirical sources.

There are several chemical networks so far applied to hot exoplanet atmospheres. One of the first networks to be used [Liang et al., 2003, unstated number of species, 253 reactions] was derived from Solar system atmosphere modelling, in

particular for the atmosphere of Jupiter [Gladstone et al., 1996, Moses et al., 2000]. The reaction rates were primarily sourced from room temperature measurements and extrapolated to the much higher temperatures present in hot Jupiter atmospheres. In addition, the model of Liang et al. [2003] did not consider the reverse (endothermic) reactions that are unimportant at low temperatures but can be for the higher temperatures in hot Jupiter atmospheres. Line et al. [2010] (32 species, 258 reactions) later provided updates to the same network with the addition of some high-temperature rate constants and several reverse reactions, though most of the forward reactions did not include a corresponding reverse reaction. The lack of reverse reactions means that the model cannot achieve chemical equilibrium kinetically, and potentially affecting the chemical timescale. This network considered chemical species consisting of carbon, oxygen, nitrogen and hydrogen.

Another chemical network [Zahnle et al., 2009, 49 species, 504 reactions] with its origins in the Solar system, and in particular for the early Earth atmosphere [Kasting et al., 1989, Kasting, 1990, Zahnle et al., 2006], expanded consideration of the chemistry to include sulphur species in addition to the carbon, oxygen, nitrogen and hydrogen chemistry of previous works [Liang et al., 2003, Line et al., 2010]. In addition, all two-body reactions were thermodynamically reversed. Zahnle et al. [2009] considered the photochemical production of HS and S_2 at low pressures.

Moses et al. [2011] also applied a chemical network (90 species, $\sim$ 800 reactions) with its heritage in Solar system atmosphere modelling [e.g. Gladstone et al., 1996] but with a large number of updates informed by the combustion-chemistry literature to improve the models applicability to higher temperatures. In addition, all reactions in the network were thermodynamically reversed that allowed the model to achieve chemical equilibrium kinetically.

Each of these chemical networks were constructed from individual reactions from many different sources. Venot et al. [2012] introduced a chemical network (105 species, $\sim$ 1000 reactions) that did not derive from Solar system atmosphere modelling and instead was sourced from the combustion industry. The network has been validated against experiment for pressures ($0.01 \lesssim P \lesssim 100$ bar), temperatures ($300 \lesssim T \lesssim 2500$ K) and compositions appropriate for application to hot Jupiter atmospheres. All reactions were thermodynamically reversed, except a small number of reactions where the measured reverse rate was preferred. A comparison of this network with that of Moses et al. [2011] revealed overall good agreement for regions of the atmosphere that remain in chemical equilibrium but significant differences for the quenched abundances of CH_4, HCN and NH_3 [Venot et al., 2012]. A more recent update expanded the number of chemical species and reactions in the network [Venot et al., 2015, 240 species, $\sim$ 2000 reactions], in particular adding a significant number of hydrocarbons with more than two carbon atoms. The work presented in

Chapter 4 adopts the chemical network of Venot et al. [2012].

Most recently Tsai et al. [2017] compiled a new chemical network (29 species, $\sim$ 300 reactions) from existing data [see references in Tsai et al., 2017, for more details] with a priority on maintaining a small network in the interest of computational efficiency. The network considers species containing carbon, oxygen and hydrogen only and is validated by comparison with the models of Rimmer and Helling [2016] and Moses et al. [2011], though not against experiments.

Horizontal non-equilibrium chemistry

An inherent limitation of 1D models is the difficulty of representing a system that is strongly non-uniform horizontally; in this case the assumption that the 1D model represents some spatial average (e.g. the dayside average) is likely to be poor. Hot Jupiters are one such example of atmospheres that are strongly asymmetric. The large horizontal temperature gradients coupled with large horizontal wind velocities is suggested to lead to strong horizontal disequilibrium chemistry that vertical 1D models cannot capture.

Attempts have been made, however, to represent this process using a "pseudo-two dimensional" chemical kinetics model [Agúndez et al., 2014a]. Here, a pseudo second spatial dimension (longitude) was represented by allowing the model parameters (e.g. P–T profile, irradiation) to vary periodically with time. In effect, the model represents a column of atmosphere rotating around the equator of the planet with a constant solid-body rotation.

Agúndez et al. [2014a] found that the mole fractions of certain species were strongly affected by the "horizontal wind". In particular, the abundances of CH_4, NH_3 and HCN diverge significantly by several orders of magnitude compared with a more traditional 1D chemical kinetics model that only accounts for vertical transport. This is essentially due to horizontal quenching of the chemistry as the timescale for the rotation of the column around the equator, representing the horizontal wind, is faster than the chemical timescale. Due to the large temperature gradient between the dayside and nightside the chemical timescale can vary significantly with longitude.

The results of Agúndez et al. [2014a] provide a valuable insight into the potential significance of horizontal non-equilibrium chemistry in hot Jupiter atmospheres, however it is important to consider the limitations of the model. The representation of the chemistry remains inherently 1D and horizontal transport is accounted for as a solid body rotation of the column around the equator: in effect representing a wind that is uniform in time, pressure and longitude. The model therefore fails to account for the structure of the equatorial jet where the wind velocity is a function of pressure, longitude and latitude [Amundsen et al., 2016, Showman et al., 2009].

The model also does not consider the effect of meridional transport on the chemistry.

Consistency with the thermal structure

A common limitation of the chemical kinetics models discussed so far is a dependence on an input P–T profile; the kinetics models do not generally calculate the thermal structure self-consistently. Instead, a P–T profile is usually adopted from other sources.

The P–T profile is usually prescribed as a model parameter, typically deriving from other models such as 1D radiative-convective equilibrium models [e.g. Agúndez et al., 2014b, Zahnle and Marley, 2014] or 3D models [e.g. Line et al., 2010, Moses et al., 2011, Venot et al., 2012]. In each case, the models used to calculate the P–T profile (whether 1D [e.g. Fortney et al., 2008] or 3D [e.g. Showman et al., 2009]) assume chemical equilibrium when calculating the thermal profile. If the same thermal profiles are then used as input for the chemical kinetics models to calculate the departure from chemical equilibrium, the effect of changing abundances of absorbing species on the P–T profile should be accounted for. The resolution of this problem, by coupling the radiative-convective equilibrium and chemical kinetics calculations in a single model, is the main subject of Chapter 4.

1.3.3 Three-dimensional models

The second class of forward models applied to hot exoplanet atmospheres are the 3D models [Showman and Guillot, 2002, Dobbs-Dixon and Lin, 2008, Showman et al., 2009, Menou and Rauscher, 2009, Thrastarson and Cho, 2010, Heng et al., 2011, Dobbs-Dixon and Agol, 2013, Mayne et al., 2014a, Amundsen et al., 2016]. Most of these models have heritage in modelling the Earth atmosphere and are termed General Circulation Models (GCMs); with the exception of Dobbs-Dixon and Lin [2008] and Dobbs-Dixon and Agol [2013] who use a 3D hydrodynamics code.

These 3D models are applied to solve for the large scale, long term 3D dynamical flow of the atmosphere and therefore provide a complimentary capability compared with the 1D column models. Though these models can represent the 3D structure of the atmosphere they are significantly more complicated and computationally expensive than their 1D counterparts and therefore the accurate representation of other atmospheric processes, such as radiative transfer and chemistry, are often sacrificied. For instance, several models [e.g. Showman and Guillot, 2002, Heng et al., 2011, Mayne et al., 2014a] parameterise the radiative transfer using a "Newtonian cooling" or "temperature-forced" method, where the P–T profile is relaxed toward an equilibrium profile on a characteristic timescale.

Many GCMs [Showman and Guillot, 2002, Showman et al., 2009, Menou and

Rauscher, 2009, Thrastarson and Cho, 2010, Heng et al., 2011] apply a series of approximations to the equations of motion to simplify the problem, for instance the assumption of vertical hydrostatic balance and constant gravity which, together with other approximations, form a set of equations termed the primitive equations; we will return to describe these in more detail in Chapter 5. On the other hand, Dobbs-Dixon and Lin [2008] and Dobbs-Dixon and Agol [2013] solve the full Navier-Stokes equations and Mayne et al. [2014a] and Amundsen et al. [2016] solve the full Euler equations, respectively, and do not assume the same approximations.

Chemistry in exoplanet GCMs: links to the radiative transfer

Due to the significant computational expense of GCM simulations the treatment of chemistry within them has so far been limited. An important motivation to include a treatment of chemistry in a GCM is for the subsequent calculation of the total gas opacity and then heating rates [e.g. Amundsen et al., 2014, 2016]. Of course, in cases where the thermal evolution is parameterised using a Newtonian cooling method the requirement to include chemistry calculations for this purpose becomes redundant. Therefore, current models that take the Newtonian cooling approach do not include chemistry calculations at all [Showman and Guillot, 2002, Menou and Rauscher, 2009, Heng et al., 2011, Mayne et al., 2014a].

On the other hand, models that include a full radiative transfer approach [e.g. Showman et al., 2009, Amundsen et al., 2016] need to account for the composition of the gas. A common approximation employed by radiative transfer schemes in GCMs is the correlated-k approximation [Goody et al., 1989, Lacis and Oinas, 1991, Thomas and Stammes, 1999] whereby the spectrum is divided into a number of radiative bands and the opacity in each band is described by a number of k-coefficients [see Amundsen et al., 2017, for more details]. Showman et al. [2009] (and later works using the same model [e.g. Lewis et al., 2010, Kataria et al., 2014, 2016]) provide the k-coefficients in each band via a look-up table in terms of pressure and temperature. Assumptions about the composition are made during the calculation of the k-coefficients and the common approach is to assume local chemical equilibrium; this is called the pre-mixed k-coefficients method [Goody et al., 1989, Amundsen et al., 2017]. GCMs that employ the pre-mixed k-coefficients method do not calculate the chemical abundances within the model, with obvious computational efficiency benefits. However, the method is inflexible as new pre-mixed k-coefficient look-up tables must be calculated if the composition changes (e.g. different metallicities). In addition, it has been shown to be less accurate than other methods [Amundsen et al., 2017].

An alternative approach is to combine the k-coefficients due to individual gases on-the-fly in the model, using one of several available methods [see Amundsen

et al., 2017, and references therein]. This approach offers greater flexibility as assumptions about the chemical composition are not as important as in the pre-mixed k-coefficient method and also has been shown to yield more accurate heating rates [Amundsen et al., 2017], at the expense of computational efficiency. In this case, the chemical abundances of each absorbing species must be available in the model to combine the individual k-coefficients and a chemistry scheme within the GCM is required.

Amundsen et al. [2016] take this approach by including a very simple chemical equilibrium scheme in their GCM. An analytical solution to chemical equilibrium [Burrows and Sharp, 1999] is used to give the abundances of CH_4, CO, H_2O and NH_3 as well as a simple parameterisation for alkali species, based on the chemical transformation curves of the atomic alkali species into the alkali chlorides [Burrows and Sharp, 1999], to determine the abundances of each species for a given temperature and pressure. This method is limited in that the analytical solution to chemical equilibrium adopts assumptions that the elemental abundances are roughly Solar and is only able to derive the abundances of a small subset of molecules that are likely to be important in terms of the radiative transfer and chemistry (e.g. CO_2, C_2H_2, HCN, etc.).

In Chapter 5 and Chapter 6 we describe, test and apply a coupled Gibbs energy minimisation scheme to the Met Office Unified Model. This new development expands on the capabilities of Amundsen et al. [2016] by providing a more flexible chemistry scheme that can be applied to a wide range of elemental abundances and to calculate the abundances of a large number of chemical species.

Chemistry in exoplanet GCMs: non-equilibrum chemistry

The chemical composition is required by GCMs that employ a full radiative transfer scheme, whether it is accounted for prior to the GCM simulation in the case of pre-mixed k-coefficients or through a chemistry scheme coupled to the GCM itself. However, the interest in the atmospheric chemistry extends beyond an input for the radiative transfer. One of the long standing problems in the field is quantifying and understanding the importance of horizontal wind-driven non-equilibrium chemistry.

The large temperature contrast between the dayside and nightside hemispheres of hot Jupiters leads to predictions of large composition gradients under the assumption of chemical equilibrium [e.g. Kataria et al., 2016]. However, the large zonal wind velocities are expected to remove this chemical equilibrium through large scale advection and horizontal mixing if the dynamical/mixing timescale is faster than the chemical timescale. If the abundances of absorbing species like CH_4 and NH_3 are affected this may have consequences on the heating rates and thermal evolution of the atmosphere. All GCMs applied to exoplanets using a full radiative transfer

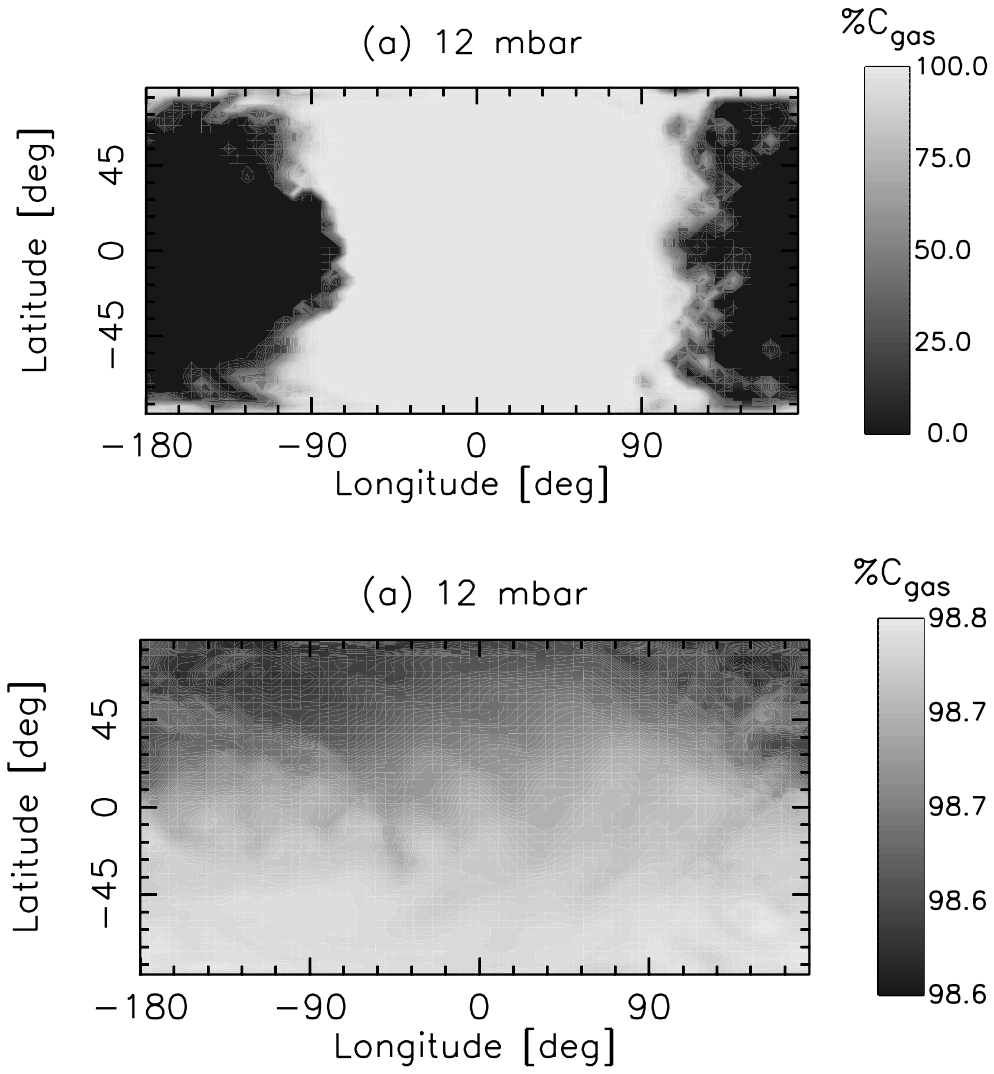

Figure 1.5: A figure showing the percentage of carbon as CO (grayscale) on a constant pressure surface of 12 mbar, for the initial chemical equilibrium (*top*) and after 1000 days (*bottom*), from Cooper and Showman [2006]. The effect of mixing and advection has efficiently homogenised the carbon chemistry. Note the varying scale.

method currently assume chemical equilibrium.

Cooper and Showman [2006] applied a GCM, using a Newtonian cooling scheme, to investigate the importance of non-equilibrium chemistry of CO and CH_4 for a typical hot Jupiter atmosphere. The advection of CO was included through the use of a passive tracer; i.e. the tracer is advected with the flow but does not effect the flow. The interconversion of CO and CH_4 was parameterised through an approach similar to the Newtonian cooling scheme for the temperature where the CO abundance was relaxed towards a chemical equilibrium profile on a characteristic timescale. In this case, the timescale corresponds to the chemical timescale for the interconversion of CO and CH_4 estimated from kinetics studies [Bézard et al., 2002].

Fig. 1.5 shows the fraction of carbon as CO assuming chemical equilibrium and after 1000 days integration in the model accounting for the advection of CO as a free tracer. In the initial chemical equilibrium CO dominates the carbon species on the hot dayside where it is thermodynamically favoured but has a much lower abundance on the cooler nightside where CH_4 is favoured. However, due to the very slow timescale for the conversion of CO and CH_4, the advection of CO from the dayside homogenises the chemistry horizontally leading to much larger CO abundances on the nightside.

This work [Cooper and Showman, 2006] provides an important insight into the balance between the chemical and dynamical timescales in the atmospheres of hot Jupiters and shows that the effect of horizontal non-equilibrium chemistry is likely to be important for species like CH_4 and CO. However, the model has several limitations, primarily:

- the adoption of a Newtonian cooling scheme means that the effect of departures of the chemistry from chemical equilibrium do not feedback into the thermal evolution of the atmosphere

- the conversion of CH_4 and CO is represented as a simple equilibrium relaxation parameterisation (i.e. not a true chemical kinetics calculation) that may not accurately represent the true chemical system.

- the disequilibrium chemistry of additional species may also be important, such as H_2O, NH_3, etc.

In Chapter 5 we describe the coupling of a full chemical kinetics scheme to the Met Office Unified Model that will enable the consistent treatment of advection, chemical evolution and feedback onto the thermal structure in a 3D model, along with the results of early tests.

1.4 Chapter overview

The main goals of this work are to improve the accuracy and flexibility of the treatment of chemistry in both a 1D and 3D atmosphere model. This includes making the treatment of chemistry and radiative transfer more consistent in an existing 1D model as well as coupling new chemistry schemes to a 3D model to expand the current capabilities and increase the flexibility. These developments are important as, particularly in 3D models, much of the focus to date has been on the treatment of dynamics and radiative transfer, at the expense of chemistry. However, the chemical composition is likely to have an important influence on the overall observable properties of the atmosphere.

In Chapter 2 we introduce some of the fundamental concepts of atmospheric chemistry such as definitions of important quantities and the theory of chemical kinetics. In Chapter 3 we describe and test the implementation of two chemistry schemes in the 1D atmosphere model ATMO: a Gibbs energy minimisation scheme that yields the chemical equilibrium abundance and a chemical kinetics scheme that allows for non-equilibrium processes. In Chapter 4 we present and analyse results of a 1D self-consistent non-equilibrium chemistry model applied to two typical hot Jupiters. In Chapter 5 we introduce the Met Office Unified Model and describe the coupling of the ATMO chemistry schemes. We then perform a series of tests to validate the implementation of these schemes. This includes a series of idealised experiments of a fully-coupled chemical kinetics model that accounts for advection and chemical evolution. Finally in Chapter 6 we investigate the effect of the metallicity on the dynamical and thermal structure of the atmosphere of GJ 1214b using the UM with the coupled Gibbs energy minimisation scheme. In Chapter 7 we present final conclusions and future prospects of this work.

1.5 Statement of contribution to other works

The majority of the results presented in Chapter 4 were published in Drummond et al. [2016]. Results were obtained and then analysed by myself, with contributions from Pascal Tremblin, Isabelle Baraffe, David S Amundsen, Nathan Mayne, Olivia Venot and Jayesh Goyal, and I wrote the paper.

I was also involved in papers led by Pascal Tremblin [Tremblin et al., 2015, 2016]. I contributed to the development of the chemical kinetics scheme, and in particular the vertical mixing scheme in ATMO. I was involved in discussion of the results. The results of these works are not presented in this thesis.

I contributed to the mainly observational work of Evans et al. [2016] by calculating 1D ATMO models of WASP-121b that aided with interpretation of the

observational data. These results are not discussed in this thesis.

I am a co-author on the paper Boutle et al. [2017], where I calculated the emission/reflection spectra and phase curves, and contributed to the interpretation of those spectra and phase curves. These results are not discussed in this thesis. I am also co-author on the paper Amundsen et al. [2016] where I was involved in discussion of the results. These results are not discussed in detail but the method of calculating the chemical abundances in the model is reviewed in Chapter 5.

Chapter 2

Chemistry of Planetary Atmospheres

In this chapter we introduce some fundamental concepts related to modelling atmospheric chemistry. We begin by defining the various quantities that are used to describe the abundance of chemical species in an atmosphere (Section 2.1). We then summarise how the elemental composition of an atmosphere is described with relation to gas giant planets (Section 2.2). Next, we introduce the idea of chemical reactions and the state of chemical equilibrium (Section 2.3) before finally describing the theory of chemical kinetics including some physical processes involved in non-equilibrium chemistry (Section 2.4).

2.1 Quantifying the chemical abundance

The abundance of a chemical species in the atmosphere can be expressed via several different quantities. We define these quantities in this section.

2.1.1 Mole fractions

The mole faction (or molar fraction) is defined as the fractional amount of a substance contributing to the total amount of the mixture [Schwarz and Warneck, 1995]. It can therefore be equivalently expressed as the ratio of several different quantities: the number of moles, the partial pressure and the number density. The name *mole fraction* therefore is misleading, as it does not strictly refer to the ratio of the number of moles. The mole fraction of a species j can be expressed as

$$f_j = \frac{N_j}{N} = \frac{P_j}{P} = \frac{n_j}{n}, \tag{2.1}$$

where N_j and N are the number of moles of species j and of the mixture, respectively, P_j and P are the partial pressure of species j and the total pressure, respectively, and n_j and n are the number density of species j and the total number density, respectively.

2.1.2 Mass fractions

The mass fraction, w_j, is related to the mole fraction via

$$w_j = \frac{m_j}{\mu} f_j, \tag{2.2}$$

where m_j is the molar mass of the species j, and μ is the mean molar mass of the background gas; e.g. for the Earth atmosphere $\mu = \mu_{\rm air} \sim 28.97$ g mol^{-1} and for a hydrogen-dominated atmosphere $\mu \sim 2.33$ g mol^{-1}.

2.1.3 Mixing ratios

The mixing ratio of a species is defined as the ratio of the amount of substance to the *remaining* amount of substance. For example, the mole mixing ratio, q_j, is given by

$$q_j = \frac{N_j}{N - N_j}. \tag{2.3}$$

Of course, in cases where the species j is a trace species ($N_j << N$) then the mole mixing ratio is effectively equivalent to the mole fraction.

2.1.4 Concentrations

The concentration of an atmospheric constituent is defined by the amount of substance *per unit volume*; for example, the mass concentration (in kg m^{-3}), the number concentration (or number density, as above, in m^{-3}) and the volume concentration (unitless). In most cases, the mole fraction, mass fraction or mixing ratio is preferred to the concentration, as the concentration depends on the local thermodynamical conditions [Schwarz and Warneck, 1995] while the former quantities do not.

2.2 Composition: abundance of the elements

At the most fundamental level, the composition of an atmosphere is determined by the availability of chemical elements in the system; for example, the availability of carbon determines the overall abundance of carbon-bearing species. As a secondary

effect, the thermodynamical conditions then determine how those elements are distributed amongst all of the possible chemical species: i.e. atoms, molecules and ions.

For instance, methane (CH_4) and carbon monoxide (CO) are usually the most abundant carbon-species in a hydrogen-dominated atmosphere and the local temperature and pressure determine the equilibrium ratio of their mole fractions, f_{CH_4}/f_{CO}. Generally, CH_4 is favoured for low temperatures ($T \lesssim 1000$ K) and the ratio f_{CH_4}/f_{CO} is large while CO is favoured for high temperatures ($T \gtrsim 1000$ K) and the ratio f_{CH_4}/f_{CO} is small.

We will return to discuss the reason behind the dependence of this ratio on temperature in Section 2.3. In this section we focus on the elemental composition of the system.

2.2.1 The Solar composition

In the field of hot Jupiter atmosphere modelling it is common to assume a Solar composition of the elements [e.g. Moses et al., 2011, Venot et al., 2012, Agúndez et al., 2014a]. This assumes that these planetary systems formed in similar ways and from similar material to the Solar system.

The photospheric composition of the Sun is taken to be representative of the composition of material from which the Solar system formed, and abundances of the elements in the Solar photosphere can be inferred through the comparison of observations with theoretical models [e.g. Asplund et al., 2009].

The elemental abundances A_i are often quoted in values normalised to 10^{12} atoms of hydrogen [Asplund et al., 2009, Caffau et al., 2011, Lodders et al., 2009]. The normalised values are related to the number ratio between element i and hydrogen via

$$\frac{N_i^{\text{atoms}}}{N_{\text{H}}^{\text{atoms}}} = \frac{N_i^{\text{atoms}}}{10^{12}} = 10^{(A_i - 12)}, \tag{2.4}$$

where N_i^{atoms} is the number of atoms of element i and $N_{\text{H}}^{\text{atoms}}$ is the number of atoms of hydrogen. By definition then, in this form, the solar abundance of hydrogen is $A_{\text{H}} = 12$.

Alternatively, the abundance can be expressed as the number fraction, B_i, the ratio of the number of atoms of element i to the total number of atoms in the mixture

$$B_i = \frac{N_i^{\text{atoms}}}{\sum N_i^{\text{atoms}}} = \frac{10^{(A_i - 12)}}{\sum 10^{(A_i - 12)}}. \tag{2.5}$$

2.2.2 Metallicity

The metallicity of an astrophysical object is a measure of the total amount of elements that are heavier than helium. The metallicity Z is defined as the sum of the mass fractions of all elements heavier than helium

$$Z = \sum_{i>\mathrm{He}} \frac{M_i}{M}, \tag{2.6}$$

where M_i is the total mass of the element i and M is the total mass of the system.

Alternatively, the metallicity is commonly expressed as a ratio of the number of atoms of a particular metal to the number of atoms of hydrogen [e.g. Wheeler et al., 1989]

$$[X] = \log(X) - \log(X)^{\mathrm{Sun}}$$

where X represents the number ratio between two species; typically, in the stellar community, this is taken as the ratio of the number of iron atoms to the number of hydrogen atoms $X = N_{\mathrm{Fe}}^{\mathrm{atoms}}/N_{\mathrm{H}}^{\mathrm{atoms}}$. Here, we will take the ratio of the sum of all metal elements, $N_{\mathrm{M}}^{\mathrm{atoms}}$, to the number of atoms of hydrogen $X = N_{\mathrm{M}}^{\mathrm{atoms}}/N_{\mathrm{H}}^{\mathrm{atoms}}$, writing the metallicity factor [M/H] as

$$[\mathrm{M/H}] = \log\left(\frac{N_{\mathrm{M}}^{\mathrm{atoms}}}{N_{\mathrm{H}}^{\mathrm{atoms}}}\right) - \log\left(\frac{N_{\mathrm{M}}^{\mathrm{atoms}}}{N_{\mathrm{H}}^{\mathrm{atoms}}}\right)^{\mathrm{Sun}}$$
$$[\mathrm{M/H}] = \log\left(\frac{N_{\mathrm{M}}^{\mathrm{atoms}}/N_{\mathrm{H}}^{\mathrm{atoms}}}{N_{\mathrm{M}}^{\mathrm{atoms,Sun}}/N_{\mathrm{H}}^{\mathrm{atoms,Sun}}}\right).$$

Finally, we can rearrange the above equation to express the number of atoms of metals relative to the number of atoms of hydrogen as

$$\frac{N_{\mathrm{M}}^{\mathrm{atoms}}}{N_{\mathrm{H}}^{\mathrm{atoms}}} = \left(\frac{N_{\mathrm{M}}^{\mathrm{atoms}}}{N_{\mathrm{H}}^{\mathrm{atoms}}}\right)^{\mathrm{Sun}} 10^{[\mathrm{M/H}]}. \tag{2.7}$$

From this we can see that an atmosphere with a metallicity factor [M/H] = 1.0 will have an order of magnitude higher metal content than a solar atmosphere, whilst a factor [M/H] = 2.0 will have two orders of magnitude higher metal content, and so on. A solar metallicity composition is described by [M/H] = 0.

2.2.3 The carbon to oxygen ratio

Another common parameter used to define the elemental abundances is the carbon to oxygen ratio $X^{\mathrm{C/O}}$ that defines the ratio of the number of carbon atoms to the number of oxygen atoms $X^{\mathrm{C/O}} = N_{\mathrm{C}}^{\mathrm{atoms}}/N_{\mathrm{O}}^{\mathrm{atoms}}$. This has been a quantity of interest in the exoplanet community for some time, and was held as a potential explanation

for an apparent lower than solar abundance of water inferred from observations [e.g. Madhusudhan et al., 2011b, Madhusudhan, 2012, Moses et al., 2013b]. The solar value is $X^{\mathrm{C/O}} \sim 0.55$ [Asplund et al., 2009].

For a given number of oxygen atoms, the number of carbon atoms for a given C/O ratio is written as

$$N_{\mathrm{C}}^{\mathrm{atoms}} = X^{\mathrm{C/O}}\ N_{\mathrm{O}}^{\mathrm{atoms}}, \tag{2.8}$$

or alternatively we can find the number of oxygen atoms given the number of carbon atoms

$$N_{\mathrm{O}}^{\mathrm{atoms}} = \frac{N_{\mathrm{C}}^{\mathrm{atoms}}}{X^{\mathrm{C/O}}}. \tag{2.9}$$

2.3 Chemical reactions and the equilibrium composition

The abundance of the elements has a strong influence on the overall chemical composition of an atmosphere. However, for a given elemental composition, the equilibrium distribution of these elements amongst all of the possible atomic, molecular and ionic species is determined by thermodynamic conditions. In addition, physical processes such as mixing, transport and photodissociation can play a role, we will return to these processes in Section 2.4. In this section we introduce the idea of chemical reactions and the equilibrium composition.

2.3.1 The balance of CH_4 and CO

For hydrogen-dominated atmospheres it is found that at low temperatures (and high pressures) CH_4 is the favoured carbon-bearing species whilst at high temperatures (and low pressures) CO is the most stable carbon-species. To understand why, we must consider the processes that lead to the interconversion of these two species and how the net direction and magnitude of this conversion depends on the thermodynamic conditions.

The net chemical reaction for the conversion of CH_4 and CO is given by

$$\mathrm{CH_4 + H_2O \leftrightarrow CO + 3H_2}.$$

This simple net reaction hides the complexity of the actual process. In reality this conversion proceeds via a series of individual *elementary* reactions. For low pressures, these elementary reactions were determined by Moses et al. [2011] to be

$$\mathrm{H + CH_4 \leftrightarrow CH_3 + H_2}$$
$$\mathrm{H + H_2O \leftrightarrow OH + H_2}$$

$$\begin{aligned} OH + CH_3 &\leftrightarrow CH_2OH + H \\ CH_2OH + M &\leftrightarrow H + H_2CO + M \\ H_2CO + H &\leftrightarrow HCO + H_2 \\ HCO + M &\leftrightarrow CO + H + M \end{aligned}$$

and for higher pressures we have

$$\begin{aligned} H + CH_4 &\leftrightarrow CH_3 + H_2 \\ H + H_2O &\leftrightarrow OH + H_2 \\ OH + CH_3 + M &\leftrightarrow CH_3OH + M \\ CH_3OH + H &\leftrightarrow CH_2OH + H_2 \\ CH_2OH + M &\leftrightarrow H + H_2CO + M \\ H_2CO + H &\leftrightarrow HCO + H_2 \\ HCO + M &\leftrightarrow H + CO + M \\ H_2 + M &\leftrightarrow 2H + M. \end{aligned}$$

Therefore, in order to accurately determine the conversion between these two carbon molecules, not only must the complicated reaction pathway be understood but the rates of these elementary reactions must also be accurately determined. However, for the current discussion we can limit our argument to the more simple net reaction.

Enthalpy of reaction

The net reaction that converts CH_4 and CO is a reversible reaction: it can proceed in both directions. To determine which direction proceeds the fastest, and hence to determine which carbon-species is favoured, we can consider the energy exchange during the reaction.

During a chemical reaction chemical bonds are both broken and formed resulting in an exchange of energy. This energy change is quantified in the enthalpy of reaction $\Delta_r H^0$ (see Appendix C). Table 2.1 shows the enthalpies of formation for the four chemical species involved in the net reaction at two temperatures: a "low" temperature value of 500 K and a "high" temperature value of 2000 K. From these enthalpies of formation we can compute $\Delta_r H^0$ for these two temperature regimes, and for each direction of the reaction, and these are shown in Table 2.3.

For both temperatures, the forward reaction (converting CH_4 to CO) yields a positive $\Delta_r H^0$, whilst the reverse process (converting CO to CH_4) is negative. A negative $\Delta_r H^0$ indicates an exothermic reaction in which energy is lost to the environment, reducing the energy of the system. Following the tendancy of a physical

Table 2.1: The enthalpies of formation of CH_4, H_2O, CO and H_2 at 500 and 2000 K; units are kJ mol^{-1}.

	$T = 500$ K	$T = 2000$ K
CH_4	-80.8	-93.0
H_2O	-243.8	-251.7
CO	-110.0	-118.8
H_2	0.	0.

Table 2.2: The entropies of CH_4, H_2O, CO and H_2 at 500 and 2000 K; units are kJ mol^{-1} K^{-1}.

	$T = 500$ K	$T = 2000$ K
CH_4	0.207	0.306
H_2O	0.206	0.265
CO	0.212	0.259
H_2	0.145	0.187

system to spontaneously move towards a state of lower energy we can conclude that, in terms of the energy of the system, the reverse reaction is most favourable and that CH_4 will be the more abundant carbon-species at both temperatures.

This conclusion is not correct, as we have already stated that whilst CH_4 *is* favoured for low temperatures it is actually CO that is favoured for high temperatures. To resolve this we must extend our approach to include the entropy change of the reaction.

Entropy of reaction

As well as changes of energy, a chemical reaction also results in changes in entropy. Thermodynamical systems have a tendency to spontaneously move toward a state of higher entropy. Table 2.2 shows the entropies of the same four molecules at 500 K and 2000 K. Similarly to before, we can calculate the entropy of the reaction $\Delta_r S^0$ and this is shown in Table 2.3 for both reaction directions and at both temperatures.

From this we can readily see that at both low and high temperature the forward reaction leads to a positive $\Delta_r S^0$, whilst the reverse reaction leads to a negative $\Delta_r S^0$. Due to the tendancy of a physical system to spontaneously increase its entropy we can conclude that, in terms of the entropy change only, it is the forward reaction that is favoured for both temperatures and therefore CO should be the more abundant carbon-species.

Gibbs energy of reaction

We now have two competing tendancies for this system, driving the reaction in opposite directions. In terms of minimising energy, the reverse reaction is favoured

and therefore CH_4 should be the more abundant carbon-species for both low and high temperature scenarios. In terms of maximising entropy, it is the forward reaction that is favoured and CO should be the more abundant carbon-species.

The balance of these two competing processes, minimsation of energy and maximisation of entropy, are combined in the thermodynamic quantity termed the Gibbs energy

$$G = H - TS. \tag{2.10}$$

As the temperature increases, the scaling of the second term on the right-hand side with T increases the importance of the entropy term. Therefore, from this equation we can predict that at low temperatures it is the enthalpy term that dominates the Gibbs energy and the net direction of reaction will be the direction that reduces the energy of the system. However, at high temperatures it is the entropy term that is more important and the net direction of reaction will be the direction that increases the entropy.

The Gibbs energy is analogous to the mechanical potential and a thermodynamic system will spontaneously minimise this thermodynamical potential to reach an equilibrium state. We can now consider the Gibbs energy of reaction $\Delta_r G^0$, combining both the energy and entropy effects, to determine which direction of reaction is favoured due to the tendancy of the system to minimise the Gibbs energy.

Table 2.3 shows $\Delta_r G^0$ for both directions of the net reaction and for both temperature cases. Now considering the tendency for a thermodynamic system to reduce the Gibbs energy we can see that at low temperatures the reverse of the reaction, forming CH_4, results in a negative $\Delta_r G^0$ and is therefore the favourable direction and we would expect CH_4 to be the most stable carbon molecule. On the other hand, at the higher temperature of 2000 K, the forward reaction forming CO results in a negative $\Delta_r G^0$ and we would instead expect CO to be the most stable carbon molecule.

By considering the Gibbs energy of reaction and understanding that a thermodynamical system moves towards a state of lower G we can predict the preferred direction of a chemical reaction and ultimately the equilibrium composition.

2.3.2 Solving for chemical equilibrium by minimising the Gibbs energy

The concept of the Gibbs energy provides a very powerful technique in the field of atmospheric chemistry. In a thermodynamical system any process that results in a reduction of the Gibbs energy of the system will occur spontaneously; just as a free moving object (mass) will spontaneously reduce its potential energy in a gravitational field. Given enough time, the Gibbs energy of the system will minimise

Table 2.3: The enthalpy, entropy and Gibbs energy of reaction at 500 and 2000 K.

	$T = 500$ K	$T = 2000$ K
Forward ($CH_4 \rightarrow CO$)		
$\Delta_r H^0$ [kJ mol^{-1}]	214.6	225.9
$\Delta_r S^0$ [kJ mol^{-1} K^{-1}]	0.234	0.249
$\Delta_r G^0$ [kJ mol^{-1}]	97.6	-272.1
Reverse ($CH_4 \leftarrow CO$)		
$\Delta_r H^0$ [kJ mol^{-1}]	-214.6	-225.9
$\Delta_r S^0$ [kJ mol^{-1} K^{-1}]	-0.234	-0.249
$\Delta_r G^0$ [kJ mol^{-1}]	-97.6	272.1

and the system will reach a state of equilibrium. Appendix C.4 explains in more detail why the minimum of the Gibbs energy relates to an equilibrium state.

By solving for the set of chemical abundances that minimise the Gibbs energy of the system we can find the chemical equilibrium abundances for a given set of thermodynamic conditions. Whilst chemical equilibrium is generally not a good description for the chemical composition of an atmosphere, it can be a useful starting point, and indeed many atmosphere models include schemes that solve for the chemical equilibrium abundances through minimisation of the Gibbs energy [e.g. Burrows and Sharp, 1999, Fortney et al., 2005, Venot et al., 2012, Blecic et al., 2015].

This method is particularly powerful as the complicated reaction pathways (for instance, the many elementary reactions involved in the conversion of CH_4 and CO) that are important in the interconversion of the chemical species in the system do not need to be known. Instead, only the enthalpies and entropies of each chemical species as a function of temperature, from which we can calculate the Gibbs energy of the system, are required. The method is therefore much simpler to implement, as well as more flexible in terms of adding and removing chemical species from the mixture, than the alternative method of chemical kinetics (the topic of the next section) that deals with the individual chemical reactions.

However, implicit in the method is the assumption of local chemical equilibrium which generally is not an accurate description of planetary atmospheres. To include non-equilibrium effects, such as mixing, transport and photochemical dissociation, we must instead consider the method of chemical kinetics, the focus of the next section.

2.4 Chemical kinetics

In this chapter we have so far introduced the idea of the interconversion of one chemical species into another and how we can determine the equilibrium composition using the Gibbs energy of the system. In this section we introduce an alternative

method of solving for the chemical composition, one that deals with the individual chemical reactions involved in the conversion of each species in the system: chemical kinetics.

2.4.1 The continuity equation

The fundamental equation behind the method of chemical kinetics is the "continuity equation"

$$\frac{\partial n_j}{\partial t} = P_j - L_j - \nabla\Phi_j, \tag{2.11}$$

where $j = 1, \ldots, J$ and J is the number of chemical species in the system; n_j is the number density of species j; P_j and L_j are the production and loss terms, respectively; $\nabla\Phi_j$ is a term that describes the net transport of the species j.

This continuity equation describes the net rate of change of each species j due to the production and loss of the species due to the various chemical reactions and the net transport of species j into the system. Each chemical species in the system is described by a continuity equation and the total system is therefore described by J coupled continuity equations.

2.4.2 Thermochemical reactions: the production and loss terms

In the absence of non-equilibrium processes (e.g. transport, photochemistry) the production and loss terms P_j and L_j are determined by the sum of all of the thermochemical reactions in which j appears as either a product or reactant, respectively.

For a general chemical reaction aA + bB $\rightarrow$ cC + dD, where X represents a chemical species with a stoichiometric value x, the rate of reaction R^* can be described by the following rate law

$$R^* = -\frac{1}{a}\frac{\partial n_{\mathrm{A}}}{\partial t} = -\frac{1}{b}\frac{\partial n_{\mathrm{B}}}{\partial t} = \frac{1}{c}\frac{\partial n_{\mathrm{C}}}{\partial t} = \frac{1}{d}\frac{\partial n_{\mathrm{D}}}{\partial t} = k n_{\mathrm{A}}^a n_{\mathrm{B}}^b, \tag{2.12}$$

where k is the bimolecular rate constant [cm^3 s^{-1}] and n_{A} and n_{B} are the number densities [cm^{-3}] of the reactants A and B, respectively.

For the general reversible reaction aA + bB $\leftrightarrow$ cC + dD, where the reaction can proceed in both directions, we have both the forward rate R_f^* and the reverse rate R_r^*

$$\begin{aligned} R_{\mathrm{f}}^* &= k_{\mathrm{f}} n_{\mathrm{A}}^a n_{\mathrm{B}}^b \\ R_{\mathrm{r}}^* &= k_{\mathrm{r}} n_{\mathrm{C}}^c n_{\mathrm{D}}^d, \end{aligned} \tag{2.13}$$

where k_f and k_r are the forward and reverse rate constants.

Overall, for this simple system with four species and one reversible reaction, we can write the continuity equation for each species

$$\begin{aligned}
\frac{1}{a}\frac{\partial n_{\mathrm{A}}}{\partial t} &= k_{\mathrm{r}} n_{\mathrm{C}}^{c} n_{\mathrm{D}}^{d} - k_{\mathrm{f}} n_{\mathrm{A}}^{a} n_{\mathrm{B}}^{b} = \frac{1}{a}\left(P_{\mathrm{A}} - L_{\mathrm{A}}\right) \\
\frac{1}{b}\frac{\partial n_{\mathrm{B}}}{\partial t} &= k_{\mathrm{r}} n_{\mathrm{C}}^{c} n_{\mathrm{D}}^{d} - k_{\mathrm{f}} n_{\mathrm{A}}^{a} n_{\mathrm{B}}^{b} = \frac{1}{b}\left(P_{\mathrm{B}} - L_{\mathrm{B}}\right) \\
\frac{1}{c}\frac{\partial n_{\mathrm{C}}}{\partial t} &= -k_{\mathrm{r}} n_{\mathrm{C}}^{c} n_{\mathrm{D}}^{d} + k_{\mathrm{f}} n_{\mathrm{A}}^{a} n_{\mathrm{B}}^{b} = \frac{1}{c}\left(P_{\mathrm{C}} - L_{\mathrm{C}}\right) \\
\frac{1}{d}\frac{\partial n_{\mathrm{D}}}{\partial t} &= -k_{\mathrm{r}} n_{\mathrm{C}}^{c} n_{\mathrm{D}}^{d} + k_{\mathrm{f}} n_{\mathrm{A}}^{a} n_{\mathrm{B}}^{b} = \frac{1}{d}\left(P_{\mathrm{D}} - L_{\mathrm{D}}\right). \qquad (2.14)
\end{aligned}$$

For some initial values of n_{A}, n_{B}, n_{C} and n_{D} we can solve this system of coupled ordinary differential equations to find the steady-state solution. In the absence of any non-equilibrium processes, this will correspond to the chemical equilibrium composition.

In a more complicated system with multiple reversible reactions and more species, the production and loss of each species due to each reaction are simply summed together.

2.4.3 The equilibrium constant

In the specific case of chemical equilibrium, the forward and reverse reactions must be balanced; i.e. $R_{\mathrm{f}}^{*} - R_{\mathrm{r}}^{*} = 0$. For the example chemical reaction (Section 2.4.2), from Eq. (2.13) we can see that this means

$$\frac{k_f}{k_r} = \frac{n_{\mathrm{C}}^{\mathrm{c}} n_{\mathrm{D}}^{\mathrm{d}}}{n_{\mathrm{A}}^{\mathrm{a}} n_{\mathrm{B}}^{\mathrm{b}}} = K_{\mathrm{eq}}, \qquad (2.15)$$

where we have introduced the *equilibrium constant* K_{eq} as the ratio of the forward and reverse rate constants. The equilibrium constant is related to the Gibbs energy of reaction (see Appendix C.5) as

$$K_{\mathrm{eq}} = \exp\left(-\frac{\Delta_r G}{RT}\right), \qquad (2.16)$$

where R is the molar gas constant.

The independent determination of K_{eq} from the Gibbs energy is very important as it allows for k_r to be determined with knowledge of k_f, using Eq. (2.15), and vice versa. Indeed, often it is only possible to accurately measure the rate of the exothermic (forward) reaction and the rate of the endothermic (reverse) reaction is usually determined from k_f and K_{eq}; a process termed "thermochemically reversing" the reaction. For example, the chemical network of Venot et al. [2012] includes

only the forward reaction rates k_f for the majority of the reactions and the reverse reaction rate k_r must be computed from $K_{\rm eq}$ and k_f.

The above formalism for $K_{\rm eq}$ is only valid when the number of reactants $N_{\rm r}$ equals the number of products $N_{\rm p}$. For cases where $N_{\rm r} \neq N_{\rm p}$ a pressure correction term must be applied [Visscher and Moses, 2011]. Redefining the equilibrium constant in terms of partial pressure, rather than number density,

$$K_P = \frac{P_{\rm C}^c P_{\rm D}^d}{P_{\rm A}^a P_{\rm B}^b} = \exp\left(-\frac{\Delta_{\rm r}{\rm G}}{\rm RT}\right), \tag{2.17}$$

where $P_{\rm j}^x$ is the partial pressure of species j with stoichiometric coefficient x. Now replacing the partial pressure with number density (Eq. (2.1)) we find

$$K_P = \frac{n_{\rm C}^c n_{\rm D}^d}{n_{\rm A}^a n_{\rm B}^b}\left(\frac{P}{n}\right)^{(c+d-a-b)} = K_{\rm eq}\left(\frac{P}{n}\right)^{(c+d-a-b)} \tag{2.18}$$

Note that when $N_{\rm r} = N_{\rm p}$ this formalism reverts to $K_P = K_{\rm eq}$.

Using the definition of $K_{\rm eq}$ (Eq. (2.16)) and rearranging for $k_{\rm r}$, we can finally express k_r in terms of k_f and $\Delta_r G$

$$k_r = \frac{k_f}{K_P}\left(\frac{P}{n}\right)^{N_p - N_r} = \frac{k_f}{\exp\left(-\frac{\Delta_{\rm r}{\rm G}}{\rm RT}\right)}\left(k_B T\right)^{N_p - N_r}. \tag{2.19}$$

2.4.4 The rate constant: bimolecular reactions

The rate constant k referred to in previous sections quantifies the rate at which a reaction proceeds. In this section we introduce two theories that explain the physical meaning of the rate constant and detail the calculation of k for bimolecular reactions. Later sections describe the method for unimolecular, three-body and photodissociation reactions.

A bimolecular reactions consists of two reactants forming two products: A + B $\rightarrow$ C + D. Experimentally, such bimolecular reactions are observed to follow the *Arrhenius equation*

$$k = A\exp\left(-\frac{E_{\rm a}}{RT}\right), \tag{2.20}$$

where $E_{\rm a}$ is the activation energy, or the energy required for the reaction to proceed, and A is a pre-exponential factor. Here we will introduce two theories behind this empirical relation: the collision theory and the transition state theory.

Collision theory

In the collision theory it is proposed that for a reaction to occur the reactants must collide with each other and the energy of that collision must be at least as large as

the activation energy E_a.

Assuming two spherical reactants, with radii r_A and r_B, the cross section of collision σ_col is given by

$$\sigma_\mathrm{col} = \pi \left(r_\mathrm{A} + r_\mathrm{B}\right)^2. \tag{2.21}$$

The rate of collisions k_col between the reactants A and B is then given by [Yung and DeMore, 1999]

$$k_\mathrm{col} = \int\int \sigma_\mathrm{col}(w) f(v_\mathrm{A}) f(v_\mathrm{B}) w d^3 a_\mathrm{A} d^3 v_\mathrm{B},$$

where f are the normalised molecular velocity distributions and $w = |\vec{v_\mathrm{A}} - \vec{v_\mathrm{B}}|$. Assuming the Maxwell-Boltzmann distribution, at a temperature T the double integral can be evaluated as

$$k_\mathrm{col} = \sigma_\mathrm{col} v = \sigma_\mathrm{col} \sqrt{\frac{8 k_B T (\bar{m}_\mathrm{A} + \bar{m}_\mathrm{B})}{\pi \bar{m}_\mathrm{A} \bar{m}_\mathrm{B}}}, \tag{2.22}$$

where v is the mean speed of the particles and $\bar{m}_\mathrm{A}$ and $\bar{m}_\mathrm{B}$ are the masses of A and B in kg, respectively. Assuming a Boltzmann distribution of energies, the fraction of molecules with the required energy E_a is proportional to $\exp\left(-\frac{E_\mathrm{a}}{RT}\right)$. Therefore, the bimolecular rate coefficient k as described by collision theory is

$$k = \sigma_\mathrm{col} v \exp\left(-\frac{E_\mathrm{a}}{RT}\right). \tag{2.23}$$

Comparing the collision theory rate constant with the empirical Arrhenius equation (Eq. (2.20)), we see that the empirical pre-exponential factor A corresponds with the rate of collisions $\sigma_\mathrm{col} v$. This theory successfully explains several key observations. Increasing the concentration of reactants will directly increase the rate of reaction. In addition, increasing the temperature will also increase the rate of reaction by (1) increasing the rate of collisions and (2) increasing the mean energy per molecule leading to a higher fraction of collisions that match or exceed the activation energy.

However, the collision theory fails in predicting accurate rate coefficients. It is found that the experimentally measured A is typically much less than $\sigma_\mathrm{col} v$ [Wayne, 1991]; collision theory overpredicts the rate constant. In addition, the collision rate term shows dependence on the temperature T, $\sigma_\mathrm{col} v \propto T^{\frac{1}{2}}$, however, the temperature dependence of A is unobtainable from experiment due to the dominating exponential term. Therefore, it may not be accurate to extrapolate A over large temperature ranges.

The neglect of internal motions of the molecules (translations, vibrations and rotations) is ultimately responsible for the failure of collision theory in predicting accurate rate coefficients [Wayne, 1991].

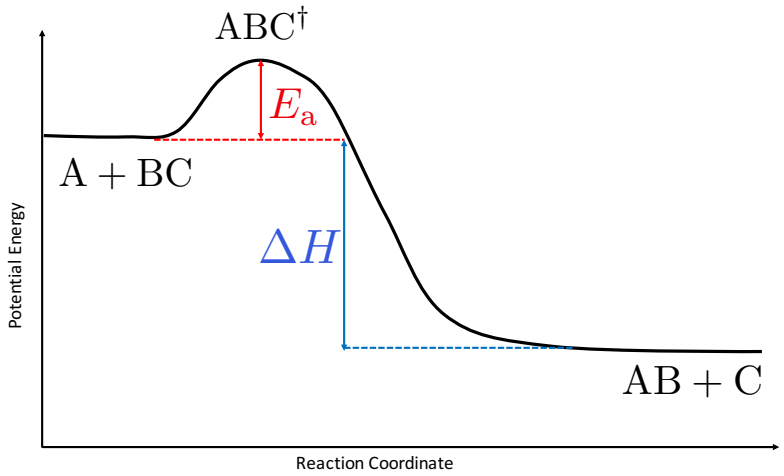

Figure 2.1: The potential energy as a function of the reaction coordinate. Adapted from Wayne [1991], Yung and DeMore [1999]

Transition state theory

A more detailed theory has the potential to provide far more accurate numerical predictions of rate coefficients, as well as an alternative idea about the physical process occuring during a reaction; the transition state theory (TST).

TST states that when two reactants collide with sufficient energy (E_a) they do not immediately form the products but instead form an intermediate activated complex $ABC^\dagger$. The activated complex can then either fall apart and revert back to the initial reactants, or proceed to a successful reaction. For the reactants A and BC this can be written

$$A + BC \rightleftharpoons ABC^\dagger \rightarrow AB + C. \tag{2.24}$$

Fig. 2.1 illustrates the formation of the activated complex. Initially the reactants A and BC are separate and they require an input of energy to overcome the potential energy barrier E_a to form the activated complex $ABC^\dagger$. It is now energetically favourable for the activated complex to form the lower energy products, releasing an amount of energy $E_a + \Delta H$, where ΔH is the enthalpy of reaction. Therefore, though overall the reaction is exothermic, releasing energy, an initial input of energy is required to form the activated complex. In addition, this explains why the reverse of the reaction is far less successful, since it requires a much greater input of energy, $E_a + \Delta H$, to form the activated complex.

TST can also provide numerical predictions of the rate coefficients, yet the theory is not yet developed such that this can be put into practice in most cases

[Yung and DeMore, 1999]. The rate coefficient as calculated from TST is given by [Wayne, 1991]

$$k_{\mathrm{TST}} = \frac{k_B T}{h} \frac{Q(ABC^{\dagger})}{Q(A)Q(BC)} \exp\left(-\frac{E}{RT}\right), \tag{2.25}$$

where h is Planck's constant, E is the enthalpy of the reaction and Q are the partition functions. These partition functions account for the translation, vibration and rotation effects neglected in the collision theory. However, these partition functions cause difficulty in this approach, as they are often unknown [Wayne, 1991], particularly for the activated complex.

However, TST does motivate an important adaptation to the Arrhenius equation. Eq. (2.25) can be rewritten as the *modified* Arrhenius equation [Wayne, 1991]

$$k = A' T^n \exp\left(-\frac{E}{RT}\right) \tag{2.26}$$

where A' is now the temperature-independant pre-exponential factor and n is an exponent that can be estimated from TST. For reactions involving only monatomic species $n = 1/2$, as predicted by collision theory assuming reactants as hard spheres [Wayne, 1991].

Rate coefficients for bimolecular reactions

In summary, the rate coefficients for bimolecular reactions can be expressed using the modified Arrhenius equation (2.26) which has roots in empirically observed trends but informed by TST. TST states that an intermediate complex is formed from two reactants that can proceed to form the products or decay back into the reactants.

2.4.5 Three-body reactions

When two reactants collide with adequate energy an intermediate complex is formed, as stated by TST. The intermediate complex often possesses a relatively large amount of energy. One method of releasing this energy is to dissociate to form two products, as in the case of a bimolecular reaction (Section 2.4.4). Another method of releasing this energy is to interact with a third-body that will remove this excess energy as translational energy, stabilising the intermediate complex. These reaction types are termed three-body reactions and the net three-body reaction can be written generally as

$$\mathrm{A} + \mathrm{B} + \mathrm{M} \leftrightarrow \mathrm{AB} + \mathrm{M}, \tag{2.27}$$

where M is some third body. The net rate law for this reaction can be written

$$\frac{\partial n_{\mathrm{AB}}}{\partial t} = k n_{\mathrm{A}} n_{\mathrm{B}} n_{\mathrm{M}}, \tag{2.28}$$

where k is the three-body rate constant [$\mathrm{cm}^6\ \mathrm{s}^{-1}$].

This net reaction actually contains three elementary steps

$$\begin{aligned} \mathrm{A} + \mathrm{B} &\rightarrow \mathrm{AB}^\dagger \\ \mathrm{AB}^\dagger &\rightarrow \mathrm{A} + \mathrm{B} \\ \mathrm{AB}^\dagger + \mathrm{M} &\rightarrow \mathrm{AB} + \mathrm{M}, \end{aligned}$$

which are association, decay and stabilisation, with rate constants k_a, k_b and k_c, respectively. Following TST, the intermediate complex $\mathrm{AB}^\dagger$ is in a state of equilibrium (steady-state), leading to the balanced rate law for $\mathrm{AB}^\dagger$

$$k_a n_\mathrm{A} n_\mathrm{B} = k_b n_{\mathrm{AB}^\dagger} + k_c n_{\mathrm{AB}^\dagger} n_\mathrm{M}. \tag{2.29}$$

We can also write the rate law for AB as

$$\frac{\partial n_\mathrm{AB}}{\partial t} = k_c n_{\mathrm{AB}^\dagger} n_\mathrm{M}. \tag{2.30}$$

Solving equation (2.29) for $n_{\mathrm{AB}^\dagger}$ and substituting into equation (2.30) yields the rate law for AB derived from the three elementary reactions

$$\frac{\partial n_\mathrm{AB}}{\partial t} = \frac{k_a k_c n_\mathrm{A} n_\mathrm{B} n_\mathrm{M}}{k_b + k_c n_\mathrm{M}}. \tag{2.31}$$

Comparing the rate law derived from the elementary reactions (Eq. (2.31)) with the rate law determined from the net reaction (Eq. (2.28)) we see that the three-body rate constant k can be written

$$k = \frac{k_a k_c}{k_b + k_c n_\mathrm{M}}. \tag{2.32}$$

This formulation is known as the *Lindemann rate constant*.

Equation (2.32) is often considered in two extreme scenarios. Firstly at low pressures, where n_M is small, equation (2.32) reduces to

$$\lim_{n_\mathrm{M} \to 0} k = k_0 = \frac{k_a k_c}{k_b}. \tag{2.33}$$

In this limit the rate coefficient k_0 depends on the lifetime of the intermediate complex. On the other hand, at high pressures where n_M is large, equation (2.32) reduces to

$$\lim_{n_\mathrm{M} \to \infty} k = k_\infty = \frac{k_a}{n_\mathrm{M}}. \tag{2.34}$$

and the three-body rate becomes effectively a bimolecular rate law

$$\lim_{n_{\mathrm{M}}\to\infty} \frac{\partial n_{\mathrm{AB}}}{\partial t} = k_\infty n_{\mathrm{A}} n_{\mathrm{B}} n_{\mathrm{M}} = k_a n_{\mathrm{A}} n_{\mathrm{B}}$$

Physically, this means that in high pressure regions, where there is a plentiful supply of particles to act as M, the intermediate complex will be very quickly stabilised once formed. On the other hand, at low pressures there are fewer particles to act as third bodies and the lifetime of the intermediate complex becomes more important, as the chance of a rapid stabilisation event by a third body is lower.

Troe formalism

The Troe formalism is used to express the three-body rate constant at any pressure. The Troe rate constant k_{Troe} is given by

$$k_{\mathrm{Troe}} = k_\infty \left(\frac{P_r}{1+P_r} \right) F, \tag{2.35}$$

where F is the Troe parameter and P_r is the 'reduced pressure',

$$P_r = \frac{n_{\mathrm{M}} k_0}{k_\infty}.$$

The Troe parameter F can be calculated using

$$\log_{10} F = \frac{\log_{10} F_{cent}}{1 + \left[\frac{\log_{10}(P_r)+c}{N - d(\log_{10}(P_r)+c)} \right]^2},$$

where

$$\begin{aligned} c &= -0.4 - 0.67 \log_{10}(F_{cent}) \\ N &= 0.75 - 1.27 \log_{10}(F_{cent}) \\ d &= 0.14 \end{aligned}$$

and

$$F_{cent} = (1-a) \exp\left(-\frac{T}{T^{***}} \right) + a \exp\left(-\frac{T}{T^{*}} \right) + \exp\left(-\frac{T^{**}}{T} \right),$$

where a, T^{***}, T^{*} and T^{**} are species dependent parameters.

2.4.6 Unimolecular reactions

The unimolecular dissociation of a chemical species can be written generally as

$$\mathrm{AB} \rightarrow \mathrm{A} + \mathrm{B}. \tag{2.36}$$

However, once again this simple net reaction hides some of the complexity.

In order for the molecule AB to dissociate it must first gain energy. In a unimolecular reaction this will be through collision with other AB molecules and we write the three elementary steps as

$$\begin{aligned} \mathrm{AB} + \mathrm{AB} &\rightarrow \mathrm{AB}^{\dagger} + \mathrm{AB} \\ \mathrm{AB}^{\dagger} + \mathrm{AB} &\rightarrow \mathrm{AB} + \mathrm{AB} \\ \mathrm{AB}^{\dagger} &\rightarrow \mathrm{A} + \mathrm{B}, \end{aligned}$$

which are activation, deactivation and decay with rate constants k_a, k_b and k_c, respectively.

Performing a similar analysis as for the three-body reactions, we assume that the intermediate complex is in a state of equilibrium and we write the net rate law for $\mathrm{AB}^{\dagger}$

$$k_a n_{\mathrm{AB}} n_{\mathrm{AB}} = k_b n_{\mathrm{AB}^{\dagger}} n_{\mathrm{AB}} + k_c n_{\mathrm{AB}^{\dagger}}, \tag{2.37}$$

and the rate law for A (or, equivalently, B) from the elementary reactions is

$$\frac{\partial n_{\mathrm{A}}}{\partial t} = k_c n_{\mathrm{AB}^{\dagger}}. \tag{2.38}$$

Now, rearranging Eq. (2.37) for $n_{\mathrm{AB}^{\dagger}}$ and substituting into Eq. (2.38) we find

$$\frac{\partial n_{\mathrm{A}}}{\partial t} = \frac{k_c k_a n_{\mathrm{AB}} n_{\mathrm{AB}}}{k_b n_{\mathrm{AB}} + k_c}. \tag{2.39}$$

In the limit of low pressure this equation reduces to

$$\lim_{n_{\mathrm{AB}} \rightarrow 0} \frac{\partial n_{\mathrm{A}}}{\partial t} = k_a n_{\mathrm{AB}} n_{\mathrm{AB}}, \tag{2.40}$$

and the reaction is second-order in nature (scales as n_{AB}^2). In the limit of high pressure we have

$$\lim_{n_{\mathrm{AB}} \rightarrow \infty} \frac{\partial n_{\mathrm{A}}}{\partial t} = \frac{k_c k_a}{k_b} n_{\mathrm{AB}} = k n_{\mathrm{AB}}, \tag{2.41}$$

and the reaction is first-order in nature (scales as n_{AB}), resembling the simple net reaction.

2.4.7 Photochemical Reactions

The chemical reactions discussed so far result from the energy gained by molecules due to thermal collisions with other molecules. However, energy can also be acquired through absorption of radiative energy from a photon. Following an absorption

event, a molecule is excited to a higher energy state

$$\mathrm{AB} + h\nu \rightarrow \mathrm{AB}^{\dagger}. \tag{2.42}$$

Now in this higher energy state, the excited molecule can undergo one of several processes to release the energy and stabilise. These include re-emission of the energy as a photon or interacting with a third-body to remove the energy and stabilise. The process that results in chemical change is dissociation. In this case, the energy is used by the molecule to break the bonds and form two or more daughter products, i.e.

$$\mathrm{AB}^{\dagger} \rightarrow \mathrm{A} + \mathrm{B}. \tag{2.43}$$

The photon absorption rate [s^{-1}] is given by

$$J^{*} = \int \sigma(\lambda) F(\lambda) d\lambda, \tag{2.44}$$

where $\sigma(\lambda)$ is the absorption cross section [cm^2] and $F(\lambda)$ is the photon flux [photons $\mathrm{cm}^{-2}\ \mathrm{s}^{-1}$].

To convert Eq. (2.44) into a photodissociation rate we must include an additional term: the quantum yield $q(\lambda)$. The quantum yield quantifies the number of dissociation events per photon absorption and can be thought of as the probability for a molecule to dissociate, along a particular reaction pathway, following a photon absorption. The probability of a molecule to dissociate, and the products that result from that dissociation, can vary depending on the wavelength (or energy) of the absorbed photon.

The photodissociation rate is finally given by

$$J = \int \sigma(\lambda) q(\lambda) F(\lambda) d\lambda. \tag{2.45}$$

The values of $\sigma(\lambda)$ and $q(\lambda)$ can be determined through experiment, allowing for J to be calculated in atmosphere models due to a radiative flux $F(\lambda)$. However, often $\sigma(\lambda)$ and $q(\lambda)$ are only available from room temperature measurements and not for the high temperatures present in hot exoplanet atmospheres. Venot et al. [2013] included cross sections of CO_2 measured at high temperatures and found a significant impact on the resulting chemical abundances, demonstrating the potential inaccuracies introduced when extrapolating data over large temperature ranges.

2.4.8 Chemical Transport

The continuity equation (Eq. (2.11)) describes the rate of change of the amount of a chemical species j. In addition to chemical change, through thermochemical

or photochemical reactions, the number density of a species can evolve due to net transport of material into the system. This transport contribution is taken into account in the final term of Eq. (2.11), $\nabla\Phi_j$.

In real atmospheres, transport of particles results from large-scale three-dimensional circulations as well as smaller scale turbulent and diffusive processes. It is not possible to accurately represent these processes in a one-dimensional model, and so instead transport is assumed to occur only in the vertical direction and is assumed to be a diffusive process [e.g. Yung and DeMore, 1999].

The vertical transport of molecules can be thought of as a combination of three seperate processes. On the microscopic level, a temperature gradient will drive molecular mixing due to thermal diffusion. Particles in a hotter region of the atmosphere will have a higher mean velocity than particles in cooler regions. If the atmosphere is chemically different between these two regions, the heat flow induced by this temperature gradient will lead to chemical mixing. In addition, if there exists a concentration gradient in the atmosphere, then random molecular motions will act to maximise the entropy of the system by removing such a concentration gradient, leading to molecular diffusion.

On the macroscopic scale, dynamical motions of the atmosphere will lead to the mixing of chemical species. This process is often parameterised in one-dimensional models as a diffusive process that represents the small-scale mixing caused by turbulent eddy formation.

Combining these three diffusion proccesses into one vertical flux term we can write [e.g. Gladstone et al., 1996] the flux of the particles of species j as

$$\Phi_j = -D_j \left(\frac{\partial n_j}{\partial z} + \frac{n_j}{H_j} + \frac{n_j(1+\alpha_j^{\text{th}})}{T}\frac{\partial T}{\partial z} \right) - K_{zz} \left(\frac{\partial n_j}{\partial z} + \frac{n_j}{H_a} + \frac{n_j}{T}\frac{\partial T}{\partial z} \right), \quad (2.46)$$

where H_j and H_a are the individual and bulk scale heights, respectively, α_j is the thermal diffusion parameter and K_{zz} and D_j are the eddy diffusion and molecular diffusion coefficients, respectively. This can be rewritten in terms of the mole fraction

$$\Phi_j = -nD_j \left(\frac{\partial f_j}{\partial z} - \frac{f_j}{H_a} + \frac{f_j}{H_j} + \frac{f_j \alpha_j^{\text{th}}}{T}\frac{\partial T}{\partial z} \right) - nK_{zz} \left(\frac{\partial f_j}{\partial z} \right), \quad (2.47)$$

where we have used the hydrostatic equation to simply the expression

$$\frac{\partial n}{\partial z} = -\frac{n}{H_a} - \frac{n}{T}\frac{\partial T}{\partial z} \quad (2.48)$$

The molecular diffusion coefficient can be calculated via the kinetic theory of

gases [e.g. Wayne, 1991]

$$D = \frac{1}{3}\bar{c}\lambda_m, \tag{2.49}$$

where $\bar{c}$ is the mean molecular velocity $\sqrt{3k_BT/\bar{m}}$, where $\bar{m}$ is the mass of the molecule, and λ_m is the mean free path of the molecule

$$\lambda_m = \frac{1}{\sqrt{2}\pi d^2}\frac{k_BT}{P}, \tag{2.50}$$

where d is the molecular diameter. From this we can see that D_j is inversely proportional to the pressure and we can expect the molecular diffusion to become more important with increasing altitude/decreasing pressure.

Unlike the molecular diffusion coefficient, the eddy diffusion coefficient is very poorly constrained. In previous works, K_{zz} has been estimated from wind velocities derived from 3D general circulation models as $K_{zz} = w(z)L(z)$ [e.g. Moses et al., 2011] where $w(z)$ is the horizontally averaged vertical wind velocity and $L(z)$ is a length scale usually taken to be equivalent to the atmospheric scale height $L(z) \sim H$. An alternative approach has been to produce a parameterisation based on the advection of passive tracers within a GCM [Parmentier et al., 2013]. The value of K_{zz} is typically in the range of $10^6 - 10^{11}$ cm^2 s^{-1} [e.g. Moses et al., 2011, Miguel and Kaltenegger, 2014].

2.5 Conclusions

In this chapter we have introduced various important aspects of atmospheric chemistry that are key to the work presented in the following chapters. We have

- defined the various quantities that can be used to describe the abundance of a chemical species
- described how the elemental composition of a gas giant atmosphere is defined, usually as some multiple of the Solar elemental composition (e.g. metallicity and carbon to oxygen ratio)
- introduced the idea of chemical transformation and the determination of the chemical equilibrium composition by minimising the Gibbs energy
- introduced the idea of chemical kinetics and described the methods and theory behind calculating the rate constants for unimolecular, bimolecular and three-body reactions
- introduced the non-equilibrium processes of photodissociation and transport

In Chapter 3 we will describe in detail the implementation of numerical schemes that solve for the chemical composition using both the Gibbs energy minimisation and chemical kinetics methods in the model ATMO, before applications of this model to the atmospheres of hot Jupiters are presented in Chapter 4.

Chapter 3

Implementing and Testing the ATMO Chemistry Schemes

In this chapter the implementation of two chemistry schemes in the 1D atmosphere model ATMO is described. The first scheme solves for the chemical abundances consistent with local chemical equilibrium by minimising the Gibbs free energy of the system. The second scheme deals with chemical kinetics and solves a continuity equation for the steady-state solution, allowing for the inclusion of non-equilibrium processes such as vertical transport and photochemistry.

As well as a description of these schemes, we present various tests in order to benchmark and validate their implementation within the code by comparing with previously published works.

We begin by briefly introducing the 1D atmosphere model ATMO in Section 3.1. We then describe the implementation of the Gibbs energy minimisation scheme in Section 3.2 and present several tests to validate the scheme in Section 3.3. We then describe the implementation of the chemical kinetics scheme including the vertical transport and photodissociation methods in Section 3.4 and then test this by reproducing the previously published results of HD 209458b [Venot et al., 2012, Moses et al., 2011] in Section 3.5. Finally, the findings of this chapter are summarised in Section 3.6.

3.1 The 1D atmosphere model ATMO

ATMO is a 1D atmosphere code written in Fortran 90 that has several capabilities, including:

- solving for the pressure-temperature profile consistent with hydrostatic equilibrium and radiative-convective equilibrium
- solving for the equilibrium and non-equilibrium chemical composition for a given pressure-temperature profile
- solving for the equilibrium and non-equilibrium composition consistently with the pressure-temperature profile
- calculating the synthetic transmission and emission spectrum for a given pressure-temperature profile and abundance profiles of the chemical species.

The code is modular in design and the primary modules are the radiative transfer, opacity and chemistry modules, with these being the most sophisticated and physics-oriented sections of the code. Additional modules contain routines related to input/output, numerical solvers and other utilities.

The origins of ATMO can be traced to an IDL code, written by Wolfgang Hayek, which solved purely for the radiative transfer in stellar atmospheres and was based on the `MARCS` code [Gustafsson et al., 2008]. However, the code in this form was never fully applied or published. At this point Pascal Tremblin performed a major rewriting of the code, converting it into Fortran 90, and included new modules to handle the calculation of opacities, using the correlated-k method, and also modules to solve for the chemical abundances using two different methods: Gibbs energy minimisation and chemical kinetics. From this point, the application of the code has been focused on sub-stellar atmospheres; brown dwarfs and gas-giant exoplanets.

In this thesis we focus on the treatment of chemistry in this code. In particular we describe, test and apply the coupling of the chemical kinetics and radiative-convective equilibrium calculations, in order to consistently calculate the chemical abundances with the temperature profile. Pascal Tremblin wrote the majority of the code that solves for the chemical abundances using both the Gibbs energy minimisation and the chemical kinetics methods. I wrote the section of code that calculates the vertical mixing and the photodissociation rates, and was involved with many other small code developments.

3.2 Implementing the Gibbs energy minimisation scheme

3.2.1 Gibbs energy and the chemical potential

The Gibbs energy of a system of J chemical species, at constant pressure and temperature, is given by

$$G = \sum^{J} \mu_j N_j, \tag{3.1}$$

where μ_j is the chemical potential of species j and N_j is the number of moles of species j per kilogram of the total mixture. At constant temperature, pressure and composition, μ_j is defined as the change in G with respect to N_j

$$\mu_j = \left(\frac{\partial G}{\partial N_j}\right)_{T,P,N_{i\neq j}}. \tag{3.2}$$

For gas-phase species, where $j \leq J_g$ and J_g is the number of gas-phase species in the mixture, μ_j at any pressure and temperature can be calculated from the standard chemical potential μ_j^0 with the relation

$$\mu_j\left(T,P\right) = \mu_j^0\left(T\right) + RT\ln P_j, \tag{3.3}$$

where P_j is the partial pressure of the species j. The standard chemical potential is the value of μ_j at the standard reference pressure. It is convenient to express Eq. (3.3) in terms of the total pressure of the system P and the mole fraction of the species

$$\mu_j\left(T,P\right) = \mu_j^0\left(T\right) + RT\ln P + RT\ln\left(\frac{N_j}{N}\right), \tag{3.4}$$

where we have used the relation $P_j = P(N_j/N)$ and N is the total number of moles per kilogram of mixture.

For solid and liquid phase species μ_j at any temperature and pressure is simply equal to the standard chemical potential

$$\mu_j = \mu_j^0, \tag{3.5}$$

where $j = J_g + 1, \ldots, J$.

3.2.2 Condition for chemical equilibrium

The condition for chemical equilibrium is that G is minimised for the system (see Appendix C.4). This minimisation is performed under the constraint of conservation

of the total amount of each element (C, O, N, H, etc) in the mixture of chemical species (CH_4, H_2O, NH_3, etc). Conservation of the elements can be expressed mathematically by

$$\sum_{j=1}^{J} a_{ij} N_j - b_i^0 = 0, \tag{3.6}$$

where $i = 1, ..., I$ and I is the total number of different elements in the mixture, a_{ij} is the integer number of atoms of element i per species j and b_i^0 is the total number of atoms of element i per kilogram of the mixture. b_i^0 can be written as

$$b_i^0 = \frac{B_i}{\sum_{i=1}^{I} B_i m_i},$$

where B_i is the number fraction of element i in the mixture and m_i is the elemental mass of element i. Eq. (3.6) ensures that the sum of the number of atoms of element i which are distributed amongst all species j is equal to the total number of atoms of that element in the mixture.

The method of Lagrange multipliers is used to minimise G (Eq. (3.1)) under the constraint of elemental conservation (Eq. (3.6)). A brief description of the method of Lagrange multipliers is included in Appendix A.

We begin by defining a new Lagrange function

$$\bar{G} = G + \sum_{i=1}^{I} \lambda_i \left(\sum_{j=1}^{J} a_{ij} N_j - b_i^0 \right),$$

where λ_i are the Lagrangian multipliers, with $i = 1, \ldots, I$. Substituting in Eq. (3.1) then taking the derivative of $\bar{G}$ with respect to the independent variables N_j and λ_i and finally equating to zero yields the minimum of the Lagrange function

$$\nabla \bar{G} = \sum_{j=1}^{J} \left(\mu_j + \sum_{i=1}^{I} \lambda_i a_{ij} \right) \partial N_j + \sum_{i=1}^{I} \left(\sum_{j=1}^{J} a_{ij} N_j - b_i^0 \right) \partial \lambda_i = 0.$$

Since the variations due to N_j and λ_i are independent [Gordon and McBride, 1994] we obtain the pair of equations

$$\begin{aligned} \mu_j + \sum_{i=1}^{I} \lambda_i a_{ij} &= 0 \\ \sum_{j=1}^{J} a_{ij} N_j - b_i^0 &= 0, \end{aligned} \tag{3.7}$$

where we have returned the original element conservation equation (Eq. (3.6)) and derived a new equation which we will call the 'molecule equation'. To this pair of

equations we add a third which describes the total number of moles per kilogram N as the sum of N_j over *only* the gas-phase species $j \leq J_g$,

$$N - \sum_{j=1}^{J_g} N_j = 0. \tag{3.8}$$

This last expression assumes that condensed species do not count towards the molecular weight of the mixture [Gordon and McBride, 1994]. Finally, for convenience we rewrite Eq. (3.7) as a dimensionless relation by dividing by RT

$$\frac{\mu_j}{RT} + \sum_{i=1}^{I} \pi_i a_{ij} = 0, \tag{3.9}$$

where $\pi_i = \lambda_i / RT$.

We have now three sets of equations that describe the chemical system: Eq. (3.9), the molecule equations, which describe the contribution of each species to G, Eq. (3.6), the element conservation equations, which ensure that the total number of atoms of each element is conserved in the mixture and finally Eq. (3.8), which describes the total number of moles per kilogram of mixture as the sum of the number of moles per kilogram of the gas-phase species.

The problem now is to find the set of values for N_j, N and π_i that satisfy these equations simultaneously, and this is solved for using a Newton-Raphson iteration method.

3.2.3 The Newton-Raphson iterations

To find the set of N_j, N and π_i that satisfy Eq. (3.9), Eq. (3.8) and Eq. (3.6) we iteratively improve the values by finding corrections to the current values. The first step is to reformulate Eq. (3.9), Eq. (3.8) and Eq. (3.6) to contain the correction terms ΔN_j, ΔN and $\Delta \lambda_i$. In practice, following Gordon and McBride [1994], we find corrections for N_j and N in terms of the logarithm $\Delta \ln N_j$ and $\Delta \ln N$ to improve stability towards convergence as N_j and N can vary by many orders of magnitude. This approach is only applied for the gas-phase species, as it cannot be applied to the condensed-phase species as they can have abundances of zero.

To introduce the correction terms we state that the improved values in the next iteration $k+1$ are determined from the values in the current iteration k by

$$\ln N^{k+1} = \ln N^k + \Delta \ln N \tag{3.10}$$

$$\pi_i^{k+1} = \pi_i^k + \Delta \pi_i \tag{3.11}$$

for N and π_i, then for N_j for the gas-phase species ($j = 1, \ldots, J_g$)

$$\ln N_j^{k+1} = \ln N_j^k + \Delta \ln N_j, \tag{3.12}$$

and finally for the condensed-phase species ($j = J_g + 1, \ldots, J$)

$$N_j^{k+1} = N_j^k + \Delta N_j. \tag{3.13}$$

The elemental conservation equations

We begin with the element conservation equations for gas-phase species and re-express it in terms of the improved value $\ln N_j^{k+1}$

$$\sum_{j=1}^{J_g} a_{ij} \exp(\ln N_j^{k+1}) - b_i^0 = 0. \tag{3.14}$$

By substituting in Eq. (3.12) and assuming that $\exp(\Delta \ln N_j) \sim 1 + \Delta \ln N_j$ we find

$$\begin{aligned} \sum_{j=1}^{J_g} a_{ij} N_j^k + \sum_{j=1}^{J_g} a_{ij} N_j^k \Delta \ln N_j - b_i^0 = 0 \\ \sum_{j=1}^{J_g} a_{ij} N_j^k \Delta \ln N_j = b_i^0 - \sum_{j=1}^{J_g} a_{ij} N_j^k \end{aligned} \tag{3.15}$$

The same process is performed for condensed-phase species, without taking the logarithm of N_j, and substituting instead Eq. (3.13), yielding

$$\sum_{j=J_g+1}^{J} a_{ij} \Delta N_j = b_i^0 - \sum_{j=J_g+1}^{J} a_{ij} N_j^k \tag{3.16}$$

We now have a set of linear equations given by Eq. (3.15) and Eq. (3.16) of the form $Ax = b$, where x are the unknown correction variables $\Delta \ln N_j$ and ΔN_j for gas-phase and condensed-phase species, respectively.

The total number of moles equation

The same operation as above is performed for the total number of moles equation, firstly re-expressing Eq. (3.8) in terms of the improved variables $\ln N^{k+1}$ and $\ln N_j^{k+1}$ and then substituting in Eqs. (3.10) and (3.12)

$$
\begin{aligned}
N - \sum_{j=1}^{J_g} N_j &= 0 \\
\exp(\ln N^{k+1}) - \sum_{j=1}^{J_g} \exp(\ln N_j^{k+1}) &= 0 \\
N^k \exp(\Delta \ln N) - \sum_{j=1}^{J_g} N_j^k \exp(\Delta \ln N_j) &= 0 \\
N^k + N^k \Delta \ln N - \sum_{j=1}^{J_g} N_j^k - \sum_{j=1}^{J_g} N_j^k \Delta \ln N_j &= 0 \\
N^k \Delta \ln N - \sum_{j=1}^{J_g} N_j^k \Delta \ln N_j &= \sum_{j=1}^{J_g} N_j^k - N^k. \qquad (3.17)
\end{aligned}
$$

The molecule equation

Finally, we rewrite the molecule equations in the same form. Starting from Eq. (3.9), for gas-phase species we substitue in Eq. (3.4)

$$\frac{\mu_j^0}{RT} + \ln N_j - \ln N + \ln P + \sum_{i=1}^{I} \pi_i a_{ij} = 0$$

and rewrite in terms of the improved variables

$$\frac{\mu_j^0}{RT} + \ln N_j^{k+1} - \ln N^{k+1} + \ln P + \sum_{i=1}^{I} \pi_i^{k+1} a_{ij} = 0.$$

Now, substituting in Eqs. (3.10) to (3.12) and rearranging we find

$$
\begin{aligned}
\frac{\mu_j^0}{RT} + \ln N_j^k + \Delta \ln N_j - \ln N^k - \Delta \ln N + \ln P + \sum_{i=1}^{I} \pi_i a_{ij}^k + \sum_{i=1}^{I} \Delta\pi_i a_{ij} &= 0 \\
\Delta \ln N_j - \Delta \ln N + \sum_{i=1}^{I} \Delta\pi_i a_{ij} = -\frac{\mu_j^0}{RT} - \ln N_j^k + \ln N^k - \ln P - \sum_{i=1}^{I} \pi_i^k a_{ij}. \qquad (3.18)
\end{aligned}
$$

For condensed-phase species we also start from Eq. (3.9) but substitute in Eqs. (3.5) and (3.11) and rearrange to find

$$\sum_{i=1}^{I} \Delta\pi_i a_{ij} = -\frac{\mu_j^0}{RT} - \sum_{i=1}^{I} \pi_i a_{ij}. \qquad (3.19)$$

3.2.4 Solution of the linear equations

The set of linear equations given by Eqs. (3.16) to (3.19) are solved for the unknown correction terms using the LAPACK library routine DGESV, which solves the general system of linear equations $A\mathbf{x} = \mathbf{b}$ for $\mathbf{x}$.

In this problem, A is a square matrix of size $J+I+1$ by $J+I+1$ with values of the coefficients on the left-hand side of Eqs. (3.16) to (3.19) whilst $\mathbf{x}$ and $\mathbf{b}$ are column vectors of size $J+I+1$, where $\mathbf{x}$ are the unknown correction variables and $\mathbf{b}$ are the right-hand sides of the Eqs. (3.16) to (3.19).

In each iteration of the Newton-Raphson method, the DGESV routine is used to find the new correction variables $\Delta \ln N_j$, $\Delta \ln N$, $\Delta \pi_i$ and ΔN_j (the latter for condensed species) which are used to improve the values of N_j, N and π_i to satisfy Eq. (3.9), Eq. (3.8) and Eq. (3.6). The iterations continue until the solution has reached the desired accuracy.

3.2.5 Initial values

For the initial values of N_j, N and π_i we follow Gordon and McBride [1994] and set $N = 0.1$, $\pi_i = 0$ and $N_j = 0.1/J_g$ $(j = 1, \ldots, J_g)$ for the gas-phase molecules. As discussed in more detail later, condensed-phase species are not initially included in the calculation, and so initial estimates are not required.

3.2.6 Step size and convergence

In each iteration of the Newton-Raphson technique, the values of N_j, N and π_i are improved using the calculated correction variables. To aid stability of the numerical calculation, we follow empirical the method of Gordon and McBride [1994] and limit the magnitude of the corrections to avoid excessively large steps by introducing a step size variable λ. Rewriting Eqs. (3.10) to (3.13) to introduce λ

$$\ln N^{k+1} = \ln N^k + \lambda \Delta \ln N \tag{3.20}$$

$$\pi_i^{k+1} = \pi_i^k + \lambda \Delta \pi_i \tag{3.21}$$

$$N_j^{k+1} = N_j^k + \lambda \Delta N_j \tag{3.22}$$

$$\ln N_j^{k+1} = \ln N_j^k + \lambda^k \Delta \ln N_j. \tag{3.23}$$

For species with mole fractions $(N_j/N) > 10^{-20}$ the step size λ_1 is determined by

$$\lambda_1 = \frac{2}{\max(5\,|\Delta \ln N|\,, |\ln N_j|)}, \tag{3.24}$$

whereas for species with mole fractions $(N_j/N) \leq 10^{-20}$ *and* $\Delta \ln N_j \geq 0$ the step

size λ_2 is

$$\lambda_2 = \min \left| \frac{-\ln N_j + \ln N - S/2}{\Delta \ln N_j - \Delta \ln N} \right|, \tag{3.25}$$

where $S = -\ln 10^{-20} \sim 46$. The overall step size is then determined by $\lambda = \min(1, \lambda_1, \lambda_2)$.

The criteria for convergence is set by three separate error terms relating to the elemental conservation, total number of moles and molecule equations discussed above; we will refer to these error terms as E_{ele}, E_N and E_{mol}, respectively. These error terms are given by

$$\begin{aligned} E_{\text{ele}} &= \frac{\left| -\sum_{j=1}^{J} a_{ij} N_j + b_i^0 \right|}{b_i^0} \\ E_N &= \frac{N - \sum_{j=1}^{J} N_j}{N} \\ E_{\text{mol}} &= \frac{\left| -\mu_j^0 - \ln\left(\frac{P}{P^0}\right) + \ln N - \sum_{j=1}^{J} \lambda_i a_{ij} \right|}{\left| \mu_j^0 + \ln\left(\frac{P}{P^0}\right) \right|} \end{aligned} \tag{3.26}$$

Convergence is deemed to be reached when the maximum of these three error terms is less than a specified accuracy, which by default we take as 1×10^{-6}.

3.2.7 Condensation

At the beginning of the calculation, it is assumed that only gas-phase species are present in the mixture. Once the gas-phase only mixture has reached a converged state with a minimum in G, a test is performed to assess whether the inclusion of one or more condensed species to the mixture can further reduce G. This test takes the form

$$\frac{\partial G}{\partial N_j} = \left(\frac{\mu_j^0}{RT} \right)_c - \sum_{i=1}^{I} \pi_i a_{ij} \leq 0, \tag{3.27}$$

for $j = J_g + 1, \ldots, J$.

If the above relation is satisfied for a condensed species then that species is added to the mixture and the new mixture is re-converged to a state of minimum G. The process is repeated until G cannot be further reduced by the addition of a new condensed species. Only one condensed species is added to the mixture at a time, and if multiple species satisfy the above test, then the species that leads to the largest reduction in G is included.

Condensed species are removed from the mixture if the number of moles of that species reaches negative values, and the mixture is reconverged.

The schematic shown in Fig. 3.1 presents the flow chart for the minimisation of the Gibbs energy with condensed species.

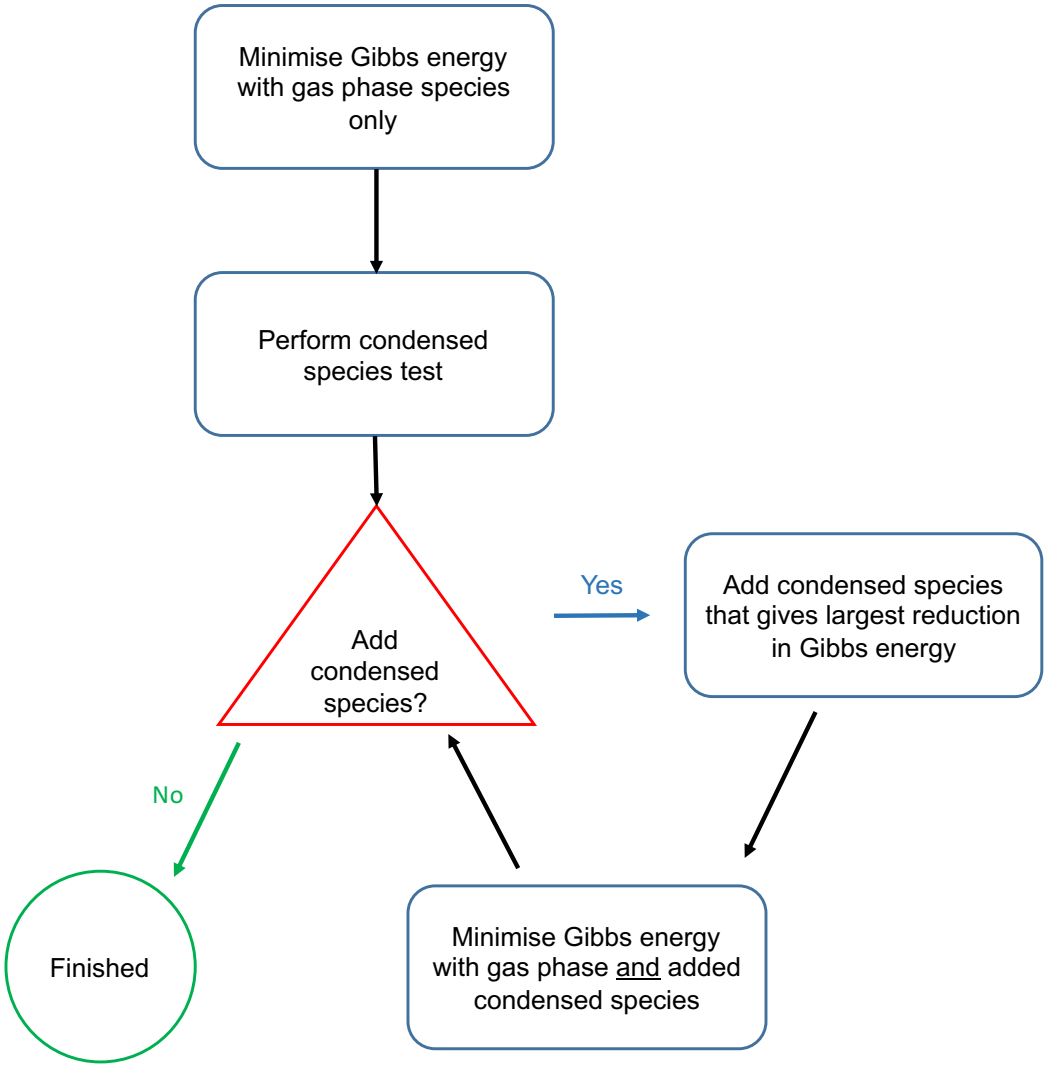

Figure 3.1: A flow chart illustrating the calculation of the minimisation of the Gibbs energy when condensed species are included.

3.3 Validation: calculating equilibrium abundances of a 1D profile

The calculations described above are performed for a single pressure and temperature point (i.e. model grid cell) in isolation. To calculate the equilibrium composition for an entire 1D atmospheric profile, the calculation is repeated independently for each grid cell in the model. In this way, the solution in each grid cell is entirely independent of the other grid cells in the model.

In practice, this method of treating each grid cell entirely independently can lead to inaccuracies when condensed species form. Several articles in the literature discuss the concept of 'rainout' chemistry [e.g. Burrows and Sharp, 1999, Lodders, 1999, Mbarek and Kempton, 2016] whereby any condensates that form are assumed to settle out of the atmosphere as soon as they form. This process effectively leads to a depletion of elements from the gas-phase and the availability of elements at all lower pressures will be altered, ultimately affecting the overall composition at lower pressures.

In this section, the Gibbs energy minimisation scheme is first validated against another model which takes a very similar method, and then against two analytical solutions to chemical equilibrium, for gas-phase only chemical mixtures. The implementation of rainout chemistry is then described and tested qualitatively.

3.3.1 Validating the Gibbs energy minimisation scheme

In this section the implementation of the Gibbs energy minimisation scheme is validated by reproducing the results from previously published works. Firstly we compare our result with the Gibbs energy minimisation model (TECA) presented in Venot et al. [2012] by reproducing the equilibrium abundances for the pressure-temperature profile for HD 209458b [Moses et al., 2011], shown in Fig. 3.2.

Fig. 3.3 shows the comparison between the abundances as calculated with ATMO with those from the Venot et al. [2012] model, for the same pressure-temperature profile. The agreement between the two models is very good. The differences between ATMO and Venot et al. [2012] for the important species (CH_4, CO, NH_3, etc) are typically $\sim 0.1\%$. Note that only gas-phase species are included in both models for this test.

As an additional test, we compare our model to two analytical solutions to chemical equilibrium by Burrows and Sharp [1999] and Heng and Tsai [2016]. Fig. 3.4 compares the three methods for two isothermal profiles with temperatures of 1000 and 2000 K. Overall there is an excellent agreement between the three methods. In particular, the difference between the ATMO profiles and the Heng

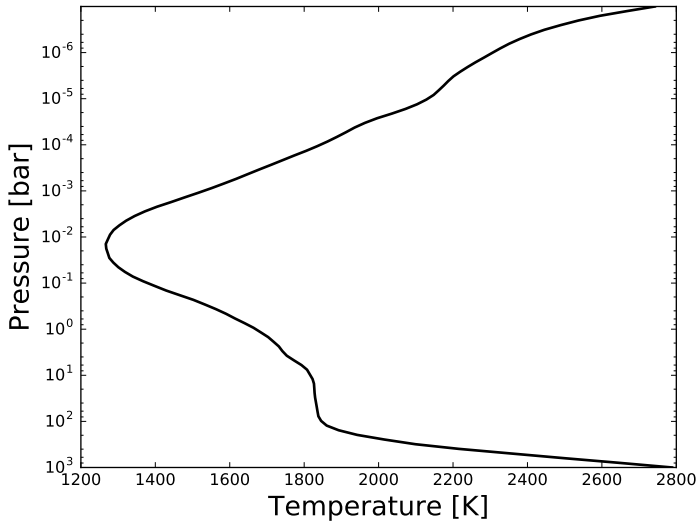

Figure 3.2: The dayside-average pressure-temperature profile for HD 209458b constructed by Moses et al. [2011] from the GCM simulations of Showman et al. [2009] and the 1D models of Fortney et al. [2006, 2010]. Note the large temperature-inversion at low pressures due to the inclusion of gaseous TiO and VO in these models.

and Tsai [2016] results are negligible for most of the molecules. Only for H_2O does the discrepancy between the ATMO and Heng and Tsai [2016] methods become appreciable, though this remains small. The agreement between our model and the method of Burrows and Sharp [1999] is also very good with only very minor apparent differences. Note that at low pressures in the hotter 2000 K profile, both analytical solutions break down as they do not account for thermal dissociation of H_2 that affects the mole fractions of the other species.

The excellent agreement between the chemical abundance profiles obtained using the ATMO Gibbs energy minimisation scheme and the model of Venot et al. [2012] (better than $\sim 0.1\%$), which takes a similar approach, and also with the analytical solutions of both Burrows and Sharp [1999] and Heng and Tsai [2016] validates the accurate implementation of this scheme.

3.3.2 Rainout chemistry

For the method described so far each model grid cell is treated entirely independently, solving for the set of chemical abundances that satisfy local chemical equilibrium for the given pressure and temperature of that grid cell. The elemental abundances are assumed to be constant throughout the model domain. There is evidence that such a 'pure chemical equilibrium' approach may not be an accurate representation of these atmospheres, with the most well-known case being the detection of H_2S in the atmosphere of Jupiter [Niemann et al., 1998].

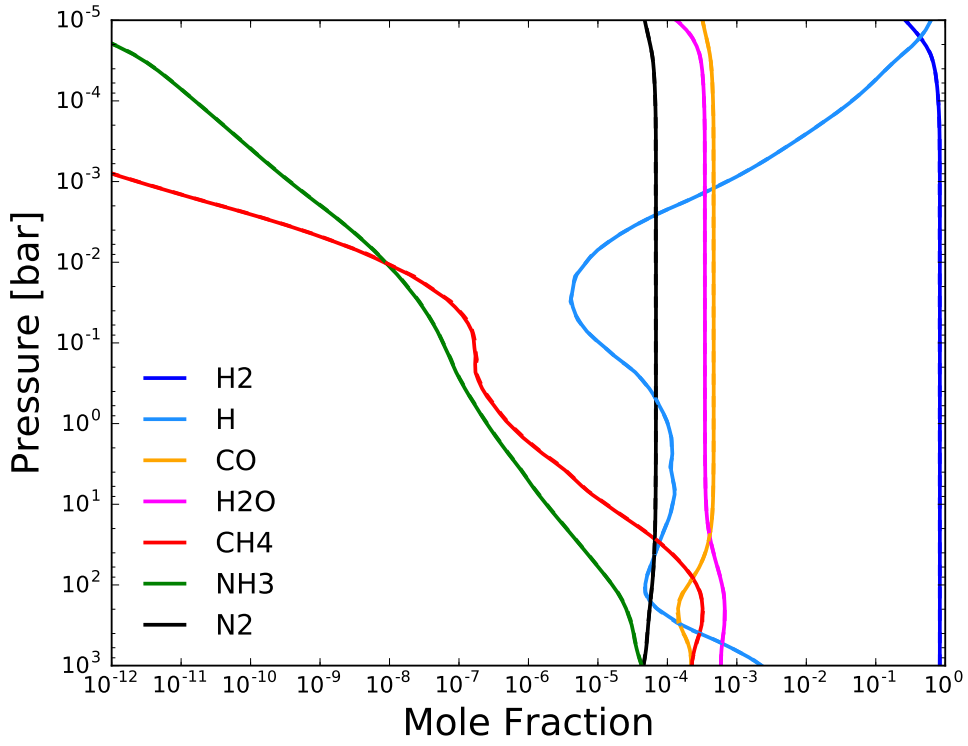

Figure 3.3: A figure showing the chemical equilibrium abundances of some important molecules as calculated using the ATMO Gibbs energy minimisation scheme (solid) and from the model of Venot et al. [2012] which employs a similar method (dashed). There is negligible difference between the two models, validating the ATMO scheme. The abundances were calculated using the pressure-temperature profile for HD 209458b from Moses et al. [2011].

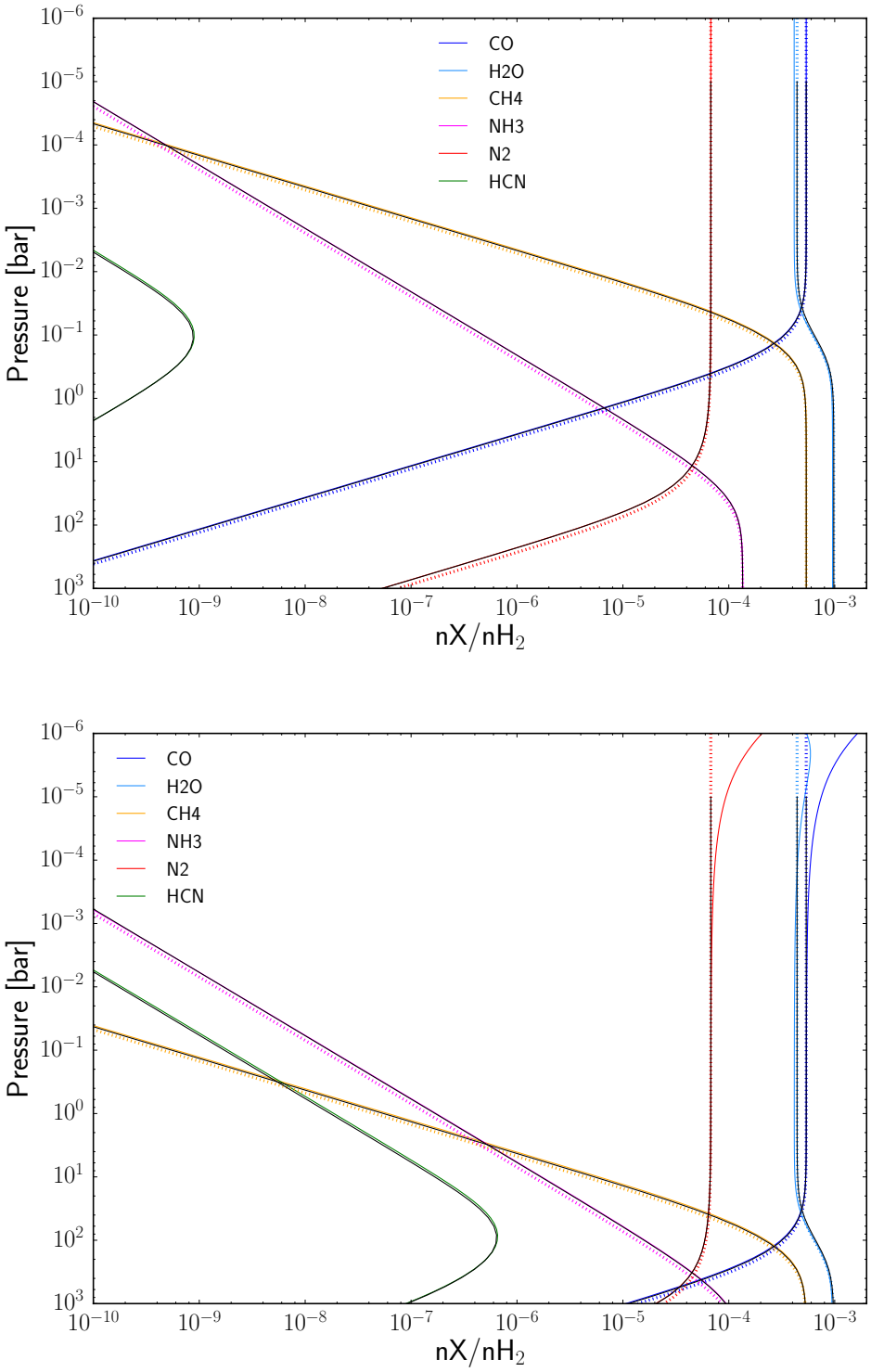

Figure 3.4: A figure comparing the abundances from the ATMO Gibbs energy minimisation scheme (coloured solid lines) with the Burrows and Sharp [1999] (coloured dotted lines) and Heng and Tsai [2016] (black lines) analytical solutions for isothermal profiles with temperatures of 1000 K (top) and 2000 K (bottom).

Chemical modelling of the Jovian atmosphere in the pure chemical equilibrium approach shows that the condensate FeS depletes all sulphur from the gas-phase for the relevant temperatures [Burrows and Sharp, 1999] and therefore the formation of gas-phase H_2S is not possible, contrary to its detection.

If, however, the effect of the rainout of elements due to condensation in the deeper levels of the atmosphere is accounted for, it is found that Fe is entirely depleted from the upper atmosphere due to condensation at higher pressures and temperatures. Therefore, in the observable region of the atmosphere the depletion of Fe will mean FeS can no longer form to deplete the sulphur, consequently allowing H_2S to form, as observed [Barshay and Lewis, 1978, Fegley and Lodders, 1994].

To take into account this rainout process, the elemental composition is allowed to vary along the 1D profile. Specifically, following the formation of a condensed species in a model level, the elemental composition in the next model level of the profile (towards lower pressure) is adjusted to take into account the stoichiometric depletion of elements that form that condensate.

Beginning the calculation along the profile at the model level with the highest pressure $l = 1$, the elemental abundances in this level will simply be equal to the initial, prescribed elemental abundances $B_i^{l=1} = B_i$. Once the Gibbs energy minimisation iterations are complete in this model level, the elemental abundances in the next model level ($l = 2$) are calculated as

$$B_i^{l=2} = B_i^{l=1} - \sum_{j=J_g+1}^{J} a_{ij} \frac{N_j^{l=1}}{N^{l=1}},$$

where the elemental abundance is reduced by the sum of the number of atoms of that element in each condensed species, multiplied by the mole fraction of that condensed species. More generally, we write this for all $l > 1$ as

$$B_i^l = B_i^{l-1} - \sum_{j=J_g+1}^{J} a_{ij} \frac{N_j^{l-1}}{N^{l-1}}. \tag{3.28}$$

If the abundance of an element reaches negative values ($B_i^l < 0$) then that element and all of the chemical species that contain it are removed entirely from the calculation, as that element is assumed to have been completely depleted from the atmosphere for all lower pressures. This process therefore has the effect of reducing both the number of elements I and the number of chemical species J in the calculation as we move up the 1D profile, and therefore decreasing calculation time significantly compared to the pure chemical equilibrium calculation; at least for a profile where condensed species form.

Rainout chemistry is also considered for models applied to exoplanets [e.g.

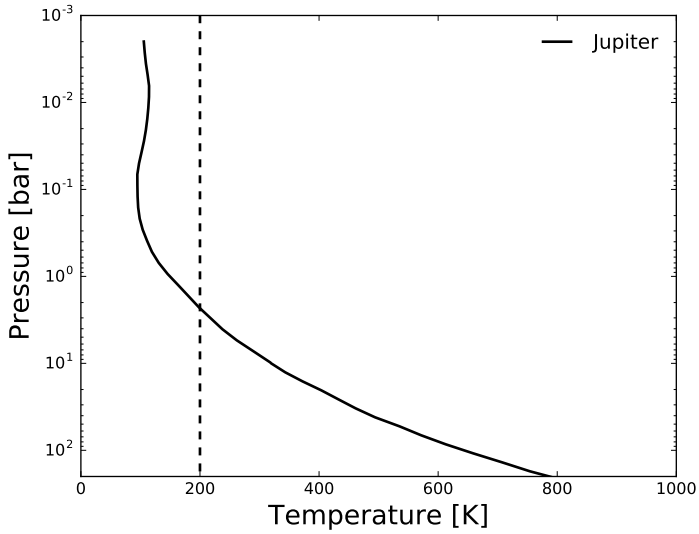

Figure 3.5: A figure showing a P–T profile representative of the Jovian atmosphere. The profile is a combination of the deep atmosphere profile ($P > 10^1$ bar) from Fegley and Lodders [1994] and the profile from Marley [1997] for lower pressures. The dashed line indicates 200 K, which is the temperature cut-off applied to the thermodynamic data in this test.

Madhusudhan et al., 2011a, Mbarek and Kempton, 2016].

Rainout chemistry on Jupiter

Here, we qualitatively assess the implementation of this rainout scheme with the H_2S–FeS problem for Jupiter as outlined above.

The pressure-temperature profile for Jupiter is constructed by combining the deep atmosphere profile ($10^4 > P > 10^1$ bar) of Fegley and Lodders [1994] with the profile taken from Marley [1997] for lower pressures; a small shift in the latter profile of < 10 K was applied for a smooth transition between the two profiles. This temperature profile is shown in Fig. 3.5.

Due to the lower temperature limit of the coefficients used to calculate the thermodynamic properties of the species [McBride et al., 1993] we must place a lower temperature limit of 200 K on the calculation. In effect, this means that where the P–T profile, shown in Fig. 3.5, is below 200 K the temperature is instead artificially fixed to 200 K. In this particular case, this means that the P–T profile effectively transitions to an isothermal profile with $T = 200$ K at around 2 bar, with respect to the chemistry calculation.

Fig. 3.6 shows the abundance of H_2S obtained from both the pure chemical equilibrium and rainout chemistry calculations, using the P–T profile shown in Fig. 3.5. In the pure chemical equilibrium calculation, H_2S is present in significant abundance only at very high pressures. For $P < 10^2$ bar the formation of FeS

condensates significantly depletes the abundance of H_2S by reducing the availability of sulphur. Note that condensed Fe is the most abundant form of iron due to its higher (roughly double) solar elemental abundance compared to sulphur.

On the other hand, H_2S is abundant throughout the entire atmospheric profile when taking into account the rainout of elements due to condensation. The formation of the Fe condensates at very high pressures rapidly depletes iron entirely from the atmosphere, within the deepest few model levels, meaning that FeS condensates cannot form at lower pressures and H_2S is instead abundant.

This simple test qualitatively reproduces the behaviour of the FeS-H_2S system as has been previously modelled [Barshay and Lewis, 1978, Fegley and Lodders, 1994] and observed [Niemann et al., 1998] using the chemical rainout scheme implemented in ATMO.

3.4 Implementing the chemical kinetics scheme

In this section the implementation of the chemical kinetics scheme in ATMO is described. Firstly, the reader is reminded of the continuity equation in Section 3.4.1 before describing the solution of this equation using a solver package for Ordinary Differential Equations (ODEs) in Section 3.4.2. The implementation of the vertical transport and photodissociation schemes is then presented in Sections 3.4.4 and 3.4.5, respectively.

3.4.1 The continuity equation

In the chemical kinetics method, the evolution of the number density of a chemical species with time is described by the continuity equation Eq. (2.11), which has already been introduced and described in Section 2.4 and is shown again for clarity below

$$\frac{\partial n_j}{\partial t} = P_j - L_j - \nabla\Phi_j,$$

where P_j and L_j are the production and loss terms of the species j due to the chemical transformations and the final term on the right describes the net transport of j.

Since for atmospheres we consider long timescales, the goal is to find the steady-state solution where $\frac{\partial n_j}{\partial t} = 0$ and there is no more evolution of the chemical system. In the case with no transport terms ($\nabla\Phi_j = 0$) and no photochemical reactions, or any other 'non-equilibrium terms', the steady-state solution corresponds to chemical equilibrium with balance between the production and loss terms. The steady-state is found by solving the system of coupled Ordinary Differential Equations (ODEs) (one for each chemical species in the system) as a function of time

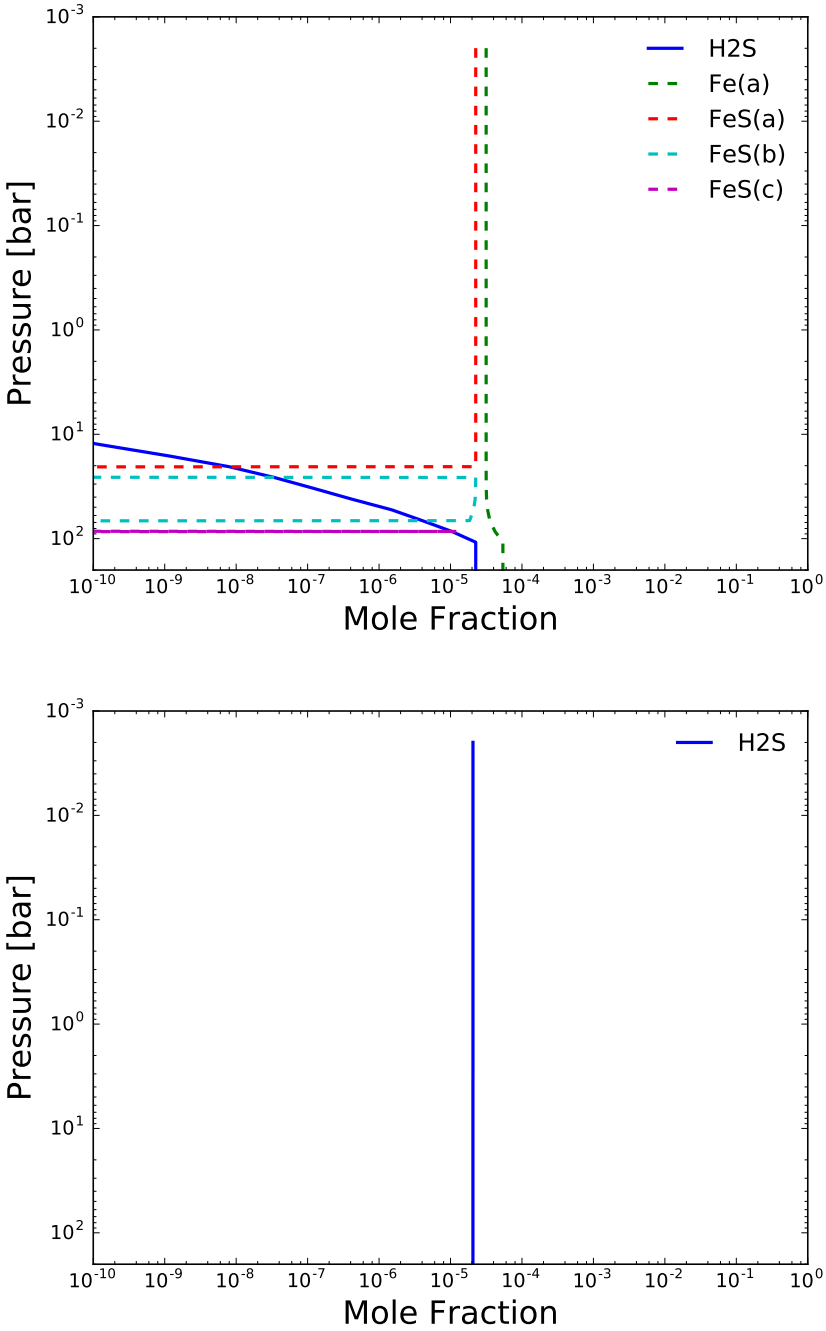

Figure 3.6: A figure showing the abundance of H_2S for the P–T profile of Jupiter (Fig. 3.5) in the pure chemical equilibrium (*top*) and rainout chemistry (*bottom*) cases. For the pure chemical equilibrium case, the abundance of the important condensed species are also shown. Condensed species are shown as dashed lines, whilst gas-phase species are shown as solid lines. Note that these iron condensates do not form in the rainout calculation as iron is depleted from the atmosphere at very high pressures.

until there are no more variations in n_j to within some prescribed tolerance.

3.4.2 Solution of the continuity equation: DLSODES

The system of ODEs describing the evolution of each chemical species is solved using a Fortran solver that is part of the Livermore Solver for Ordinary Differential Equations (LSODE) package [Hindmarsh, 1983, Radhakrishnan and Hindmarsh, 1993], which contains a collection of routines that provide a numerical solution to a general initial value problem. In particular, we use the DLSODES double-precision variant of the solver which employs the Backward Differentiation Formula (BDF) methods (see Appendix D), well suited for stiff problems [Radhakrishnan and Hindmarsh, 1993]; typical for chemical kinetics problems where the reaction rates can vary by many orders of magnitude. A brief outline of the method of the DLSODES solver is presented below.

For the initial value problem where the initial number densities of the species $j = 1, \ldots, J$ at a time t_0 are given by

$$\mathbf{n}(t_0) = \mathbf{n}_0,$$

where $\mathbf{n}$ is a column vector of size J, the time dependence is described by

$$\frac{d\mathbf{n}}{dt} = \dot{\mathbf{n}} = \mathbf{f}(t, \mathbf{n}),$$

where $\mathbf{f}(t, \mathbf{n})$ is some function that in general depends on t and $\mathbf{n}$.

In this specific case, the function $\mathbf{f}$ is the system of ODEs, or continuity equations, for the chemical species such that

$$\frac{d\mathbf{n}}{dt} = \dot{\mathbf{n}} = \mathbf{f}(t, \mathbf{n}) = \mathbf{P} - \mathbf{L} - \nabla\mathbf{\Phi}.$$

The BDF method allows us to find the values of $\mathbf{n}(t)$ on a discrete grid of time points $t = 0, \ldots, t_k$. For a particular time interval Δt we can write $\mathbf{n}_k = \mathbf{n}(t + \Delta t)$

$$\mathbf{n}_k = \sum_{i=1}^{q} \alpha_i \mathbf{n}_{k-i} + \Delta t \beta_0 \mathbf{f}(t, \mathbf{n}_k)$$

$$\mathbf{n}_k = \mathbf{a}_k + \Delta t \beta_0 \mathbf{f}_k, \tag{3.29}$$

where q is the order and the coefficients α_i and β_0 depend on q; see Appendix D. The first term on the right-hand side contains information about previous iterations. Since $\mathbf{n}_k$ appears on both sides of Eq. (3.29), the solution must be found iteratively. An option is to use a Newton-Raphson iteration procedure, which is the method

employed by DLSODES.

We can rewrite Eq. (3.29) as

$$\mathbf{R}(\mathbf{n}_k^m) = \mathbf{n}_k^m - \mathbf{a}_k - \Delta t \beta_0 \mathbf{f}(t, \mathbf{n}_k^m) = 0, \tag{3.30}$$

where $\mathbf{R}(\mathbf{n}_k)$ is the residual factor and $\mathbf{n}_k^m$ is the mth estimate of $\mathbf{n}_k$. The goal is to find the $m+1$th estimate of $\mathbf{n}_k$ which satisfies $\mathbf{R}(\mathbf{n}_k^{m+1}) = 0$. Performing a Taylor series expansion about the mth estimate yields

$$\mathbf{R}(\mathbf{n}_k^{m+1}) = \mathbf{R}(\mathbf{n}_k^m) + \frac{\partial \mathbf{R}}{\partial \mathbf{n}}(\mathbf{n}_k^{m+1} - \mathbf{n}_k^m) = 0. \tag{3.31}$$

Rearranging Eq. (3.31) and substituting in Eq. (3.30) yields

$$\underline{\mathbf{P}}(\mathbf{n}_k^{m+1} - \mathbf{n}_k^m) = -\mathbf{R}(\mathbf{n}_k^m) = \mathbf{a}_k + \Delta t \beta_0 \mathbf{f}(t, \mathbf{n}_k^m) - \mathbf{n}_k^m \tag{3.32}$$

where

$$\underline{\mathbf{P}} = \frac{\partial \mathbf{R}}{\partial \mathbf{n}} = \mathbf{I} - \Delta t \beta_0 \mathbf{J}$$

and $\mathbf{I}$ is the identity matrix and $\mathbf{J}$ is the Jacobian matrix

$$\mathbf{J} = \frac{\partial \mathbf{f}}{\partial \mathbf{n}}.$$

The solver package allows two options related to the construction of $\mathbf{J}$, which can either be provided by the user within a Fortran subroutine, or the user can request that $\mathbf{J}$ is generated internally. In this work, the latter option is used. Likewise, Δt can either be provided directly by the user or the solver generates a timestep internally, and again we take the latter approach.

The user must provide the initial values $\mathbf{n}_0$, or more generally the values from the previous timesteps $\mathbf{n}_{k-i}$ $(i = 1, \ldots, q)$, as well as a Fortran subroutine which calculates the function $\mathbf{f}(t, \mathbf{n}_k^m)$, which in this case is the system of continuity equations described by Eq. (2.11).

3.4.3 The choice of chemical network

To solve for the chemical abundances with the chemical kinetics method one must make a choice of the chemical network that should be used. We have previously reviewed the range of chemical networks that have so far been applied to the atmospheres of hot exoplanets in Section 1.3.2.

The factors that control the choice of chemical network are based on the current application (i.e. does that network contain the relevant species/reactions), the accuracy of the network and also the availability. In this work we choose to use

the chemical network of Venot et al. [2012] which is publicly available as part of the Kinetic Database for Astrochemistry (KIDA)[1].

In addition to the public availability, we choose this network because it includes the chemical species that are sources of opacity in ATMO (H_2O, CH_4, CO, NH_3, etc.). Finally, the Venot et al. [2012] network is currently unique in the field in that it has been experimentally validated, as a complete network, for thermodynamic conditions relevant to hot Jupiters ($300 < T < 2500$ K and $0.01 < P < 100$ bar). Other networks applied to hot atmospheres in the literature (Section 1.3.2) have not undergone such rigorous validations against experiment.

3.4.4 Implementation of vertical transport

The final term in Eq. (2.11) accounts for the net transport of material from the model level. As has been previously derived in Section 2.4.8 the vertical flux can be shown to be described by

$$\Phi_j = -nD_j \left(\frac{\partial f_j}{\partial z} - \frac{f_j}{H_a} + \frac{f_j}{H_j} + \frac{f_j \alpha_j}{T} \frac{\partial T}{\partial z} \right) - nK_{zz} \left(\frac{\partial f_j}{\partial z} \right),$$

where the total flux is the sum of two components due to small-scale diffusion (first term on right) and a parameterisation of the larger scale vertical motions of the atmosphere, the eddy-diffusion term (second term on right). The small-scale diffusion term is in turn composed of three parts that are due to 1) a gradient in the mixing ratio, 2) a gradient in the temperature and 3) the separation of species due to their individual scale heights.

In the current implementation of ATMO, we approximate the first term on the right-hand side of Eq. (2.47) by assuming that the molecular diffusion is *only* driven by the gradient in the mole fraction and that the other terms are not important, giving

$$\Phi_j = -nD_j \left(\frac{\partial f_j}{\partial z} \right) - nK_{zz} \left(\frac{\partial f_j}{\partial z} \right). \tag{3.33}$$

Overall, this approximation is not likely to affect our results as in all applications of the model presented in later chapters vertical transport due to eddy diffusion dominates over molecular diffusion. Indeed, to simplify matters further, it would likely be acceptable to neglect the molecular diffusion term altogether. For the pressure ranges that we model ($10^3 > P > 10^{-5}$ bar) K_{zz} is several orders of magnitude larger than D_j. Note that D_j scales inversely with pressure and will become important at very low pressures.

In the current version of the scheme, the diffusion coefficient D_j is calculated

[1] http://kida.obs.u-bordeaux1.fr/ - 25/05/17

as a self-diffusion coefficient [Wayne, 1991]; i.e. it is the diffusion of the species within itself. A better approach is to use a binary diffusion coefficient that accounts for the diffusion of a species within another species [e.g. Poling et al., 2001]. For instance, in the case of hydrogen-dominated gas giant atmospheres it is likely more important to include the diffusion of trace species within the dominant H_2 and He background gas than it is to include self-diffusion of these trace species.

However, as noted before, for the models presented in this work the vertical transport due to molecular diffusion is several orders of magnitude lower than that due to eddy diffusion and this will therefore not affect our results. In potential future applications that model much lower pressure ranges, where molecular diffusion becomes more important, it will be important to reassess the representation of molecular diffusion in the model.

Discretisation onto the model grid

The divergence of the flux Φ_j yields the net transport of species into the model level i. For the case of a 1D column model with only one spatial (vertical) dimension, the divergence of Φ_j is

$$\nabla\Phi_j = \frac{\partial\Phi_j}{\partial z}. \tag{3.34}$$

In ATMO, the number densities and mole fractions of the species are defined on cell faces for the model levels $i = 1, \ldots, I$ where I is the number of vertical levels, whilst the fluxes Φ_j are defined in the cell centers $i = 1/2, \ldots, I - 1/2$. The divergence of the flux is calculated on the cell faces. We write divergence of the flux on some cell face i as

$$\left.\frac{\partial\Phi_j}{\partial z}\right|^i = \frac{\Phi_j^{i+1/2} - \Phi_j^{i-1/2}}{|z^{i+1/2} - z^{i-1/2}|}. \tag{3.35}$$

We now write $\Phi_j^{i+1/2}$ and $\Phi_j^{i-1/2}$ discretised onto the model grid using Eq. (3.33)

$$\Phi_j^{i+1/2} = -n^{i+1/2} D_j^{i+1/2} \left[\frac{f_j^{i+1} - f_j^i}{|z^{i+1} - z^i|}\right] - n^{i+1/2} K_{zz}^{i+1/2} \left[\frac{f_j^{i+1} - f_j^i}{|z^{i+1} - z^i|}\right] \tag{3.36}$$

$$\Phi_j^{i-1/2} = -n^{i-1/2} D_j^{i-1/2} \left[\frac{f_j^{i} - f_j^{i-1}}{|z^{i} - z^{i-1}|}\right] - n^{i-1/2} K_{zz}^{i-1/2} \left[\frac{f_j^{i} - f_j^{i-1}}{|z^{i} - z^{i-1}|}\right]. \tag{3.37}$$

Boundary conditions

At the boundaries of the model grid we assume a zero flux. Physically this assumption means that no mass is being lost at the top boundary of the model atmosphere, and no mass is transferred through the bottom boundary. This latter point is valid if the deepest level of the atmosphere remains in chemical equilibrium [e.g. Moses et al., 2011].

We write the divergence of the flux at the boundaries as

$$\left.\frac{\partial \Phi_j}{\partial z}\right|^{i=1} = \frac{\Phi_j^{1+1/2} - 0}{\Delta z^1} \tag{3.38}$$

$$\left.\frac{\partial \Phi_j}{\partial z}\right|^{i=I} = \frac{0 - \Phi_j^{I-1/2}}{\Delta z^I}, \tag{3.39}$$

where we approximate $\Delta z^1 \sim |z^2 - z^1|$ and $\Delta z^I \sim \left|z^I - z^{I-1}\right|$, and

$$\Phi_j^{1+1/2} = -n^{1+1/2} D_j^{1+1/2} \left[\frac{f_j^2 - f_j^1}{|z^2 - z^1|}\right] - n^{1+1/2} K_{zz}^{1+1/2} \left[\frac{f_j^2 - f_j^1}{|z^2 - z^1|}\right] \tag{3.40}$$

$$\Phi_j^{I-1/2} = -n^{I-1/2} D_j^{I-1/2} \left[\frac{f_j^I - f_j^{I-1}}{|z^I - z^{I-1}|}\right] - n^{I-1/2} K_{zz}^{I-1/2} \left[\frac{f_j^I - f_j^{I-1}}{|z^I - z^{I-1}|}\right]. \tag{3.41}$$

3.4.5 Implementation of photochemical dissociations

There are 34 photochemical reactions involving the dissociation of 22 chemical species in the Venot et al. [2012] chemical network. The computation of the photodissociation rate J_i first requires the calculation of the spectral radiative flux on each model level. In ATMO, the radiative flux is calculated using the same radiative transfer code as for the radiative-convective equilibrium P–T profile iterations. The implementation and testing of this radiative-transfer scheme in ATMO has been described and tested elsewhere [e.g. Amundsen et al., 2014, Amundsen, 2015] and is not the focus of this work.

In this section, the calculation of the absorption and scattering coefficients and the photodissociation rate is described.

The absorption and scattering coefficients

The absorption and scattering coefficients are required to solve for the radiative flux. Following the method of Venot et al. [2012] we include absorption due to 22 molecules and scattering due to the dominant species H_2 and He.

The total absorption coefficient per unit mass of the mixture $\alpha(\lambda)$ is calculated from the absorption cross sections of the individual species $\alpha_j(\lambda)$ using

$$\alpha(\lambda) = \sum_j^{N_{\rm abs}} \frac{\alpha_j(\lambda) f_j}{\mu}, \tag{3.42}$$

where μ is the mean molecular mass of the mixture [kg] and the sum is over the number of absorbing species $N_{\rm abs}$.

Likewise, the total Rayleigh scattering coefficient per unit mass of the mixture

$\sigma^{RAY}(\lambda)$ is given by

$$\sigma^{RAY}(\lambda) = \sum_{j}^{N_{\rm sc}} \frac{\sigma_j^{RAY}(\lambda) f_j}{\mu}, \tag{3.43}$$

where the sum is over the number of scattering species $N_{\rm sc}$. The Rayleigh scattering cross section is given by

$$\sigma_j^{RAY}(\lambda) = \frac{8\pi}{3}\left(\frac{2\pi}{\lambda}\right)^4 \alpha_p^2 \left[\frac{6+3\delta}{6-7\delta}\right], \tag{3.44}$$

where δ and α_p are the depolarisation factor and polarisability of the species respectively, with

$$\alpha_p = \frac{n_r^2 - 1}{4\pi n_l}, \tag{3.45}$$

where n_r is the refractive index and n_l is the Loschmidt constant.

The references for α_j for each species can be found in Venot et al. [2012], and n_r and δ for H_2 and He are taken from Cox [2000].

The photodissociation reactions

Following the method of Venot et al. [2012], the photodissociation reaction that follows a photon absorption event depends on the energy (wavelength) of that photon. Therefore, whilst 22 reactant species are included in the photodissociation scheme there are actually 34 possible dissociation reactions. Where multiple dissociation reactions can occur for a single absorbing species, the likelihood of each possible reaction is quantified in the quantum yield $q_{i,j}(\lambda)$: the probability ($0 < q_{i,j}(\lambda) < 1$) of photodissociation reaction i occuring following the absorption of a photon of wavelength λ by the molecule j. The sum of all possible dissociation events for a molecule is unity

$$\sum_i q_{i,j}(\lambda) = 1.$$

As a particular example, there are four possible photodissociation reactions for CH_4 [see Venot et al., 2012, and references therein]. For photon wavelengths $\lambda = 121.6$ nm, the Lyman α line, there are four possible dissociation reactions which are

- $CH_4 + h\nu \rightarrow CH_3 + H$
- $CH_4 + h\nu \rightarrow {}^1CH_2 + H_2$
- $CH_4 + h\nu \rightarrow {}^3CH_2 + H + H$
- $CH_4 + h\nu \rightarrow CH + H_2 + H$

with $q_{i,j}(\lambda = 121.6 \text{ nm}) = 0.42$, 0.48, 0.03 and 0.07 for these dissociations, respectively. However, for photons at all other wavelengths only the first dissociation reaction is possible with $q_{i,j} = 1$ and the quantum yield is zero for the other dissociations.

The photodissociation rate

The equation describing the photodissociation rate J_i has already been introduced in Section 2.4.7. To solve for J_i we discretise Eq. (2.45) onto a fixed wavelength grid so that the photodissociation rate due to flux at the wavelength point k is

$$J_i^k(z) = \alpha_j^k q_{i,j}^k F^k(z). \tag{3.46}$$

The spectrally-integrated photodissociation rate is then determined by integrating Eq. (3.46) across the spectral range using the trapezoidal rule, with $K+1$ wavelength points in the grid this gives

$$J_i(z) = \int \alpha_j(\lambda) q_j(\lambda) F(z,\lambda) d\lambda \approx \frac{1}{2} \sum_{k=1}^{K} \left(\lambda^{k+1} - \lambda^k\right) \left(J_i^{k+1} + J_i^k\right). \tag{3.47}$$

The production and loss terms due to these photodissociation reactions are added to the P_j and L_j terms in Eq. (2.11).

3.5 Validating and testing the chemical kinetics scheme

In this section we validate the implementation of the chemical kinetics scheme, including the implementation of vertical transport and photochemical dissociations, by reproducing the results of previously published models and comparing the results from our model with those from both Venot et al. [2012] and Moses et al. [2011].

We begin by performing 0D box models in Section 3.5.1 to test the implementation of the chemical kinetics scheme in isolation (i.e. no vertical transport or photochemistry is included) and validate the code by matching the results of Venot et al. [2012]. Secondly, we perform 1D models of HD 209458b in Section 3.5.2, including vertical transport and photochemistry, and compare with the results of both Venot et al. [2012] and Moses et al. [2011]. We find that differences in the implementation of both vertical transport and radiative transfer can have small impacts on the final chemical abundance profiles, but overall we achieve a close match to both these previous works. The largest discrepancies are found at low pressures where photochemical processes and molecular diffusion are important.

Table 3.1: Initial conditions for the 0D box model

	Mole Fraction
H_2	0.853
He	0.145
O_2	5.78×10^{-4}
CH_4	5.66×10^{-4}
N_2	7.11×10^{-5}

3.5.1 Testing the kinetics scheme in a 0D box model

In this section we test the implementation of the Venot et al. [2012] chemical network and the solution of the continuity equation using the DLSODES solver [Hindmarsh, 1983] in ATMO using a simple 0D box model setup. The chemistry is evolved towards the steady-state solution from a prescribed set of initial conditions (i.e. initial chemical abundances) for a given temperature T and pressure P. There is no inclusion of vertical transport or photochemistry in this simple box model and the evolution of the chemistry is solely due to the thermochemical reactions.

As the initial condition all of the mass is assumed to be contained within five main species, with all carbon contained in CH_4, all nitrogen contained in N_2, all oxygen contained in O_2 and the remaining hydrogen (that is not in CH_4) contained in H_2 consistent with the Solar abundances; helium is also included as background gas with its Solar abundance. These initial abundances are shown in Table 3.1 and taken from Venot [2012]. As the continuity equation is evolved the elements are redistributed amongst the 105 chemical species within the chemical network due to the thermochemical reactions. The calculation is continued until the steady-state solution has been reached. Note that in these tests only the chemical species contained in the Venot et al. [2012] chemical network (i.e. species composed of C, O, H and N) are included in the calculation and other species that are also implemented in the model (e.g. the alkali species) are removed.

We follow the tests presented in Venot et al. [2012] in order to compare with their results and perform two separate box model simulations with different thermodynamic conditions. The first test has $P = 0.1$ bar and $T = 1800$ K whilst the second test has $P = 100$ bar and $T = 2200$ K. These pressure and temperature combinations are typical of those found in hot Jupiter atmospheres.

The time-evolution of the chemistry for four important species (H, NH_3, CH_4 and H_2O) in both box model tests are shown in Fig. 3.7 along with the same model results from Venot et al. [2012]. The mole fractions of H, NH_3 and H_2O all increase from their initial values of zero to their eventual steady-state (chemical equilibrium) values as the elements H, N and O are redistributed from their initial 'reservoirs' in H_2, N_2 and O_2. On the other hand, the mole fraction of CH_4 decreases from its

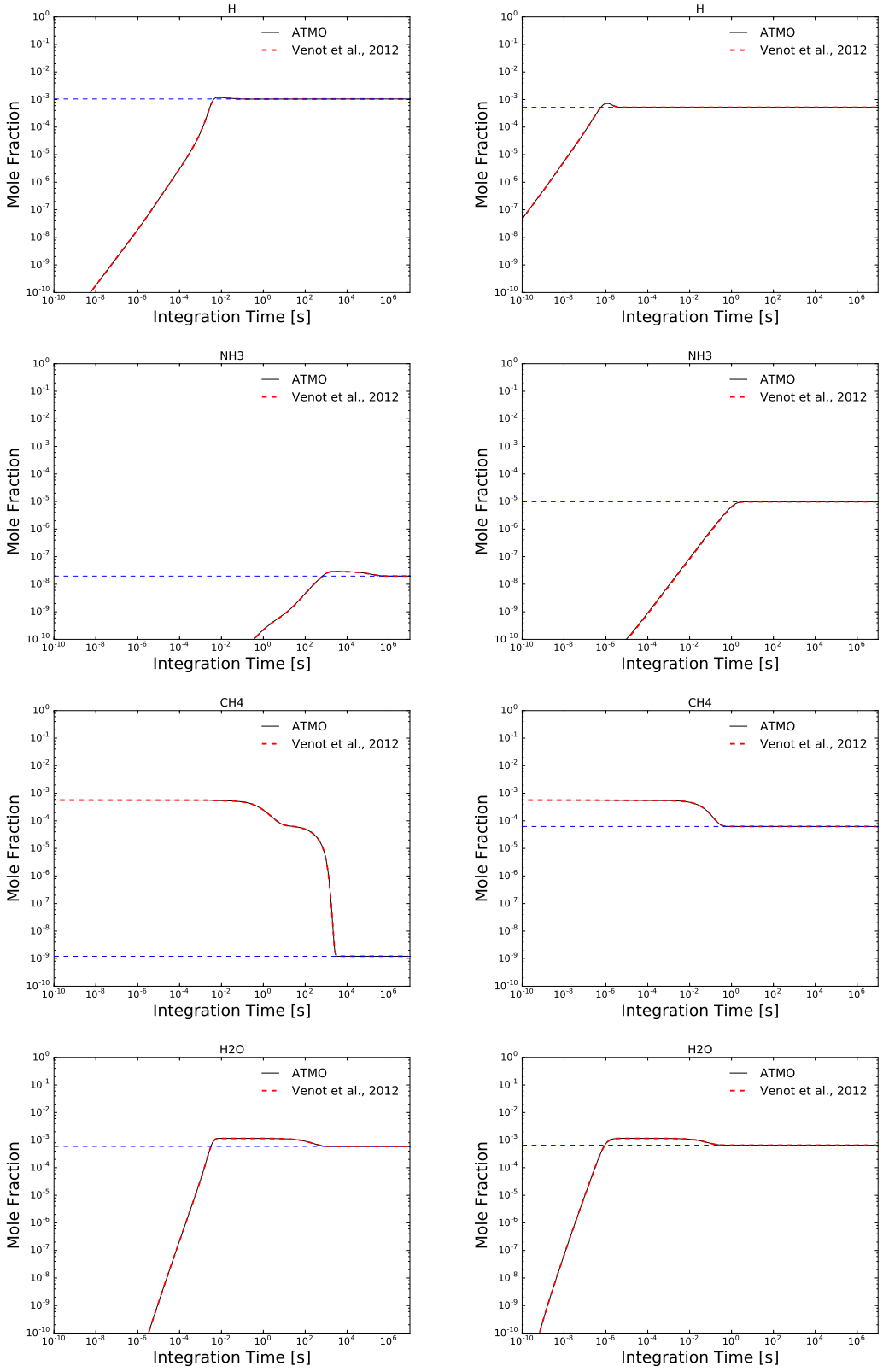

Figure 3.7: The chemical evolution of H, NH_3, CH_4 and H_2O (top to bottom) for $P = 0.1$ bar and T =1800 K (left) and $P = 100$ bar and $T = 2200$ K (right). The ATMO results are shown in the solid black line and the results from Venot et al. [2012] are shown in the dashed red line. The dashed blue line shows the chemical equilibrium abundance calculated from minimising the Gibbs energy.

initial value as carbon is redistributed amongst the other chemical species; in this case, principally into the other major form of carbon CO.

The agreement between the results from our model ATMO and those from Venot et al. [2012] is excellent both in terms of the shape of the evolution profiles and the final steady-state abundances, with no apparent discrepancies for these four major chemical species. These simple box model tests validate the implementation of the chemical network, the calculation of the rate coefficients and the solution of the continuity equation using the DLSODES solver in ATMO by matching the previously published results of Venot et al. [2012].

3.5.2 Reproducing the non-equilibrium models of HD 209458b

In this section, we reproduce the chemical abundance profiles for a 1D model of the atmosphere of HD 209458b including vertical mixing and photochemistry. We use the prescribed P–T and K_{zz} profiles of Moses et al. [2011] and compare the results with both Moses et al. [2011] and Venot et al. [2012]. The implementation of the chemical kinetics calculation in a simple box model has already been validated in the previous section, and this present comparison places more focus on testing the vertical transport and photochemistry schemes.

The P–T profile of HD 209458b constructed by Moses et al. [2011] is derived from the GCM simulations of Showman et al. [2009] and the 1D models of Fortney et al. [2006, 2010] and is shown in Fig. 3.2. Importantly, this P–T profile contains a large temperature inversion where the temperature increases with altitude at low pressures. The presence of this temperature inversion has important consequences on the predicted chemical composition as the large increase in temperature leads to a faster chemical timescale than for a cooler atmosphere without an inversion. This fast chemical timescale at low pressures led to the conclusion that photochemistry is likely to be relatively unimportant in atmospheres with a temperature inversion [Moses et al., 2011]. More recent evidence has suggested that such temperature inversions are uncommon or non-existent in hot Jupiter atmospheres [Diamond-Lowe et al., 2014, Evans et al., 2015]. However, the intentions here are simply to reproduce the results of previous works to validate our model.

The K_{zz} profile was also constructed by Moses et al. [2011] using free-convection and mixing length theories in the deep atmosphere and by estimating the value from the vertical wind velocity fields from the GCM simulations of Showman et al. [2009].

These P–T and K_{zz} profiles were used by both Moses et al. [2011] and Venot et al. [2012] to calculate the non-equilibrium chemical abundance profiles of HD 209458b by taking into account the processes of vertical transport and photochemical dissociation. Here we repeat this calculation with our model using the same inputs

Table 3.2: Elemental abundances used in this test [Venot, 2012]

	Fractional Abundance
H	0.910950
He	0.0882812
O	4.41758×10^{-4}
C	2.52885×10^{-4}
N	7.45642×10^{-5}

Table 3.3: Planetary and stellar parameters for HD 209458b [Venot et al., 2012]

	HD 209438b
a [AU]	0.047
R_s [$R_\odot$]	1.118
$\cos\mu$	2/3
R_p [R_J]	1.339

and model parameters to compare with both of these previous works. As we use the same chemical network as Venot et al. [2012] discrepancies in the abundance profiles will be due to variations in the implementation of the physics schemes (vertical transport, radiative transfer, etc) only. On the other hand, Moses et al. [2011] use their own chemical network and therefore discrepancies between our model and theirs may be due to both differences in the chemical network and in the physics schemes of the models.

The elemental abundances used in this test are presented in Table 3.2 and are taken from Venot [2012]. These correspond to protosolar elemental abundances with a 20% reduction of oxygen to account for depletion due to the rainout of silicates and metals [Venot et al., 2012, Moses et al., 2011]. The planetary and stellar parameters are also taken from Venot et al. [2012] and are summarised in Table 3.3, and we use the same stellar irradiance spectrum [Venot, priv. comm.] to calculate the radiative flux.

Firstly, we consider the comparison with Venot et al. [2012], shown in Fig. 3.8. In the deep atmosphere, where the abundances retain their chemical equilibrium values, the agreement between the two models is excellent. This agreement at high pressures is not surprising since the equilibrium values only depend on the thermodynamic conditions and the thermochemical data used to calculate the equilibrium constant, and our excellent agreement with the chemical equilibrium model (TECA) of Venot et al. [2012] has already been demonstrated in Section 3.3.

Toward lower pressures, in the region $P \sim 1$ bar, the abundances of both CH_4 and NH_3 depart from their respective chemical equilibrium profiles due to transport-induced quenching. Importantly, the agreement between the two models for the location of the quenching point is good, with only minor differences. Physically, the

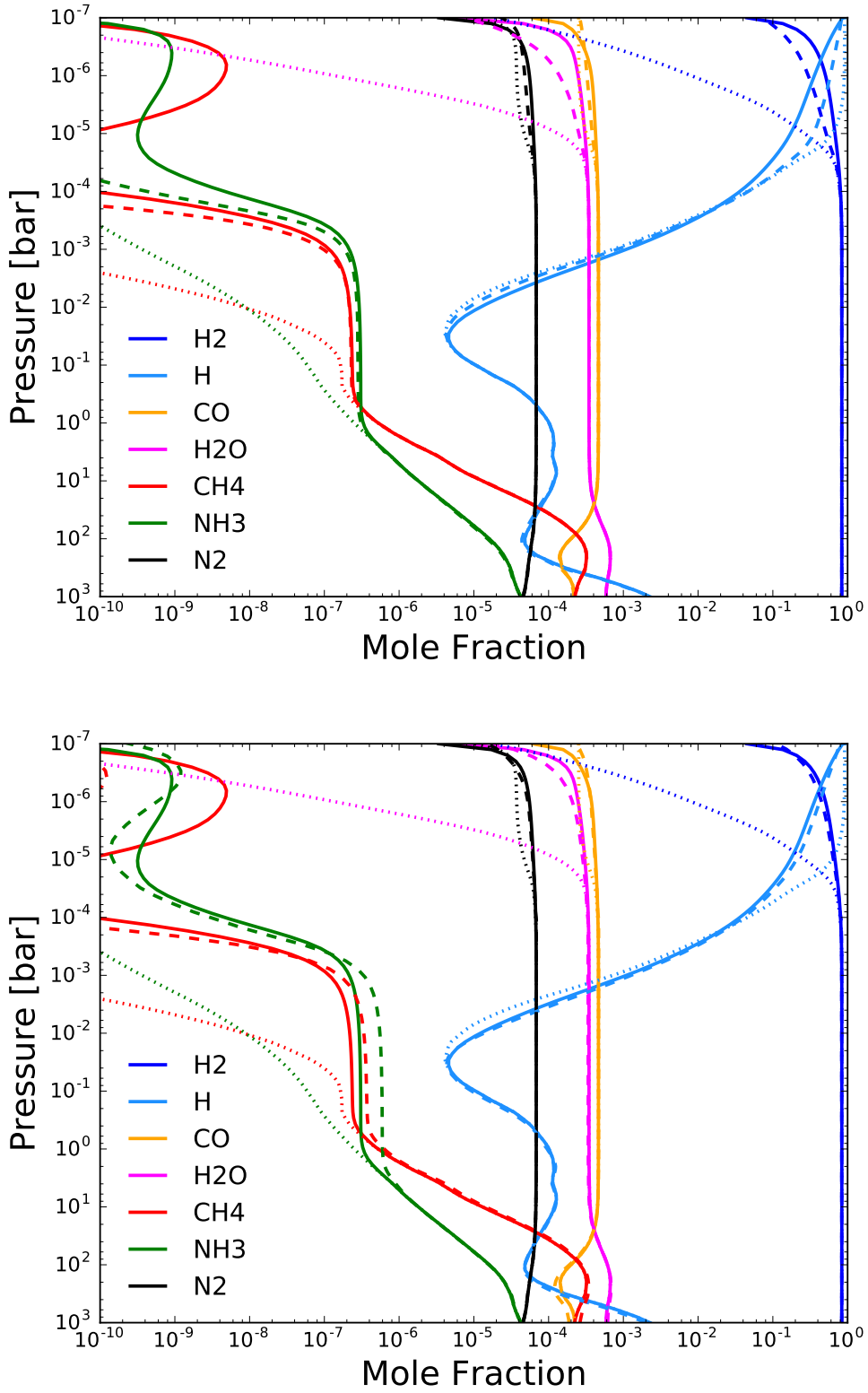

Figure 3.8: The abundance profiles for the major species using the test HD 209458b model. The top panel compares the ATMO result (solid) with the abundances from Venot et al. [2012] (dashed), whilst the lower panel compares the same ATMO result (solid) with those of Moses et al. [2011] (dashed). The initial chemical equilibrium abundances are shown (dotted) in both cases.

precise pressure level of the quench point depends on the thermodynamic structure (i.e. the P–T profile), the strength of the vertical transport (i.e. the K_{zz} profile) and the chemical timescale for these species which depends on the choice of chemical network. Given that these three components are identical in these two models for this test, the differences must lie in the implementation of vertical mixing, the discretisation of the flux terms on the model grid, or the structure of the vertical grid of the model atmosphere itself.

In this test, the structure of the vertical grid in our model is such that there are 100 grid points evenly spaced in terms of $\log P$. On the other hand, Venot et al. [2012] use a larger number of grid points ($\sim$ 300) and the spacing of the grid points are such that the layers have a thickness of $\Delta z = \frac{H(z)}{8}$, where $H(z)$ is the pressure scale height. Overall, this results in a rather different vertical grid structure with a higher resolution compared to ATMO and with grid points that are not uniformly spaced. These differences, as well as any additional variations in the vertical transport scheme, likely explain the small differences in the quench points of CH_4 and NH_3 between our model and that of Venot et al. [2012].

At lower pressures still, the chemistry becomes unquenched due to the increasing temperature and consequent decreasing chemical timescale. However, the availability of high energy photons also increases leading to photochemical dissociation which drives the chemistry at low pressures. Generally we find significant differences between the two models in this low pressure region, and overall we find larger mole fractions of the molecules presented in Fig. 3.8 as well as others that are not shown. Conversely, we find lower abundances of the free-radical species (H, OH, etc) that are a product of photochemical dissociation. This suggests that the photodissociation rate is not as efficient in our model compared to that of Venot et al. [2012]. As the chemical network and other model inputs, including the absorption and scattering coefficients of the molecules, are the same between the two models, the cause of this discrepancy is likely due to a difference in the implementation of the model schemes.

The most likely cause for this discrepancy at low pressures is the representation of radiative transfer in the two models that determines the radiative flux to drive the photodissociations. Our model uses a radiative transfer scheme that includes isotropic scattering and solves for the intensity in a series of ray directions in a discrete-ordinate method, usually using 16 rays in total [Amundsen et al., 2014, Tremblin et al., 2015, Amundsen, 2015]. On the other hand, the Venot et al. [2012] model employs the Isaksen et al. [1977] method where the radiative flux is solved for only in two directions (up and down) and the treatment of scattering is more simplified compared to the approach in our model. These differences are ultimately likely to lead to a discrepancy in the calculated radiative flux in each level that will

propagate into the photodissociation rates.

Fig. 3.8 also shows the comparison with the results of Moses et al. [2011], who use both a different model and a different chemical network. At high pressures, the agreement between the two models is overall good with small variations particularly in the abundances of CH_4 and CO. This is likely to be due to differences in the thermochemical data used between the two models. At lower pressures ($P \sim 1$ bar) the disagreement in the location of the quench points is significant for both CH_4 and NH_3, though this is not surprising. The dominant cause of this discrepancy is the different choice of chemical network, and this has been discussed in depth in Venot et al. [2012] and Moses et al. [2013b]. Again, variations in the model grid and vertical transport schemes may also play role; Moses et al. [2011] use a model grid with ~ 200 grid points with a variable spatial resolution that increases toward higher pressures.

In the lowest pressure regions, $P < 10^{-4}$ bar, where photochemistry is important we find larger abundances of the molecules compared with Moses et al. [2011], similar to the comparison with Venot et al. [2012] shown previously. However, the discrepancy is significantly smaller and despite the differences in the chemical network we find a better match to the results of Moses et al. [2011] than with those of Venot et al. [2012] for this pressure region. The model of Moses et al. [2011] employs a more sophisticated radiative transfer calculation than that of Venot et al. [2012], including multiple scattering due to H_2 and He using a Feautrier method [Michelangeli et al., 1992]. Indeed, Venot et al. [2012] comment on significant sensitivity of the abundance profiles at low pressures to the treatment of Rayleigh scattering. The results presented here add further evidence to the suggestion that it is the calculation of the radiative flux, and not the choice of chemical network, that holds the greatest control over the abundance profiles in low pressures regions that are dominated by photochemical processes.

We compare the abundance profiles in more detail by calculating the absolute and relative differences. The absolute difference is calculated as the difference between the logarithm of the mole fraction from ATMO with the logarithm of the mole fraction from either Venot et al. [2012] or Moses et al. [2011], generally model X

$$\delta_i^{\mathrm{abs}}(P) = \log(f_i^{\mathrm{ATMO}}(P)) - \log(f_i^{\mathrm{X}}(P)) = \log\left(\frac{f_i^{\mathrm{ATMO}}(P)}{f_i^{\mathrm{X}}(P)}\right) \tag{3.48}$$

and the relative difference is calculated as

$$\delta_i^{\mathrm{rel}}(P) = \frac{\delta_i^{\mathrm{abs}}(P)}{\log\left(f_i^{\mathrm{ATMO}}(P)\right)}. \tag{3.49}$$

Figs. 3.9 to 3.11 show the profiles of δ_i^{abs} and δ_i^{rel} for H_2, H, CH_4, CO, NH_3 and

N_2. For H_2 the differences are negligible for $P > 10^{-4}$ bar, but at lower pressures we find a H_2 abundance larger than both Moses et al. [2011] and Venot et al. [2012], and the discrepancy is larger for the latter. The case is similar for H, where the agreement is relatively good except in the photodissociation region where we find lower amounts of H, with again the discrepancy being larger with Venot et al. [2012].

For CH_4 we find a significantly lower abundance in the mid-atmosphere compared to Moses et al. [2011], due to the difference in the quenching point from the different choice of chemical network, whilst we agree very well with Venot et al. [2012]. At lower pressures, we find a greater abundance of CH_4 compared to both models, with again the greatest discrepancy being with Venot et al. [2012]. The abundance profile for CO agrees well with both models.

This behaviour is repeated for the abundance profiles of the nitrogen species. The abundance profile of N_2 agrees well with both models, but we find a lower abundance of NH_3 in the mid-atmosphere compared to Moses et al. [2011], again due to the chemical network yielding a different quench point, but agree well with Venot et al. [2012]. At lower pressures we find a larger abundance of NH_3 compared to both models, with the greatest discrepancy with Venot et al. [2012].

In summary, we find good agreement in the deep atmosphere compared with both Venot et al. [2012] and Moses et al. [2011] where the chemistry is in a state of chemical equilibrium. In the mid-atmosphere, we agree very well with Venot et al. [2012] with only minor discrepancies in the quenched abundances of CH_4 and NH_3, likely due to differences in the discretisation of the model grid and the implementation of the vertical transport. The agreement with Moses et al. [2011] in this pressure range is poorer, though this is predominantly due to the different choice of chemical network and has been previously discussed in detail elsewhere [Venot et al., 2012, Moses et al., 2013b]. At lower pressures, where photochemical processes are important, we generally find a smaller impact due to photodissociations with larger abundances of the molecules (e.g. CH_4, H_2O, etc) and lower abundances of the photochemical products (e.g. H, etc). Interestingly, despite the fact that we use the same chemical network as Venot et al. [2012] we find a better agreement with Moses et al. [2011] in this low pressure region, suggesting that the treatment of scattering, and hence ultimately the calculation of the radiative flux and photodissociation rate, are as important as the choice of chemical network in this region.

In this section we have performed a comparison of our model with two other published chemical kinetics codes in the literature, by matching the model inputs and parameters as closely as possible. However, as shown there can be significant variations in the results from these models, particularly in the low pressure region dominated by photochemistry. There is currently no detailed comparison of these codes in the literature. It would be beneficial to perform a coherent and in depth

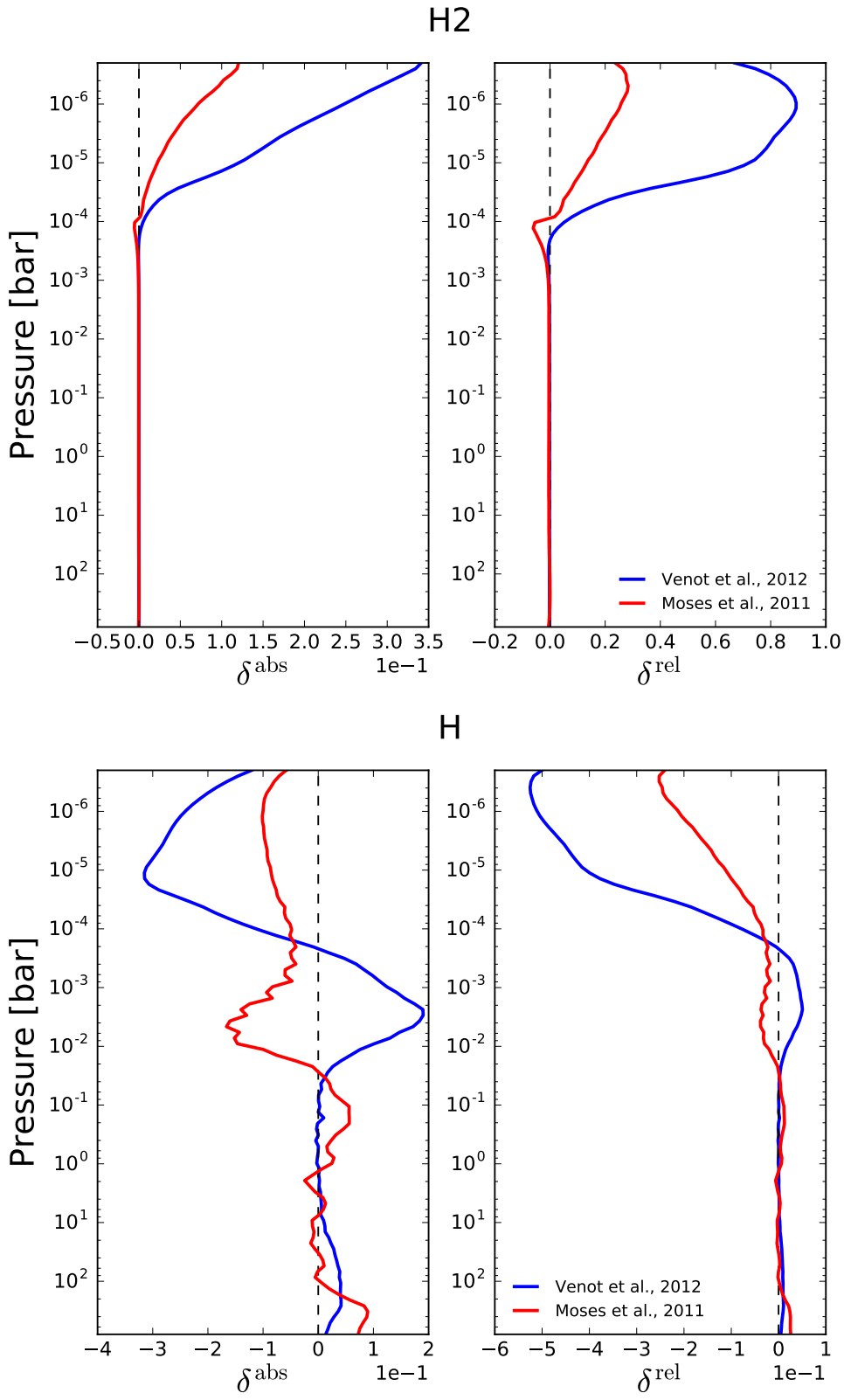

Figure 3.9: The absolute (*left*) and relative (*right*) differences between ATMO and Venot et al. [2012] (blue) and Moses et al. [2011] (red) for the HD 209458b model. The differences in the steady-state non-equilibrium abundance profiles for H_2 (*top*) and H (*bottom*) are shown with the black dashed line indicated zero in both cases.

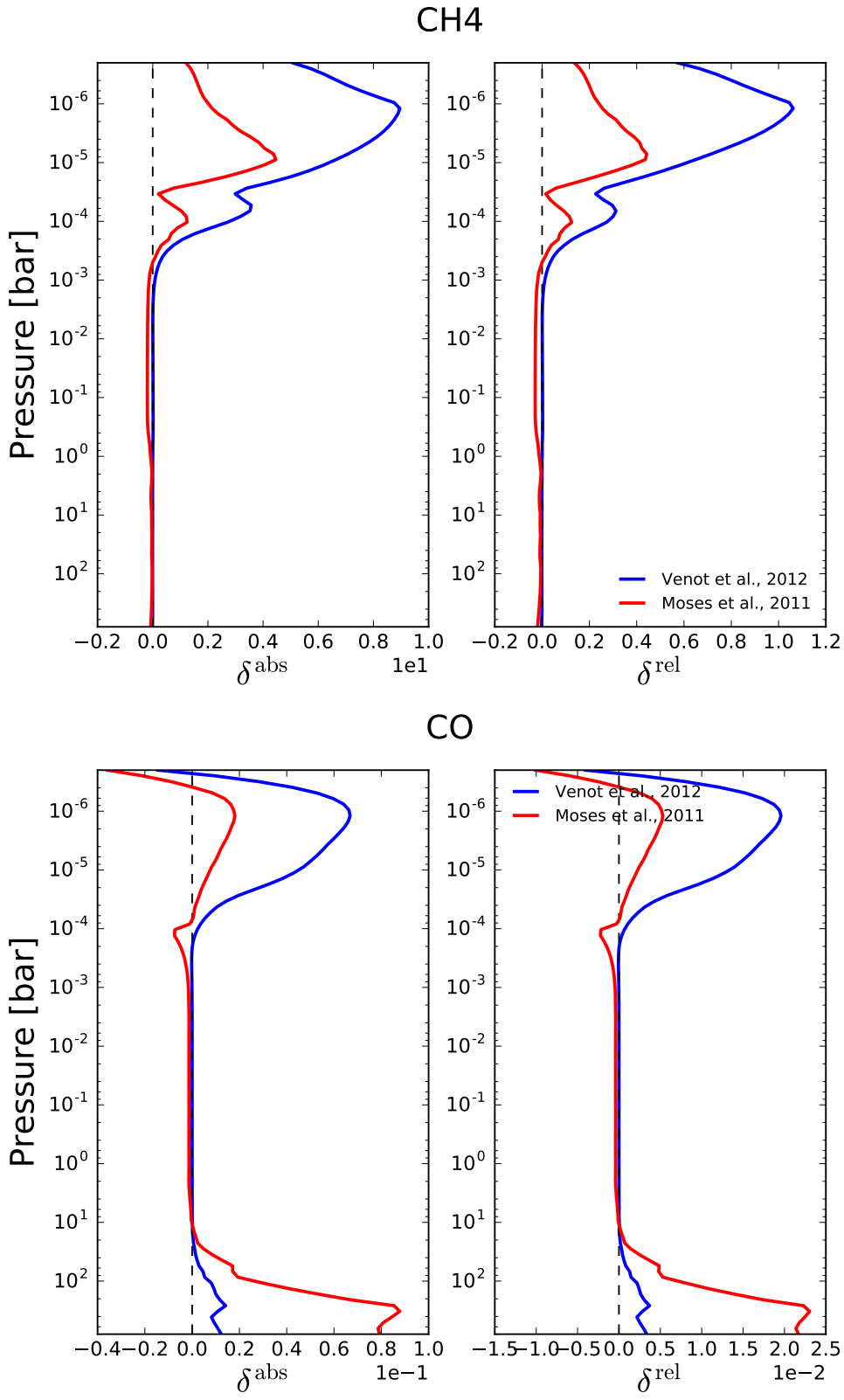

Figure 3.10: As Fig. 3.9 but for CH_4 (*top*) and CO (*bottom*).

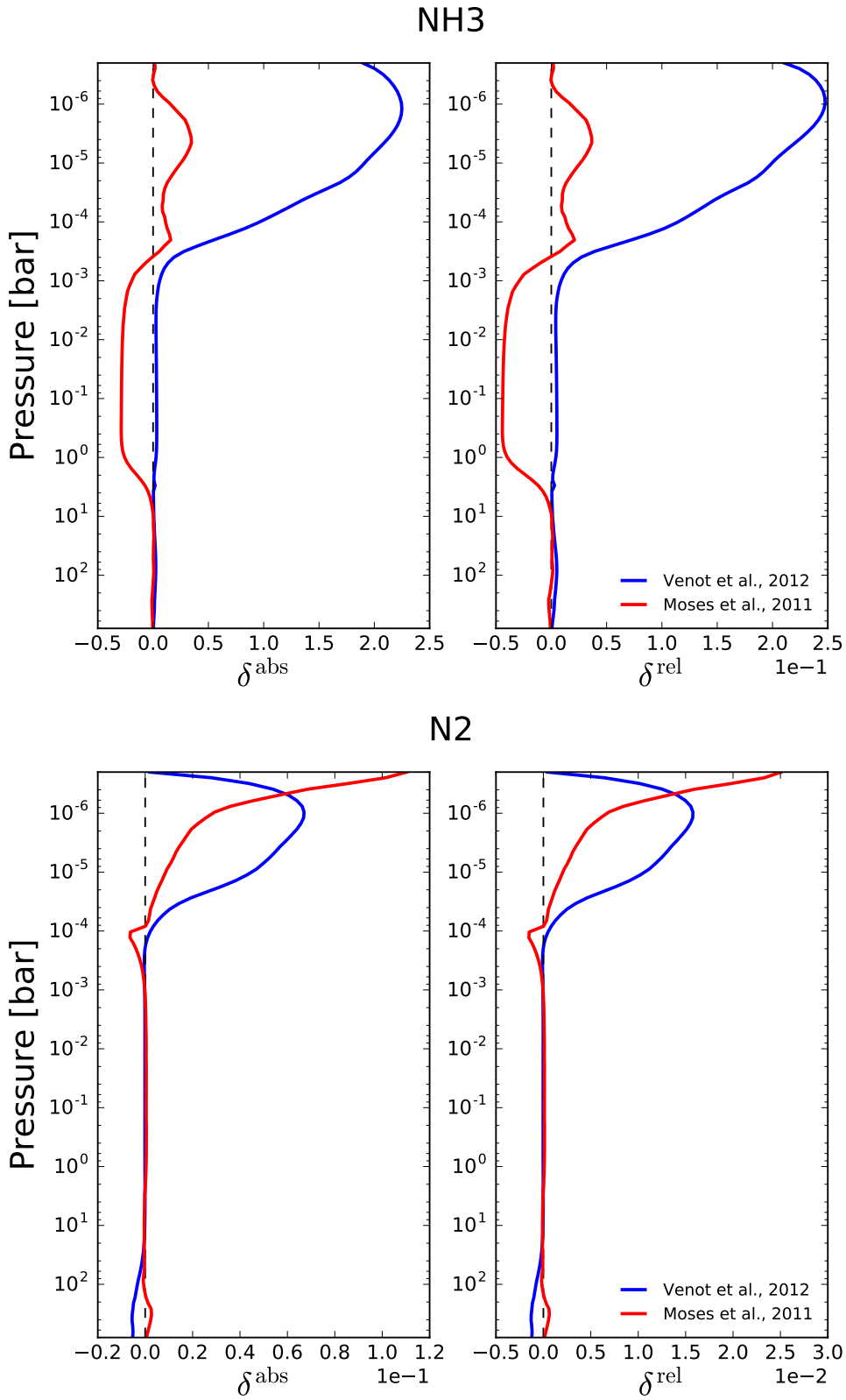

Figure 3.11: As Fig. 3.9 but for NH_3 (*top*) and N_2 (*bottom*).

code comparison to identify and understand the different approaches to model discretisation, vertical transport and radiative transfer (amongst other things) and how this effects the final abundance profiles.

3.6 Summary

In this section the implementation of the Gibbs energy minimisation scheme, that yields the chemical abundances consistent with local chemical equilibrium, and the chemical kinetics scheme, that allows for the inclusion of non-equilibrium processes like vertical transport and photodissociations, has been described. In addition, several test cases have been presented that benchmark and validate the implementation of these schemes. These tests have shown that:

- the Gibbs energy minimisation scheme gives an excellent agreement with the TECA chemical equilibrium code of Venot et al. [2012]
- the Gibbs energy minimisation scheme agrees well with the analytical solutions to chemical equilibrium by both Burrows and Sharp [1999] and Heng and Tsai [2016]
- the rainout condensation chemistry scheme qualitatively reproduces the behaviour of H_2S and Fe for a P–T profile representative of Jupiter
- simple box model tests compare very well with the kinetics code of Venot et al. [2012] thus validating our implementation of the chemical network, calculation of the rate coefficients and solution of the continuity equation using the DLSODES solver
- comparisons of our model with Venot et al. [2012] and Moses et al. [2011] for a 1D model of HD 209458b shows very good agreement with the former in both the deep (chemical equilibrium) and middle (mixing dominated) atmosphere with a poorer match at low pressures. The better agreement with Moses et al. [2011] at low pressures suggests that the method of solving for the radiative transfer is as important as the choice of chemical network in situations where photochemistry is important.

Chapter 4

Consistent Chemical Kinetics in a 1D Model

This chapter describes the development of a consistent non-equilibrium chemistry model and presents results of this model applied to the atmospheres of hot Jupiter atmospheres. In this work, the term consistent is used to describe the fact that the chemical abundances are calculated fully-consistently with the temperature profile of the atmosphere. The model is applied to the atmospheres of the hot Jupiters HD 209458b and HD 189733b. The results presented in this chapter are an expansion of work that has been previously published in Drummond et al. [2016].

In Section 4.1 the context to the problem of non-consistent chemistry models is provided, before our consistent 1D chemical kinetics model is described in Section 4.2 and the results of the application of the model to the atmospheres of HD 209458b and HD 189733b in Section 4.3. In Section 4.4 some additional tests are presented before concluding remarks in Section 4.5

4.1 Context

Chemical kinetics models have been routinely applied to the atmospheres of hot Jupiters and other types of exoplanet to determine the gas-phase chemical composition [e.g. Moses et al., 2011, Venot et al., 2012, Agúndez et al., 2014b] and more recently to examine the kinetic formation of condensate particles [Zahnle et al., 2016]. A key advantage of employing a chemical kinetics approach over other methods (e.g. Gibbs energy minimisation) is that terms which account for physical processes that can drive the abundances away from local chemical equilibrium, such as turbulent mixing and photodissociation, can be included. Often, the overall aim is to investigate whether non-equilibrium chemical abundances can influence the oberved spectra or phase curves [e.g. Moses et al., 2011, Agúndez et al., 2014b].

A common feature amongst published chemical kinetics models is that they require an *input* pressure–temperature (P–T) profile meaning that the chemical abundances are not computed self-consistently with the temperature of the atmosphere. In a real atmosphere, the temperature structure is largely determined by the chemical composition via gas-phase molecular absorption and scattering in addition to the presence of reflecting and absorbing clouds. On the other hand, it is the temperature that controls the precise chemical composition through the temperature-dependent chemical rate constants which determine the interconversion of chemical species.

The source of the P–T profiles used in previous kinetics models of hot Jupiters is varied but generally they are derived from other atmosphere models. For instance, Moses et al. [2011] constructed their P–T profiles for HD 209458b and HD 189733b by combining spatial averages of results from a 3D general circulation model (GCM) [Showman et al., 2009] with results from a separate 1D radiative-convective model [Fortney et al., 2006, 2010] as well as artificially extending the profiles to lower pressures using either isothermal profiles or profiles which increase in temperature (representing a hot thermosphere). Line et al. [2011, 2010] also adapted 1D temperature profiles using spatial averages of output from the same 3D GCM for their studies of HD 189733b [Showman et al., 2009] and GJ 436b [Lewis et al., 2010]. Others have taken P–T profiles from 1D radiative-convective models [e.g. Agúndez et al., 2014b, Venot et al., 2014, 2016, Zahnle et al., 2016].

In each case, the model that calculates these P–T profiles, whether they are 1D or 3D, make the assumption of local chemical equilibrium. A problem therefore arises when such a P–T profile is used within a kinetics code to calculate non-equilibrium abundances. Any departure from chemical equilibrium will change the opacity of the atmosphere and hence the temperature. This process cannot be accounted for in a model where the P–T profile is treated as a fixed input parameter.

During the kinetics calculation, as the chemistry is evolved from chemical equilibrium (the usual initial condition for such models) towards the non-equilibrium steady-state solution, the abundance profiles of the molecules will be adjusted due to vertical mixing and photodissociation. Significant alterations in the abundance profiles of radiatively active molecules (important absorbers or scatterers) *should* correspond to a change in the opacity and consequently to a change in the P–T profile. In turn, any adjustments to the temperature profile *should* produce a response in the chemical abundances themselves due to the temperature-dependence of the rate constants. In previous models the link between the composition-dependent temperature profile and the temperature-dependent composition is broken.

This is a recognised deficiency of these models and several attempts to investigate the importance of this have been made. In the context of brown dwarf atmospheres, where transport-induced quenching of CH_4/CO and NH_3/N_2 is expected to

be important, Hubeny and Burrows [2007] performed non-equilibrium calculations consistently with the P–T profile. However, the quenching of these molecules was performed using timescale arguments, rather than a full chemical kinetics approach. They found corrections of 50–100 K to the P–T profile due to the quenching of CH_4/CO and NH_3/N_2.

In a more recent study, Agúndez et al. [2014b] tested an iterative approach to calculating the P–T profile. Initially, the P–T profile was computed within a 1D radiative-convective model [Iro et al., 2005, Agúndez et al., 2012] assuming local chemical equilibrium. This first P–T profile was used to compute a first set of non-equilibrium chemical abundances, which were subsequently used to generate a second P–T profile. This second P–T profile was finally used to calculate the final set of non-equilbrium abundances. Agúndez et al. [2014b] found adjustments to the temperature profile of <100 K in this 'two iteration' approach, similar to what was found by Hubeny and Burrows [2007].

In the first approach by Hubeny and Burrows [2007], the representation of the quenching of CH_4/CO and NH_3/N_2 via a simple timescale argument is not necessarily accurate. The precise timescale of these processes is determined by the complex chemical pathways for the interconversion of CH_4/CO and NH_3/N_2 respectively, which is poorly constrained. In the attempt by Agúndez et al. [2014b], the 'two iteration' approach is likely to be insufficient, and many iterations could be required in order to converge on the stable solution.

In this rest of this chapter, the results of a 1D atmosphere model that consistently couples the calculation of the P–T profile with the non-equilibrium chemistry calculations is presented. Fundamentally, the key difference between this model and those of the studies previously discussed is that the chemical kinetics code is included within the framework of a 1D radiative-convective model. Crucially, this means that the P–T profile is *not* required as a model input, and is instead calculated self-consistently with the chemical abundances.

4.2 Model description and setup

To investigate the importance of performing non-equilibrium chemistry calculations consistently with the P–T profile we apply our 1D radiative-convective atmosphere model ATMO, previously described in Chapter 3, to the atmospheres of the well studied hot Jupiters HD 189733b and HD 209458b. Though we focus on these two specific planets our aim is not to attempt to reproduce the available observations. Our focus is to investigate the theoretical consequence of performing consistent chemical kinetics calculations, and we simply use the parameters of these two systems as test cases.

Table 4.1: Parameters used in this study.

	HD 209458b	HD 189733b
Mass M_J	0.714	1.150
Radius R_J	1.380	1.151
Orbital Dist. AU	0.047	0.031
Stellar Spectral Type	G0V	K1-K2
Stellar Radius $R_{\rm Sun}$	1.162	0.752

In this section, we detail the model inputs and initial conditions for these two test case atmospheres.

4.2.1 Planetary and stellar parameters

The planetary and stellar parameters of Southworth [2010] are adopted for both HD 189733b and HD 209458b and are reproduced in Table 4.1. Whilst HD 189733b has a much smaller semi-major axis, it is actually the cooler of the two planets due to the lower effective temperature of its host star. It is also worth noting that HD 189733b has a bulk density similar to that of Jupiter, whilst HD 209458b has a vastly inflated radius and consequently a bulk density much lower than that of Jupiter. For both cases we have assumed solar elemental abundances [Caffau et al., 2011] and an internal temperature of 100 K.

For the irradiation spectrum we use the Kurucz stellar spectra[1] for both HD 209458 and HD 189733. It is with this irradiation spectrum that we solve for the P–T profile. The ultra-violet (UV) radiative flux is required for the calculation of the photodissociation rate, however, the Kurucz spectra do not extend to low enough wavelengths; $\lambda < 200$ nm. Therefore, we use a separate irradiation spectrum that does cover to the required spectral range for the calculation of the UV flux.

For the UV irradiation flux of HD 209458 we follow the approach of Moses et al. [2011] and Venot et al. [2012] and use the solar irradiation spectrum. For HD 189733 we take the same approach as Moses et al. [2011] and use the UV flux of a K2 V star, epsilon Eridani, taken from the CoolCAT database[2], for $115 < \lambda < 230$ nm, the solar UV flux for wavelengths below this range, and the solar flux divided by ten for longer wavelengths. The adopted UV irradiation spectra for both models are shown in Fig. 4.1.

[1] http://kurucz.harvard.edu/stars.html
[2] http://casa.colorado.edu/∼ayres/CoolCAT/

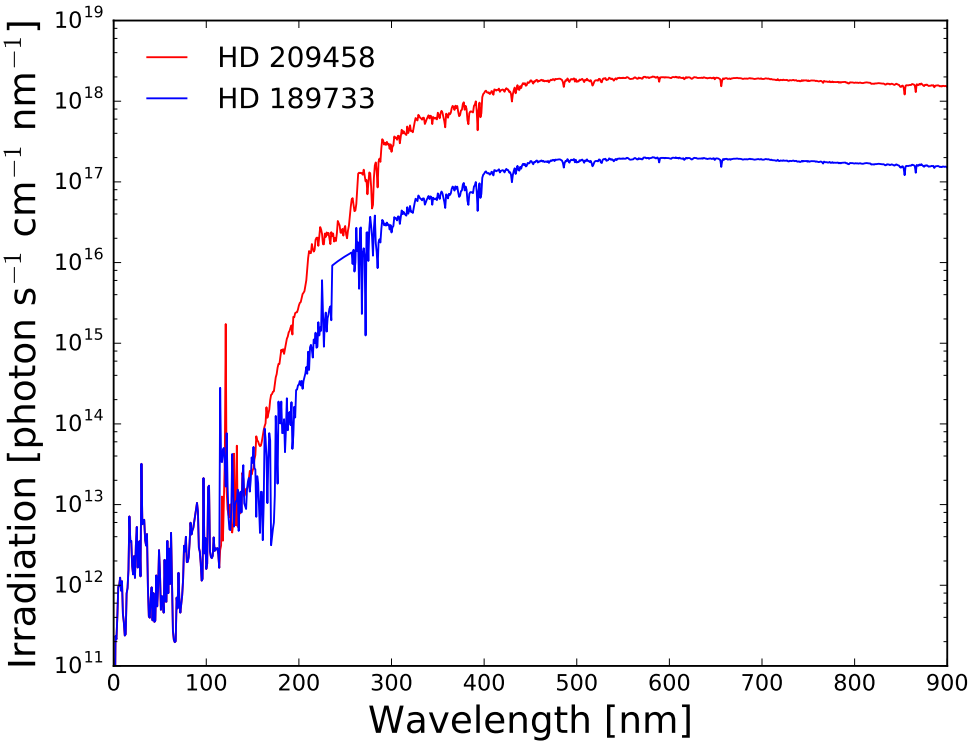

Figure 4.1: The adopted UV irradiation fluxes for HD 209458 (red) and HD 189733 (blue).

4.2.2 Model domain

We model the pressure range $10^3 > P > 10^{-5}$ bar with 100 vertical levels. The choice of the lower pressure limit was set as the atmosphere transitions into the thermosphere at around this region and a different modelling approach is required [e.g. Yelle, 2004, Koskinen et al., 2013]. Correct modeling of the atmosphere below $P \sim 10^{-5}$ bar requires consideration of non-local thermodynamic equilibrium, not currently included in ATMO. Many previous studies have extended their model domain to much lower pressures (e.g. $P = 10^{-11}$ bar [Moses et al., 2011]) though the validity of the results in this region of the model are questionable. The effects of photochemistry begin to become important for $P \leq 10^{-5}$ bar in this model. Therefore, due to the choice of lower pressure limit of our model, whilst we include photochemistry only the 'edge' of the photodissociation zone is captured.

The higher pressure limit of the model $P \sim 10^3$ bar is chosen to ensure that the chemistry at and near to the lower boundary remains in chemical equilibrium for all cases. The presence of chemical equilibrium at the lower boundary is required to satisfy the assumption that there is no net flux of material across the lower boundary; previously discussed in Section 3.4.4.

4.2.3 Initial conditions

As this is a steady-state problem the initial conditions do not affect the final solution, though sensible choices may increase model stability or decrease computation time; this is unlike 3D hydrodynamics simulations where the initial conditions will have some or even significant influence on the results [Mayne et al., 2014a].

The calculation can be considered to be in two parts. Firstly, the P–T profile and chemical abundances are calculated assuming chemical equilibrium. Here, the temperature profile is initialised to an isothermal profile typically with a temperature of 1000 K, though the choice of temperature does not affect the final result. For the chemical abundances the mole fractions are initialised to $0.1/N$, where N is the number of gas species, as in Gordon and McBride [1994]; see Section 3.2.5. For the second part of the calculation, where the temperature profile is reconverged iteratively with the chemical kinetics calculation, the model is initialised with the temperature profile and chemical abundance profiles of the prior chemical equilibrium calculation.

4.2.4 Eddy diffusion coefficient

A vital input to the non-equilibrium chemistry calculation is the eddy diffusion coefficient K_{zz}, which is poorly constrained both observationally and theoretically. In previous studies, this term has been estimated using wind velocity fields derived from 3D general circulation models [e.g. Moses et al., 2011] or parameterised using the advection of passive tracers [Parmentier et al., 2013]; in both of these cases, the value of K_{zz} varies with pressure. Other studies treat K_{zz} as a free model parameter and test a range of plausible values [e.g. Miguel and Kaltenegger, 2014], usually taking a constant value across the modelled pressure range. In this work we take the latter approach and choose two plausible values for K_{zz}.

Values of K_{zz} for hot Jupiter atmospheres used in other works vary between $\sim 10^7$–10^{12} cm^{2}s^{-1} [e.g. Moses et al., 2011, Miguel and Kaltenegger, 2014]. We take one case roughly in the middle of this range ($K_{zz} = 10^9$ cm^{2}s^{-1}) and one towards the upper limit of this range ($K_{zz} = 10^{11}$ cm^{2}s^{-1}). These values are assumed to be constant with pressure.

4.2.5 Chemical network

The carbon-oxygen-hydrogen-nitrogen (C-O-H-N) chemical network of Venot et al. [2012], previously applied in several models of hot, hydrogen-dominated exoplanet atmospheres [Agúndez et al., 2012, 2014a,b, Venot et al., 2014] and also for the atmospheres of brown dwarfs [Tremblin et al., 2015, 2016] is adopted. The network

contains 105 chemical species linked via ∼1000 reversible reactions and has been experimentally validated within the region 300 - 2500 K and 0.01 - 100 bar.

We choose to use the original C_0-C_2 network of Venot et al. [2012], with hydrocarbon species of up to two carbon atoms, rather than the more recent C_0-C_6 network which extends the network to higher-order hydrocarbons with up to six carbon atoms [Venot et al., 2015]. The overall aim of this work is to investigate the importance of solving for the non-equilibrium chemical abundances consistently with the *P–T* profile. Therefore, for the purposes of this study it is most important to accurately determine the abundances of the molecules that contribute to the opacity of the gas mixture (e.g. CH_4, H_2O, etc). The inclusion of higher-order hydrocarbons was found not to affect the abundances of these main species [Venot et al., 2015]. Therefore we choose to use the smaller and less computationally expensive C_0–C_2 network for this work.

In total ∼140 chemical species are included. Of these, 105 are those from the Venot et al. [2012] chemical network. In addition, we include Na, K, Li, Cs and Rb in monatomic form and their important molecular gas-phase species (e.g. NaCl, NaOH, etc) which can deplete the abundance of the monatomic forms. These additional alkali species are included in the chemical equilibrium calculation, since they are included as opacity sources in our model. However, as these species are not incorporated in the Venot et al. [2012] network we hold these species at their equilibrium values throughout kinetics calculation. Note that this is a limitation of our model, in that whilst the C-O-H-N chemistry is evolved consistently with the temperature, the abundances of the alkali species are held fixed at their equilibrium values from the initial *P–T* profile.

Condensation is included in ATMO through equilibrium condensation in the Gibbs energy minimisation calculation (Section 3.2.7). However, for the temperatures typical of these hot Jupiter profiles condensation is not likely to be important in determining the abundances of the alkali species, and therefore condensation is not included in these calculations, and the mixture is assumed to be gas-phase only.

4.2.6 Opacities

The radiative transfer equation is solved in 1D plane-parallel geometry including isotropic scattering. We include CH_4, H_2O, CO, CO_2, NH_3, TiO, VO, Na, K, Li, Cs and Rb and collision induced absorption due to H_2-H_2 and H_2-He as opacity sources in the atmosphere. The source of these opacity data is explained in detail in Amundsen et al. [2014, 2017].

In the current work ATMO is used with the correlated-k approximation using the random overlap method to compute the total mixture opacity (see Lacis and

Oinas [1991] and Amundsen et al. [2017]) for moderate resolution emission and transmission spectra with 500 or 5000 bands and, for a rapid computation of the radiative flux, with 32 bands in the Newton-Raphson iterations. The number of k-coefficients per band is not fixed but is instead computed based on a specified precision; the number of k-coefficients therefore varies depending on the band and the gas [this is explained in detail in Amundsen et al., 2014]. The results obtained using the correlated-k approximation have been compared with the full line-by-line result, which agree very well.

4.2.7 Consistent chemical kinetics calculations

The calculation of the self-consistent non-equilibrium chemical abundances involves two stages. Firstly, the P–T profile is calculated assuming chemical equilibrium, where the abundances are calculated in each iteration using the Gibbs energy minimisation method. This first calculation produces the P–T profile and chemical abundance profiles which are self-consistent and assume local chemical equilibrium.

In the second stage of the calculation, the P–T profile and chemical abundance profiles from the first stage are used as initial conditions, and the chemical continuity equation is solved for the steady-state solution, whilst periodically reconverging (re-calculating) the P–T profile. During each reconvergence of the P–T profile, the abundance profiles are frozen at their current values. After each successful reconvergence of the P–T profile, the integration of the continuity equation is continued until the next P–T reconvergence, and ultimately until the model has reached overall convergence (discussed shortly).

During this second part of the calculation, a choice is made about the frequency f_{P-T} on which to reconverge the P–T profile. Following testing, it was found that $f_{P-T} = 10$ (i.e. ten iterations of the chemistry solver between each P–T profile reconvergence) was found to give the best compromise between accuracy and efficiency. The dependence of the final P–T profile on the choice of f_{P-T} is examined later in Section 4.4.1.

Convergence

The convergence criterium of this model is composed of a series of individual criteria. Firstly, we require that the errors in the energy flux balance and hydrostatic equations are $< 10^{-4}$. Simultaneously, we require that the maximum relative change in the abundances of the chemical species ($\max(dn_i/n_i)$) is $< 10^{-4}$ and that the model has reached a total integration time of 10^{12} s, to ensure that a chemical steady-state has been achieved. When both of these 'chemical' and 'thermal' convergence criteria are *simultaneously* achieved, the consistent chemical kinetics model is deemed to

have reached convergence.

The total walltime for these simulations is typically several hours on a single core. In comparison, a non-consistent model with a fixed P–T, for otherwise similar parameters, requires typically 20–30 minutes.

4.3 Results

In this section we present the P–T profiles, chemical abundances and simulated spectra derived from our fully-consistent 1D model for the two test case hot Jupiter atmospheres outlined in the previous section.

For each of these two test cases we show a series of models with different treatments of the chemistry. Firstly, we show models which assume local chemical equilibrium (EQ). We then present *non-consistent* non-equilibrium (NEQ) models where the P–T profile is fixed throughout the calculation, emulating the method employed by previous studies. Finally, we include *consistent* non-equilibrium (CNEQ) models where the abundances are calculated iteratively with the P–T profile, allowing for the feedback between the non-equilibrium abundances and the temperature structure.

4.3.1 HD 189733b

Fig. 4.2 shows the P–T profiles of our EQ and CNEQ HD 189733b models assuming two different values of K_{zz}, as described in Section 4.2. For the model with stronger vertical mixing there is a significant influence of non-equilibrium chemistry on the P–T profile. The CNEQ P–T profile is $\sim$100 K warmer than the EQ profile for P > 0.1 bar. In the model with the smaller K_{zz} parameter, and hence weaker mixing, the CNEQ P–T profile is warmer than the EQ profile by about 15 K.

The equilibrium and consistent non-equilibrium chemical abundances for these HD 189733b models are shown in Fig. 4.3 for the models using $K_{zz} = 10^{11}$ and 10^{9} cm^{2}s^{-1}. Qualitatively, we find similar behaviour to previous studies [Moses et al., 2011, Venot et al., 2012] where the chemistry remains in chemical equilibrium in the hot deep atmosphere, the mid-regions of the atmosphere are dominated by vertical mixing, and photochemistry begins to become important for $P \sim 10^{-5}$ bar.

The model using the stronger K_{zz} shows significant increases in the abundance of both CH_4 and NH_3 compared to chemical equilibrium, which are quenched at around 10 bar and 100 bar, respectively. In chemical equilibrium, H_2O is more abundant than CO in the deep atmosphere, with CO becoming more abundant than H_2O at around 10 bar. This transition between the two molecules is removed with the inclusion of vertical mixing, as H_2O and CO are quenched below the transi-

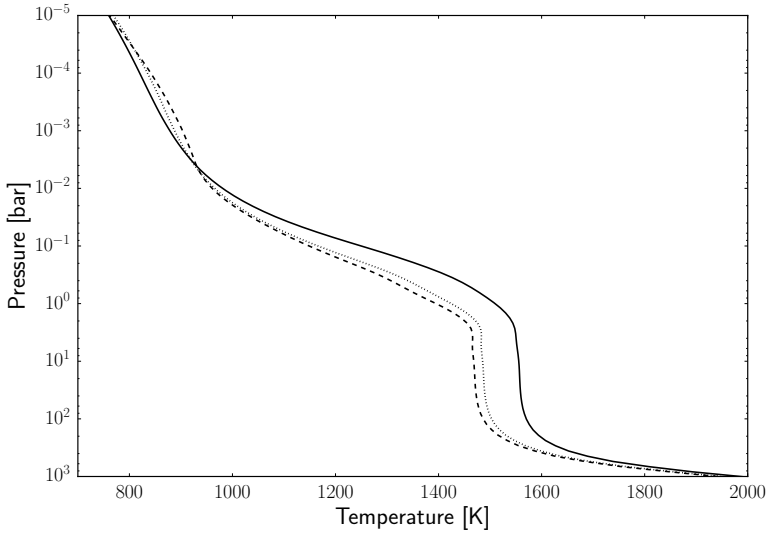

Figure 4.2: The P–T profiles for HD 189733b assuming equilibrium chemistry (EQ model, dashed), consistent non-equilibrium chemistry with $K_{zz} = 10^{11}$ cm^{2}s^{-1} (CNEQ model, solid) and with $K_{zz} = 10^{9}$ cm^{2}s^{-1} (CNEQ model, dotted). Note that the NEQ models referred to in the text use the same EQ P–T profile as plotted in this figure.

tion, increasing the abundance of H_2O for all lower pressures. The model with the smaller eddy diffusion coefficient shows a smaller increase in both CH_4 and NH_3 as their quench points are both shifted to lower pressures, and reducing the quenched abundance. The effect on H_2O and CO is also much smaller in this model.

The temperature increase due to non-equilibrium chemistry has a feedback impact on the temperature-dependent chemical abundances. Comparing the chemical abundances (Fig. 4.4) between the consistent and non-consistent (CNEQ and NEQ) models we see that for the strong vertical mixing case the abundances of CO and CH_4 are essentially reversed, due to an increase in CO and a decrease in CH_4 in the CNEQ model. Similarly, in the NEQ model we find that NH_3 should be the dominant nitrogen species throughout the atmosphere, whereas in the CNEQ model we find that N_2 is the dominant nitrogen species (below 100 bar).

The temperature change induces different abundances via two processes. Firstly, the chemistry in the deep atmosphere remains in chemical equilibrium, and as the temperature increases the chemistry moves towards a new chemical equilibrium with abundances which are consistent with the new temperature.

The second effect is caused by changing the location of the quench point. The quench point occurs at the pressure level where the chemical timescale $\tau_{\rm chem}$ is equal to the mixing timescale $\tau_{\rm mix}$. Since $\tau_{\rm chem}$ is dependent on temperature the quench point is shifted to a lower pressure level, in the case of a warmer atmosphere. This leads to a different quenched mole fraction affecting the quenched abundances for

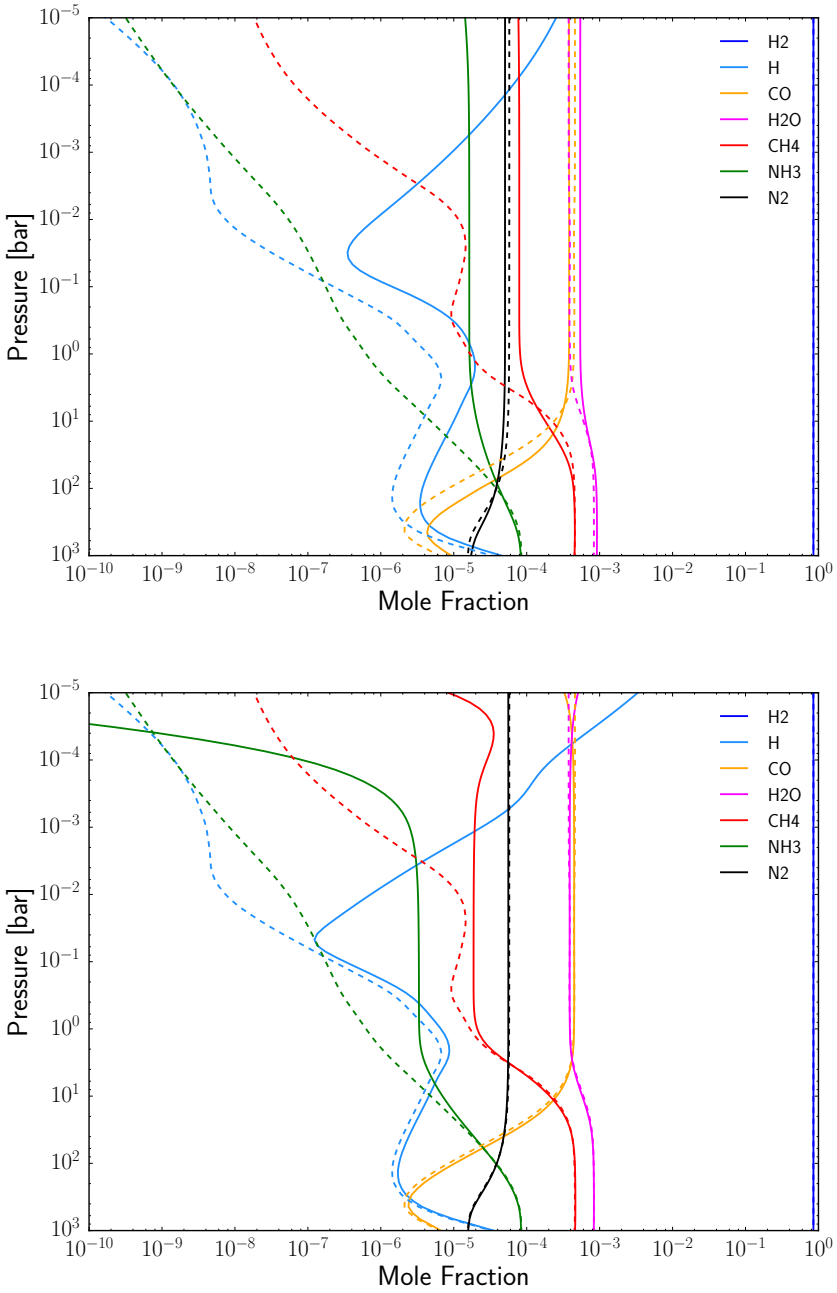

Figure 4.3: The chemical abundances of the major chemical species for the HD 189733b model with abundances from the EQ calculation (dashed) and abundances from the CNEQ calculation including vertical mixing and photochemistry (solid) with eddy diffusion coefficient of $K_{zz} = 10^{11}$ cm^{2}s^{-1} (*top*) and $K_{zz} = 10^9$ cm^{2}s^{-1} (*bottom*).

pressures below the quench point. This is complicated by the fact that the mole fractions of individual species have changed in the region of the quench point as they now exist in the new higher temperature chemical equilibrium, due to the first process explained.

These processes also occur in the model with weaker vertical mixing but to a smaller degree since the departure from chemical equilibrium and the induced temperature change is less.

Tests including photochemistry only (without vertical mixing) show that the photochemistry has a negligible impact on the P–T profile. Photodissociations become important for pressures below $\sim 10^{-5}$ bar depending on the temperature and the UV flux. At these pressure levels the optical depth is small and changes in the chemical composition have negligible effect on the temperature structure. Transport–induced quenching is effective at higher pressures and higher optical depths has the potential to alter temperature stucture. However, it may be that photochemical production of chemical species not included in our model, or not included as opacity sources in our model, could contribute to heating at low pressures; for example, ozone in the Earth atmosphere. We investigate the importance of photochemistry in more detail in Section 4.4.2.

Overall, we find that for our model atmosphere of HD 189733b the process of transport-induced quenching causes temperature increases of up to 100 K between 10^{-1}–10^{2} bar. This temperature increase, in turn, effects the calculated mole fractions by 1) inducing a new chemical equilibrium consistent with the higher temperature in the deep atmosphere and 2) shifting the quench point ($\tau_{\rm chem}$=$\tau_{\rm mix}$) to lower pressures and altering the quenched abundances at low pressures; these two processes act simultaneously. For the strong vertical mixing case CO is the dominant carbon species for P<10 bar in the CNEQ model whereas CH_4 is instead the dominant carbon species throughout the whole atmosphere in the NEQ model. A similar process occurs for the N_2-NH_3 system leading to an N_2 dominated atmosphere in the CNEQ model but an NH_3-dominated atmosphere in the NEQ model.

Simulated emission spectra

In this section we present the simulated emission spectra for this series of models of HD 189733b. Fig. 4.5 shows the simulated emission spectrum for the stronger vertical mixing case for all three chemistry models (EQ, NEQ and CNEQ). Non-equilibrium chemistry has a strong impact on the simulated emission spectrum in the NEQ model. The NEQ spectrum has a significantly reduced flux ratio compared with the EQ model at almost all wavelengths. On the other hand, the CNEQ model shows a smaller discrepency with the EQ model, except at around 4.5 µm where the CNEQ model shows a greater flux ratio than both the EQ and NEQ models.

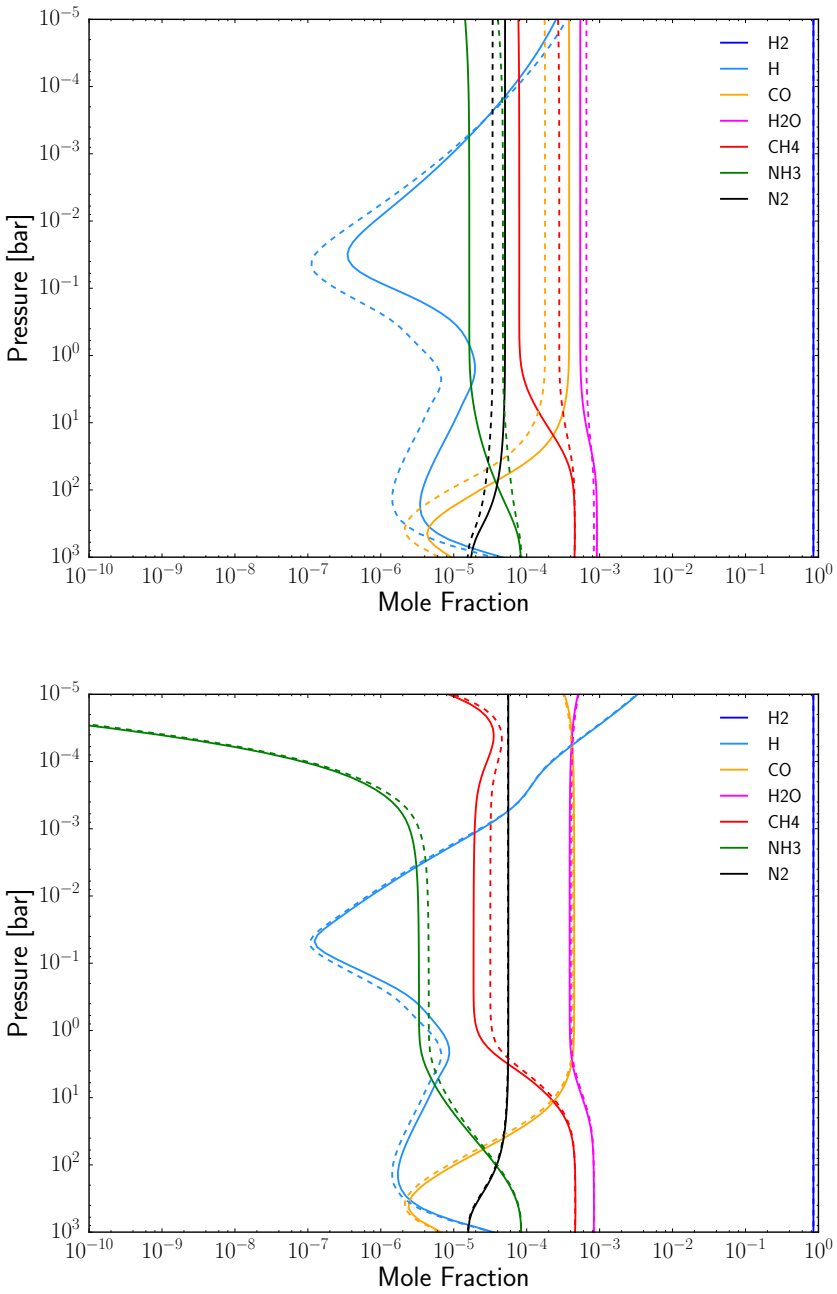

Figure 4.4: A comparison of the chemical abundances between the CNEQ model (solid) and the NEQ model (dashed) for HD 189733b with $K_{zz} = 10^{11}$ cm^{2}s^{-1} (*top*) and $K_{zz} = 10^{9}$ cm^{2}s^{-1} (*bottom*).

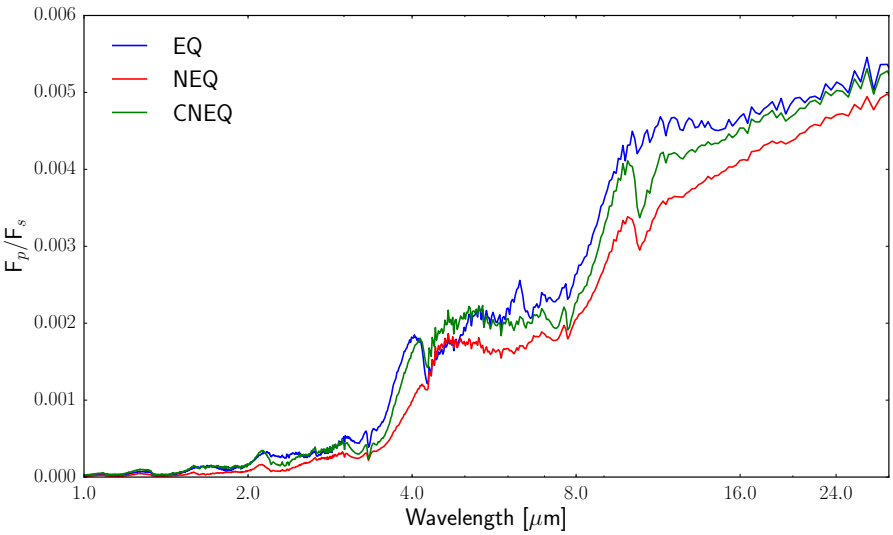

Figure 4.5: The emission spectra of the HD 189733b model with $K_{zz} = 10^{11}$ cm^{2}s^{-1}, showing calculations based on the EQ calculation (blue), the NEQ calculation (red) and the CNEQ calculation (green).

The model with the lower K_{zz} value (Fig. 4.6) shows similar trends, though the difference between all three chemistry cases is smaller as the departure from chemical equilibrium is not as strong. Our EQ and NEQ simulated spectra for this case agree well with the spectra of the 'thermochemical model' and 'photochemical model' of Moses et al. [2011, their Fig. 11]. We also find a reduction in flux at around 4 µm and at longer wavelengths for our NEQ model. Interestingly, however, performing the chemical kinetics calculations consistently (CNEQ model) completely removes this signature of non-equilibrium chemistry at 4 µm and also reduces the impact at longer wavelengths.

Most of the spectral features here are due to CH_4 (particularly around 3.6 µm) and, at longer wavelengths, to NH_3 whilst CO is the dominant absorber around 4.5 µm. Increases in the mole fractions of CH_4 and NH_3 due to transport-induced quenching increase the opacity in the wavelengths regions where they have absorption bands.

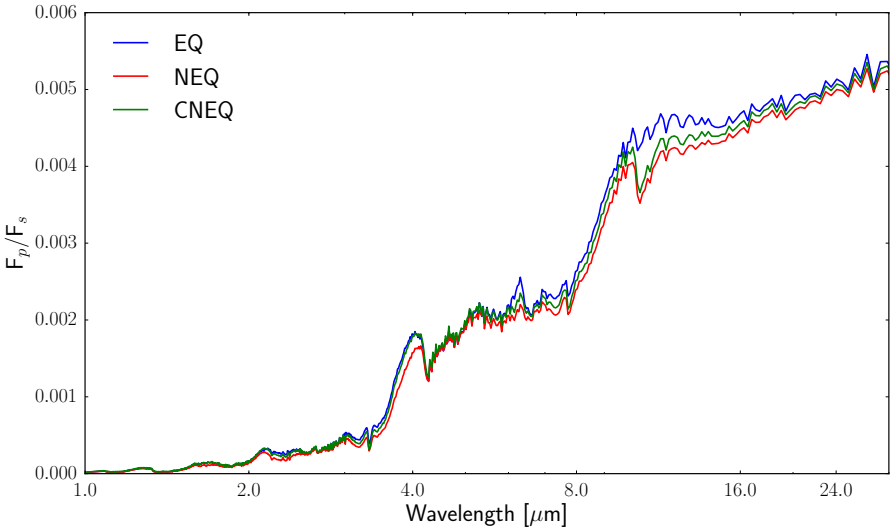

Figure 4.6: Same as Fig. 4.5 but for the $K_{zz} = 10^9$ cm^{2}s^{-1} model.

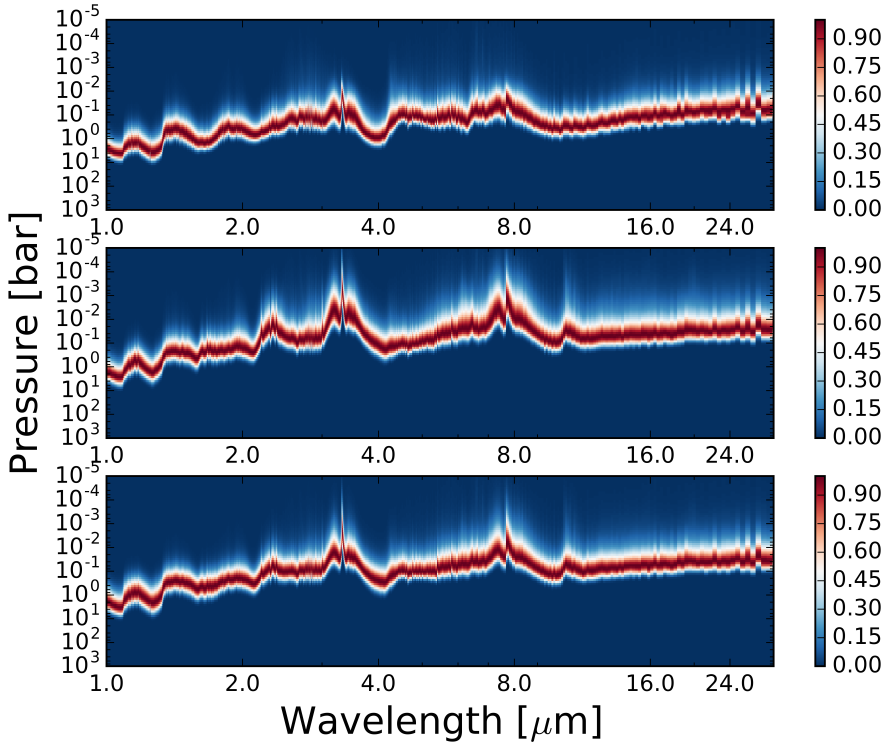

Figure 4.7: The spectral contribution functions for the EQ (*top*), NEQ (*middle*) and CNEQ (*bottom*) models of HD 189733b, for the $K_{zz} = 1 \times 10^{11}$ cm^{2}s^{-1} case.

To aid interpretation of the emission spectrum we can consider the contribution function [e.g. Knutson et al., 2009b, Griffith et al., 1998] which quantifies the pressure range from where the observed flux is originating. Effectively it shows the pressure level of the photosphere, where the atmosphere becomes optically thin, as a function of wavelength.

Fig. 4.7 shows the contribution function for each of the models of HD 189733b, for the $K_{zz} = 1 \times 10^{11}$ cm^{2}s^{-1} case. Generally the contribution function peaks for pressures between 10 and $1{\times}10^{-3}$ bar with spectral variations due to the wavelength-dependent opacities of the absorping species like H_2O. Comparing the contribution functions for the EQ and NEQ models, the peak in the contribution function shifts to slightly lower pressures, particularly around 3.6 and 8 μm, that correspond to absorption features of CH_4 and NH_3, respectively. This shifting of the peak of the contribution function to lower pressures, and therefore lower temperatures, is consistent with a reduction in the flux for the NEQ model, compared to the EQ model, seen in Fig. 4.5. Similar trends are seen for the CNEQ model but to a lesser degree.

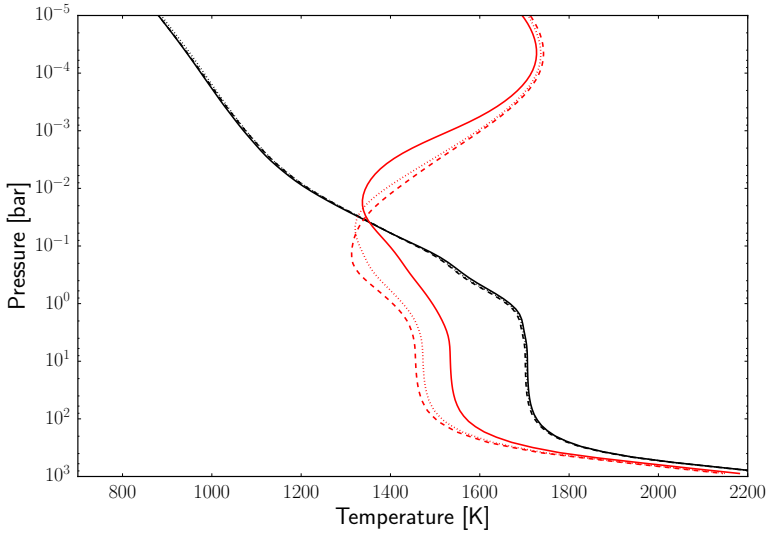

Figure 4.8: The P–T profiles for HD 209458b assuming equilibrium chemistry (EQ models, dashed), consistent non-equilibrium chemistry with $K_{zz} = 10^{11}$ cm^{2}s^{-1} (CNEQ models, solid) and with $K_{zz} = 10^{9}$ cm^{2}s^{-1} (CNEQ models, dotted), with the model including TiO and VO (red) and without TiO/VO (black). Note that the NEQ models referred to in the text use the same EQ P–T profile as plotted in this figure.

4.3.2 HD 209458b

We now present a series of models for the atmosphere of HD 209458b, which overall is much warmer than the atmosphere of HD 189733b due to its orbit around a hotter star. There has been much debate about the presence of a thermal inversion in the atmosphere of HD 209458b, with early observations favouring the presence of an inversion [Knutson et al., 2008, Beaulieu et al., 2010]. However, more recent re-analyses of these datasets suggest that this atmosphere does not contain a temperature inversion [Diamond-Lowe et al., 2014, Evans et al., 2015]. In this study, we present both cases, as a way to explore a larger diversity of atmosphere types.

Fig. 4.8 shows the P–T profiles for the two different atmosphere types of HD 209458b. In each case we show P–T profiles for both the EQ and CNEQ chemistry models and with two different strenghs of vertical mixing; $K_{zz} = 10^{11}$ and $K_{zz} = 10^{9}$ cm^{2}s^{-1}, as in the previous section. For the rest of this analysis, however, we discuss only the $K_{zz} = 10^{11}$ cm^{2}s^{-1} case, where the impact of non-equilibrium chemistry is larger, and instead focus on the difference between the temperature inversion and non-temperature inversion cases.

For the case without a temperature inversion there are very small differences between the EQ and CNEQ P–T profiles. For pressures greater than $\sim$0.1 bar the CNEQ model is marginally warmer than the EQ model; in the isothermal plateau region (1 bar $< P <$ 100 bar) the temperature is $<$ 10 K warmer. On the other hand,

the case with a temperature inversion shows a much greater discrepancy between the EQ and CNEQ models. The CNEQ *P–T* profile is > 100 K hotter than the EQ *P–T* profile for pressures greater than 0.1 bar. At lower pressures the CNEQ *P-T* profile is cooler than the EQ case by a similar amount. Interestingly, the position of the thermal inversion is also shifted to lower pressures.

Fig. 4.9 (top) shows the abundances of the major chemical species for the model without a temperature inversion. NH_3 and CH_4 are quenched at around 10 and 1 bar respectively. This has the effect of increasing their abundances with respect to chemical equilibrium by several orders of magnitude for pressures lower than the quench point. Despite this, their molar fractions do not exceed 1×10^{-6} and N_2 and CO remain the dominant nitrogen and carbon species, which are unaffected by vertical mixing processes, and retain constant mixing ratios below 10 bar. The effects of photochemistry can be seen in the very upper regions of the model, particularly by the dissociation of NH_3 at 0.1 mbar and photochemical production of atomic H from 10 mbar.

Fig. 4.9 (bottom) shows the abundances for the model with a temperature inversion which shows a much greater departure from chemical equilibrium. Though this model contains a hotter upper atmosphere, at depth the atmosphere is actually considerably cooler than the model without a temperature inversion. TiO and VO absorb visible photons at low pressures forming the temperature inversion. However, this reduces the flux of high energy photons which penetrate to depth and heat the lower atmosphere. This reduction of heating at high pressures leads to a cooler deep atmosphere. Due to the temperature dependence of the chemical timescale the quench point is shifted to higher pressures in the temperature inversion model, leading to larger quenched abundances of both CH_4 and NH_3. The quench points for CH_4 and NH_3 now lie at 10 and 100 bar, respectively. At around 1 mbar, where the temperature begins to increase again, the chemical timescale begins to speed up once more, and the species begin to move back towards their chemical equilibrium state, as seen in previous studies [Moses et al., 2011, Venot et al., 2012].

The chemical abundances in the CNEQ and NEQ models (Fig. 4.10) show important differences for the temperature inversion model. The NEQ model gives a CH_4 mole fraction around 5× larger than the CNEQ model. Similarly, the NH_3 mole fraction is ∼3.5× larger in the NEQ model compared with the CNEQ model. These discrepancies between the two models occur in the pressure range where observations are available. The differences are, again, due to the increase in temperature at depth which 1) changes the chemical equilibrium abundances in the deep atmosphere and 2) shifts the location of the quench point.

There is negligible difference between the CNEQ and NEQ abundances for the model without a temperature inversion; only minor decreases in CH_4 and NH_3 in

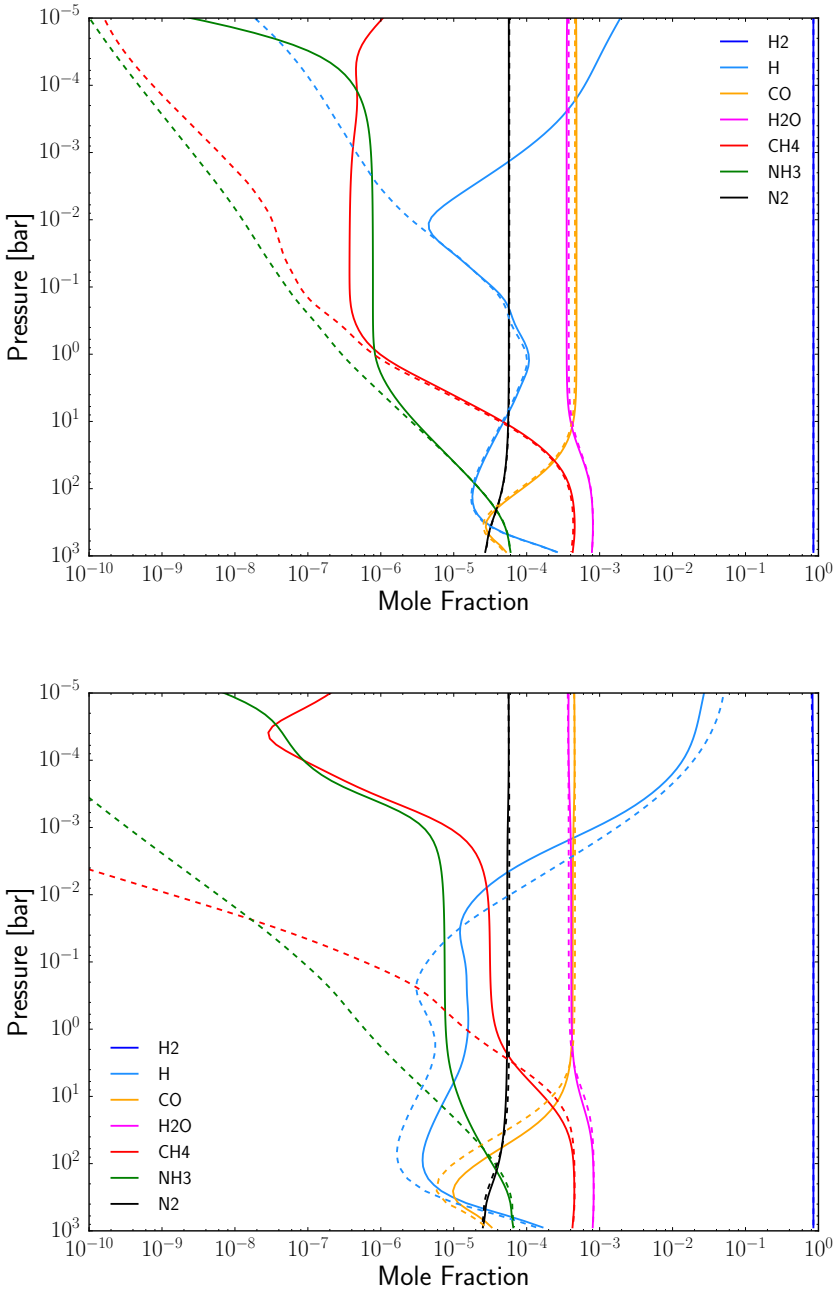

Figure 4.9: The chemical abundances of the major chemical species from the EQ calculation (dashed) and abundances from the CNEQ calculation including vertical mixing and photochemistry (solid) for HD 209458b without a temperature inversion (*top*) and with a temperature inversion (*bottom*) with $K_{zz} = 10^{11}$ cm^{2}s^{-1}.

the CNEQ case. This is to be expected since the temperature difference between the CNEQ and NEQ model is also very small.

We find that in the case of HD 209458b hosting a temperature inversion the deep atmosphere is cool enough to have significant non-equilibrium chemical abundances. This leads to a temperature increase of more than 100 K between 0.1-100 bar, and a temperature decrease at lower pressures. The location of the temperature inversion is also shifted to lower pressures. These temperature changes have important consequences on the chemical abundances and we find significantly smaller mole fractions of CH_4 and NH_3 in the consistent (CNEQ) model compared with the non-consistent (NEQ) model.

For the model without a temperature inversion the deep atmosphere is much hotter and the quench point exists at much lower pressures. This limits the influence of non-equilibrium chemistry and only a small temperature change is seen even for the strong vertical mixing case. Consequently there is little difference between the mole fractions of the consistent and non-consistent models.

Simulated emission spectra

In this section we show the simulated emission spectra for the series of HD 209458b models discussed above.

For the model without a temperature inversion (Fig. 4.11) there is a very small difference in the flux between the EQ, NEQ and CNEQ cases. This is not surprising since the departure from chemical equilibrium is small; and consequently the induced change in the P–T profile is small.

However, the models including a temperature inversion do show important differences (Fig. 4.12). The NEQ spectrum shows a greater flux over most of the wavelength range compared with the EQ and CNEQ spectra. In particular there is a large increase in flux around 3.6 µm due to a large increase in the methane abundance due to transport–induced quenching. This is the opposite to what was found for the HD 189733b models where the flux was seen to decrease in the NEQ model. The primary difference between these models is that, in this HD 209458b model, at low pressures the temperature is increasing inversely with pressure, due to the presence of a temperature inversion.

On the other hand, the EQ and CNEQ spectra are remarkably similar, despite the fact the abundances of methane and ammonia are driven far from chemical equilibrium and the P–T profile is altered considerably. The increase in flux around 3.6 µm and at longer wavelengths present in the NEQ model are not apparent in the CNEQ model, removing the signatures of non-equilibrium chemistry. The cause of this will be explained in detail in the next section.

In this particular case, the overall effect of calculating the non-equilibrium

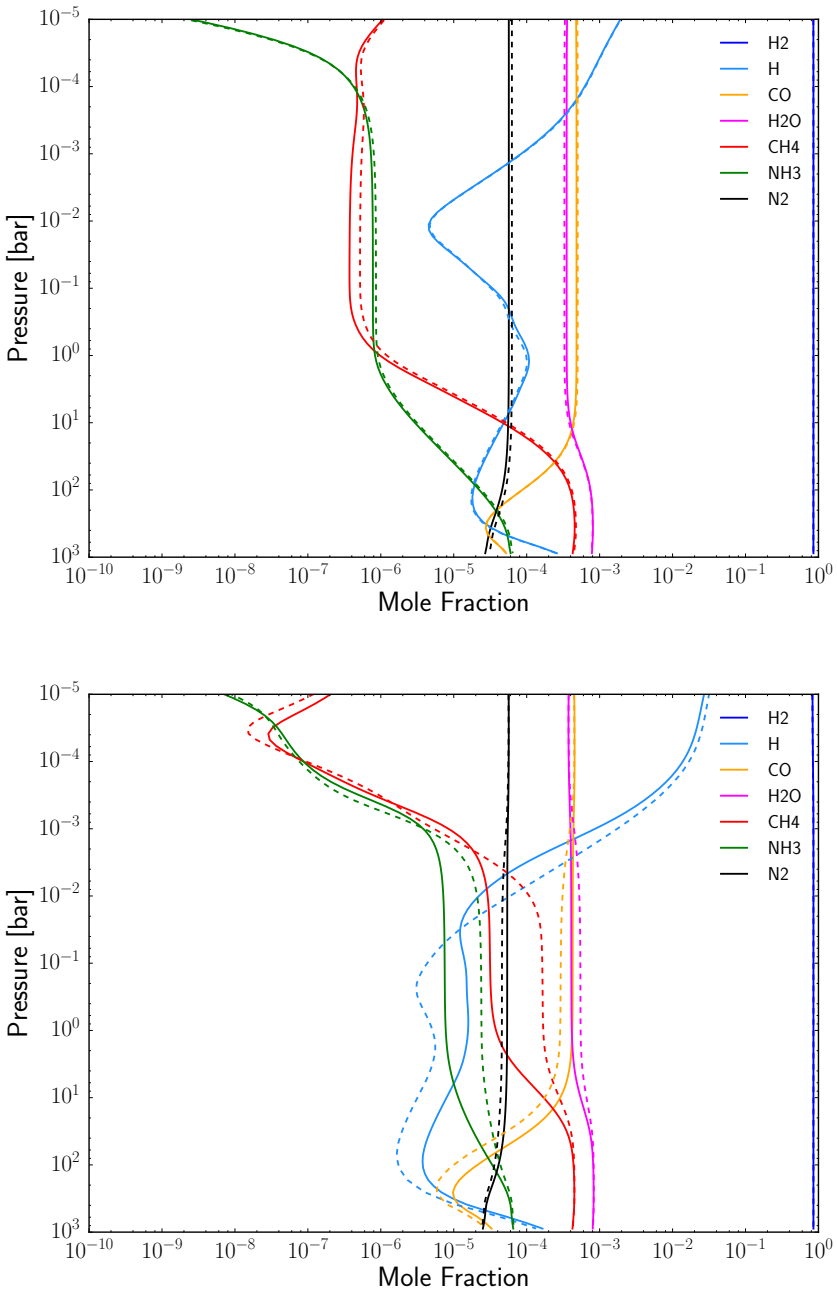

Figure 4.10: A comparison of the chemical abundances between the CNEQ model (solid) and the NEQ model (dashed) for HD 209458b without a temperature inversion (*top*) and with a temperature inversion (*bottom*) with $K_{zz} = 10^{11}$ cm^{2}s^{-1}.

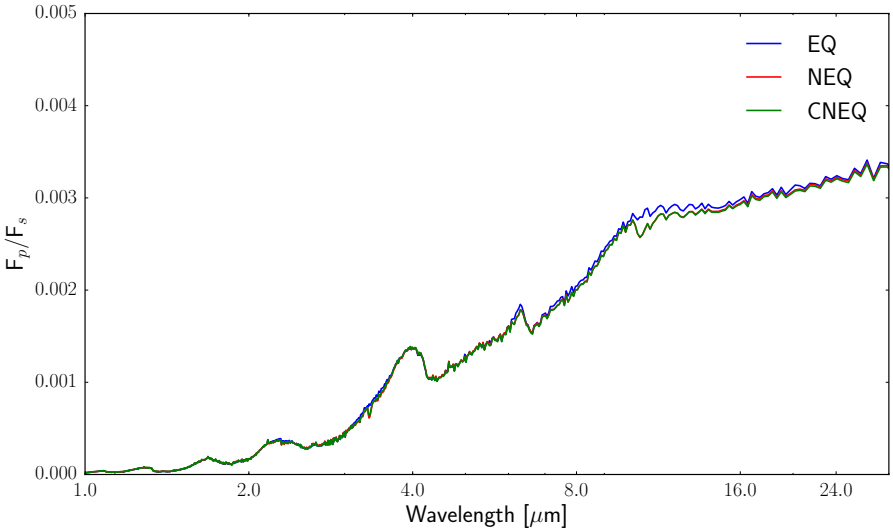

Figure 4.11: The emission spectra of the HD 209458b model without a temperature inversion, showing calculations based on the EQ calculation (blue), the NEQ calculation (red) and the CNEQ calculation (green); $K_{zz} = 10^{11}$ cm^{2}s^{-1}.

chemistry consistently with a coupled temperature structure, rather than on a fixed P–T profile, is to reduce the influence of non-equilibrium chemistry on the emission spectrum, as found for the HD 189733b model, as the CNEQ spectrum tends back towards the EQ result.

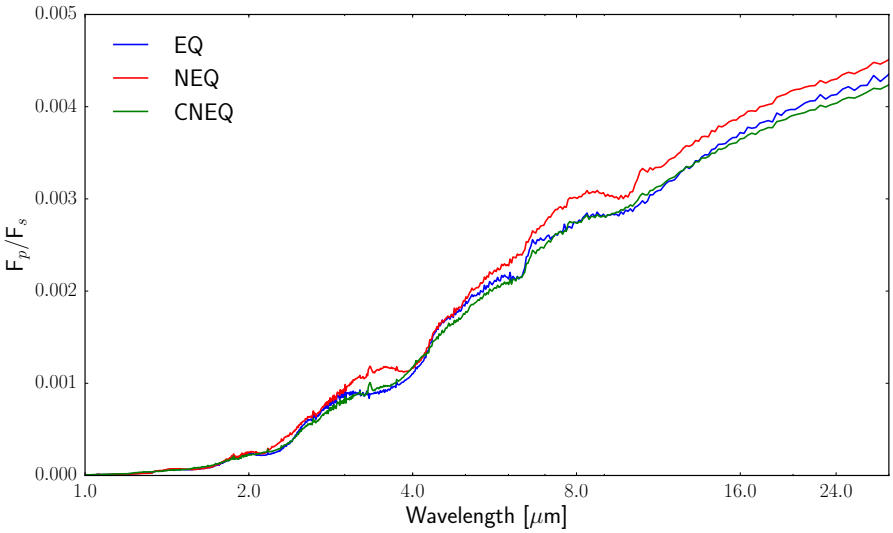

Figure 4.12: Same as Fig. 4.11 but for the HD 209458b model with a temperature inversion.

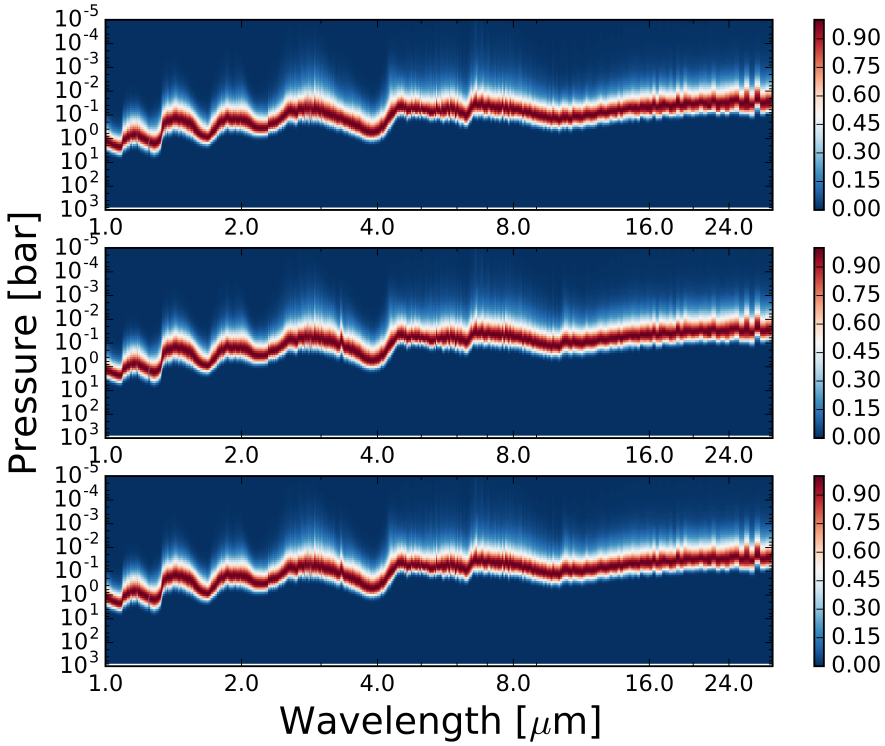

Figure 4.13: The spectral contribution functions for the EQ (*top*), NEQ (*middle*) and CNEQ (*bottom*) models of HD 209458b, for the model without TiO/VO.

Fig. 4.13 shows the contribution function for the HD 209458b model without TiO/VO. Contrasting with the earlier HD 189733b case, the contribution function peaks within a narrower pressure range of approximately 10 to 0.01 bar. There are few notable differences between each chemistry case, as seen in the emission spectra previously.

Fig. 4.14 shows the contribution function for the HD 209458b model with TiO/VO. In this case, the contribution function peaks at considerably lower pressures in some spectral regions, due to the presence of a thermal inversion in this model. Differences are also notable between each of the different chemistry models. In particular, the peak in the contribution function is pushed to lower pressures in both the NEQ and CNEQ model in wavelength regions between 2 and 4 μm, and between 8 and 16 μm. In this model, the shift of the contribution function to lower pressures and higher temperatures corresponds to the larger fluxes seen in the emission spectra in Figs. 4.11 and 4.12.

4.3.3 Energy balance considerations

In this section we further investigate the differences resulting from a consistent treatment of calculating non-equilibrium chemical compositions.

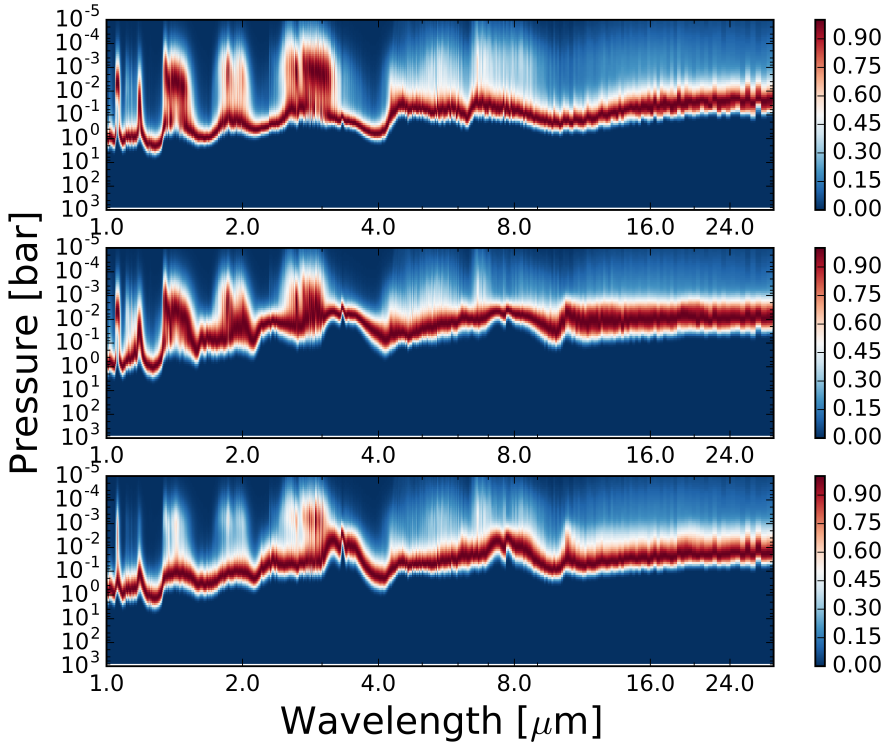

Figure 4.14: The spectral contribution functions for the EQ (*top*), NEQ (*middle*) and CNEQ (*bottom*) models of HD 209458b, for the model with TiO/VO.

Figs. 4.15 and 4.16 show the thermal emission spectra of the atmosphere (not divided by $F_{\rm star}$) for the HD 189733b models with $K_{zz} = 10^{11}$ and 10^{9} cm^{2}s^{-1}, respectively. In both cases, the emission is lower at all wavelengths for the NEQ models, compared to both the EQ and CNEQ models. This discrepancy is larger for the model with stronger vertical mixing. By eye, one can already see that the total energy emission of the atmosphere (i.e. the wavelength-integrated flux) is less in the NEQ model, compared with the EQ and CNEQ models.

Indeed, this is the case, as shown in Tables 4.2 and 4.3 which present the integrated top of atmosphere flux (not including the reflected component) and corresponding blackbody temperatures for both K_{zz} cases and for all chemistry models. In both K_{zz} cases, the integrated flux for the EQ and CNEQ models agree well with each other, conserving the total energy being emitted by the atmosphere. On the other hand, the NEQ models show strongly reduced integrated fluxes. The integrated flux in the NEQ models is $\sim$38% and $\sim$11% smaller than the EQ integrated flux for the $K_{zz} = 10^{11}$ cm^{2}s^{-1} and $K_{zz} = 10^{9}$ cm^{2}s^{-1} models, respectively.

These calculations show that the NEQ models do not conserve energy and the model atmosphere is not in a state of energy balance. The incoming energy (irradiation and internal heating) has not changed, only the chemical abundance profiles have changed, yet the atmosphere is emitting less energy. However, the

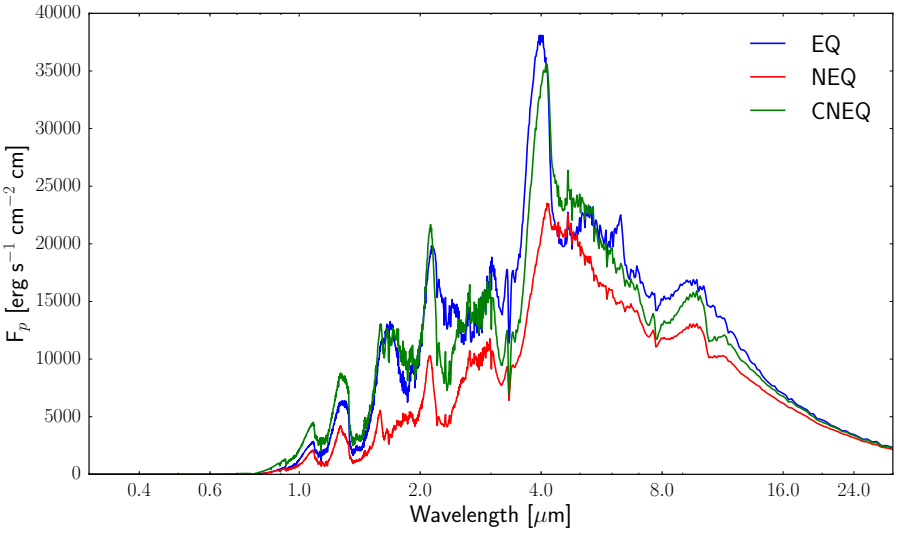

Figure 4.15: The atmosphere emission spectrum of the HD 189733b model with K_{zz} = 10^{11} cm^{2}s^{-1} showing calculations based on the EQ calculation (blue), the NEQ calculation (red) and the CNEQ calculation (green).

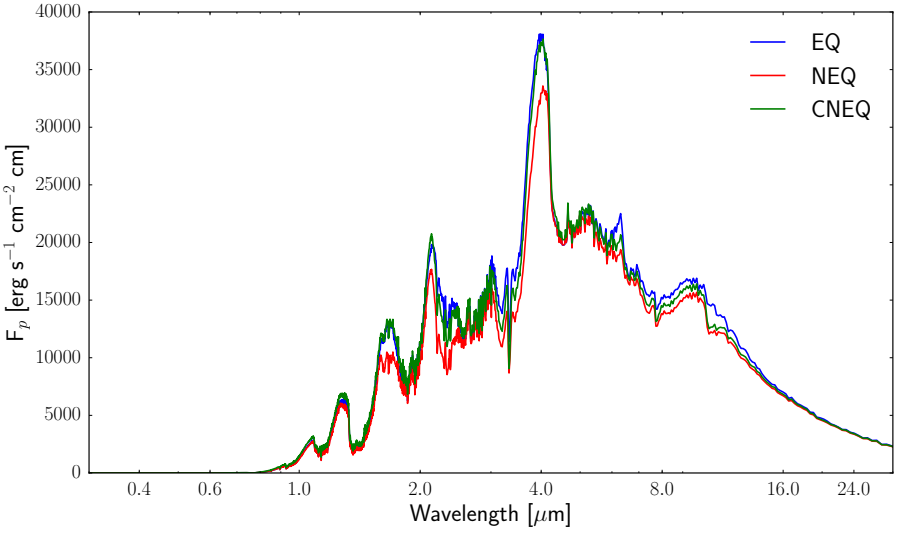

Figure 4.16: Same as Fig. 4.15 but for the $K_{zz} = 10^9$ cm^{2}s^{-1} model.

Table 4.2: Integrated flux and corresponding blackbody temperatures for the HD 189733b model with $K_{zz} = 10^{11}$ cm^{2}s^{-1}.

	Flux (kWm^{-2})	T$_{BB}$ (K)
EQ	106.6	1171
NEQ	66.1	1039
CNEQ	106.4	1170

Table 4.3: Integrated flux and corresponding blackbody temperatures for the HD 189733b model with $K_{zz} = 10^{9}$ cm^{2}s^{-1}.

	Flux (kWm^{-2})	T$_{BB}$ (K)
EQ	106.6	1171
NEQ	94.6	1137
CNEQ	106.6	1171

CNEQ models do conserve the amount of energy being lost by the atmosphere, as the integrated flux is equivalent to that found for the EQ models.

To understand this further, we show the pressure level of peak emission (i.e. the photosphere) in Figs. 4.17 and 4.18 for the 3.6 µm and 8.0 µm Spitzer/IRAC channels, respectively. Here the pressure level of the photosphere is taken as the maximum of the contribution (or weighting) function [e.g. Knutson et al., 2009b, Griffith et al., 1998]. In both cases, the pressure level of the photosphere is shifted to lower pressures, and lower temperatures, in the NEQ model. This is a result of increased opacity due transport-induced quenching of CH_4 and NH_3.

Since the emission flux is strongly dependent on temperature, the shifting of the photosphere to lower temperatures results in a decreased emission in this wavelength band. Indeed, this occurs not just in this wavelength band but also at other points where CH_4/NH_3 absorb and is evident in the decreased integrated flux value previously shown for the NEQ models. For the CNEQ model, though the photosphere is shifted to lower pressures the temperature at this lower pressure is increased compared with the EQ/NEQ model. Here we see the P–T profile adapting to maintain radiative-convective equilibrium and energy balance in reaction to the changing chemical composition due to non-equilibrium chemistry.

The case is very similar for the models of HD 209458b. Figs. 4.19 and 4.20 show the top of atmosphere emission spectrum for the models with and without a temperature inversion, respectively, in each case for the EQ, NEQ and CNEQ models. The model without a temperature inversion shows a negligible difference between all three cases. In the temperature inversion model, the NEQ case shows a greater flux at all wavelengths compared with the EQ case. In particular, there is a large increase in flux between 3 and 4 µm, which roughly corresponds to the wavelength of peak emission. Methane dominates the absorption around 3.6 µm,

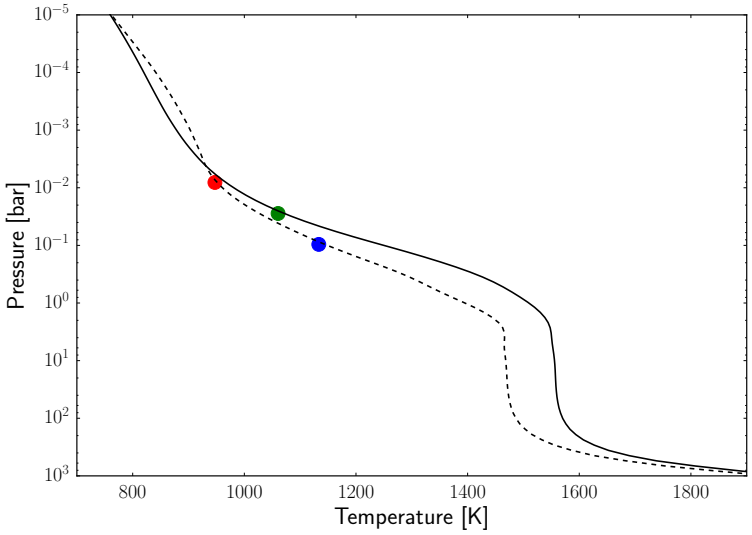

Figure 4.17: The location of the peak emission in the 3.6 µm Spitzer band for the HD 189733b $K_{zz} = 10^{11}$ cm^{2}s^{-1} model with the EQ calculation (blue), NEQ calculation (red) and CNEQ calculation (green).

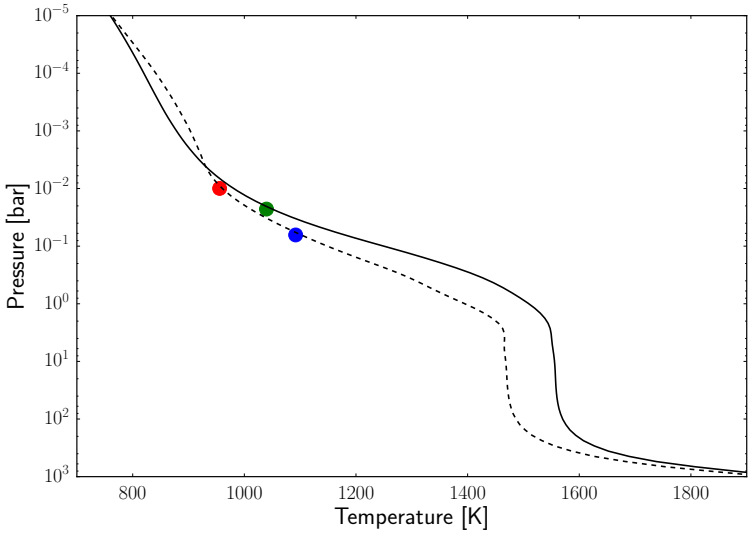

Figure 4.18: As Fig. 4.17 for the Spitzer/IRAC 8.0 µm channel.

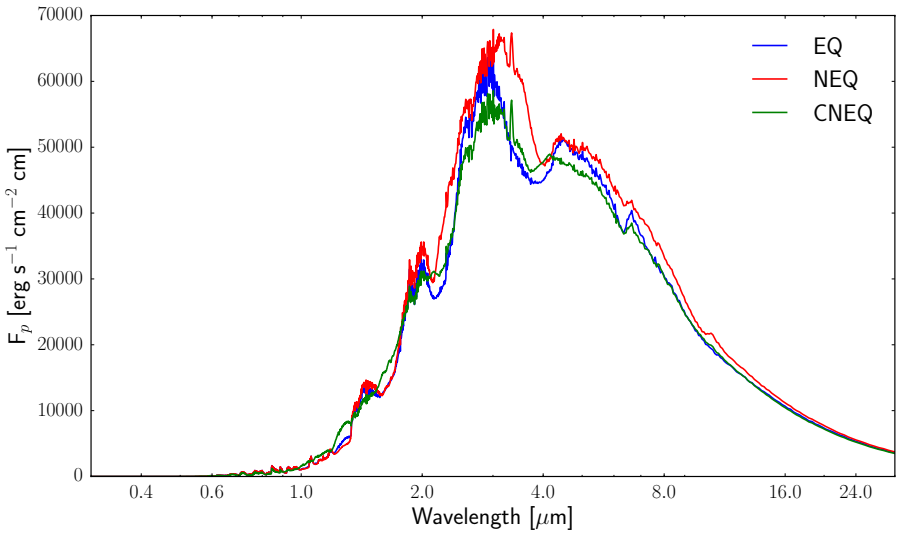

Figure 4.19: The atmosphere emission spectrum of the HD 209458b model with a temperature inversion showing calculations based on the EQ calculation (blue), the NEQ calculation (red) and the CNEQ calculation (green); $K_{zz} = 10^{11}$ cm^{2}s^{-1}.

Table 4.4: Integrated flux and corresponding blackbody temperatures for the HD 209458b temperature inversion model; $K_{zz} = 10^{11}$ cm^{2}s^{-1}.

	Flux (kWm^{-2})	T_{BB} (K)
EQ	235.4	1427
NEQ	256.5	1458
CNEQ	235.4	1428

which is increased in abundance by transport-induced quenching.

Again, by eye, it is possible to see that the NEQ models do not conserve the wavelength-integrated flux. Indeed, Table 4.4 shows the integrated flux of the atmosphere and the corresponding blackbody temperature for the temperature inversion models, where the integrated flux for the NEQ calculation is ∼10% greater than the EQ model. On the other hand, the integrated flux for the CNEQ model is in excellent agreement with the EQ model. Likewise, Table 4.5 shows the same information for the HD 209458b model without a temperature inversion. In this case, the discrepancy between EQ and NEQ is smaller. The EQ and CNEQ models show consistent outgoing fluxes, however, the NEQ model shows a very small ∼1% reduction in integrated flux.

For the model without a temperature inversion, the NEQ model shows a decreased integrated flux, similar to what was found for HD 189733b. However, the model with a temperature inversion shows an increased integrated flux for the NEQ model.

Fig. 4.21 indicates the pressure level of the photosphere in the 3.6 µm Spitzer/IRAC band for the temperature inversion model. Similarly to the HD 189733b model, we

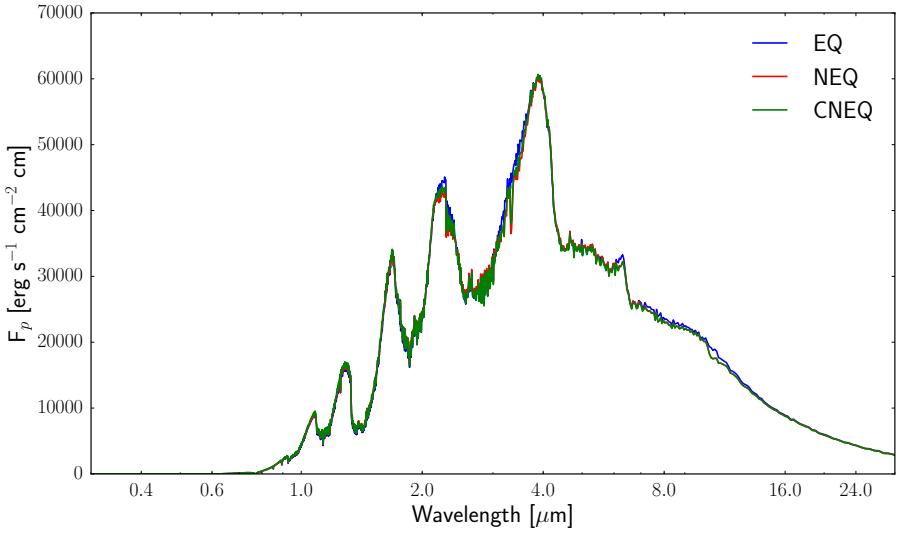

Figure 4.20: Same as Fig. 4.19 but for the model without a temperature inversion; $K_{zz} = 10^{11}$ cm^{2}s^{-1}.

Table 4.5: Integrated flux and corresponding blackbody temperatures for the HD 209458b model without temperature inversion, $K_{zz} = 10^{11}$ cm^{2}s^{-1}.

	Flux (kWm^{-2})	T$_{BB}$ (K)
EQ	222.2	1407
NEQ	221.9	1406
CNEQ	222.7	1408

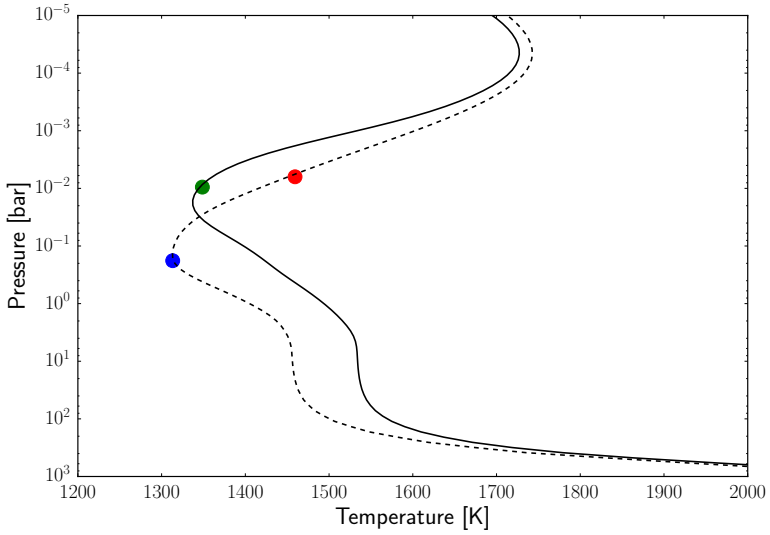

Figure 4.21: The location of the peak emission in the 3.6 µm Spitzer band for the HD 209458b model with a temperature inversion with the EQ calculation (blue), NEQ calculation (red) and CNEQ calculation (green); $K_{zz} = 10^{11}$ cm^{2}s^{-1}.

see that transport-induced quenching pushes the photosphere to lower pressures by increasing the opacity. In this model however, where temperature is increasing with decreasing pressure, the photosphere moves to a higher temperature. This explains why we see an increased integrated flux in the NEQ model. However, for the CNEQ model, though the pressure level of the photosphere is still shifted to lower pressures the P–T profile has adapted so that the temperature at this level is now cooler, conserving the integrated flux to that of the EQ model, shown in Table 4.4.

For the model without a temperature inversion, a similar process occurs. However, because temperature decreases with altitude in this model, the new photosphere is both lower in pressure *and* lower in temperature resulting in a reduced emission flux. Therefore, to compensate, the P–T structure increases in temperature at this pressure level to increase the emission flux once again, and conserve energy balance.

This understanding allows us to explain why the simulated spectra from our CNEQ models are similar to the EQ model spectra, reducing the impact of non-equilibrium chemistry. Our results show that it is not primarily the changing abundances due to non-equilibrium chemistry which effect the emission spectrum. It is instead the secondary effect of the non-equilibrium abundances shifting the location of the photosphere, by changing the opacity, which affects the calculated spectral flux, as the flux is now originating from a part of the atmosphere with a lower/higher temperature.

The NEQ models do not conserve energy balance in the atmosphere. On the other hand, in the CNEQ models, though the non-equilibrium abundances do also

change the pressure level of the photosphere, the P–T profile adapts, by either heating up or cooling down, to maintain energy balance. Therefore, the resulting spectral flux for the CNEQ model shows a smaller discrepancy with the EQ model. Previous studies using non-consistent models may have overestimated the importance of non-equilibrium chemistry on the emission spectrum.

4.4 Additional Tests

4.4.1 The sensitivity to f_{P-T}

In this work, we chose to reconverge the P–T profile once every 10 chemical iterations. The choice of this frequency is set to achieve optimal model performance.

A low value of f_{P-T}, where the P–T profile is reconverged very frequently, means that there is a small change in the abundances, and hence in the temperature, in each iteration of the model between the chemistry and P–T calculations. It was found that in this case, the model monotonically converges towards the solution in a stable way. However, frequently recomputing the P–T profile increases the computation time.

On the other hand, with a large value of f_{P-T}, when the P–T profile is reconverged less regularly, there can be a large change in the abundances between each iteration of the chemistry and P–T calculations. This can then result in large changes to the temperature. It was observed that such large shifts in the abundances/temperature with a large f_{P-T} cause the model to overshoot the solution and then to oscillate around it. Whilst the effect of reconverging the P–T profile less frequently should decrease computation time, due to the oscillatory nature of the model towards convergence, the computation time is not greatly improved. Due to these two extreme limits, it was found that a moderate value of $f_{P-T} \sim 10$ (reconverging the P–T profile every 10 iterations of the chemistry solver) provided the most efficient, and stable, model.

It is important to assess that the final result is not sensitive to this choice of f_{P-T} and here we test a range of values, for the HD 189733b model with $K_{zz} = 10^{11}$ cm^2 s^{-1}. The absolute and relative differences in the final converged P–T profile for a range of f_{P-T} are shown in Fig. 4.22. To make the comparison, we take the $f_{P-T} = 1$ case, where the P–T profile is reconverged every chemical timestep, as the baseline model and compare each of the other models to it. The relative difference in the final P–T profile remains below 1.5% across this range of models and does not exceed 0.5% for the $f_{P-T} = 10$ case, which is the value used in this study.

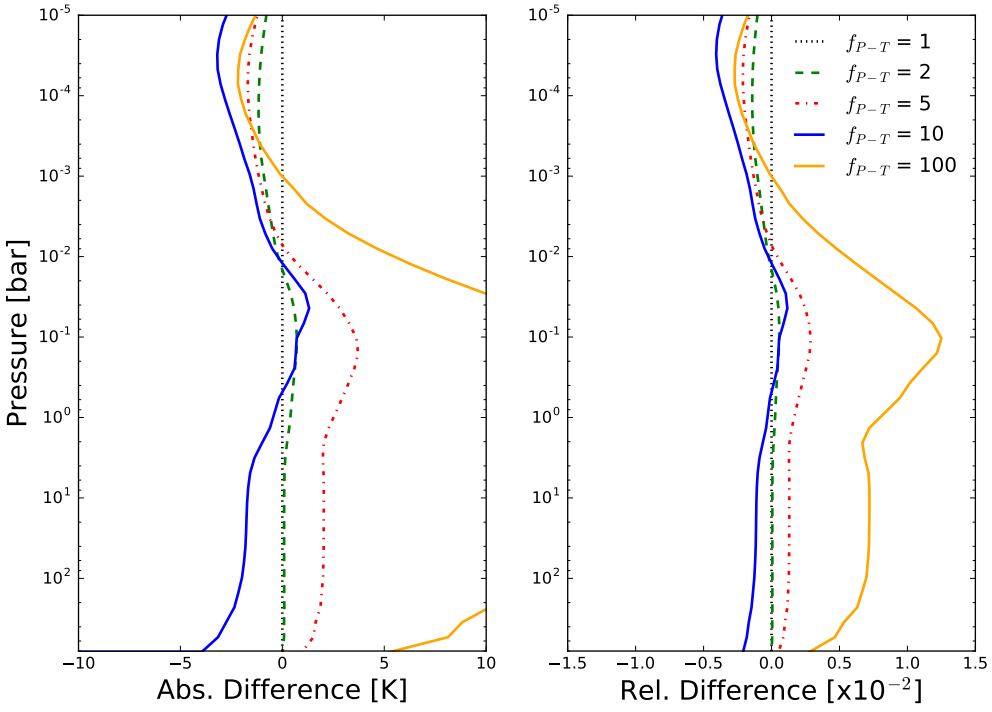

Figure 4.22: The absolute (*left*) and relative (*right*) differences in the temperature profile for a series of values of $f_{P-T} = 1, 2, 5, 10, 100$. The differences are calculated against the $f_{P-T} = 1$ case, where the P–T profile is reconverged for every chemistry iteration, which we assume to be the baseline model. The final converged P–T profile is not very sensitive to the choice of f_{P-T} with relative differences not exceeding 0.5% for $f_{P-T} \leq 10$. The discrepancy with the $f_{P-T} = 1$ model increases with f_{P-T}, with the $f_{P-T} = 100$ showing the largest relative difference with $\sim 1.25\%$.

4.4.2 Investigating the importance of photochemistry on the P–T profile

The results discussed previously have incorporated non-equilibrium effects due to both vertical mixing and photochemistry, and we have attributed the significant shifts in the P–T profile to vertical mixing, which acts at higher pressures and higher optical depths than photochemistry. In this section we present results from tests which only include photochemistry to assess the importance of photodissociation on the P–T profile in isolation from vertical mixing.

Fig. 4.23 shows the P–T profiles for the models of HD 189733b and HD 209458b (the latter with and without TiO/VO) calculated with chemical equilibrium and with photochemistry. There is a negligible shift in the P–T profile for the HD 209458b model without TiO/VO and only a very slight increase in temperature at very low pressures for the HD 189733b model. For the HD 209458b model with TiO/VO, there is a subtle change in the P–T profile at both low and high pressures, though the change is very small.

Overall, these tests show that in the current model setup, photochemistry has a negligible impact on the P–T profile, and confirms that it is the process of vertical mixing which drives the large ~ 100 K shifts in the temperature presented in previous sections. This result should come under some scrutiny however, as our choice of the modelled pressure domain only includes the very limits of the region of the atmosphere where photochemistry becomes the dominant factor controlling the chemistry. This is because at lower pressures non-LTE effects must be taken into account, which are not currently included in this model. To properly investigate the impact of photochemistry on the temperature profile, one must extend the modelled domain to lower pressures where the relevant physics important at very low pressures must be included [i.e. in the thermosphere, e.g. Yelle, 2004].

In addition to this, we currently only include opacity from gas-phase molecular species (e.g. H_2O, CH_4, etc) that are *destroyed* by photochemical processes and do not include opacity due to the important photochemical *products* (e.g. H, OH, etc), which may have non-negligible or even important contributions to the opacity. For example, the well studied photochemical production of ozone in the Earth atmosphere ultimately leads to the temperature inversion which defines the tropopause.

Therefore, though we find that photochemistry has a negligible influence on the P–T profile in the present model, it is possible that this is due to our choice of the modelled pressure range and the lack of opacity contributions from photochemical products.

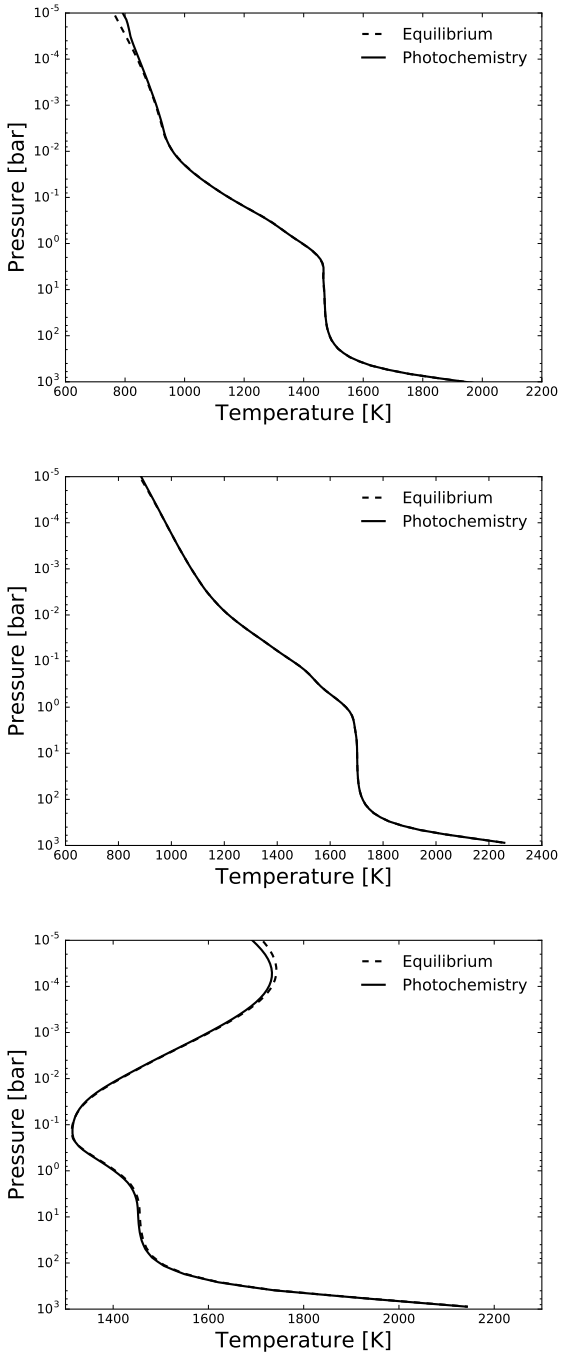

Figure 4.23: The pressure temperature profiles for HD 189733b (*top*), HD 209458b without TiO/VO (*middle*) and HD 209458b with TiO/VO (*bottom*) consistent with chemical equilibrium (dashed) and with photochemistry (solid). For the current model setup, the effects of photochemistry have a negligible impact on the P–T profile.

4.5 Conclusions

This chapter has presented results based on a fully-consistent chemical kinetics model applied to the atmospheres of HD 189733b and HD 209458b. In summary, these results have shown that:

- in cases of strong disequilibrium chemistry transport-induced quenching of absorbing species can produce changes in the P–T profile of up to 100 K
- the change in temperature can, in turn, have impacts on both the chemical abundances themselves and on the corresponding emission spectra
- consistent calculations of non-equilibrium chemistry reduce the overall impact of chemical disequilibrium on the emission spectrum
- in conventional chemical kinetics models, where the P–T profile is held fixed, the dominant mechanism for non-equilibrium chemistry to affect the emission spectrum is by changing the pressure level, and temperature, of the photosphere. The strong dependence of the emission flux on temperature will result in a very different simulated emission spectrum
- in our consistent model the P–T profile adapts to the new non-equilibrium chemical composition to retain energy balance in the model atmosphere. The consequent temperature changes mitigate the effect of changing the location of the photosphere by either heating up or cooling down at the location of the new photosphere to preserve energy balance

Based on these results, we urge caution when assessing the impact of non-equilibrium chemistry (transport-induced quenching and photochemistry) on the emission spectrum. Not including consistency between the chemical abundances and the temperature structure can lead to overestimates of the impact of non-equilibrium chemistry.

In this work the effect of photodissociations on the temperature profile was shown to be small. However, we speculate that could, at least in part, be due to the incompleteness of our model. Currently, only the major molecular species are included as sources of opacity. However, photochemical processes can lead to productions of molecules such as HCN and OH [e.g. Moses et al., 2011, 2013a] that have significant opacity. It would be an interesting extension to this work to explore the impact of including additional opacities due to such photochemical produced species, where the expected abundances and cross sections of those species have the potential to have non-negligible effects on the temperature profile.

This work presented in this chapter has only considered 1D (vertical) effects of non-equilibrium chemistry. Horizontal advection is expected to be very important in the atmospheres of tidally-locked exoplanets which possess very strong zonal wind velocities [Showman et al., 2009, Heng et al., 2011, Rauscher and Menou, 2012b, Mayne et al., 2014a]. In addition, these atmospheres can possess very large day-night temperature contrasts leading to large contrasts in horizontal chemical equilibrium abundances [Burrows et al., 2010, Kataria et al., 2016]. Disequilibrium chemistry has already been suggested as a possible explanation to explain the discrepencies between the observed and model emission phase curves [Zellem et al., 2014a]. However, this work has shown that when performed consistently, transport-induced quenching has a smaller impact on the emission spectrum than previous studies suggest. It would therefore be very interesting and timely to extend the process considered here by including horizontal advection, by coupling a chemical kinetics scheme consistently to a 3D GCM.

Chapter 5

Coupling the ATMO Chemistry Schemes to the Met Office Unified Model

The UK Met Office Unified Model (UM) is a general circulation model (GCM), a model that simulates the fluid flow of the atmosphere, that has been in continuous development for the last two decades. The UM is routinely applied to simulate the Earth's atmosphere across a wide-range of temporal and spatial scales, from Numerical Weather Prediction (NWP) operating over local and regional scales over days and weeks, to global climate models integrated for timescales of decades and centuries.

Recently, the UM has been applied to the atmospheres of exoplanets [Mayne et al., 2014a,b, Amundsen et al., 2016]. In the initial stages of the project, the dynamical core of the UM was shown to reproduce several long-term, large-scale idealised test cases [Mayne et al., 2014b] validating the application of the code for solving 3D flows over long integration times. In addition, the UM was applied to several hot Jupiter test cases using a Newtonian cooling scheme to represent the thermal evolution of the atmosphere [Mayne et al., 2014a].

The next stage involved the implementation of high-temperature radiative transfer [Amundsen et al., 2016]. This development allows for the thermal evolution of the atmosphere to be governed by the radiative heating and cooling rates of the gas due to irradiation, internal heating from the planet interior and thermal emission from the gas itself.

An important input for the radiative transfer scheme is the opacity that determines the absorption and scattering of radiation and ultimately the heating rates. In general, the opacity will be determined by the gas-phase chemical composition in addition to the presence of absorbing and scattering haze/cloud particles. In cur-

rently published works, clouds have not been included in hot Jupiter UM simulations and a cloud-free atmosphere is assumed. However, we note that an idealised kinetic cloud scheme [Lee et al., 2016] is currently being coupled to the UM for application to hot Jupiter atmospheres, but we do not discuss it here.

The models of Amundsen et al. [2016] employed a simple analytical solution to chemical equilibrium [Burrows and Sharp, 1999] to determine the gas-phase abundances of four important absorbing species: CH_4, CO, NH_3 and H_2O. In addition, a highly simplified parameterisation for the alkali species Na, K, Li, Rb and Cs was implemented. This method is highly restricted to Solar-like compositions and is inflexible in terms of adding additional chemical species as the number of opacity sources is expanded; for example, CO_2 is an important absorber that is not accounted for in the Burrows and Sharp [1999] scheme.

In this chapter, we describe and test the coupling of two chemistry schemes to the UM to increase the accuracy and flexibility of the model. The coupling of the Gibbs energy minimisation scheme gives a much higher flexibility allowing for the chemical equilibrium abundances of many chemical species to be calculated, in addition to including equilibrium condensation. Including a flexible chemical kinetics scheme within the UM will allow for the assumption of chemical equilibrium to be relaxed and to include the effect of large scale advection on the chemistry which may drive it away from equilibrium.

We begin by briefly introducing the main equations solved by the dynamical core and some common simplifications to those equations (Section 5.1) and also the method of calculating the gas-phase chemical abundances in previous UM exoplanet models (Section 5.2). We then describe the coupling and testing of the Gibbs energy minimisation including assessing the sensitivity of the model to the chemical timestep, the frequency with which the abundances are recalculated, in Section 5.3. Finally we describe (Section 5.4) and test (Section 5.5) the coupling of the chemical kinetics scheme using a simplified chemical composition.

5.1 Dynamics

The dynamical core is the component of the model that solves the equations of motion to describe the fluid flow. The latest version of the UM dynamical core, ENDGame, solves for the deep, non-hydrostatic equations of motion on a rotating sphere [Wood et al., 2014]. Importantly many of the common simplifications of the equations of motion that are often included in other GCMs are not taken here and instead the "full" equations of motion are solved. However, the model does allow for these simplifications to be invoked to allow for a comparison between the full equations and the simplified equations in the same numerical scheme.

The various assumptions to the equations of motion are as follows:

1. Shallow-fluid approximation
   The shallow-fluid approximation assumes that the atmosphere is thin compared with the radius of the planet. The *aspect ratio*, the ratio of the atmosphere extent to the planet radius, is the relevant quantity here. For the Earth the aspect ratio is $\sim 10^{-3}$, and so the shallow-fluid approximation is probably valid. However, for hot Jupiters the aspect ratio is ~ 0.1.

2. Traditional approximation
   The traditional approximation, which is taken with the shallow-fluid approximation (1), involves the neglect of several metric and rotation terms and is not strongly physically justified, but does provide the potential for energy, angular momentum and potential vorticity conservation [Mayne et al., 2014b].

3. Constant gravity (independent of height)
   The assumption of constant gravity ignores any variation of gravity with height and instead takes a constant value of the surface gravity everywhere; $g(r) = g_{\text{surface}}$. This means that there is no contribution of the atmosphere to the total gravity, which may not necessarily be accurate for massive or extended atmospheres.

4. Vertical hydrostatic balance

These first three assumptions (1-3) taken together form the *shallow-atmosphere* equations [Mayne et al., 2014b, White et al., 2005]. Furthermore, the shallow-atmosphere equations combined with the assumption of vertical hydrostatic balance (4) results in a set of equations termed the *primitive equations* (1-4), used in the majority of GCMs so far applied to hot Jupiters [e.g. Showman et al., 2009].

5.1.1 Equations of Motion

The full equations of motion solved by the ENDGame dynamical core are the zonal, meridional and vertical wind, the continuity equation and the thermodynamic equation, which are closed by the equation of state:

$$\frac{\mathrm{D}u}{\mathrm{D}t} = \frac{uv\tan\phi}{r} - \frac{uw}{r} + fv - f'w - \frac{c_p\theta}{r\cos\phi}\frac{\partial\Pi}{\partial\lambda} + \mathrm{D}(u) \tag{5.1}$$

$$\frac{\mathrm{D}v}{\mathrm{D}t} = -\frac{u^2\tan\phi}{r} - \frac{vw}{r} - uf - \frac{c_p\theta}{r}\frac{\partial\Pi}{\partial\phi} + \mathrm{D}(v) \tag{5.2}$$

$$\delta\frac{\mathrm{D}w}{\mathrm{D}t} = \frac{u^2+v^2}{r} + uf' - g(r) - c_p\theta\frac{\partial\Pi}{\partial r} \tag{5.3}$$

$$\frac{\mathrm{D}\rho}{\mathrm{D}t} = -\rho\left[\frac{1}{r\cos\phi}\frac{\partial u}{\partial\lambda} + \frac{1}{r\cos\phi}\frac{\partial(v\cos\phi)}{\partial\phi} + \frac{1}{r^2}\frac{\partial(r^2w)}{\partial r}\right] \tag{5.4}$$

$$\frac{\mathrm{D}\theta}{\mathrm{D}t} = \frac{Q}{\Pi} + \mathrm{D}(\theta) \tag{5.5}$$

$$\Pi^{\frac{1-\kappa}{\kappa}} = \frac{\bar{R}\rho\theta}{P_0}. \tag{5.6}$$

Here u, v and w are the wind velocity components in the longitudinal (λ), latitudinal (ϕ) and radial (r) directions, respectively. c_p is the specific heat capacity, $\bar{R}$ is the specific gas constant, Q is the heating rate, D is the diffusion operator and κ is the ratio $c_p/\bar{R}$. P_0 is a reference pressure, ρ is the density and $g(r)$ is the height dependent gravity

$$g(r) = g_p\left(\frac{R_p}{r}\right)^2, \tag{5.7}$$

where g_p and R_p are the surface gravity and planetary radius, respectively. f and f' are the Coriolis parameters

$$\begin{aligned} f &= 2\Omega\sin\phi \\ f' &= 2\Omega\cos\phi, \end{aligned} \tag{5.8}$$

where Ω is the planetary rotation rate. θ and Π are the potential temperature and Exner pressure, defined as

$$\theta = T\left(\frac{p_0}{p}\right)^{\frac{\bar{R}}{c_p}} \tag{5.9}$$

and

$$\Pi = \left(\frac{p}{p_0}\right)^{\frac{\bar{R}}{c_p}} = \frac{T}{\theta}. \tag{5.10}$$

The material derivitive is defined as

$$\frac{\mathrm{D}}{\mathrm{D}t} = \frac{\partial}{\partial t} + \frac{u}{r\cos\phi}\frac{\partial}{\partial\lambda} + w\frac{\partial}{\partial r}. \tag{5.11}$$

5.1.2 Tracer transport in the UM

Tracer transport is calculated in the UM dynamical core using a positive-definite, semi-Lagrangian advection scheme [Davies et al., 2005]. This allows for tracer species

to be advected with the large scale flow of the atmosphere. The UM includes the option of "free tracer" species which are available tracers in the main model.

The model includes several options for the type of high order advection scheme, including

1. Linear interpolation (i.e. not high order)
2. Cubic Lagrange interpolation
3. Bi-cubic Lagrange in the horizontal and linear interpolation in the vertical
4. Cubic Lagrange interpolation in the horizontal and quintic Lagrange interpolation in the vertical
5. Bi-cubic Lagrange interpolation in the horizontal and C1-Hermite cubic quadratic derivitive estimates in the vertical

amongst others. The default option in the UM is option 5 above and that is the method we adopt for tracer advection in the following sections. However, the choice advection scheme can have consequences on the advected tracer, with some schemes performing better (i.e. better conservation) for some advected quantities (e.g. moisture, potential temperature, etc.) whilst other schemes perform better for other quantities (C. Smith, Met Office, priv. comm). For instance, Eluszkiewicz et al. [2000] found that the choice of advection scheme can significantly effect the advected "age of air" tracer in the GFDL GCM.

In this work we simply adopt the default high order advection scheme (option 5 above). However, in future works it will be important to test the sensitivity of the results to this choice.

5.2 The chemistry scheme used in previous works

The calculation of the chemical abundances in Amundsen et al. [2016] combined two separate methods. For the species CH_4, CO, H_2O and NH_3 the analytical formulae of Burrows and Sharp [1999] was used. For the alkali species Na, K, Li, Cs and Rb a very simple parameterisation was used based on the chemical transformation curves of those respective species. These methods are described in this section.

5.2.1 The Burrows and Sharp [1999] analytical equilibrium chemistry scheme

The analytical theory is based on the assumption that the atmosphere is hydrogen-dominated, and that all of the carbon exists in CO and CH_4, all of the nitrogen

exists in N_2 and NH_3 and all of the oxygen exists in H_2O and CO. For hot (T > 1000 K), hydrogen-dominated atmospheres in chemical equilibrium, this is a good assumption [Burrows and Sharp, 1999]. The chemistry is then said to be defined by two net chemical reactions, involving the conversion of CO and CH_4, and N_2 and NH_3 respectively

$$\mathrm{CO} + 3\mathrm{H_2} \leftrightarrow \mathrm{H_2O} + \mathrm{CH_4}$$

$$\mathrm{N_2} + 3\mathrm{H_2} \leftrightarrow 2\mathrm{NH_3}.$$

The equilibrium constants for these two reactions are then described by

$$K_1(T) = \frac{P_{\mathrm{CO}} P_{\mathrm{H_2}}^3}{P_{\mathrm{CH_4}} P_{\mathrm{H_2O}}} = \exp\left[-\Delta G_1(T)/RT\right] \tag{5.12}$$

and

$$K_2(T) = \frac{P_{\mathrm{N_2}} P_{\mathrm{H_2}}^3}{P_{\mathrm{NH_3}}^2} = \exp\left[-\Delta G_2(T)/RT\right], \tag{5.13}$$

where P_{X} are the partial pressures of the species X and ΔG_1 and ΔG_2 are the Gibbs energy of reaction for the respective net reactions [see Burrows and Sharp, 1999].

In the formulae, the elemental and molecular abundances are written with respect to hydrogen: the elemental abundance is expressed as the ratio of the number of atoms of element X to the number of atoms of hydrogen $A_{\mathrm{X}} = N_{\mathrm{X}}/N_{\mathrm{H}}$ and the molecular abundance defined as the ratio of the partial pressure of molecule X to the partial pressure of molecular hydrogen $B_{\mathrm{X}} = P_{\mathrm{X}}/P_{\mathrm{H_2}}$.

Firstly, an analytical solution for the abundance of CO, B_{CO}, is determined using the first net reaction. Assuming that all carbon resides in CO and CH_4, and all oxygen resides in CO and H_2O yields the pair of equations [Burrows and Sharp, 1999]

$$\begin{aligned} B_{\mathrm{CH_4}} &= 2A_{\mathrm{C}} - B_{\mathrm{CO}} \\ B_{\mathrm{H_2O}} &= 2A_{\mathrm{O}} - B_{\mathrm{CO}}. \end{aligned} \tag{5.14}$$

Substituting the partial pressures for relative abundances of CO, CH_4 and H_2O in Eq. (5.12) yields

$$K_1(T) = \frac{P_{\mathrm{CO}} P_{\mathrm{H_2}}^3}{P_{\mathrm{CH_4}} P_{\mathrm{H_2O}}} = \frac{B_{\mathrm{CO}} P_{\mathrm{H_2}}^2}{B_{\mathrm{CH_4}} B_{\mathrm{H_2O}}}. \tag{5.15}$$

Rearranging for B_{CO} and substituting in Eq. (5.14) gives

$$B_{\mathrm{CO}} = \frac{K_1(T)}{P_{\mathrm{H_2}}^2} B_{\mathrm{CH_4}} B_{\mathrm{H_2O}} = \frac{K_1(T)}{P_{\mathrm{H_2}}^2} \left(2A_{\mathrm{C}} - B_{\mathrm{CO}}\right)\left(2A_{\mathrm{C}} - B_{\mathrm{CO}}\right)$$

$$B_{\mathrm{CO}} = \frac{K_1(T)}{P_{\mathrm{H_2}}^2}\left[4A_{\mathrm{C}}A_{\mathrm{O}} + B_{\mathrm{CO}}^2 - 2A_{\mathrm{O}}B_{\mathrm{CO}} - 2A_{\mathrm{C}}B_{\mathrm{CO}}\right] \tag{5.16}$$

and expressing it in the general quadratic form yields

$$\begin{aligned}\frac{K_1(T)}{P_{\mathrm{H_2}}^2}\left[B_{\mathrm{CO}}^2 + B_{\mathrm{CO}}\left(-2A_{\mathrm{O}} - 2A_{\mathrm{C}} - \frac{P_{\mathrm{H_2}}^2}{K_1(T)}\right) + 4A_{\mathrm{C}}A_{\mathrm{O}}\right] &= 0 \\ B_{\mathrm{CO}}^2 + B_{\mathrm{CO}}\left(-2A_{\mathrm{O}} - 2A_{\mathrm{C}} - \frac{P_{\mathrm{H_2}}^2}{K_1(T)}\right) + 4A_{\mathrm{C}}A_{\mathrm{O}} &= 0. \end{aligned} \tag{5.17}$$

Finally, we can use the general solution of quadratic formulae to solve for B_{CO}

$$B_{\mathrm{CO}} = A_{\mathrm{C}} + A_{\mathrm{O}} + \frac{P_{\mathrm{H_2}}^2}{2K_1(T)} - \sqrt{\left[A_{\mathrm{C}} + A_{\mathrm{O}} + \frac{P_{\mathrm{H_2}}^2}{2K_1(T)}\right]^2 - 4A_{\mathrm{C}}A_{\mathrm{O}}}. \tag{5.18}$$

Once B_{CO} is found, it is trivial to determine $B_{\mathrm{CH_4}}$ and $B_{\mathrm{H_2O}}$ using equations (5.14). An analogous approach can be taken to determine $B_{\mathrm{N_2}}$, yielding the equations

$$B_{\mathrm{N_2}} = A_{\mathrm{N}} + \frac{P_{\mathrm{H_2}}^2}{8K_2(T)} - \sqrt{\left[A_{\mathrm{N}} + \frac{P_{\mathrm{H_2}}^2}{8K_2(T)}\right]^2 - A_{\mathrm{N}}^2} \tag{5.19}$$

and

$$B_{\mathrm{NH_3}} = 2(A_{\mathrm{N}} - B_{\mathrm{N_2}}). \tag{5.20}$$

The above formulae provide a very computationally efficent means of determining the abundances of the important molecular species in hot Jupiter atmospheres, requiring only the local gas pressure and temperature, and not requiring an expensive iterative calculation. However, the method does suffer from several severe limitations:

- Limited to the chemistry of CH_4, CO, H_2O, NH_3 and N_2 only.
- Not applicable under H_2 dissociation; i.e. at high temperatures (> 2500 K) or low pressures.
- Holds assumptions about the composition; i.e. hydrogen-dominated and *roughly* Solar composition.

5.2.2 Parameterisations of the alkali species

The abundances of the alkali species are computed using a parameterised relative abundance profile [Amundsen et al., 2016] based on the chemical transformation temperature of the monatomic alkali species with the alkali chloride. Above the transformation temperature the species (e.g. Na) is assumed to be present with an

abundance corresponding to the Solar abundance, while below the transformation temperature the monatomic species is assumed to be completely depleted from the atmosphere due to conversion into the alkali chloride species (e.g. NaCl). The transformation temperature for each alkali chloride species was taken from Burrows and Sharp [1999].

A smoothing function was applied to avoid discontinuous abundance profiles near to the transformation temperatures. The smoothing takes the form [Amundsen et al., 2016]

$$\phi^i(T) = \frac{1}{\exp\left[-(T - T^i_{\text{trans}})/\Delta T^i_{\text{char}}\right] + 1}, \tag{5.21}$$

where $\phi^i(T)$ is the relative abundance of the species i at a temperature T, T^i_{trans} is the transformation temperature and ΔT^i_{char} the characteristic scale over which the abundance changes, taken to be $\Delta T^i_{\text{char}} = 20$ K.

5.3 Coupling and testing the Gibbs energy minimisation scheme to the UM

In this section we describe the coupling of the Gibbs energy minimisation scheme to the UM and perform a series of tests to validate the coupled model. In addition, we examine the sensitivity of the UM simulation to the frequency with which the chemical abundances are recalculated; i.e. the chemical timestep. We find that for a typical hot Jupiter simulation the model has a very low sensitivity to choice of chemical timestep for the range of values tested here.

In the current work we restrict our calculations to include only gas-phase species. However, in principle the scheme can include equilibrium condensation and will be considered in future works.

5.3.1 Coupling the Gibbs energy minimisation scheme

The Gibbs energy minimisation scheme has already been described in its implementation in the 1D model ATMO in Chapter 3. The coupling process essentially involves including the relevant Fortran subroutines within a new Fortran module in the UM source code. The subroutines can then be called to compute and return the chemical abundances for a given pressure and temperature array. The Gibbs energy minimisation scheme was originally developed within the 1D column atmosphere model ATMO and due to this legacy we iterate over the 3D grid of the UM calling the subroutine individually for each vertical column. A more detailed description of the coupling process is provided in Appendix E.1.

5.3.2 Testing the Gibbs energy minimisation scheme

In this section we validate the implementation of the Gibbs energy minimisation scheme in the UM by comparing the chemical abundance profile as calculated with the coupled scheme with the same calculation performed with ATMO. We also test the sensitivity of the UM simulation to the choice of chemical timestep.

Abundance profiles

Fig. 5.1 shows the abundance profiles of the main chemical species as calculated within the UM, using both the coupled Gibbs energy minimisation scheme and the Burrows and Sharp [1999] analytical formulae, and with the Gibbs energy minimisation scheme in ATMO. We use the same initial pressure-temperature profile in each case. Note that to obtain the abundances from the UM we output the results (abundance profiles) during the first model timestep and in this case the initial pressure-temperature profile has already been adjusted, leading to very subtle differences between the actual pressure-temperature profile used to compute the abundances in the UM compared with in ATMO.

Crucially, the abundances profiles for all species agree exceptionally well between the Gibbs energy minimisation scheme in ATMO and coupled with the UM. The only apparent discrepancy is for CH_4 at low pressures. Following testing (not shown), the cause of this was found to be due to the slight adjustments to the initial pressure-temperature profile in the UM before the chemistry calculation is performed.

There are some more significant differences between the Gibbs energy minimisation scheme and the Burrows and Sharp [1999] analytical formulae. Each species profile is shifted slightly compared with the profiles from the Gibbs energy minimisation method. The most likely cause of this is slight differences in the assumed elemental abundances or thermochemical data. In addition, a more significant difference is apparent in the abundance profile of H_2O. At around $P \sim 1$ bar, the H_2O abundance rapidly decreases by $\sim 30\%$, whereas the profile is near constant for the two Gibbs energy minimisation methods. This is due to the inclusion of the depletion of oxygen atoms for $T < 1700$ K in the Burrows and Sharp [1999] scheme which is an attempt to account for the removal of oxygen due to the formation of silicates. Condensation is not included in the present Gibbs energy minimisation calculations. However, we note that the Gibbs energy minimisation scheme is capable of including condensate species and so this process could indeed be included, though we restrict the calculation to gas-phase species here.

Overall, this test shows that the Gibbs energy minimisation scheme yields the same result when coupled with the UM as in the 1D model ATMO, for the same

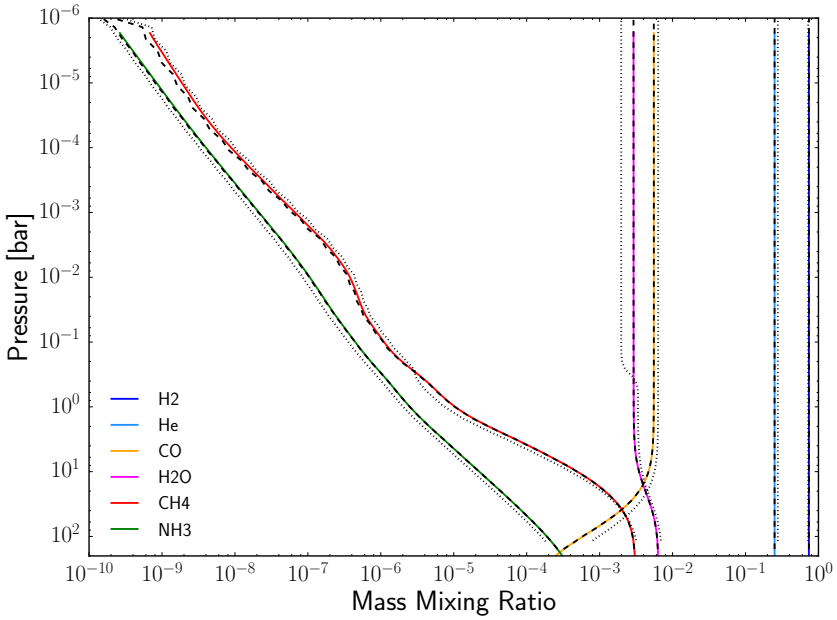

Figure 5.1: The chemical abundances for the main species as calculating with the Gibbs energy minimisation scheme in ATMO (coloured solid lines), the Gibbs energy minimisation scheme coupled with the UM (black dashed lines) and the Burrows and Sharp [1999] formulae in the UM (black dotted lines).

P–T profile.

The sensitivity to the chemical timestep

In this section we test the sensitivity of the model to the choice of chemical timestep; i.e. how frequently the chemical abundances are recalculated. There are several relevant timesteps in the UM (and GCMs generally) the most important ones are: the dynamical timestep $\Delta t_{\rm dyn}$ which is the timestep with which the atmospheric flow is integrated and is usually equivalent to the main model timestep, the radiative timestep $\Delta t_{\rm rad}$ which is the timestep with which the radiative fluxes and heating rates are calculated and the chemical timestep $\Delta t_{\rm chem}$ which is the timestep with which chemical abundances are calculated. Due to the computational expense of the radiative transfer and chemistry calculations $\Delta t_{\rm rad}$ and $\Delta t_{\rm chem}$ are usually longer than $\Delta t_{\rm dyn}$. For instance, in the model of Amundsen et al. [2016] $\Delta t_{\rm dyn} = 30$ s whilst $\Delta t_{\rm rad} = 150$ s.

Due to the very high computational efficiency of the simple chemistry calculations used in Amundsen et al. [2016] (see Section 5.2) the chemistry was actually calculated very frequently with $\Delta t_{\rm rad} = \Delta t_{\rm chem}$. However, the iterative calculation of the Gibbs energy minimisation method is considerably more expensive and so in this section we investigate the sensitivity of the model to $\Delta t_{\rm chem}$ to assess the

feasibility of using a larger chemical timestep.

To explore this we perform identical simulations for a HD 209458b model setup [Amundsen et al., 2016] and only vary $\Delta t_{\rm chem}$ in each case. As the abundances are required for the radiative transfer calculation, we explore values of $\Delta t_{\rm chem}$ that are multiples of $\Delta t_{\rm rad}$, specifically: $\Delta t_{\rm chem} = \Delta t_{\rm rad}$, $10\times\Delta t_{\rm rad}$, $25\times\Delta t_{\rm rad}$ and $100\times\Delta t_{\rm rad}$. For $\Delta t_{\rm rad} = 150$ s these correspond to 150 s, 1500 s, 3750 s, and 15 000 s. We also include a model using the Burrows and Sharp [1999] method for comparison.

We integrate each simulation for 20 days starting from initial conditions of zero winds and horizontally uniform temperature profiles. We then compare the maximum wind velocities, the total axial angular momentum and the zonal-mean zonal wind. Note that an integration of 20 days is not long enough for the model to reach a pseudo-steady-state though for the purposes of the present test we are only interesting in differences between each model.

Fig. 5.2 shows the global maximum of the three components of the wind velocity (u, v and w) as a function of the model integration time. For the range of explored $\Delta t_{\rm chem}$ the choice of chemical timestep has no apparent effect on the magnitude or evolution of the global maximum wind velocities. The discrepancy between the set of Gibbs energy minimisation models and the model that uses Burrows and Sharp [1999] is likely to be due to the difference in the abundance profile of H_2O that will effect the heating rates and hence dynamical evolution.

Fig. 5.3 shows the evolution of the total axial angular momentum (AAM) of each model over the 20 day integration. The AAM is an important global quantity that should be conserved in the model. Similar to the global maximum wind velocities there is a negligible difference between each of the Gibbs energy minimisation models with different values of $\Delta t_{\rm chem}$. There is a small difference between these models and the model using Burrows and Sharp [1999] and again we attribute this as being due to the difference in the H_2O abundance.

Finally we consider differences in the zonal-mean zonal wind ($\bar{u}$), an important quantity that characterises the dynamical structure of an atmosphere. Fig. 5.4 shows $\bar{u}$ for each of the test case models. Overall, the zonal-mean zonal wind patterns are very similar. As $\Delta t_{\rm chem}$ is increased from $\Delta t_{\rm chem} = \Delta t_{\rm rad}$ to $\Delta t_{\rm chem} = 100 \times \Delta t_{\rm rad}$ there is no obvious effect on $\bar{u}$. Across this tested regime, both the minimum and maximum values of $\bar{u}$ are consistent to within $\sim 99.9\%$. There are again more notable differences between the Gibbs energy minimisation models and the model using the Burrows and Sharp [1999] method.

Table 5.1 shows the walltime required for each test model on 96 cores on the DiRAC Complexity Cluser. For the same $\Delta t_{\rm chem}$ the Gibbs energy minimisation scheme increases the required walltime by approximately 20%; compare models B&S1999 and Gibbs1. To achieve similar walltimes requires increasing $\Delta t_{\rm chem}$ by a

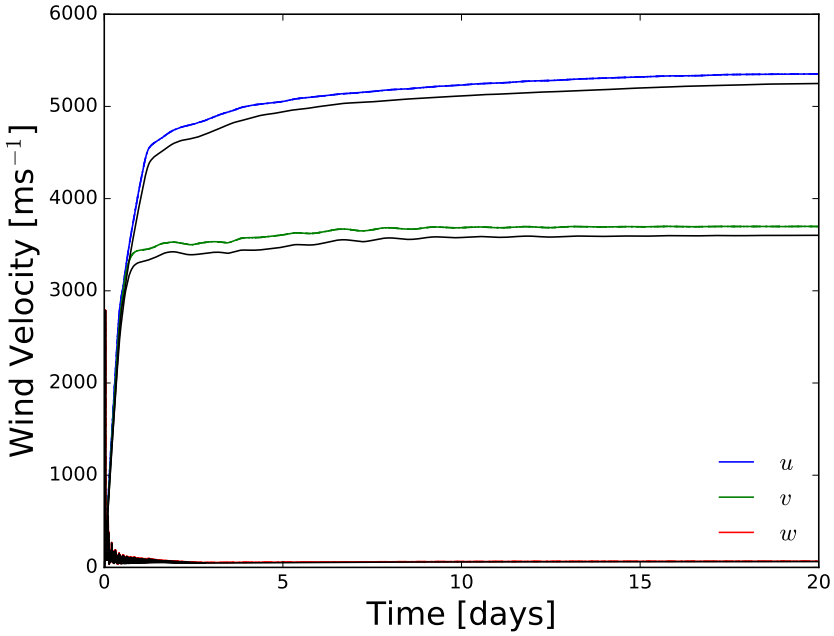

Figure 5.2: A figure showing the global maximum values of the u, v and w wind components as a function of model integration time. The models using the Gibbs energy minimisation method are shown in the coloured lines (with different linestyles for each Δt_{chem} case) whilst the model using the Burrows and Sharp [1999] method is shown in black lines. Note that the different Gibbs energy minimisation model lines overlay almost exactly.

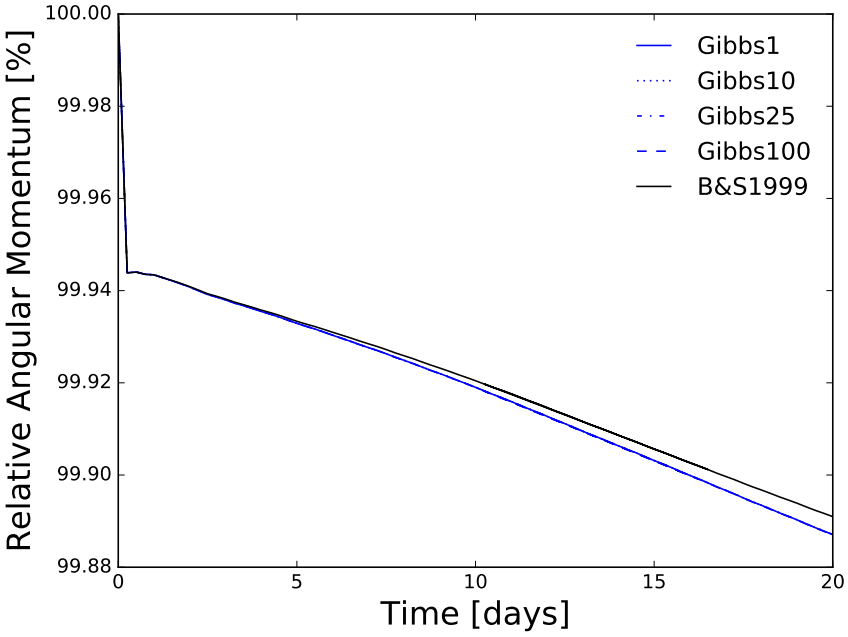

Figure 5.3: A figure showing the percentage of the initial total axial angular momentum (AAM) of the model as a function of model integration time. Over 20 days, each case conserves the total AAM to better than 99.88%. There is no apparent deviation between each of the Gibbs energy minimisation models with different Δt_{chem}.

Table 5.1: The wall time required to integrate each model for 20 days on 96 cores on the DiRAC Complexity Cluster.

Model	Δt_{chem} [s]	Δt_{chem} [$\times \Delta t_{\text{rad}}$]	Wall time [hours]
B&S1999	150	1	9.6
Gibbs1	150	1	11.6
Gibbs10	1500	10	10.3
Gibbs25	3750	25	10.2
Gibbs100	15000	100	9.5

factor of ~ 100; compare models B&S1999 and Gibbs100. We note that this simple test is not an accurate way of determining the computational efficiency, but it is a useful indicator.

5.3.3 Conclusions

Overall in this section we have described the coupling of the Gibbs energy minimisation scheme to the UM and tested the sensitivity of the model to the choice of chemical timestep. We have validated the implementation of the scheme by reproducing the abundance profiles of the major species and showed negligible differences with the same calculation performed with the Gibbs energy minimisation scheme in

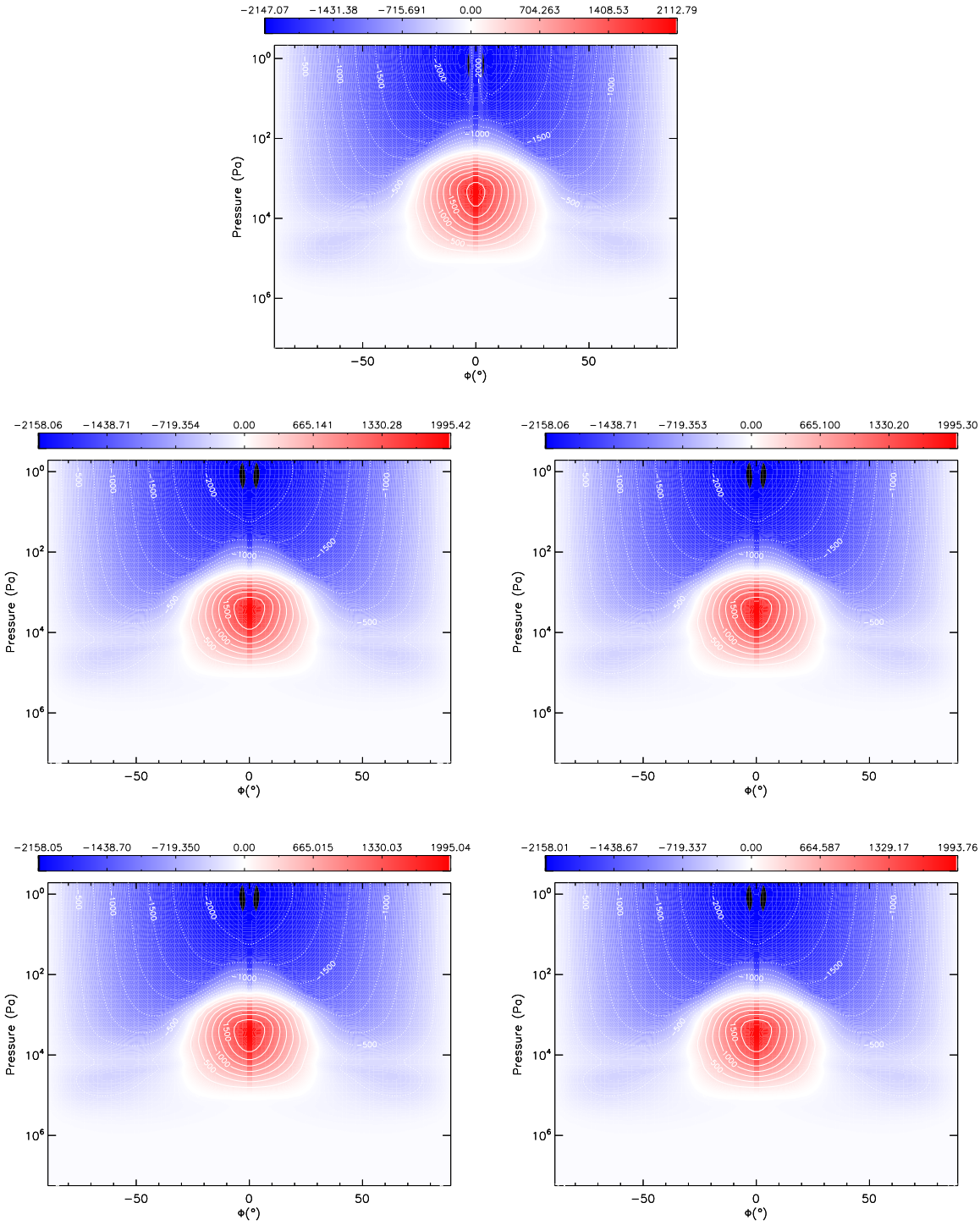

Figure 5.4: A figure showing the zonal-mean zonal wind at after 20 days with the model using the Burrows and Sharp [1999] method (*top*), and the models using the Gibbs energy minimisation method with $\Delta t_{\text{chem}} = \Delta t_{\text{rad}}$ (*middle left*), $\Delta t_{\text{chem}} = 10 \times \Delta t_{\text{rad}}$ (*middle right*), $\Delta t_{\text{chem}} = 25 \times \Delta t_{\text{rad}}$ (*bottom left*) and $\Delta t_{\text{chem}} = 100 \times \Delta t_{\text{rad}}$ (*bottom right*).

ATMO.

We also explored the sensitivity of the model to the choice of the chemical timestep. Due to the increased computational expense of the Gibbs energy minimisation scheme compared with the previous method it is desireable to increase the chemical timestep and therefore perform the chemistry calculation less frequently. We performed simulations with a chemical timestep varying between 150 s (corresponding to one radiative timestep) and 15 000 s (corresponding to 100 radiative timesteps) and found negligible difference between each case in terms of the zonal-mean zonal wind, the global maximum wind velocities and the total axial angular momentum. We therefore conclude that increasing the chemical timestep up to $\Delta t_{\text{chem}} = 100 \times \Delta t_{\text{rad}}$ yields an accurate result with a significant computational efficiency gain compared with the case where $\Delta t_{\text{chem}} = \Delta t_{\text{rad}}$.

5.4 Implementing a chemical kinetics in the UM

In this section we describe the coupling of a chemical kinetics scheme with the UM.

The chemical kinetics scheme, originally developed within the 1D model ATMO, solves the continuity equation to evolve the chemical composition for a given set of thermodynamic conditions (temperature and pressure) along a 1D profile. The coupling process is overall similar to the case for the Gibbs energy minimisation scheme (Section 5.3). The necessary Fortran subroutines are included in a new Fortran module. The subroutines can then be called, passing the temperature, pressure and initial abundances and returning the evolved chemical abundances. As the kinetics was originally written to solve for the abundances along a 1D profile we solve for the abundances in each vertical column in the 3D grid iteratively.

The primary application for the coupling of the kinetics scheme is to allow for the treatment of wind-driven advection. Therefore, in addition to adding the capability to solve for the chemical kinetics we also need to handle the advection of the chemical species with the wind. The advection is handled by the existing UM free tracers scheme. A more detailed description of the coupling is provided in Appendix E.2

5.5 Testing the chemical kinetics scheme: a simplified chemical system

In this section we test the implementation of the chemical kinetics scheme using a simplified chemistry case. We choose to initially simplify the chemical system in order to more easily test the coupled chemical kinetics scheme before repeating the

tests with a more complete number of chemical species and reactions. Note that the testing of the coupled kinetics scheme is still a work in progress and we show early results of these tests here.

We assume that the chemical system is composed only of three chemical species: H_2, H and He. We include conversion of H_2 and H via a single (reversible) thermochemical reaction, which for convenience we take from the Venot et al. [2012] chemical network ($H + H + M \leftrightarrow H_2 + M$) along with the associated parameters to calculate the forward and reverse rate constants.

In the first test, we validate the implementation of the kinetics scheme within the UM model by performing similar "box model" tests as presented in Section 3.5.1. This test demonstrates that the coupled chemical kinetics scheme (calculation of the reaction rates, solution of the continuity equation etc.) is working correctly. Secondly, we perform a full 3D model calculation that includes both advection and chemical evolution and examine the effect of advection on the chemistry. Thirdly, we perform an idealised experiment and artificially vary the chemical timescale to explore the balance between advection and chemistry. We finally examine the sensitivity of the model to the chemical timestep; how frequently we perform the kinetics calculation. Finally we summarise and discuss further tests that will be performed in the near future.

5.5.1 Validating the chemical kinetics scheme

To validate the coupling of the chemical kinetics scheme with the UM we perform similar 0D "box model" tests as in Section 3.5.1. The chemical abundances are evolved from a set of prescribed initial conditions towards the steady-state. We then compare the results of the coupled scheme with the results of the chemical kinetics scheme in ATMO. This test validates the correct coupling of the chemical kinetics scheme with the UM including the calculation of the reaction rates and the solution of the continuity equation. For this test we include only H_2, H and He and a single reversible reaction that converts H_2 and H. In the future we will repeat this test for the full chemical network of Venot et al. [2012].

For the initial condition we assume that all hydrogen is contained in H_2 and that H has an abundance of zero. Helium is also present and the abundances are set to be consistent with the Solar elemental abundances (see Section 3.5.1). We then solve the continuity equation to find the steady-state for a series of thermodynamic conditions: $P = 1$ mbar and $T = 1200$ K, $P = 100$ mbar and $T = 1800$ K and finally $P = 100$ bar and $T = 2200$ K. We compare the final abundances and chemical evolution profiles with identical tests performed with ATMO.

Fig. 5.5 shows the comparison of these box model results for the coupled

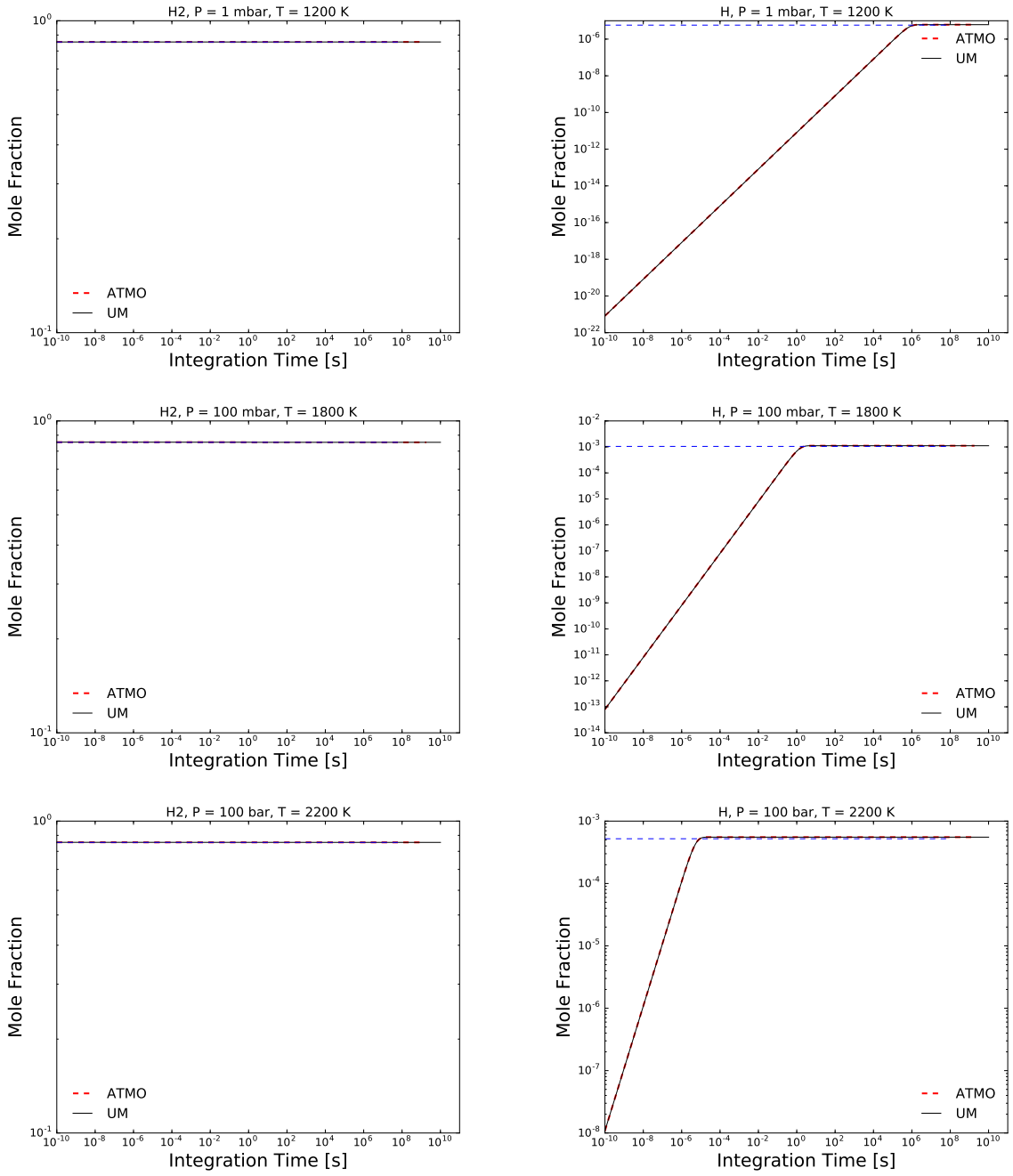

Figure 5.5: A figure comparing the chemical evolution of H_2 (*left*) and H (*right*) using the coupled chemical kinetics scheme in the UM (solid black) and the chemical kinetics scheme in ATMO (dashed red) for a set of thermodynamic conditions: $P = 1$ mbar and $T = 1200$ K (*top*), $P = 100$ mbar and $T = 1800$ K (*middle*) and finally $P = 100$ bar and $T = 2200$ K (*bottom*). The dashed blue lines indicates the chemical equilibrium abundance obtained from minimising the Gibbs energy.

kinetics scheme with the kinetics scheme within ATMO. For each case, the evolution profiles overlay exactly validating the successful implementation of the chemical kinetics scheme within the UM.

5.5.2 Advection and chemistry with a simplified chemistry case

In this section we apply the coupled chemical kinetics scheme to perform a full 3D calculation including advection of three chemical species (H_2, H and He) and the chemical transformation of H_2 and H through a single reversible reaction.

We choose to use model parameters consistent with those of HD 209458b, a typical hot Jupiter. The model setup is the same as in Amundsen et al. [2016] except we reduce the spatial resolution to 96 longitudinal points, 60 latitudinal points and 33 vertical levels (instead of 144, 90 and 33, respectively) and increase the dynamical timestep $\Delta t_{\rm dyn}$ to 60 s (instead of 30 s) to improve computational efficiency.

As the initial condition for this test we use the output from a UM simulation with the same parameters that has been integrated for 100 days from a state of zero winds and uniform temperature profiles. We use this thermodynamic and dynamic structure to initialise the model that includes the kinetics calculations. The chemical abundances are initialised to chemical equilibrium values on the first model timestep. Note that in this test the opacities are not consistent with the advected chemistry but are calculated using the abundances obtained from the Burrows and Sharp [1999] method. The consistent coupling of the advected chemistry with the radiative transfer will be a development for the future. We integrate the model for 10 days.

During the model integration the free tracers, initialised to the chemical equilibrium abundances of H_2, H and He, are advected with the flow. On some specified chemical timestep $\Delta t_{\rm chem}$ the kinetics scheme is called to integrate the chemistry to take into account the chemical conversion of H_2 and H. For the present test we choose $\Delta t_{\rm chem} = \Delta t_{\rm dyn} = 600$ s. To choose this value of $\Delta t_{\rm chem}$ we consider a parcel of gas in the super-rotating equatorial jet with wind velocities of order $u \sim 10^3$ m s^{-1}. The time for this parcel to travel one complete circuit around the planet is $\tau_{\rm adv} \sim R_p/u \sim 10^5$ s, where $R_p \sim 10^8$ m. We choose $\Delta t_{\rm chem}$ to be several orders of magnitude smaller than $\tau_{\rm adv}$ and also a multiple of $\Delta t_{\rm dyn} = 60$ s. We will return to consider the sensitivity of the model to the choice of $\Delta t_{\rm chem}$ in Section 5.5.4.

In the following analysis we place our focus on the abundance of H which is the trace consituent in this system. H_2 and He dominate the background gas with near constant mole fractions.

Fig. 5.7 shows the mole fraction of H on a surface of constant pressure with

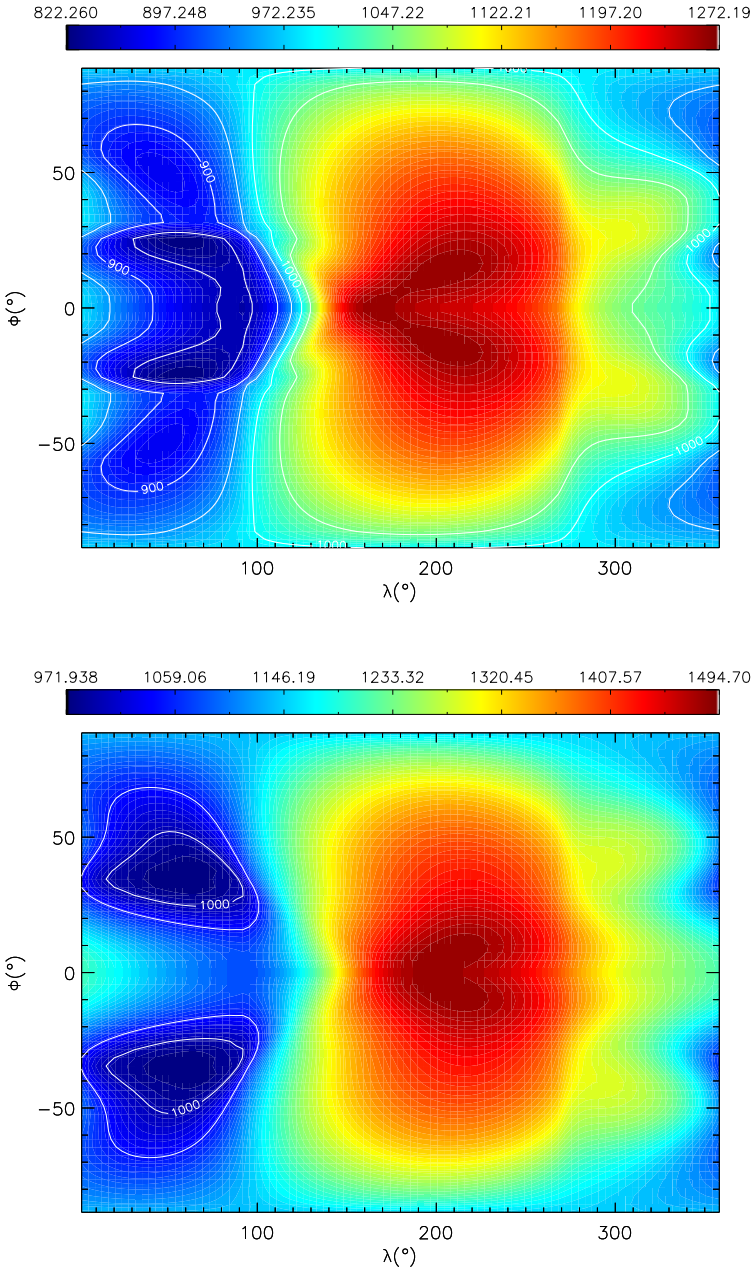

Figure 5.6: A figure showing the temperature on a surface of constant pressure with $P = 100$ Pa (*top*) and $P = 3000$ Pa (*bottom*) after 100 days. This is the initial condition for the kinetics simulations presented in this section. Note the different colour scales.

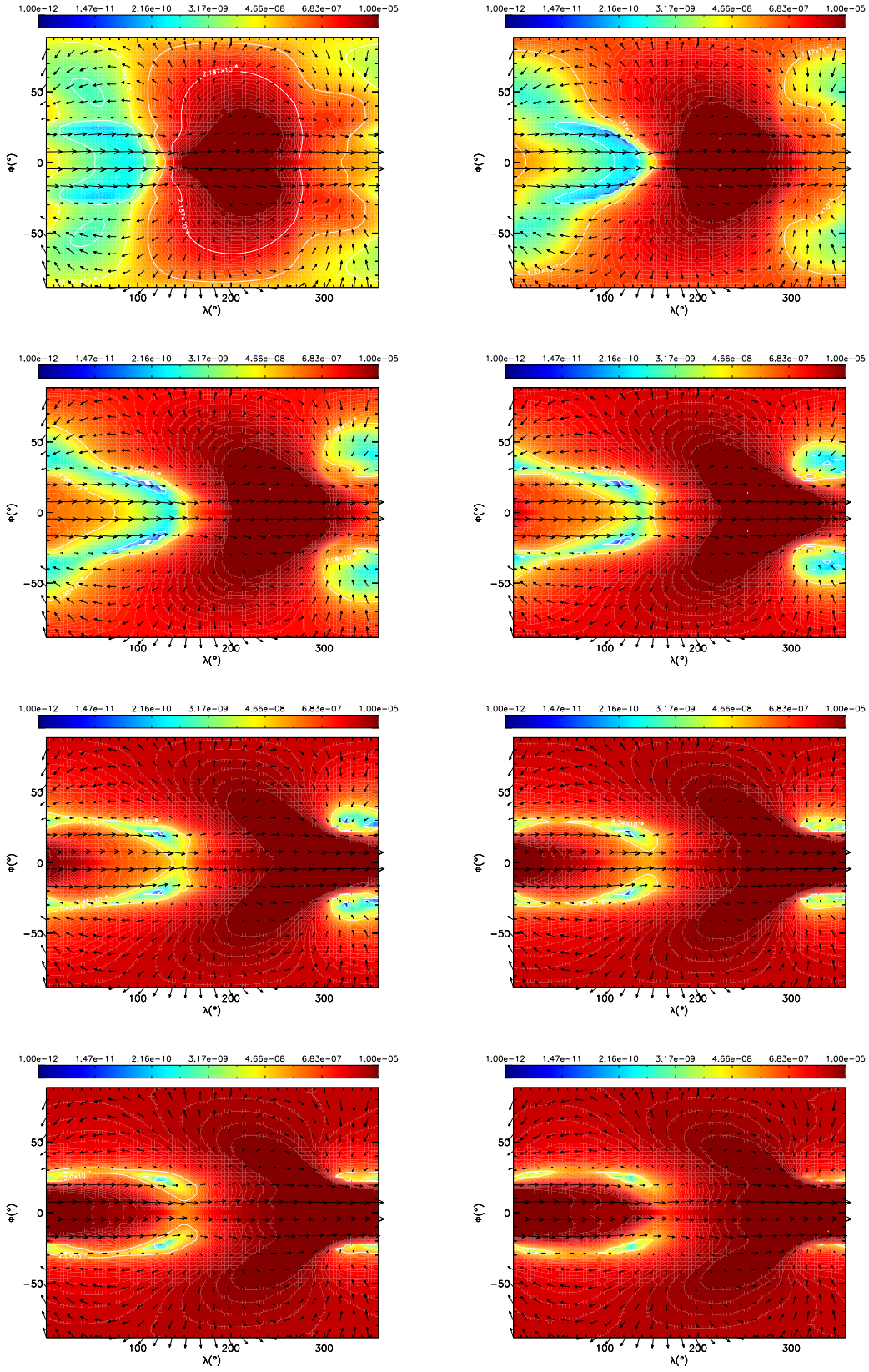

Figure 5.7: A figure showing the mole fraction of H (colour contours) and the horizontal wind velocities (vectors) on a surface of constant pressure $P = 100$ Pa for a series of instantaneous snapshots at $t = 0$ hours (*top left*), 3 hours (*top right*), 6 hours (*second row left*), 9 hours (*second row right*), 12 hours (*third row left*), 15 hours (*third row right*), 18 hours (*bottom left*) and 21 hours (*bottom right*). The model at $t = 0$ hours corresponds to the initial chemical equilibrium.

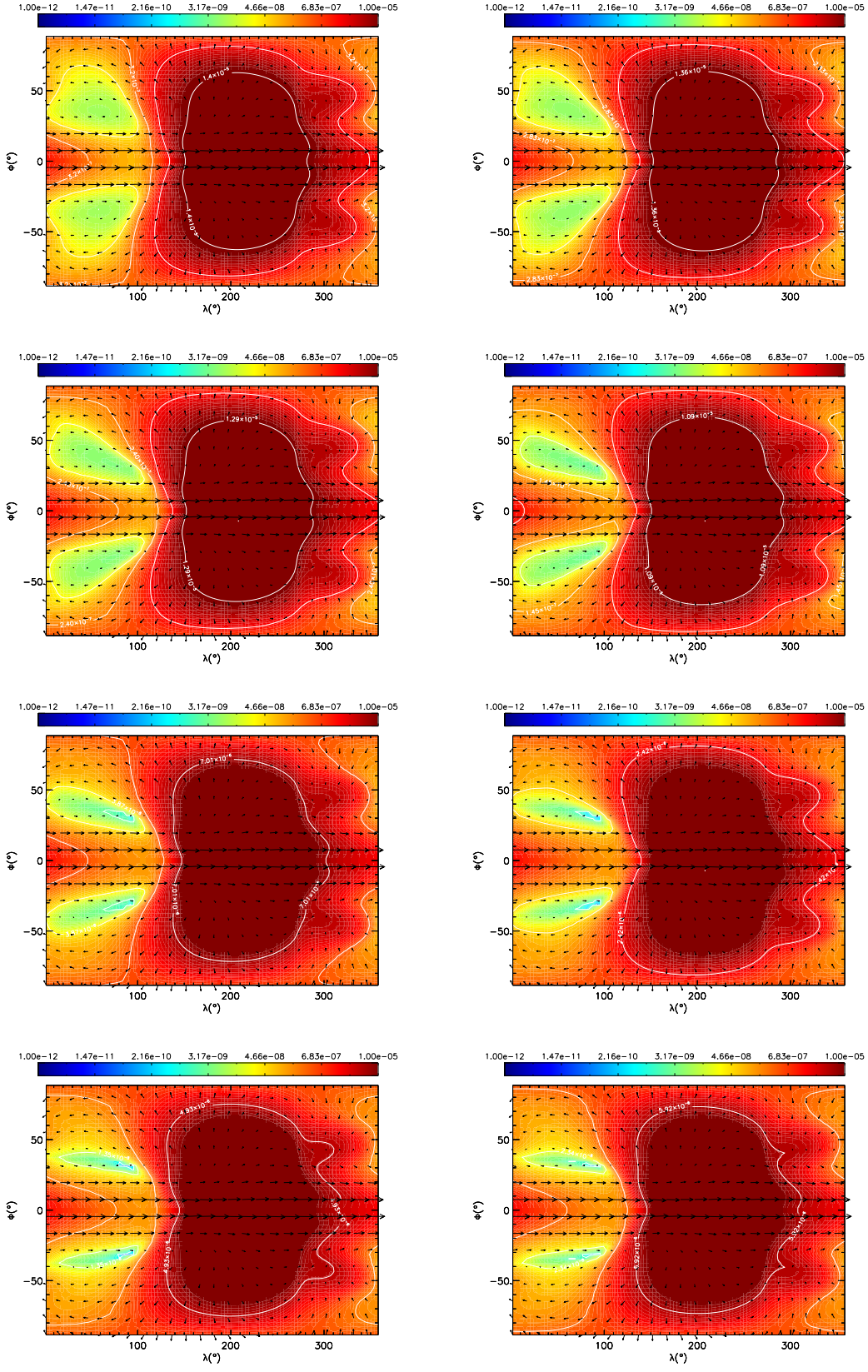

Figure 5.8: As Fig. 5.7 but at $P = 3000$ Pa.

$P = 100$ Pa at instantaneous snapshots spaced three hours apart. Note that at $t = 0$ hours the mole fraction corresponds to the initial chemical equilibrium values. Initially the mole fraction of H traces the thermal structure (see Fig. 5.6) with larger abundances corresponding to regions with higher temperatures, as expected from chemical equilibrium. As the model is integrated advection has a clear effect on the mole fraction of H. Generally we see that the mole fraction is increasing on the cooler dayside as gas is advected from the dayside by the large horizontal wind velocities. After 21 hours the abundance of H has become horizontally very uniform and the initial condition has been significantly changed. Note that the departure from chemical equilibrium is rapid, within $\sim$ 12 hours (corresponding to $\sim$ 0.1 rotations of the planet) the abundance of H has significantly homogenised.

The same simulation after 10 days of integration is shown in Fig. 5.10 (middle right). Here we can see that advection of H has efficiently homogenised the mole fraction horizontally and removed the significant dayside-nightside abundance gradient predicted by chemical equilibrium. There does remain a subtle signature of the temperature structure in the H mole fraction with slightly lower abundances on the nightside outside of the equatorial jet compared with dayside. The large effect of advection indicates that for this simple chemical system, and at this pressure level, the advection timescale $\tau_{\rm adv}$ is faster than the chemical timescale $\tau_{\rm chem}$.

Fig. 5.8 shows the same information but for a deeper surface of constant pressure with $P = 3000$ Pa. Initially the H mole fraction traces the temperature structure (Fig. 5.6) in chemical equilibrium, as was seen for the $P = 100$ Pa pressure level. However, as the model is integrated, at this higher pressure the effect of advection is much more limited with only small increases in the mole fraction on the nightside are apparent. Indeed, after 10 days of integration (see Fig. 5.11) the mole fraction still largely resembles the initial chemical equilibrium. This suggests that at this deeper pressure level, where the temperature is also higher, $\tau_{\rm chem}$ is comparable or faster than $\tau_{\rm adv}$ and the advection is not efficient enough to depart the chemistry from equilibrium significantly. We expect $\tau_{\rm chem}$ to be smaller (faster) for higher pressures and (generally) higher temperatures. The regions for which we do see a small effect on the H mole fraction due to advection correspond with the coolest region of the atmosphere at this pressure, and hence where $\tau_{\rm chem}$ is largest.

In summary, we find that at a pressure of 100 Pa advection has a large impact on the mole fraction of H and rapidly removes the initial chemical equilibrium characterised by relatively large mole fractions on the warm dayside and relatively small mole fractions on the cooler nightside. The advection efficiently homogenises the mole fraction of H horizontally having the effect of increasing the mole fraction significantly on the nightside by several orders of magnitude. However, at a deeper pressure level of 3000 Pa advection has a much more limited impact on the mole

fraction of H and only small increases in the H abundance are apparent in the coolest regions of the nightside.

These results suggest that $\tau_{\rm chem}$ for this simple chemical system is larger (slower) than $\tau_{\rm adv}$ at 100 Pa but comparable or larger (faster) than $\tau_{\rm adv}$ at 3000 Pa. In the next section we further examine the balance between $\tau_{\rm chem}$ and $\tau_{\rm adv}$ by artificially altering the former.

5.5.3 The effect of varying the chemical timescale

In this section we explore the effect of varying $\tau_{\rm chem}$ on the mole fraction of H in this simplified chemistry model. We vary $\tau_{\rm chem}$ by increasing or reducing the forward rate constant by a constant factor. Note that the reverse rate constant is calculated from the equilibrium constant and the forward rate constant (see Section 2.4.3).

In this experiment we consider three models: a "standard kinetics" model where the rate constant is at the nominal value from the Venot et al. [2012] chemical network, a "fast kinetics" model where the forward rate constant is multiplied by a factor 10^8 and finally a "slow kinetics" model where the forward rate constant is multiplied by a factor 10^{-8}.

We can estimate the value of $\tau_{\rm chem}$ for H in this simple chemical system as

$$\tau^{\rm H}_{\rm chem} \sim \frac{n_{\rm H}}{k_f n_{\rm H} n_{\rm H} n_{\rm M}} \sim \frac{n_{\rm H}}{k_r n_{\rm H_2} n_{\rm M}}, \tag{5.22}$$

where k_f and k_r are the forward and reverse rate constants. Fig. 5.9 shows the profile of $\tau_{\rm chem}$ as a function of pressure for the standard, fast and slow kinetics cases. We calculated $\tau_{\rm chem}$ using the 1D ATMO P–T profile used to initialise the UM and assuming chemical equilibrium abundances of H_2 and H. Fig. 5.9 shows that $\tau_{\rm chem}$ decreases with increasing pressure.

We also approximate the advection timescales. The horizontal advection timescales are approximated as $\tau^u_{\rm adv} \sim L/u$ and $\tau^v_{\rm adv} \sim L/v$ for the zonal and meridonal winds, respectively, where L is the typical horizontal length scale. We approximate L as the radius of the planet ($L \sim R_p \sim 10^8$ m) and therefore for wind velocities of $u \sim v \sim 10^3$ m s^{-1} this gives $\tau^u_{\rm adv} \sim \tau^v_{\rm adv} \sim 10^5$ s. For the vertical advection timescale we perform a similar approximation $\tau^w_{\rm adv} \sim H/w$, where H is the vertical scale height. For a scale height $H = \frac{k_B T}{mg} \sim 10^5$ m (where we have assumed $T \sim 1000$ K, $m \sim 2.33 m_{\rm amu}$ and $g \sim 10$ m s^{-2}) and vertical wind velocities of $w \sim 10$ m s^{-1} this gives $\tau^w_{\rm adv} \sim 10^4$ s. The advection timescales plotted in Fig. 5.9 assume $L \sim 10^8$ m and $H \sim 10^5$ m and the wind velocities as a function of pressure are sampled from the 3D UM grid at the substellar and antistellar points.

Comparing the chemical and advection timescales for each of the standard, slow and fast kinetics models we can predict whether the chemistry is likely to

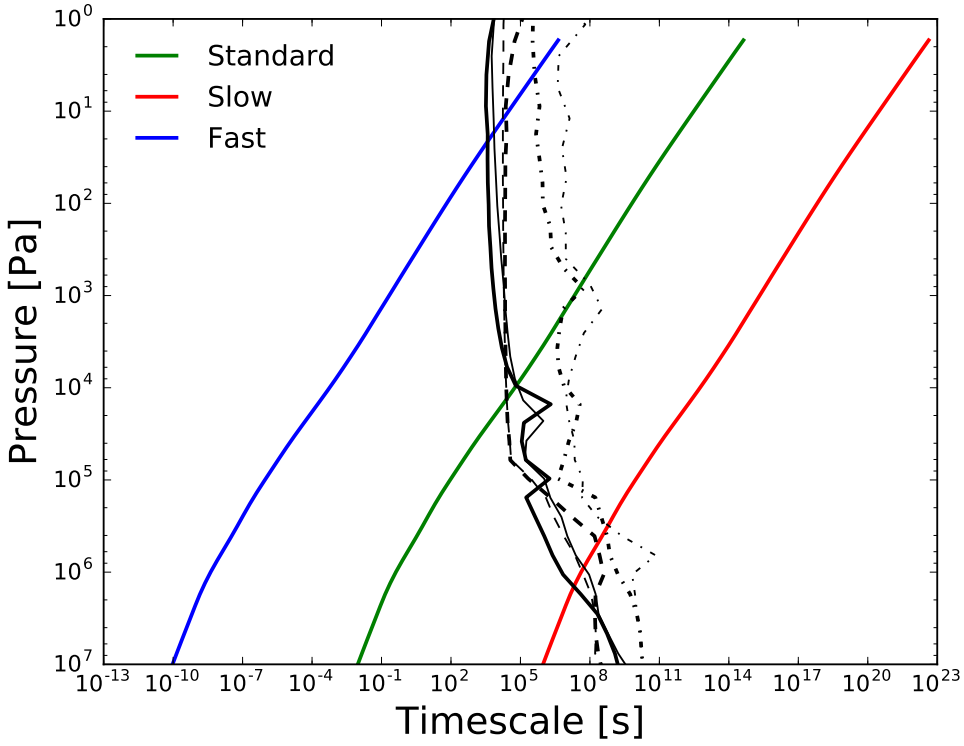

Figure 5.9: A figure showing the estimated chemical and advection timescales. The chemical timescales (coloured solid lines) are calculated as Eq. (5.22) for the 1D P–T profile used to initialise the UM and assuming chemical equilibrium abundances of H and H_2. The advection timescales (black lines) are calculated from wind velocity profiles from the UM and are shown separately for the zonal (solid), meridional (dash-dot) and vertical (dashed) components of the wind at the substellar (thick) and antistellar (thin) points.

remain in chemical equilibrium or be strongly effected by the advection. In the slow kinetics model τ_{chem} is larger (slower) than τ_{adv} over most of the modelled pressure range and therefore we would expect for the chemistry to be strongly affected by advection. On the other hand, in the fast kinetics model τ_{chem} is smaller (faster) than τ_{adv} throughout most of the pressure range and we predict that H should remain in chemical equilibrium, except for at very low pressures.

In the standard kinetics model τ_{chem} and τ_{adv} cross at around $10^4 > P > 10^3$ Pa and this suggests that for $P \lesssim 10^3$ Pa the chemistry should be strongly affected by advection but for $P \gtrsim 10^4$ Pa the chemistry should remain in chemical equilibrium. Indeed, this is approximately what was found in the previous section. We explicitly compare the standard, fast and slow kinetics models to test if these trends predicted by this timescale argument are produced by the coupled chemical kinetics model.

Fig. 5.10 shows the mole fraction of H at a constant pressure of $P = 100$ Pa after 10 days of integration for each of the slow, standard and fast kinetics models. In the standard kinetics model, advection has an important effect and significantly changes H from its chemical equilibrium abundance on the nightside. Considering τ_{chem} and τ_{adv} for this pressure level, this is to be expected as τ_{adv} is several orders of magnitude smaller (faster) than τ_{chem}. The slow kinetics model shows an even more significant departure from chemical equilibrium and the mole fraction of H is almost entirely homogenised horizontally. With an even larger τ_{chem} compared with the standard kinetics model this is expected.

On the other hand, the fast kinetics model is able to retain the initial chemical equilibrium abundance of H and advection has had no apparent effect. Considering the estimated timescales we can indeed see that at 100 Pa τ_{chem} is several orders of magnitude smaller (faster) than τ_{adv} meaning that chemical equilibrium should prevail.

The case is very similar at a higher pressure level of 3000 Pa, as shown in Fig. 5.11. Here in the standard chemical timescale model the effect of advection has only a minor effect on the abundance of H with small increases in the H mole fraction notable in the coolest regions of the nightside. Considering the timescales at this pressure level (Fig. 5.9) we can see that τ_{chem} and τ_{adv} are actually comparable. It is therefore likely that in most of the regions of the atmosphere at this pressure level τ_{chem} is slightly smaller than τ_{adv} except in the coolest regions of the nightside where τ_{chem} is larger due to its dependence on temperature (via the temperature dependent rate constant).

For the slow kinetics model advection has efficiently homogenised the H abundance horizontally whilst in the fast kinetics model the chemistry has remained in a state of chemical equilibrium everywhere at this pressure level. Both of these results are consistent with the timescales shown in Fig. 5.9 for this pressure level.

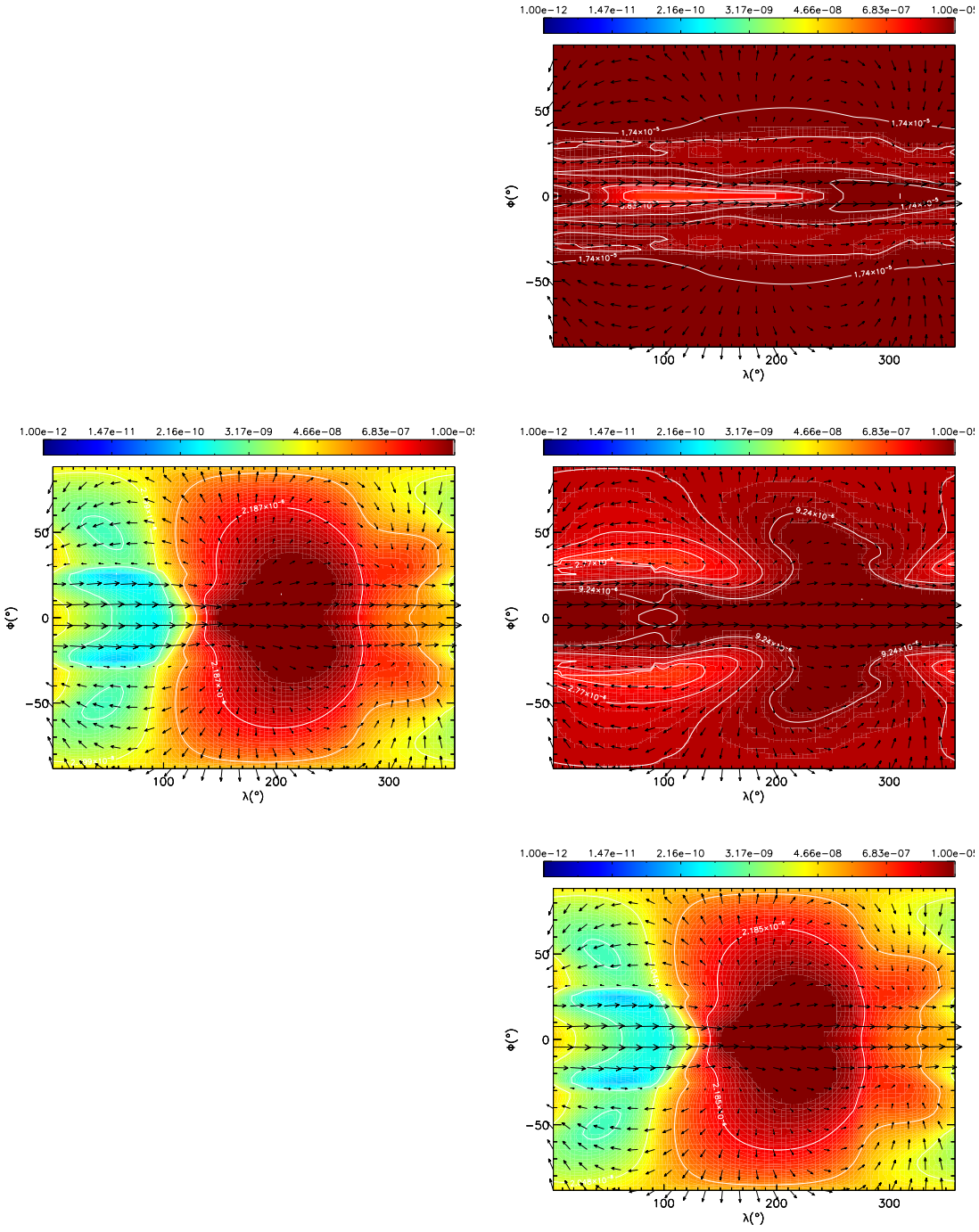

Figure 5.10: A figure showing the mole fraction of H (colour contour) and horizontal wind velocities (vectors) for the slow, standard and fast kinetics models at a constant pressure of 100 Pa. We show the chemical equilibrium structure at $t = 0$ on the left and the right panels show a model snapshot at 10 days for the slow kinetics model (*top right*), standard kinetics model (*middle right*) and fast kinetics model (*bottom right*).

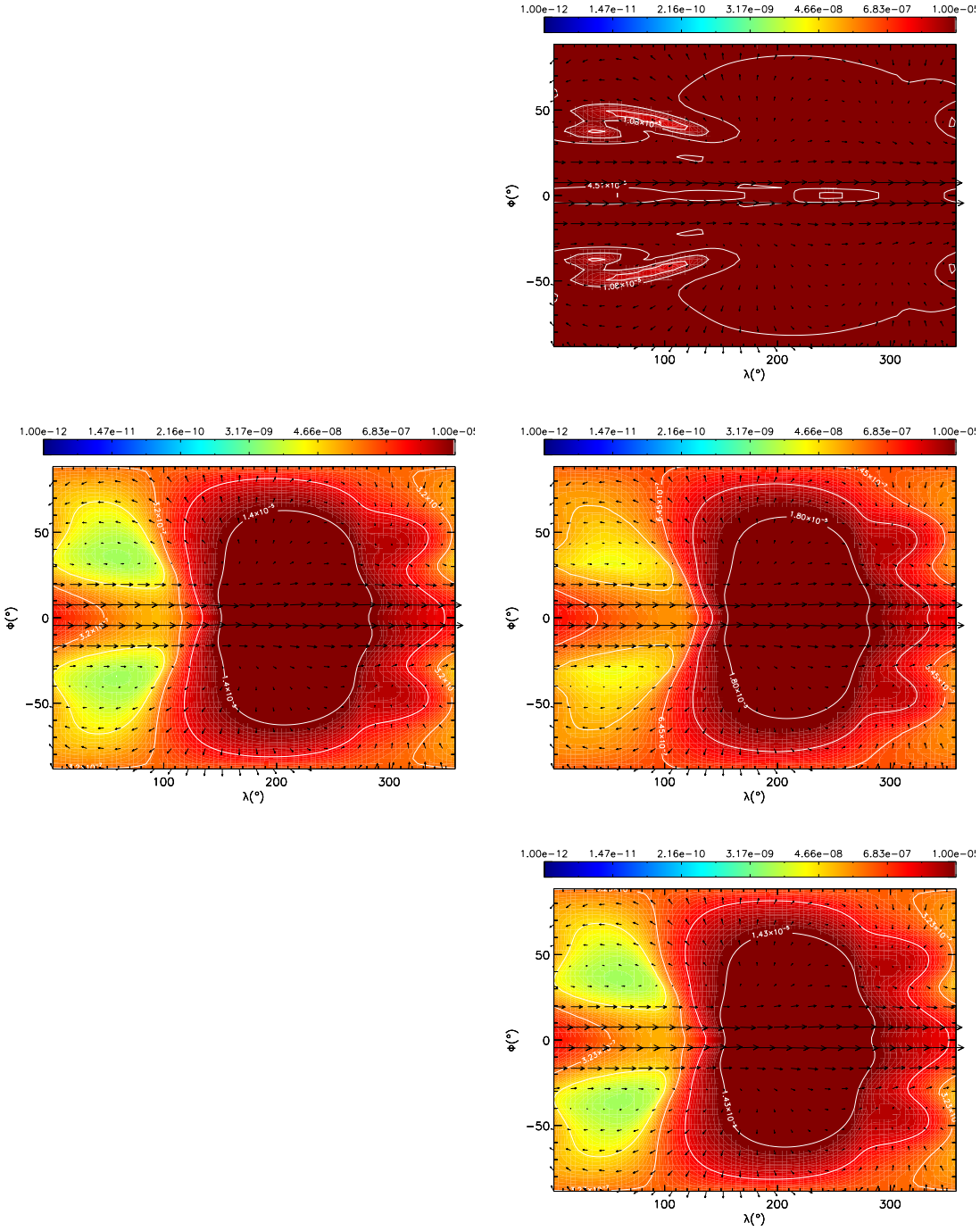

Figure 5.11: As Fig. 5.10 but at a pressure level of 3000 Pa.

We also consider the vertical profiles of H in more detail. Fig. 5.12 shows the vertical profiles of the H abundance for a series of longitude points around the equator after 10 days integration. For the standard kinetics model the abundance of H has departed from the equilibrium profiles at $\sim 10^3$ Pa and the profiles for each longitude point converge for $P \lesssim 100$ Pa where the abundance of H has effectively become horizontally homogenised. For the slow kinetics model the profiles depart from chemical equilibrium at significantly higher pressures of $P \sim 10^5$ Pa. On the other hand, for the fast kinetics model the abundances roughly follow the initial chemical equilibrium profiles across the pressure range. The slight departure from the initial equilibrium profiles in the fast kinetics model may be due to a subtle departure from equilibrium due to advection. Alternatively, the chemistry may still be in equilibrium and the abundance change may be due to slight changes in the temperature structure.

In this section we have explored the effect of varying the chemical timescale on the balance between advection-driven homogenised chemistry and chemical equilibrium. We estimated the chemical and advection timescales to predict whether the chemistry should or should not remain in chemical equilibrium and compared these predictions with idealised experiments using the coupled chemical kinetics scheme.

In cases where the estimated τ_{chem} is smaller (faster) than τ_{adv} the coupled kinetics model retains chemical equilibrium abundances of H. However, in the opposite case where τ_{adv} is smaller (faster) than τ_{chem} the advection processes efficiently homogenise the chemistry both vertically and horizontally. In the absence of an obvious benchmarking experiment, these idealised tests that reproduce the expected behaviour of the system add confidence that the coupled chemical kinetics scheme is working correctly.

In these tests we have varied the chemical timescale, by altering the rate constant, but have kept fixed the chemical timestep, the frequency with which the kinetics calculations are performed. In the next we section investigate the model sensitivity to the choice of chemical timestep.

5.5.4 Testing the sensitivity to the chemical timestep

In this section we perform experiments to test the sensitivity of the model to the choice of chemical timestep Δt_{chem}. We perform identical simulations only varying the frequency with which the chemical kinetics scheme is called. We test three values of Δt_{chem}: 60 s, 600 s and 6000 s, which in these simulations correspond to 1, 10 and 100 dynamical timesteps.

Fig. 5.13 shows the mole fraction of H on surfaces of constant pressure ($P =$ 100 Pa and $P = 3000$ Pa) for each Δt_{chem} test case after 10 days of integration from

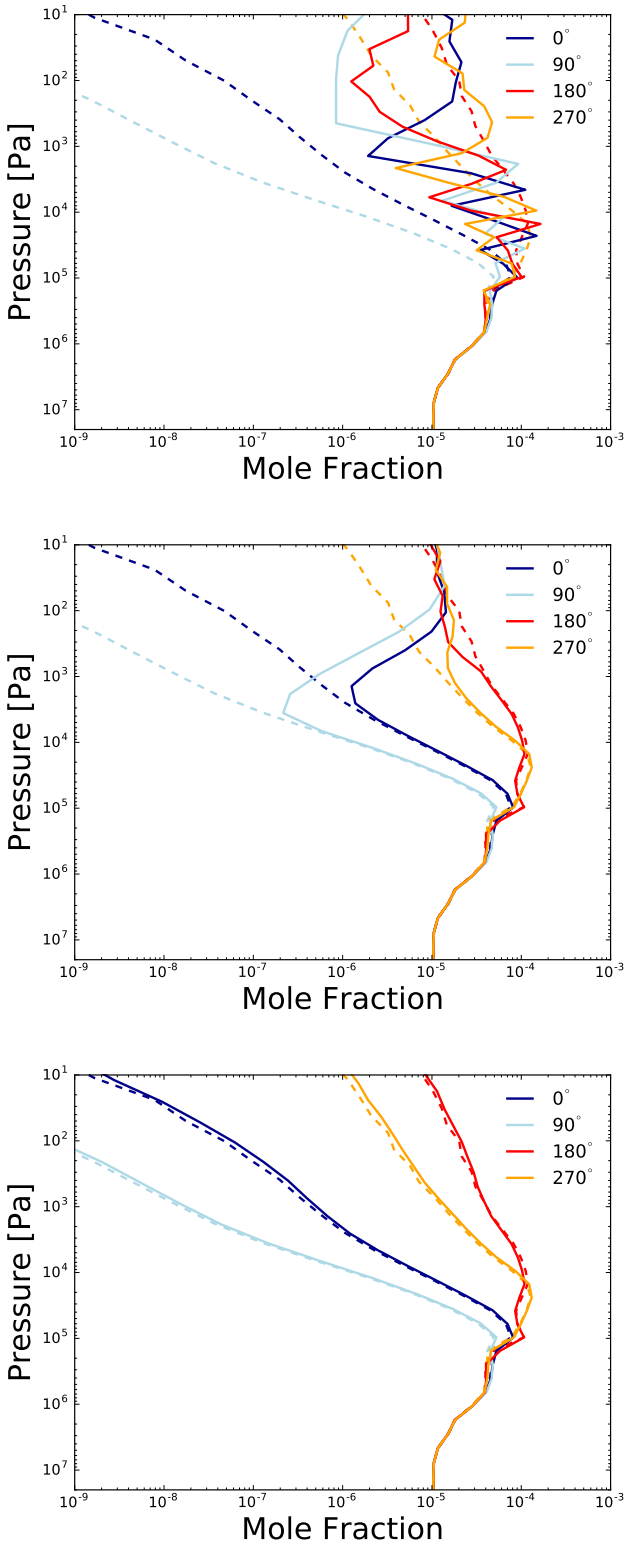

Figure 5.12: A figure showing vertical profiles of the H abundance taken from the 3D model grid at the equator for a series of longitude points. The dashed lines show the initial chemical equilibrium profiles while the solid lines show the abundance after 10 days for the slow (*top*), standard (*middle*) and fast (*bottom*) chemical timescale cases.

initial chemical equilibrium values. For both pressure levels the result is broadly similar for each value of Δt_{chem} with the only notable differences occuring in the equatorial jet region, where the wind velocities are largest.

At 100 Pa we can see that a region around $70 < \lambda < 100^{\circ}$ longitude appears to be sensitive to the choice of Δt_{chem}, with the H mole fraction increasing with increasing Δt_{chem}. Comparing this feature with the temperature at this pressure level (Fig. 5.6) it is evident that this corresponds to the coolest region of the atmosphere. Chemical equilibrium predicts lower mole fractions of H for lower temperatures. We hypothesise that this change in abundance as Δt_{chem} is increased is due to an insufficient temporal resolution. If the chemical kinetics scheme is not called frequently enough, the response of the chemical tracers to changes in temperature may not be accurate. This effect is only apparent in the equatorial jet region, where the wind velocities are largest, over the range of tested Δt_{chem}.

We find similar effects in the H mole fraction in the equatorial jet region at the deeper pressure level of 3000 Pa (compare closely the mole fraction around the equator between the $\Delta t_{\text{chem}} = 60$ s and $\Delta t_{\text{chem}} = 6000$ s models in Fig. 5.13).

To better quantify the differences in the mole fraction that result from the varying chemical timestep we consider the vertical profiles of H extracted from the 3D grid. Fig. 5.14 shows vertical mole fraction profiles of H from several points around the 3D grid, comparing the cases with different chemical timesteps. Assuming that the $\Delta t_{\text{chem}} = 60$ s simulation is the most accurate, we also calculate the relative differences between this and the models with $\Delta t_{\text{chem}} = 600$ s and $\Delta t_{\text{chem}} = 6000$ s.

For all latitude and longitude points the $\Delta t_{\text{chem}} = 60$ s and $\Delta t_{\text{chem}} = 600$ s agree well. However, the $\Delta t_{\text{chem}} = 6000$ s deviates significantly at the equator from the two models with shorter Δt_{chem}, as was seen previously in Fig. 5.13. The relative difference profiles quantify the differences between these models. The maximum relative difference between the $\Delta t_{\text{chem}} = 60$ s and $\Delta t_{\text{chem}} = 600$ s is less than 1%. On the other hand, the maximum relative difference between the $\Delta t_{\text{chem}} = 6000$ s model and the $\Delta t_{\text{chem}} = 60$ s model is $\sim 10\%$ at the equator.

In summary, these tests show that throughout most of the atmospheric domain the choice of chemical timestep does not strongly effect the mole fraction of H with differences of $\lesssim 1\%$. However, when the chemical timestep is increased to 6000 s differences of $\lesssim 10\%$ in the H mole fraction are found in the equatorial jet region where the horizontal wind velocities are largest. This is likely due to inaccuracies due to an inadequate temporal resolution.

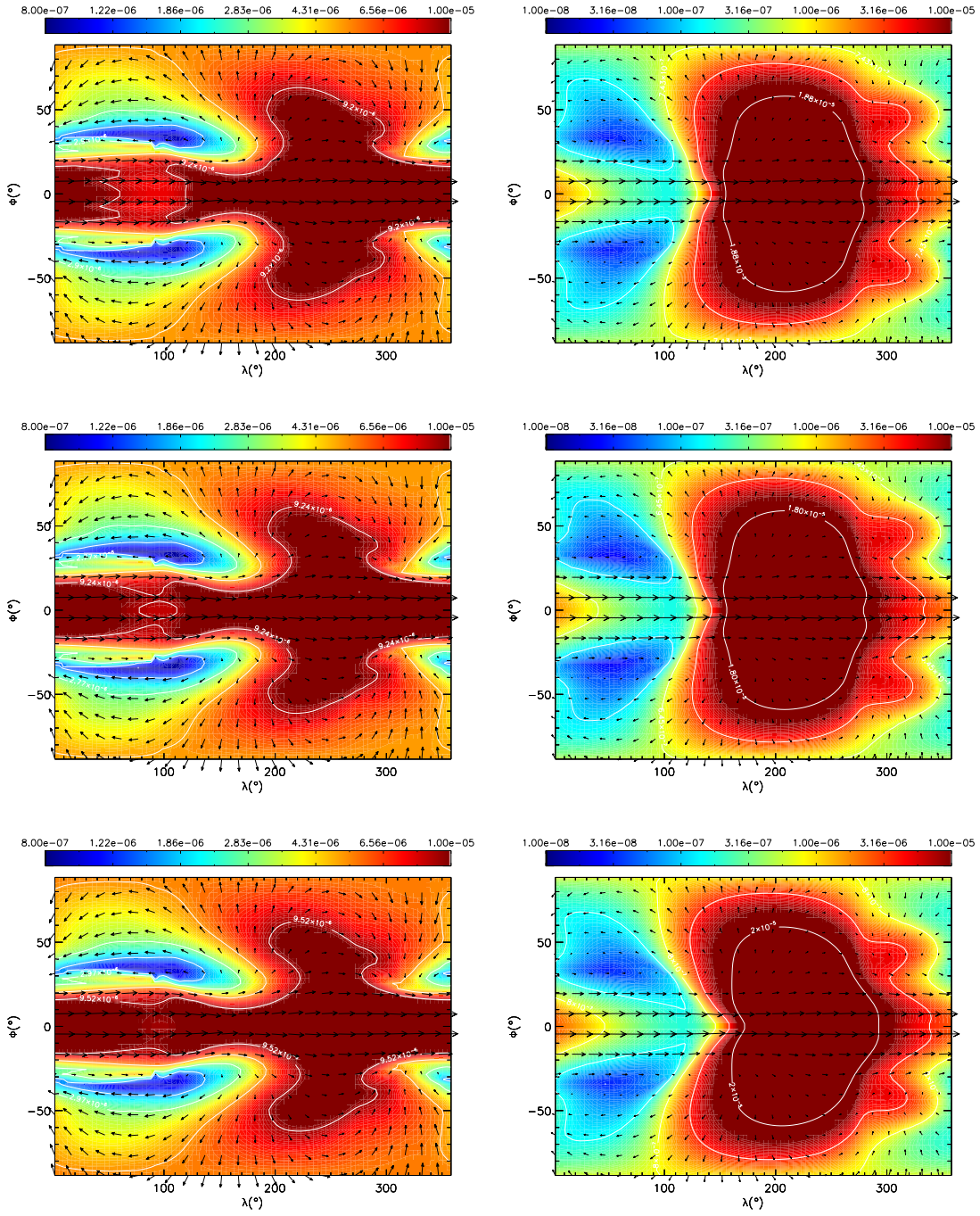

Figure 5.13: A figure showing the mole fraction of H (colour scale) and horizontal wind velocities (vectors) on constant pressure levels of 100 Pa (*left*) and 3000 Pa (*right*) after 10 days for test cases with chemical timesteps of $\Delta t_{\text{chem}} = 60$ s (*top*), $\Delta t_{\text{chem}} = 600$ s (*middle*) and $\Delta t_{\text{chem}} = 6000$ s (*bottom*). Note the varying colour scale.

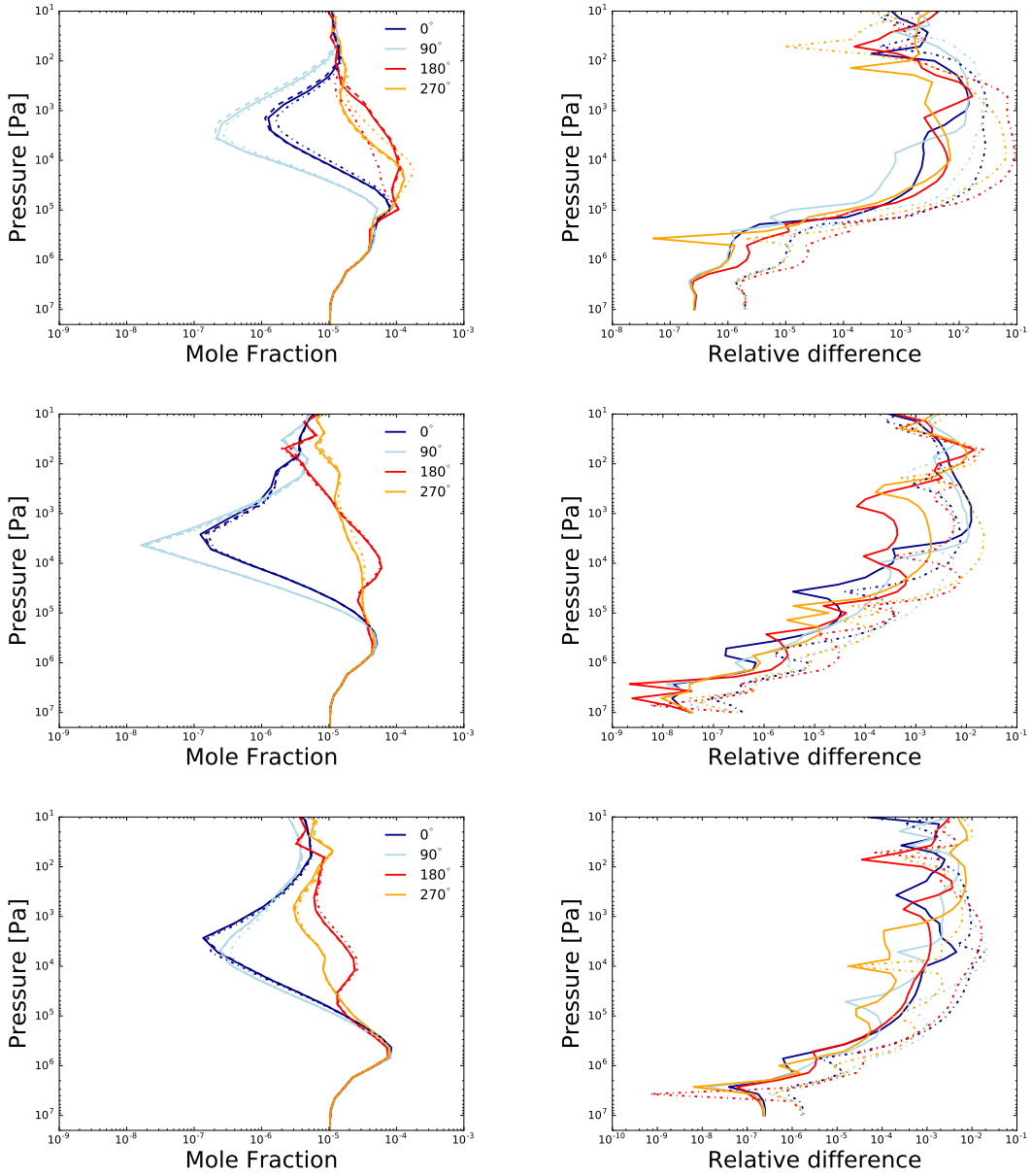

Figure 5.14: *Left:* figures showing vertical profiles of the H mole fraction extracted from the 3D UM grid after 10 days integration for $\phi = 0°$ (*top*)), $\phi = 30°$ (*middle*) and $\phi = 60°$ (*bottom*) and for a range of longitude points (colour legend) showing results from the simulations using different chemical timesteps with $\Delta t_{\text{chem}} = 60$ s (dashed), $\Delta t_{\text{chem}} = 600$ s (solid) and $\Delta t_{\text{chem}} = 6000$ s (dash-dot). *Right:* figures showing the relative difference of the $\Delta t_{\text{chem}} = 600$ s (solid) and $\Delta t_{\text{chem}} = 6000$ s (dash-dot) compared with the $\Delta t_{\text{chem}} = 60$ s model.

5.6 Future testing and developments of the coupled chemical kinetics model

In this work we assumed a simplified chemical system where the atmosphere is composed only of H_2, H and He with one reversible chemical reaction interconverting H_2 and H. This assumption of a simplified chemistry case allows for a more straightforward testing of the chemical kinetics scheme and to assess the balance between the advection and chemistry. However, the tests presented in this work should be repeated using a more complete list of chemical species and reactions to ensure that the model behaviour is not significantly changed with a more complex chemistry case. This is the next goal of the project and we will do this by including the full chemical network of Venot et al. [2012].

In addition to using a more comprehensive chemical network it will be important to test the sensitivity of the model to other factors such as the exact method taken to calculate the advection of the tracers species. The UM employs a semi-Lagrangian advection scheme to calculate the advection of the free tracers, though several subtely different method options are available within the model; see Section 5.1.2. For the present work we adopted the default option. It will be important to understand the differences between these different options and to assess the dependence of the model result to the choice of advection scheme.

Another important development, once the model has been tested using a more complete list of chemical species, will be to include radiative-feedback with the advected chemical species. In the present tests the opacities were calculated assuming local chemical equilibrium (using the Burrows and Sharp [1999] method) and the advection of the species and chemistry calculations were performed non-consistently with the temperature profile . Incorporating consistency between the advected chemical species and opacity/radiative transfer calculations will be important as horizontal advection is expected to play an important role on the abundances of absorbing species such as CH_4 and NH_3 [Cooper and Showman, 2006, Agúndez et al., 2014a] in addition to vertical mixing (Chapter 4).

5.7 Conclusions

In this chapter we have detailed the coupling of the Gibbs energy minimisation and chemical kinetics schemes to the Met Office Unified Model. In addition, we have performed a series of tests to validate the coupling of these schemes as well as assessing the performance and sensitivity of the model to various parameters.

In this chapter we have:

- described the coupling of the Gibbs energy minimisation scheme to the UM
- validated the coupled Gibbs energy minimisation scheme by reproducing chemical abundance profiles for a prescribed P–T profile
- investigated the sensitivity of the coupled Gibbs energy minimisation model to the choice of chemical timestep and found a very low sensitivity for the range of tested values
- described the coupling of the chemical kinetics scheme to the UM and validated the coupling by reproducing the chemical evolution from a prescribed initial condition in a simple box model test
- described the initial results of the coupled chemical kinetics model for a simplified chemistry case (only H_2, H and He) to investigate the effect of advection on the abundances
- investigated the effect of artificially changing the chemical timescale to reproduce the expected behaviour of the system, with chemical equilibrium prevailing when the chemical timescale is faster than the advection timescale
- tested the sensitivity of the model to the choice of chemical timestep for the coupled chemical kinetics scheme, finding that the highest sensitivity is in the equatorial jet region where inadequate temporal resolution can lead to inaccurate abundance profiles compared with using a shorter chemical timestep
- identified further testing for the coupled chemical kinetics model to be performed in the future

In the next chapter we present the results of the first application of the coupled Gibbs energy minimisation scheme, where we apply the coupled model to the atmosphere of a hydrogen-dominated super Earth type atmosphere and investigate the effect of the metallicity of the atmosphere on the dynamic and thermodynamic structure.

The coupled chemical kinetics scheme requires further testing, in particular with a more complete set of chemical species and reactions. However, potential applications of such a model are crucial for understanding the atmospheres of hot exoplanets. The importance of the lack of advection driven non-equilibrium chemistry in 3D atmosphere models of hot Jupiters has long been speculated [e.g. Moses et al., 2011, Zellem et al., 2014b], with some notable attempts at representing horizontal non-equilibrium chemistry in simplified models [e.g. Cooper and Showman, 2006, Agúndez et al., 2014a]. The large zonal temperature gradients present in hot

Jupiter atmosphere result in large abundance gradients, predicted by chemical equilibrium. However, it is also expected that the large zonal wind velocities should cause departures from this chemical equilibrium due to wind-driven advection. This could have important implications for absorbing species such as CH_4 and NH_3. A fully consistent 3D GCM with a coupled chemical kinetics scheme will be crucial in understanding and quantifying these processes.

Chapter 6

Bulk Composition: Dynamics, Radiative Transfer and Chemistry

This chapter presents the results of the first application of a Gibbs energy minimisation scheme, giving chemical equilibrium abundances, coupled to the 3D General Circulation Model (GCM), the Met Office Unified Model (UM). The model is applied to the atmosphere of GJ 1214b, which is assumed to be hydrogen-dominated, and we investigate the sensitivity of the dynamical and thermodynamical structure, and subsequently the observables, to the metallicity (elemental composition) of the atmosphere.

We begin by reviewing previously published works which investigate the role of the metallicity of an atmosphere on its dynamical and thermal structure (Section 6.1) all of which employ the same GCM (MITgcm). We then describe our model setup in Section 6.2 before presenting our results including the zonal-mean zonal wind profiles, horizontal temperature maps and simulated observables (emission/reflection spectra and phase curves) in Section 6.4. Finally we present our conclusions in Section 6.5.

6.1 Context

In this section, we summarise the results of previous studies that investigate the impact of varying the metallicity of an atmosphere on its dynamical and thermal structure using a 3D GCM.

Lewis et al. [2010] performed simulations of the hot Neptune GJ 436b adopting a range of metallicities (1×, 3×, 10×, 30× and 50× solar) using the SPARC/MITgcm model [Showman et al., 2009]. This model couples the dynamical core of the MITgcm with a sophisticated radiative-transfer model to provide accurate heating rates that drive the thermal and dynamical evolution of the atmosphere. In this model,

the opacities are provided as a pre-computed look-up table for a range of pressures and temperatures. The abundances of the gas-phase molecules are calculated assuming chemical equilibrium at the time of constructing the opacity look-up tables. This method has been shown to be less accurate than alternative methods that combine the individual opacities to give the total opacity at model run time (e.g. the method of equivalent extinction or random overlap) [Amundsen et al., 2017], particularly in the presence of sharp gradients of chemical abundances.

Lewis et al. [2010] find that the zonal ($\partial T/\partial\lambda$), as well as meridional ($\partial T/\partial\phi$), temperature gradients increase with increasing metallicity. In addition, they find that the metallicity plays a strong role in the shape of the zonal-mean zonal wind structure. In their 1× Solar metallicity model, the zonal wind pattern is dominated by two high-latitude jets and a weaker equatorial jet. As the metallicity is increased the high-latitude jets weaken and the equatorial jet strengthens. In their highest metallicity case (50×) the high-latitude jets have practically disappeared and the zonal wind structure is now dominated by an equatorial jet.

Using the same model, Kataria et al. [2014] simulated the atmosphere of GJ 1214b under a range of different elemental compositions and bulk composition scenarios. They find, similar to Lewis et al. [2010], that as the metallicity is increased the maximum zonal-mean zonal wind velocity is increased and the structure of the flow transitions from one with significant high-latitude jets to one with a dominant equatorial jet. Kataria et al. [2014] also simulate scenarios where the atmosphere is completely dominated by H_2O and/or CO_2. In the CO_2 dominated case, the zonal wind is characterised by polar jets whereas the H_2O dominated atmosphere shows a strong equatorial jet. As in Lewis et al. [2010], the opacities are provided via a pre-calculated look-up table.

More recently, again using the MITgcm, Zhang and Showman [2016] explored the effect of the bulk composition on the dynamics and thermodynamics of the atmosphere in a series of idealised experiments. Here, a temperature-forced (Newtonian cooling) approach was taken, rather than using a full radiative transfer scheme; the thermodynamic evolution is parameterised by relaxing the temperature profile to a prescribed equilibrium profile on a characteristic timescale.

Zhang and Showman [2016] focussed on the "dynamical effect" of varying the bulk composition by changing the mean molecular weight μ and molar heat capacity C_p parameters across a series of simulations. The "radiative effect" of changing the composition (the effect on the opacities and heating rates) was ignored as the same temperature-forcing parameters were assumed throughout the tested parameter space. Zhang and Showman [2016] modelled eight simple atmospheres which were assumed to be dominated by a single chemical species and μ and C_p were determined by that molecule alone: H_2, He, CH_4, H_2O, CO, N_2, O_2, CO_2. Across

this range, μ varies by a factor of ~ 20 and C_p by a factor of ~ 4.

It was found that as μ is increased:

- the zonal temperature gradient increased
- the phase curve amplitude increased and the phase offset decreased
- the global wind speed decreased
- the jet width decreased
- the jet maximum wind speed decreased
- the pressure level of the core (maximum zonal wind velocity) of the jet increased

The effect of varying C_p was found to be generally less important, primarily because C_p varies less than μ over the range of composition cases considered by Zhang and Showman [2016]. However, it was found that increasing C_p decreases the equatorial jet speed. In addition, the pressure level of the jet core, where the zonal-mean zonal wind is largest, is sensitive to C_p, with the jet core moving to higher pressures for larger values of C_p. As previously noted, this work employs a temperature-forcing method, with the same forcing profile in each case, and so the effect of changing the composition on the opacity and hence heating rates (the radiative effect) is entirely neglected in this model.

In the following sections, we apply the UM coupled with a Gibbs energy minimisation scheme to model the atmosphere of GJ 1214b across a range of atmospheric metallicities. This coupled model allows for the gas-phase abundances to be calculated in each grid cell for the current temperature and pressure. These abundances are then used to compute the opacities due to each species before being combined to give the total opacity. This method is more flexible, as new opacity tables do not need to be computed for different compositions, as well as more accurate [Amundsen et al., 2014, 2017] than using pre-computed opacity look-up tables that inherently assume some chemical composition, as used in previous GCM simulations [Showman et al., 2009, Lewis et al., 2010, Kataria et al., 2014].

6.2 Model description

In this section, we describe the setup of the UM for the atmosphere of GJ 1214b under a range of assumed atmospheric metallicities. We investigate both the dynamical and radiative effect of varying the metallicity between 1× and 100× solar elemental abundances. Note that for higher metallicities the assumption of a

Table 6.1: Parameters of the GJ 1214 system from Carter et al. [2011]

	GJ 1214b
Mass [M_J]	0.200
Radius [R_J]	0.207
Surface gravity [m s^{-2}]	12.2
Semi-major axis [AU]	0.0123
Orbital period [days]	1.58040482
	GJ 1214
Radius [$R_{\rm Sun}$]	0.179
$T_{\rm eff}$ [K]	3170
log g [cgs]	5.12

hydrogen-dominated atmosphere will no longer be valid. In this case, additional model capabilities that are not currently implemented would be required, such as scattering due to species other than H_2 and He, in addition to collision-induced-absorption (CIA) opacities due to other species such as CO_2; currently only CIA due to H_2-H_2 and H_2-He are included. We choose our upper limit of 100× solar such that we remain well within our assumption of a hydrogen-dominated atmosphere.

6.2.1 Planetary and stellar parameters

The planetary and stellar parameters for GJ 1214b and GJ 1214, respectively, are taken from Carter et al. [2011] and are reproduced in Table 6.1.

For the stellar irradiation spectrum we assume a Phoenix BT-Settl model [Allard et al., 2012] with $T_{\rm eff} = 3200$ K, $\log g = 5.0$ and solar metallicity. The wavelength range is split into a number of discrete radiation bands using the correlated-k approximation [Thomas and Stammes, 1999, Amundsen et al., 2017]. The format of the UM input is such that the normalised flux in each radiation band is provided to give the spectral distribution of the irradiation, and is computed using the offline-SOCRATES code [Edwards and Slingo, 1996]. This normalised flux is converted into an absolute flux using a 'stellar constant': the spectrally-integrated flux as received by a planet at a distance of 1 AU. For GJ 1214b the stellar constant sc was computed as

$$sc = \sigma T_{\rm eff}^4 \left(\frac{r_{\rm star}}{r_{\rm 1AU}} \right)^2 = 3.999 \text{ Wm}^{-2}. \tag{6.1}$$

6.2.2 Models of GJ 1214b

To investigate the impact of varying the metallicity on the dynamical and thermodynamical structure we perform simulations of GJ 1214b assuming metallicities of 1×, 10× and 100× solar. Furthermore, we attempt to separate the "dynamical

Table 6.2: A description of the models of GJ 1214b performed in this work

Model ID	$c_{p,\mathrm{dyn}}$	μ	Opacities and $c_{p,\mathrm{rad}}$
R1	1× solar	1× solar	1× solar
R10	10× solar	10× solar	10× solar
R100	100× solar	100× solar	100× solar
D10	10× solar	10× solar	1× solar
D100	100× solar	100× solar	1× solar

effect", the effect of changing μ and the specific heat capacity c_p, which appear in the equations solved by the dynamical core, from the "radiative effect", the effect of changing the opacities and hence the heating rate. We therefore perform five GCM simulations in total: one with 1× solar opacities and μ and c_p (the model R1), one each for 10× and 100× solar where we vary the opacities and μ and c_p (the models R10 and R100), and finally one each for 10× and 100× solar where we only change μ and c_p and hold the opacities at their 1× solar values (the models D10 and D100). These latter models attempt to emulate the recent tests in Zhang and Showman [2016]. The simulations are summarised in Table 6.2.

Note that we separate the heat capacity c_p into two separate components: the dynamical heat capacity $c_{p,\mathrm{dyn}}$ which is the quantity that appears in the equations solved by the dynamical core (see Section 5.1, e.g. c_p that appears in the momenta equations) and the radiative heat capacity $c_{p,\mathrm{rad}}$ that is used in the radiative transfer to compute the heating rate. Of course, these quantities should be consistent. However to emulate the tests of Zhang and Showman [2016], where the same temperature-forcing profile is used throughout, we choose to make this distinction to ensure that in our D10 and D100 models the heating rate remains at the 1× solar value. In the R10 and R100 models we consistently compute $c_{p,\mathrm{dyn}}$ and $c_{p,\mathrm{rad}}$ for 10× and 100× solar metallicity, respectively.

We integrate each model for 800 days ($\sim 7 \times 10^7$ s) until the maximum wind velocities have ceased to evolve. Note that due to the very long radiative and dynamical timescales in the deep atmosphere this cannot be described as a true steady state of the system. In this case the deep atmosphere is almost entirely defined by the initial condition.

6.2.3 Initialisation

The 3D atmosphere is initialised with zero winds and with a horizontally uniform pressure-temperature (P–T) profile. As in previous works [e.g. Amundsen et al., 2016, Kataria et al., 2014] the P–T profile is taken from a 1D radiative-convective model. Here, we calculate a P–T profile for GJ 1214b using the 1D model ATMO, discussed in detail in previous sections. We use the same planetary and stellar

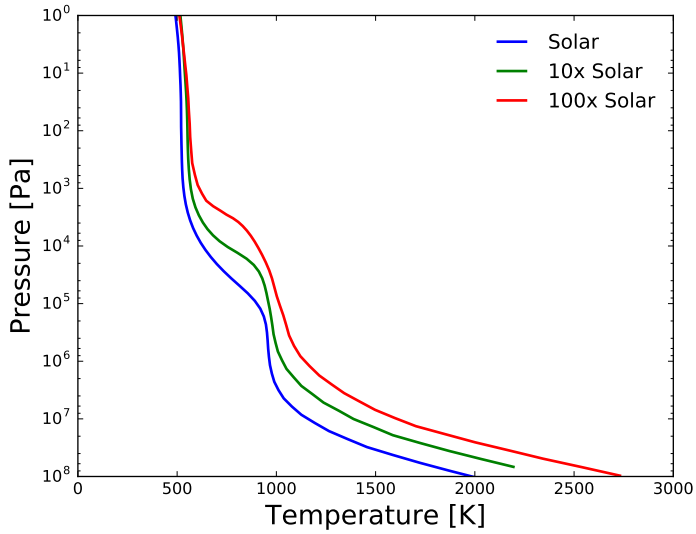

Figure 6.1: A figure showing the pressure-temperature profiles of GJ 1214b generated using ATMO assuming 1×, 10× and 100× solar metallicity.

parameters for the 1D model as in the 3D model. We use a stellar zenith angle of 60° and assume efficient heat redistribution by reducing the incoming stellar flux by 1/2. The 1D P–T profiles calculated using ATMO used to initialise the UM are presented in Fig. 6.1 for three different metallicity cases.

These 1D models show that as the metallicity of the atmosphere is increased the overall temperature of the atmosphere also increases, as found in previous works [e.g. Moses et al., 2013a, Agúndez et al., 2014b], due to the increase in the atmospheric opacity.

The equilibrium chemical abundances for these three 1D models are shown in Fig. 6.2. In the solar composition model, after H_2 and He, the chemistry is dominated by H_2O and CH_4 with mole fractions of $\sim 8 \times 10^{-4}$ and $\sim 4 \times 10^{-4}$, respectively, with abundance profiles that are constant with pressure. The abundance of CO is lower and varies significantly with pressure, having mole fractions generally $< 10^{-6}$. For $P > 10$ bar NH_3 is the most abundant nitrogen-species but this shifts to N_2 for $P < 10$ bar.

As the metallicity is increased to 10× solar, the N_2/NH_3 ratio increases and N_2 becomes the dominant nitrogen molecule throughout the modelled pressure range. CH_4 and H_2O are still the most abundant trace species with near-constant vertical abundance profiles with mole fractions of $\sim 4 \times 10^{-3}$ and $\sim 8 \times 10^{-3}$ respectively. CO maintains a similar dependence on pressure though its abundance increases significantly by around three orders of magnitude.

When the metallicity is increased further to 100× solar, the CO abundance increases significantly and generally becomes more abundant than CH_4 for $P > 0.1$

bar though CH_4 is still more abundant for $P < 0.1$ bar. The greater abundance of CO affects the mole fraction of H_2O as CO acquires some of the oxygen atoms. In regions where the CO abundance is largest, the H_2O abundance decreases by a factor of a few (around $0.1< P <1$ bar).

Importantly, even for the 100× solar metallicity model the composition is still dominated by H_2 and He, satisfying our assumption that the atmosphere is hydrogen-dominated.

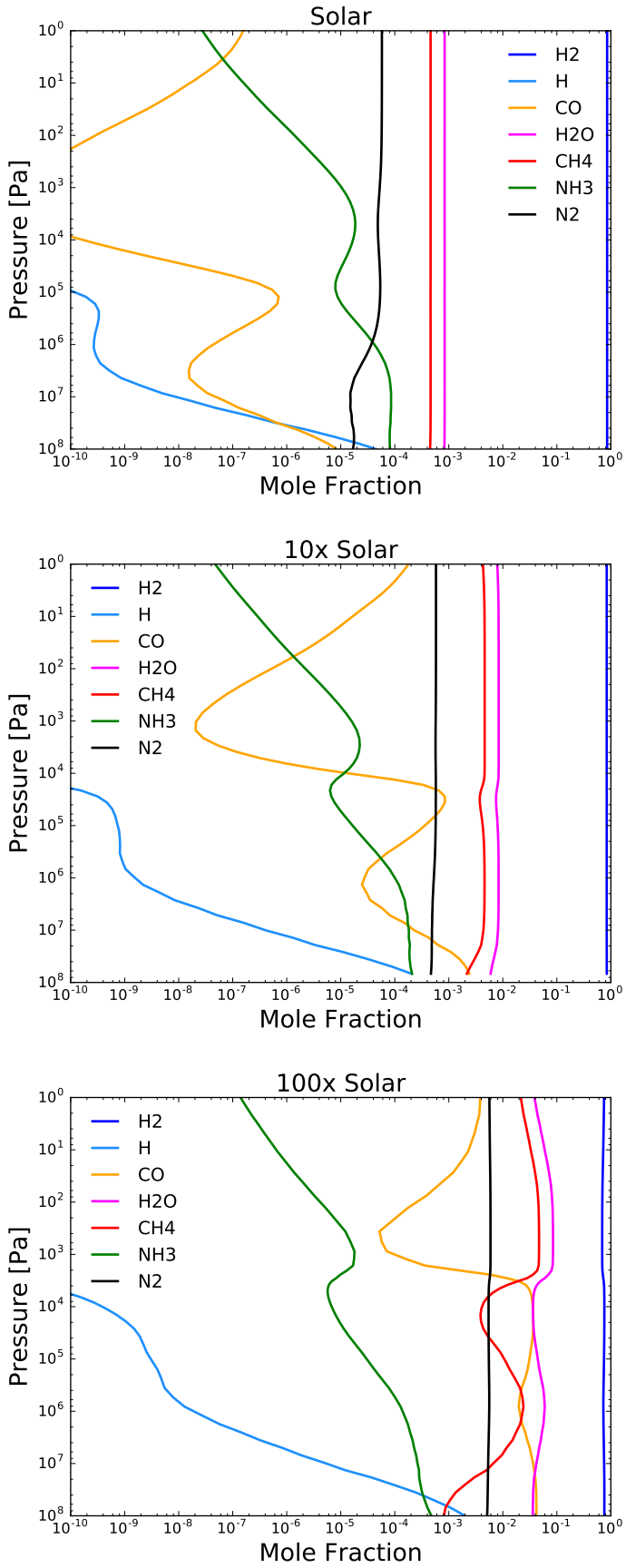

Figure 6.2: The chemical abundances of the major molecules for the 1× (*top*), 10× (*middle*) and 100× (*bottom*) solar composition models of GJ 1214b.

6.2.4 The heat capacity and mean molecular weight

The specific heat capacity c_p and mean molecular weight μ are both required inputs for the UM. We remind the reader that we split c_p into the $c_{p,\mathrm{dyn}}$ and $c_{p,\mathrm{rad}}$ variables for the c_p that appears in the equations solved by the dynamical core and used to compute the heating rate, respectively.

Both μ and $c_{p,\mathrm{dyn}}$ are globally constant values defined by a single scalar quantity in the code. We compute μ and $c_{p,\mathrm{dyn}}$ from the initial 1D ATMO profiles. We first calculate μ and c_p for each level along the 1D profile and then perform a straight average to yield the global value. Following Cooper and Showman [2006] and Kataria et al. [2014] we calculate c_p for the mixture as

$$c_p(T) = \sum_j c_{p,j}(T) f_j, \tag{6.2}$$

where f_i is the mole fraction of the species j and $c_{p,j}(T)$ is the individual heat capacity of that species for the temperature T. Similarly, we calculate μ as

$$\mu = \sum_j \bar{m}_j f_j, \tag{6.3}$$

where $\bar{m}_j$ is the mass of the species j.

Figs. 6.3 and 6.4 show the vertical profiles of μ and c_p for these 1D models. Note that μ is uniform with pressure for the 1× and 10× solar metallicity models but shows a sharp increase at ~ 0.02 bar for the 100× solar model. This is due to the transition between a part of the atmosphere where carbon is mainly in CH_4 (lower molecular weight) to one where carbon is mainly in CO (higher molecular weight). Such a transition, with a layer of higher μ above lower μ is unstable to fingering convection [Tremblin et al., 2015, 2016]. As the metallicity increases the specific heat capacity c_p decreases while the molar heat capacity C_p increases.

It is not directly μ that is an input to the UM but the specific gas constant

$$\bar{R} = \frac{R}{\mu},$$

where R is the molar gas constant. The mean values of these variables used in the UM are shown in Table 6.3.

We calculate the radiative specific heat capacity $c_{p,\mathrm{rad}}$ locally in each grid cell. This allows for a more accurate calculation of the heating rate that accounts for horizontal and vertical variations in $c_{p,\mathrm{rad}}$ due to the spatially varying chemistry.

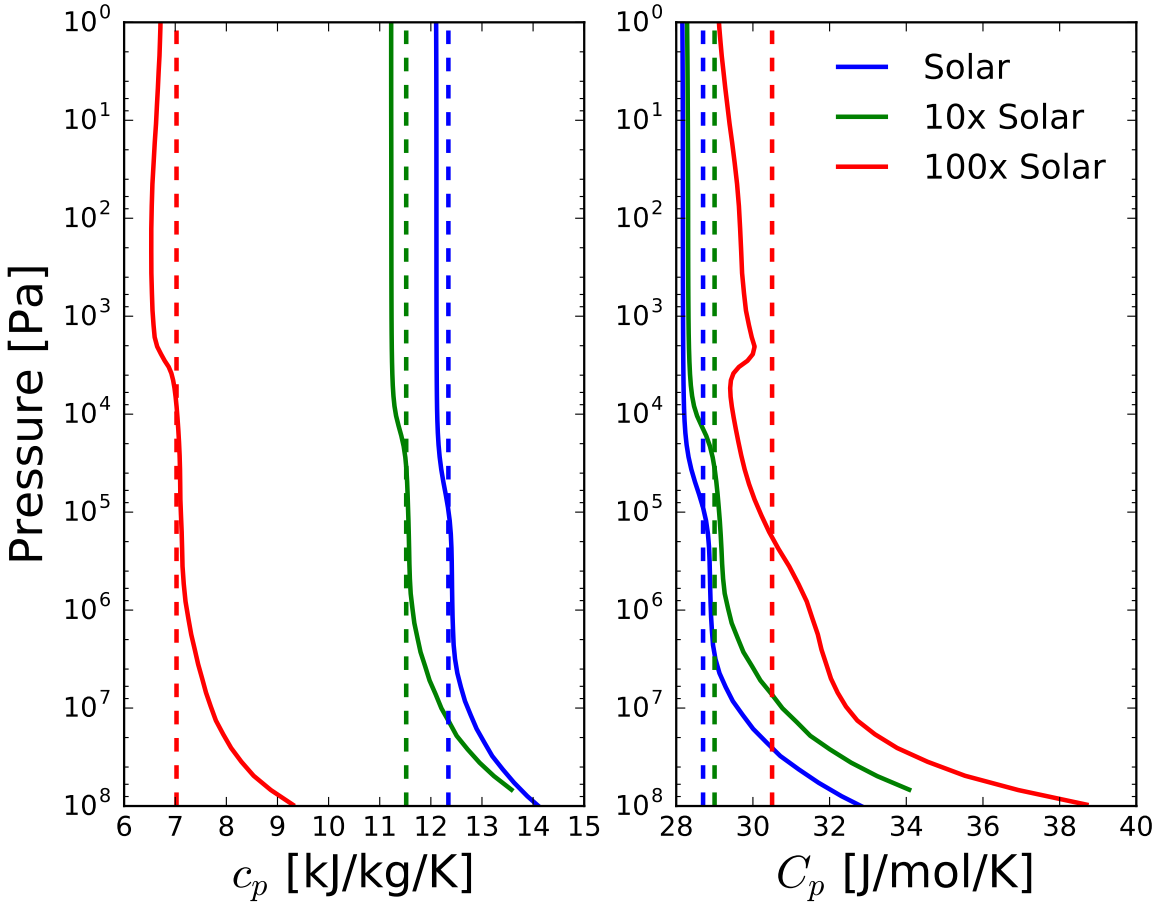

Figure 6.3: A figure showing the specific heat capacity (c_p, *left*) and the molar heat capacity (C_p, *right*) for the 1×, 10× and 100× solar composition models. The dashed lines show the calculated average of each profile shown in Table 6.3.

Table 6.3: The global values of $c_{p,\mathrm{dyn}}$ and μ for the three metallicity cases of GJ 1214b

	1× Solar	10× Solar	100× Solar
c_p Specific Heat Capacity [J kg^{-1} K^{-1}]	12343	11518	7025
C_p Molar Heat Capacity [J mol^{-1} K^{-1}]	28.7	29.0	30.5
$\bar{R}$ Specific Gas Constant [J kg^{-1} K^{-1}]	3573.5	3299.1	1917.3
μ Mean Molecular Weight [g mol^{-1}]	2.33	2.52	4.34

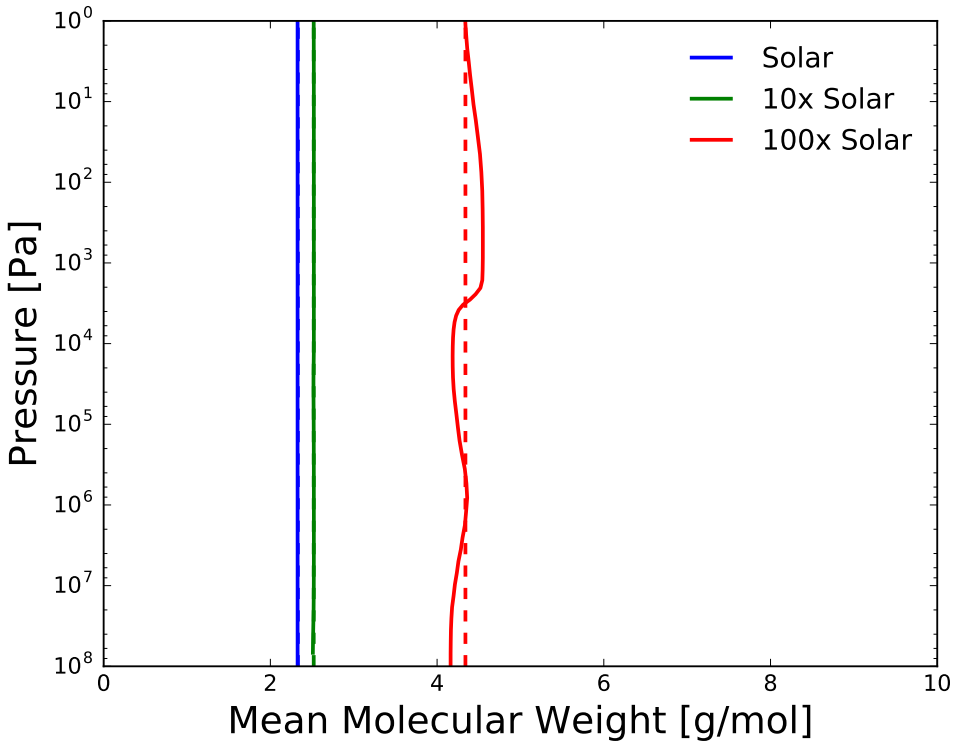

Figure 6.4: A figure showing the mean molecular weight μ for the 1×, 10× and 100× solar composition models. The dashed lines show the calculated average of each profile shown in Table 6.3.

6.2.5 Molecule list

The list of molecules to include in the chemistry calculation is an important consideration. At the very least, all of the molecules which are included as opacity sources (here H_2, He, H_2O, CH_4, CO, NH_3, Na, K, Li, Rb, Cs) must of course be included. However, it is also important to include any other species that can influence the abundance of these species that contribute to the opacity. For instance, at high temperatures sodium is found predominantly in atomic form Na, but at lower temperatures it combines with other elements to form molecular species (NaCl, NaOH, etc), and so reducing the abundance of Na.

Therefore, it is important to include all of the molecules that have appreciable abundances, even if they are not included in the opacity calculations themselves as they may affect the abundances of species which are. However, the computational expense of the calculation is increased as more chemical species are included in the model. It is therefore beneficial to find the optimum list of molecular species that accurately produces the chemical equilibrium abundances of the molecules that are included as opacity sources but also minimises the total number of species in the calculation in order to maximise computational efficiency.

In this work we include 41 chemical species in total: H_2, CO, H_2O, O_2 CH_4, CO_2, N_2, He, Ar, NH_2, NH_3, Na, NaH, NaOH, NaCl, K, KH, KOH, KCl, Cl, HCl. ClO, Cl_2, Ti, TiO, V, VO, F, HF, Li, LiCl, LiH, LiF, Cs, CsCl, CsH, CsF, Rb, RbCl, RbH, RbF. This is a subset of the larger list of species that were used in Chapter 4.

We validate the accuracy of this reduced list of species by comparing the abundance profiles of the important species with the same profiles from a calculation that uses a more comprehensive list of species. The more complete list of species ($\sim$ 140 species in total) is the same as used in Chapter 4. Fig. 6.5 shows the abundances of the important chemical species from calculations using the reduced list of species and the more complete list of species for the 1$\times$ and 100$\times$ solar 1D P–T profiles (Fig. 6.1). The agreement between the abundances of the major molecules when using the full and reduced list of species is of order 0.01% for the 1$\times$ solar model and 1% for the 100$\times$ solar model.

6.2.6 Vertical domain

The UM is a height-based GCM, using altitude as the vertical coordinate, where the upper-boundary of the model atmosphere is defined by a model top height $z_{\rm top}$ and the height variable is defined such that $z = 0$ at the lower boundary of the model; the initial pressure at the lower boundary is also defined as P_0. We must therefore set $z_{\rm top}$ appropriately to model a desired pressure range.

As the metallicity of the atmosphere is increased a consequence is to reduce

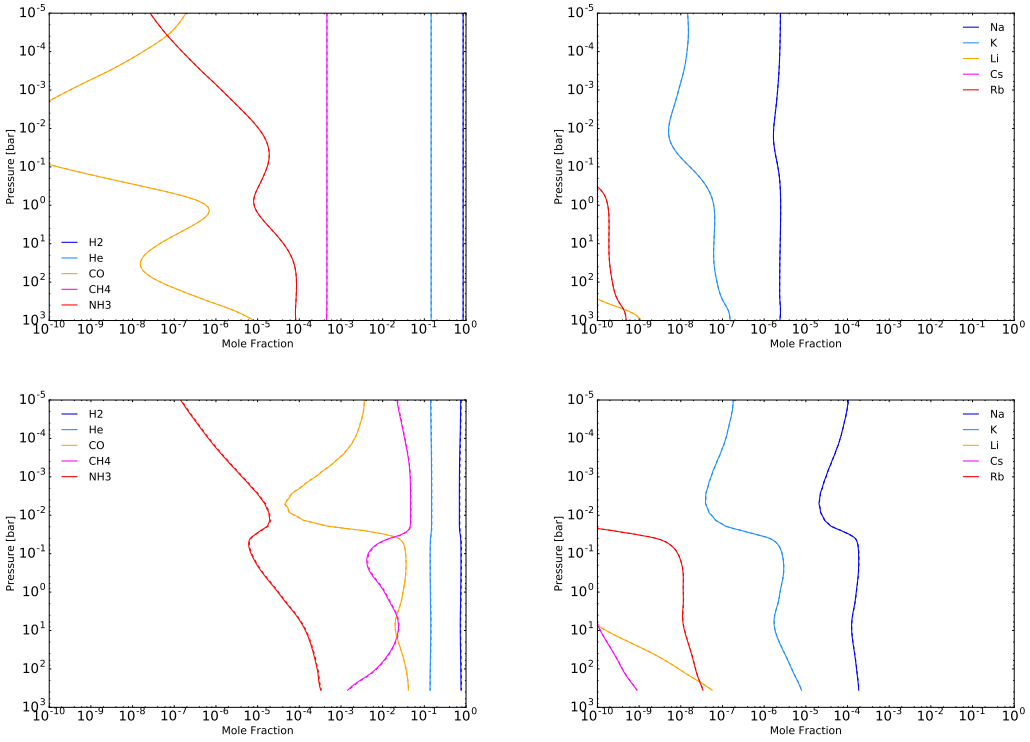

Figure 6.5: A figure showing the chemical equilibrium abundances of the species that contribute to the opacity, calculated for the P–T profiles of the 1× (*top*) and 100× (*bottom*) solar 1D models (Fig. 6.1). We show the carbon-oxygen-hydrogen-nitrogen (*left*) and alkali (*right*) species in separate plots. The abundances calculated with the reduced list of species (41 in total) are shown in solid lines whilst the abundances calculated using the more comprehensive list (> 140 species) is in dashed lines. The removal of ~ 100 species has not affected the abundances of these important species and the calculations agree very well.

Table 6.4: The values of $z_{\rm top}$ used for each model of GJ 1214b

	R1	R10	R100	D10	D100
$z_{\rm top}$ calculated [$\times 10^6$ m]	4.2	3.9	2.3	3.9	2.3
$z_{\rm top}$ used [$\times 10^6$ m]	4.9	5.5	2.4	4.5	2.3

the scale height H which scales inversely with μ. Therefore, in order to model equivalent pressure ranges in each of the models presented here $z_{\rm top}$ must be varied to take into account the variation of μ.

We can estimate the value of $z_{\rm top}$ for a desired minimum atmospheric pressure $P_{\rm min}$ using the equation of hydrostatic equilibrium

$$z_{\rm top} \sim -\frac{k_{\rm B}T}{mg} \ln\left(\frac{P_{\rm min}}{P_0}\right), \tag{6.4}$$

where T is the approximate (isothermal) temperature of the atmosphere, m is the mean molecular mass (in kg), g is the surface gravity and P_0 is the surface pressure which is defined in the model setup. For each model $P_0 = 2\times10^7$ Pa and we assume $T \sim 1000$ K as an approximate isothermal temperature (Fig. 6.1). In line with previous works [e.g. Amundsen et al., 2016] we aim to extend the model to $P \sim 10$ Pa to capture the main dynamical features.

This method provides an approximate value for $z_{\rm top}$ required to achieve the desired pressure range. However, in practice the model with the calculated $z_{\rm top}$ can prove to be sensitive to a dynamical instability due to the growth of vertical oscillations. One way to avoid these instability regions is to slightly alter $z_{\rm top}$. Table 6.4 shows the calculated $z_{\rm top}$ using Eq. (6.4) as well as the values ultimately used in the models presented in this work.

6.2.7 Vertical velocity damping: The sponge layer

Upon testing the setups of the simulations described above, it was found that the R100 model was subject to an instability, producing rapidly oscillating features in the wind profile, particular for the w (vertical) component of the wind. Though the precise cause of this is still uncertain, the features occur at the pressure level of the CO/CH_4 transition (Fig. 6.2). This transition in the dominant carbon species results in vertical gradients in the abundances of CO, CH_4 and H_2O. A possible cause of this instability is the sharp gradient in opacity resulting from this chemical transition that gives large heating rates locally at this pressure level that drives this dynamical instability.

It was found that increasing the magnitude and extent of the vertical sponge layer was sufficient to allow the model to avoid this transient instability and even-

tually the oscillations reduce as the model is integrated out to larger times.

The sponge layer damps the vertical velocities through the damping coefficient R_w as

$$w^{t+\Delta t} = w^t - R_w \Delta t w^{t+\Delta t}, \tag{6.5}$$

where $w^{t+\Delta t}$ and w^t are the vertical wind velocities in the next and the current time step and Δt is the size of the timestep. R_w is given by

$$R_w = \begin{cases} C \sin^2\left(\frac{1}{2}\pi\left(\eta' - \eta_s\right)\left(\frac{1.0}{1.0-\eta_s}\right)\right), & \eta' \geq \eta_s \\ 0, & \eta' < \eta_s \end{cases}$$

where η_s is the start point of the sponge, C is a coefficient and η' is a dimensionless height that in this case is given by

$$\eta' = \frac{z}{z_{\text{top}}}\cos(\phi) + (1 - \cos(\phi)),$$

where z is altitude and ϕ is latitude; i.e. η' increases toward the equator.

The values of C and η_s that control the magnitude and vertical extent of the sponge, respectively, were set to $C = 0.15$ and $\eta_s = 0.75$ in previous works [Mayne et al., 2014a, Amundsen et al., 2016]. Here we adjust these to $C = 0.20$ and $\eta_s = 0.70$; i.e. we slightly increase the magnitude and extend the vertical extent of the sponge layer to damp the spurious vertical velocities.

6.3 Checking the accuracy of the k-coefficients

The correlated-k approximation is a method of increasing the computational efficiency of otherwise expensive radiative-transfer calculations. The k-coefficients are an approximation to the full line-by-line (LbL) opacities. The LbL opacities can contain up to a few billion lines for a single molecule, however this can be described by a much smaller number of k-coefficients. Both the UM and ATMO employ the correlated-k approximation, and the implementation and testing of these methods (for conditions relevant to hot exoplanet atmospheres) are described in detail in Amundsen et al. [2014] and Amundsen [2015].

The k-coefficients themselves are calculated with several assumptions about the typical temperatures and compositions for the application in which they are intended to be used. The k-coefficients used here were initially calculated with conditions typical of hot Jupiters at solar composition; more specifically they were calculated for the conditions representative of HD 209458b. Therefore the accuracy of these particular k-coefficients when used for thermodynamic conditions and chemical compositions that deviate from this is not guaranteed. With relation to

the work presented here, we perform models with metallicities that deviate from the solar composition, and in addition the typical temperatures for the target atmosphere are significantly cooler than that of HD 209458b. In this section, we test the accuracy of the k-coefficients for the thermodynamic and composition conditions relevant to GJ 1214b.

To assess the accuracy of the k-coefficients, profiles of the net radiative flux as well as the net heating rate are calculated using the correlated-k approximation and compared with the same profiles calculated using the LbL method, in tests similar to those presented in Amundsen et al. [2014, 2017]. For temperature and composition profiles relevant to HD 209458b, these k-coefficients were found to produce errors of $\sim$10% in the heating rate compared to the LbL result, a value similar to that found in Amundsen et al. [2014] that is deemed acceptable.

Radiative flux

Firstly we examine the net radiative flux profiles. ATMO was used to calculate the radiative flux using both the LbL method and the correlated-k approximation for a given P–T profile. In addition, the net radiative flux was also calculated with the correlated-k approximation using the offline-SOCRATES code [Edwards and Slingo, 1996] with the same pressure and abundance profiles. SOCRATES is also used within the UM to calculate the heating rates.

To assess the accuracy of these k-coefficients we compare the ATMO LbL result with the ATMO correlated-k result and the SOCRATES correlated-k result. We show separate results from SOCRATES using the Random Overlap (RO) and Equivalent Extinction (EE) methods, which represent different methods of combining the k-coefficients of individual gases in the mixture. The RO method is used in ATMO and is more accurate than the EE method but also more computationally expensive. In practice the EE method is currently used within the UM due to its greater computational efficiency whilst also providing a satisfactory level of accuracy [Amundsen et al., 2017].

Fig. 6.6 shows the net radiative flux profile for the 1$\times$ solar GJ 1214b model using the P–T profile presented in Fig. 6.1. For all models and methods the relative error is $< 5\%$. The ATMO correlated-k and SOCRATES RO methods yield an error of $\sim$ 3%. The profile labeled ATMO, 32 bands, nkmix=120 is a higher precision calculation than the profile labeled ATMO, 32 bands which uses a value of nkmix = 30; this parameter defines the total number of k-coefficients in each band. The higher precision calculation shows a better match to the LbL profile. The relative error in the SOCRATES EE, which is the method employed in the UM, is $\sim$1%.

The equivalent net radiative flux and corresponding error profiles for the 100$\times$ solar metallicity models are shown in Fig. 6.7. The errors in the flux are generally

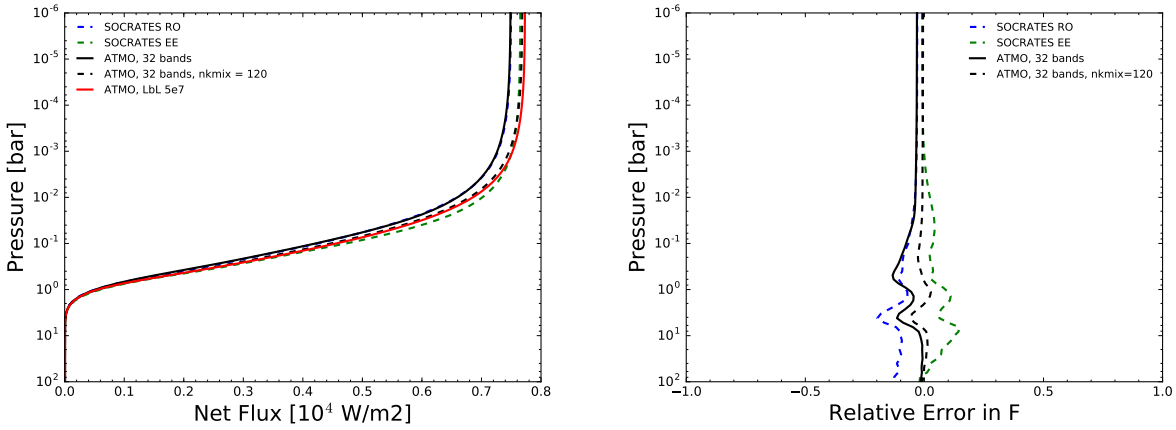

Figure 6.6: The net radiative flux (*left*) and the relative error (*right*) for the GJ 1214b solar composition model. The relative error in the correlated-k models is calculated against the `ATMO` LbL result.

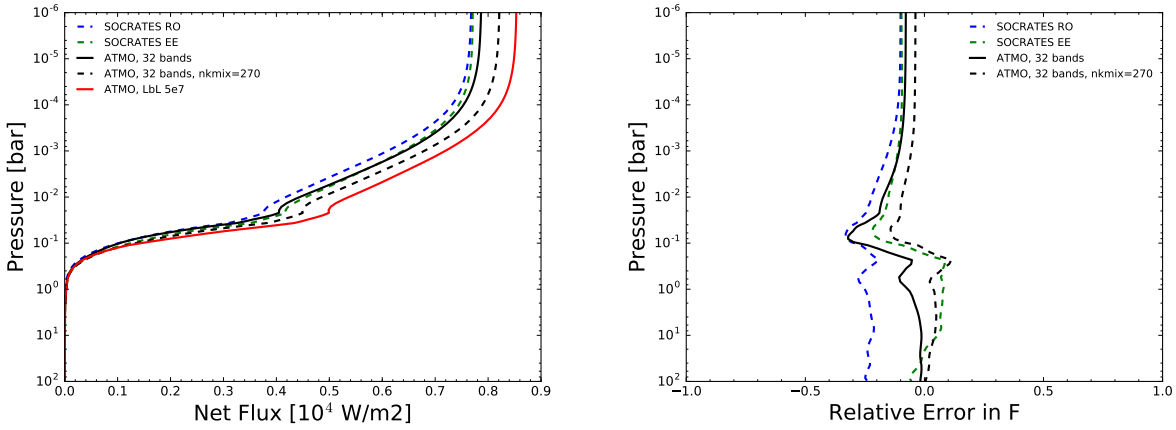

Figure 6.7: As Fig. 6.6 for the 100× solar model.

larger compared to the solar model with errors of ∼10%. The decrease in accuracy compared with the LbL result is perhaps not surprising, as the composition is now far removed from the solar HD 209458b-like conditions for which the k-coefficients were initially calculated. The relative error in the net radiative flux is ∼10% for both SOCRATES models, and less for the ATMO 32 bands model. The profile labeled nkmix = 270 represents a higher precision calculation compared with the standard ATMO correlated-k calculation. The higher precision improves the agreement with the LbL result.

Overall, we find that the relative error in the net radiative flux between the ATMO LbL method and the SOCRATES EE method is ∼1% and ∼10% for the 1× solar and 100× solar metallicity models of GJ 1214b models, respectively.

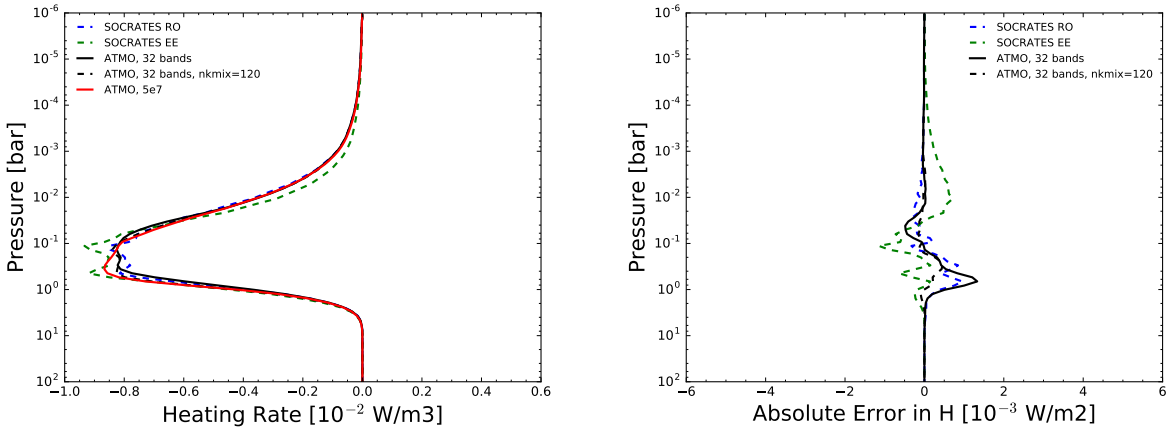

Figure 6.8: The heating rate (*left*) and the absolute error (*right*) for the GJ 1214b solar composition model. The absolute error in the correlated-k models is calculated against the `ATMO` LbL result.

Heating Rates

The accuracy of the calculated heating rates are perhaps of more importance than the net radiative flux, as it is the heating rate which ultimately is used by the UM to evolve the dynamic and thermal structure of the model. As above, we compare the ATMO LbL method with the ATMO correlated-k method and with the SOCRATES model using the RO and EE methods.

Figs. 6.8 and 6.9 show the heating rate profiles, along with the *absolute* error, for the 1× solar and 100× solar models of GJ 1214b. In both metallicity cases, over the whole profile each of the correlated-k methods performs similarly in terms of the accuracy levels compared with the LbL case. For both the 1× and 100× solar metallicity models the errors in heating rate are around ∼10%. This accuracy is actually similar to that found for the HD 209458b profiles for which the k-coefficients were initially developed [Amundsen et al., 2014, 2017]. This test validates our use of these k-coefficients in the GJ 1214b models presented in this chapter.

6.4 Results

In this section we present the dynamical and thermodynamical structures of the atmosphere of GJ 1214b calculated using the UM, as well as the corresponding simulated observables.

6.4.1 Conservation of axial angular momentum

An important first aspect to consider is the conservation of axial angular momentum of the system which must be conserved for the resulting dynamical flow to be deemed

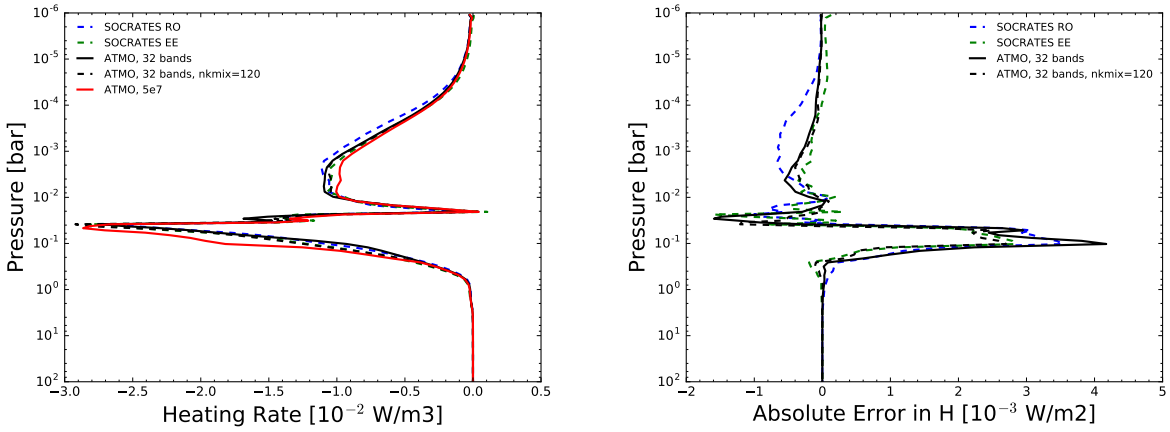

Figure 6.9: As Fig. 6.8 for the 100× solar model.

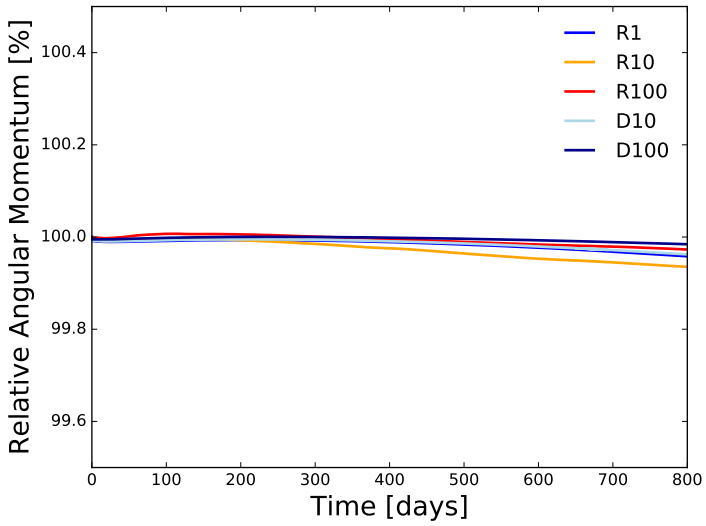

Figure 6.10: A figure showing the total axial angular momentum of the model as a percentage of the initial total axial angular momentum throughout the simulation.

accurate. Fig. 6.10 shows the percentage of the initial total angular momentum throughout the simulation. The conservation of angular momentum for all models presented here is better than 99.9% over an integration time of 800 days.

6.4.2 The dynamical structure: zonal-mean zonal-wind

Firstly we consider the effect of the metallicity on the large scale dynamical structure. A very informative quantity often used to understand the large scale flow is the zonal-mean zonal wind ($\bar{u}$) pattern, shown in Fig. 6.11. This is the zonal component of the wind (u) averaged over all longitudes. We also perform a temporal average between 600 and 800 days.

The R1 model shows a large scale eastward (prograde) circulation across the

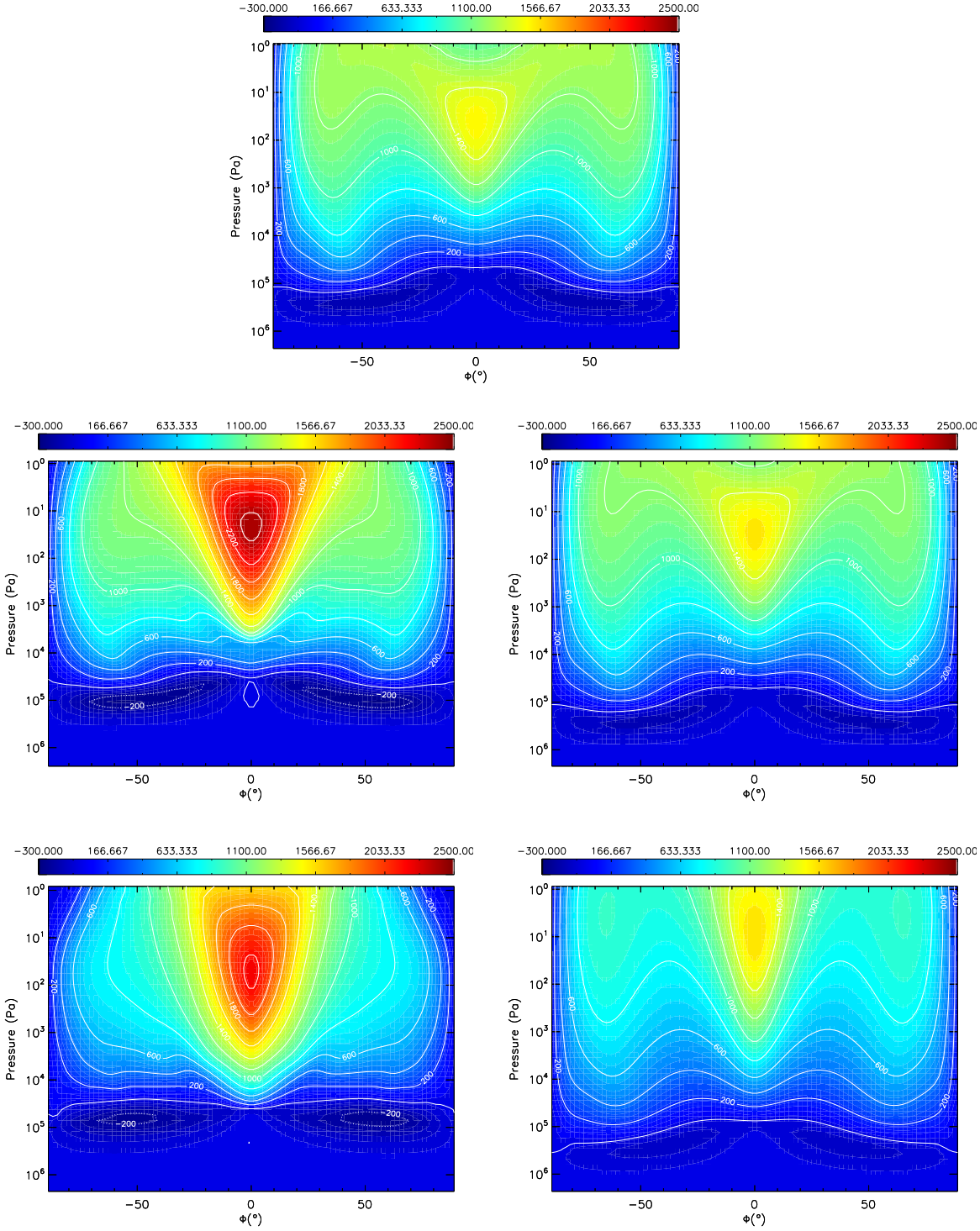

Figure 6.11: A figure showing the zonal-mean zonal wind temporally averaged between 600 and 800 days for the models R1 (*top*), R10 (*middle left*), D10 (*middle right*), R100 (*bottom left*) and D100 (*bottom right*).

entire latitude range and across a large pressure range with typical wind velocities of $\bar{u} \sim 1000$ m s^{-1}. The circulation pattern comprises of three jets, similar to previous GCM models of this atmosphere [Kataria et al., 2014], one each at high latitudes ($\phi \sim \pm 70°$) and one at the equator. The winds in the equatorial jet have $\bar{u} > 1400$ m s^{-1}. At very high pressures ($P \sim 10^5$ Pa) a region of retrograde westward flow with relatively small velocities of a few hundred m s^{-1} exists.

As the metallicity is increased, the R10 model shows a significant increase in the wind velocities of the equatorial jet with $\bar{u} \sim 2400$ m s^{-1} at the core of jet. The vertical extent of the equatorial jet has also increased, with the base of the jet penetrating to deeper pressures. The high latitude jets have decayed in both the typical velocities and the pressure range of their vertical extent.

In the R100 model, as the metallicity is increased further, the wind velocities at high latitudes have decayed further in both magnitude and in vertical extent. The equatorial jet has also continued to grow in vertical extent, with the base of the jet now penetrating deeper than 10^4 Pa. However, the maximum wind velocities are not as large as in the R10 model with $\bar{u} \sim 2200$ m s^{-1} at the core of the jet. There are no other published exoplanet GCM simulations with metallicities that exceed 50× solar; both Kataria et al. [2014] and Lewis et al. [2010] model metallicity ranges of 1–50× solar. It is interesting that here the maximum $\bar{u}$ of the equatorial jet does not continue to increase with metallicity, though the evolution of the structure of the jet with increasing metallicity has previously been shown to be complex [Lewis et al., 2010]. However, the trend of a shifting toward a dynamical structure that is more characterised by a dominant equatorial jet as the metallicity is increased in consistent with previous works [Kataria et al., 2014, Lewis et al., 2010].

For the models D10 and D100, where only μ and $c_{p,\mathrm{dyn}}$ are varied with the metallicity (the opacities being held at their solar values) we find overall a more subtle effect on the dynamical structure. This is not surprising but does highlight the dominance of the "radiative effect" in the dependence of the dynamical structure on the metallicity. As the metallicity is increased from R1 to D100 μ increases by a factor of ~ 2 and $c_{p,\mathrm{dyn}}$ decreases by a factor of ~ 2.

These experiments show similar trends to the fully-consistent "radiative" models (R10 and R100), though to a lesser degree, with the zonal winds at high latitudes decaying in terms of magnitude and vertical extent, while the equatorial jet deepens and strengthens. However, unlike the R10 and R100 models the core of the jet (the pressure level where $\bar{u}$ is at a maximum) shifts to lower pressures.

The mechanism behind these trends is likely to be different for the two series of models. For the R10 and R100 models the key is the increasing opacities that lead to increasing the heating rates. The shortwave and longwave heating rates are shown in Fig. 6.12. As the metallicity is increased both the maximum heating rate

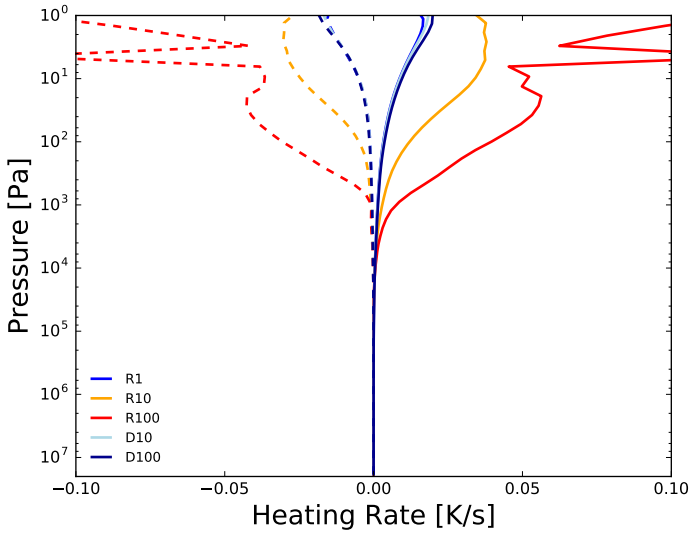

Figure 6.12: A figure showing the heating rates (K s^{-1}) for each model at the sub-stellar point. Shown are the total shortwave (solid) and total longwave (dashed) heating rates.

and vertical extent of the heating deepens, leading to significantly more heating at higher pressures. This deeper heating pushes the vertical extent of the equatorial jet to higher pressures.

The heating rates do not vary significantly for the D10 and D100 models, as the opacities and $c_{p,\mathrm{rad}}$ are calculated assuming solar metallicity. The subtle variations in the heating rate between each model therefore results from differences in the thermal structure of the atmosphere, leading to subtle differences in abundances and opacities.

The mechanism behind the more subtle changes in the zonal-mean zonal wind pattern as the metallicity is increased for the D10 and D100 models is more complex to identify. However, we can attempt to understand it by examining where c_p and R appear in the set of equations solved by the dynamical core.

The thermodynamical energy equation

We begin by considering the thermodynamical energy equation, which we rewrite from Eq. (5.5) as

$$\frac{\mathrm{D}\theta}{\mathrm{D}t} = \frac{Q}{\Pi},$$

where Q is the heating rate (in K s^{-1}), Π is the Exner function and we have omitted the diffusion operator $D(\theta)$ in the interest of clarity. By rearranging and substituting

in the equation of state (Eq. (5.6)) we can obtain

$$\frac{\mathrm{D}\theta}{\mathrm{D}t} = Q\frac{1}{(R\rho\theta/P_0)^{1/\bar{\kappa}}} = Q\frac{1}{R^{1/\bar{\kappa}}}\frac{1}{(\rho\theta/P_0)^{1/\bar{\kappa}}}, \tag{6.6}$$

where $\bar{\kappa} = \frac{1-\kappa}{\kappa}$ and $\kappa = R/c_p$. For the models presented in this work, as we increase the metallicity from 1× to 100× solar we decrease R by a factor of ∼2 and $\bar{\kappa}$ decreases by around 7%. Therefore, from the above equation we can see that as R and $\bar{\kappa}$ decrease $\mathrm{D}\theta/\mathrm{D}t$ will increase. Physically this means that for a given heating rate Q, the change in potential temperature θ of the gas will be larger for a higher metallicity atmosphere.

Practically, this mechanism has the same effect as increasing the heating rate by increasing the opacity as in the R10 and R100 models. However, the magnitude of the change is much smaller, leading to a more subtle impact on the zonal-mean zonal wind, as seen in Fig. 6.11.

The momentum equations

We next consider the momentum equations, taking the u component as an example. We rewrite Eq. (5.1) and for clarity collect the terms that do not contain R, c_p or $\bar{\kappa}$ into a single variable a

$$\frac{\mathrm{D}u}{\mathrm{D}t} = a - c_p\frac{\theta}{r\cos\phi}\frac{\partial\Pi}{\partial\lambda}.$$

Substituting in the equation of state and bringing the constants outside of the derivitive we find

$$\frac{\mathrm{D}u}{\mathrm{D}t} = a - c_p R^{1/\bar{\kappa}}\frac{\theta}{P_0 r\cos\phi}\frac{\partial}{\partial\lambda}.\left(\rho\theta\right)^{1/\bar{\kappa}}.$$

Since the decrease in c_p and R (factor of ∼2) is significantly larger than the decrease in $\bar{\kappa}$ (∼7%) overall this means that as the metallicity increases the acceleration of the winds is smaller. Analogous considerations can be applied to the v and w components of the wind.

As R and c_p decrease due to the increasing metallicity the overall trend seen in Fig. 6.11 is for $\bar{u}$ to decrease, except in the core of the equatorial jet. The above analysis supports this observation as it shows that a given gradient in the Exner function (or in $(\rho\theta)^{1/\bar{\kappa}}$) leads to a smaller acceleration of the winds as the metallicity is increased.

The Rossby deformation radius

The Rossby deformation radius (L_R) is an informative length scale in the atmosphere that characterises at what point rotational effects become as important as gravity and bouyancy effects. This length scale indicates the typical size of dynamical

features in the atmosphere. L_R can be approximated at the equator as [e.g. Zhang and Showman, 2016]

$$L_R \sim \left(\frac{NH}{\beta}\right)^{1/2} \sim \left[\frac{\bar{R}T}{\beta^2\mu}\left(\frac{\bar{R}}{C_p} - \frac{\partial \ln T}{\partial \ln P}\right)\right]^{1/4}, \tag{6.7}$$

where N is the Brunt-Vaisaila frequency, H is the scale height, β is the meridional gradient of the Coriolis parameter. Note that here C_p is the *molar* heat capacity and $\bar{R} = 8.314$ J mol^{-1} K^{-1} is the *molar* gas constant, not to be confused with c_p and R.

From this equation we can see that as μ increases L_R decreases and the size of the typical dynamical features should decrease. In addition, for a fixed profile of P and T, L_R decreases as the *molar* heat capacity C_p increases. In our simulations, both μ and C_p increase as the metallicity is increased meaning that L_R should decrease. This is reflected in the zonal-mean zonal wind (Fig. 6.11) as the equatorial jet becomes narrower in latitudinal extent. This trend is similar to that found in Zhang and Showman [2016].

6.4.3 Horizontal thermal structure

In this section we consider the horizontal gradients in the thermodynamic structure and how this varies across the five models.

Fig. 6.13 shows the temperature and horizontal wind vectors on a surface of constant pressure at 100 Pa. There is a negligible difference in the temperature maps for the R1, D10 and D100 models, demonstrating that changing μ and $c_{p,\mathrm{dyn}}$ (the "dynamical effect") has very little impact on the thermodynamic structure for this pressure region.

On the other hand as the metallicity is increased across the R1, R10 and R100 models (including the "radiative effect") there is a significant difference between the models. Generally, the zonal and meridional temperature gradients both increase with increasing metallicity. Therefore, the R100 model has a warmer dayside and cooler nightside than the R1 model, which shows a relatively small horizontal temperature gradient, particularly in the zonal direction. In addition, it is clear that the 'hot spot', the warmest region at this pressure level, is being shifted closer to the sub-stellar point as the metallicity is increased.

These trends are consistent with a decreasing radiative timescale as the metallicity is increased. As the total opacity increases with metallicity so too does the heating rate, leading to a shorter radiative timescale. This shifts the thermal structure of the atmosphere closer to the radiative equilibrium state (the thermal structure if there was no dynamical advection of heat) leading to a warmer dayside and

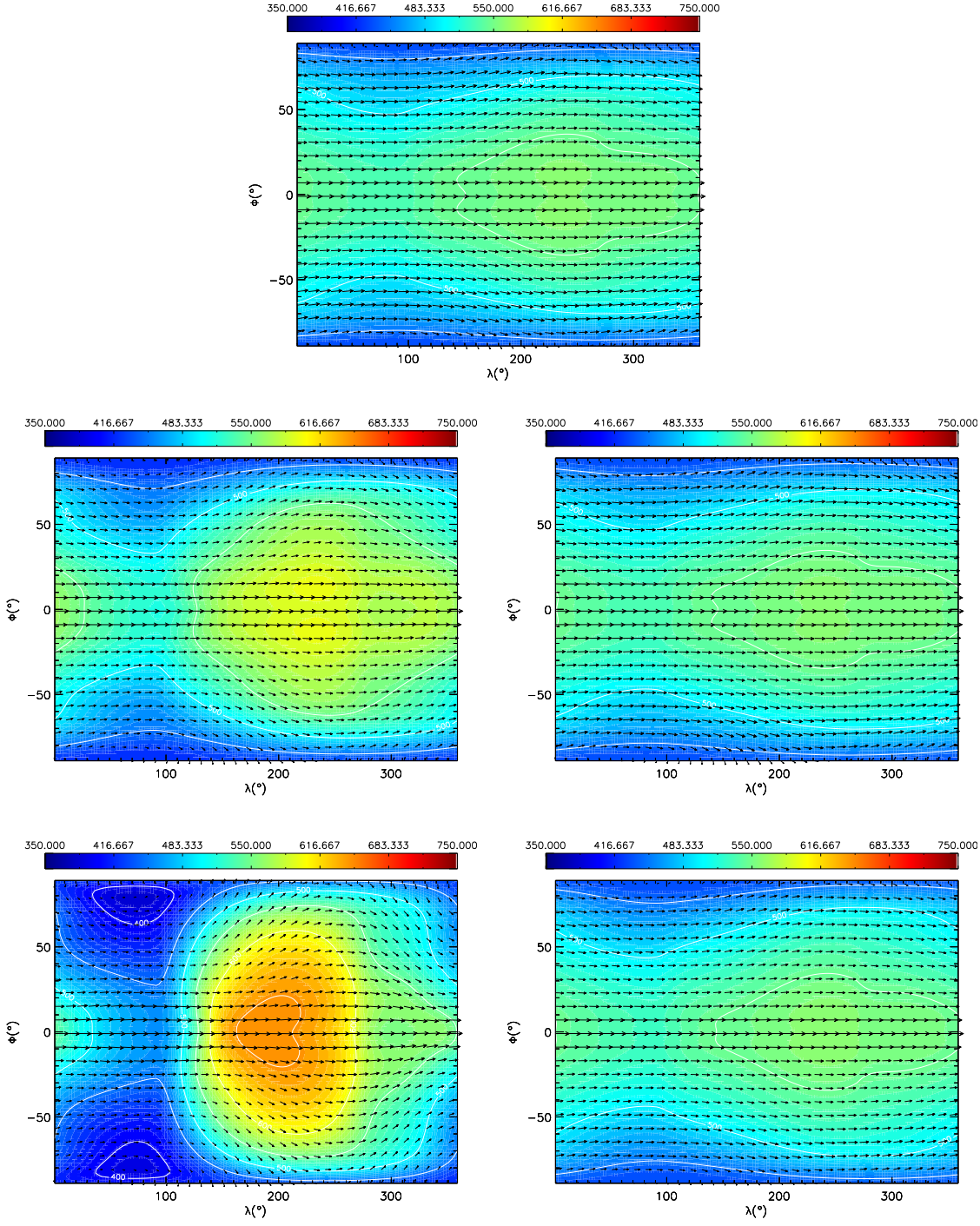

Figure 6.13: A figure showing the horizontal wind velocity (vector arrows) and temperature (colour map) at a pressure level of 100 Pa for the models R1 (*top*), R10 (*middle left*), D10 (*middle right*), R100 (*bottom left*) and D100 (*bottom right*) after 800 days.

cooler nightside and shifting the hot spot closer to the region of peak stellar irradiation, the sub-stellar point.

There is also some influence on the horizontal winds (also shown in Fig. 6.11) where the winds at high latitudes ($|\phi| > 40°$) transition from being predominantly in the zonal eastwards direction in the R1 model to having a significant meridional component (towards the poles on the dayside and towards the equator on the nightside) in the R100 model. The decay in the zonal component of the wind ($\bar{u}$) at high latitudes was already seen in Fig. 6.11.

Fig. 6.14 shows the same information but deeper in the atmosphere at a pressure level of 3000 Pa. Again there is a negligible difference between the R1, D10 and D100 models, highlighting the relative unimportance of the "dynamical effect" on the thermodynamical structure, across the range of μ and c_p simulated in this work.

However, as the metallicity is increased in the models R1, R10 and R100 we again see a significant increase in the horizontal temperature gradient. At this pressure level the main effect is to increase the meridional temperature gradient with a more subtle increase in the zonal temperature gradient. In each model the temperatures above $|\phi| = 50°$ are very similar but for lower latitudes towards the equator the temperature increases significantly by around 200 K as the metallicity is increased. In addition, we also see a weakening of the zonal component of the winds as the metallicity is increased; note the decreasing length of the wind vectors at high latitudes as the metallicity is increased.

Moving to higher pressures still, Fig. 6.15 shows the temperature and horizontal wind vectors at 1×10^5 Pa. Once again there is negligible difference between the R1, D10 and D100 models. Overall, the temperature is rather uniform at this pressure level, particularly for the R10 and R100 models, with the temperature increasing with increasing metallicity. Note that the wind vectors have shifted to a predominantly westward retrograde motion, particularly in the mid latitudes; this pressure level corresponds to the location of the deep and relatively slow westward winds seen in Fig. 6.11.

6.4.4 Vertical pressure-temperature profiles

In this section we examine vertical pressure-temperature profiles extracted from the 3D grid around the globe. Fig. 6.16 shows a series of pressure-temperature profiles around the equator ($\phi = 0°$) for a series of longitude points. Also shown in these figures are the 1D ATMO dayside average pressure-temperature profiles used to initialise the UM simulations.

For all simulations, and particularly for the R1, D10 and D100 models, the

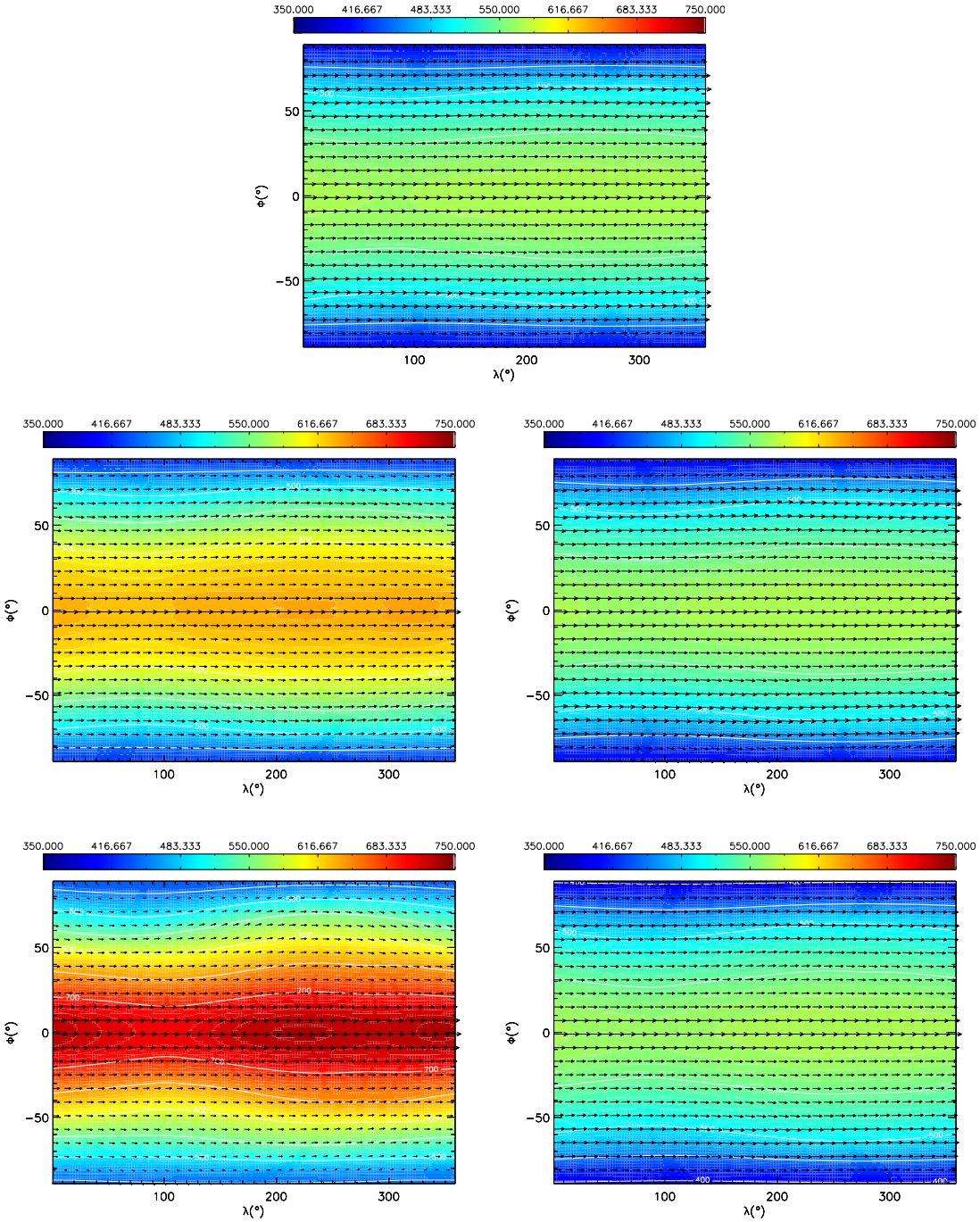

Figure 6.14: As Fig. 6.13 but at $P = 3000$ Pa.

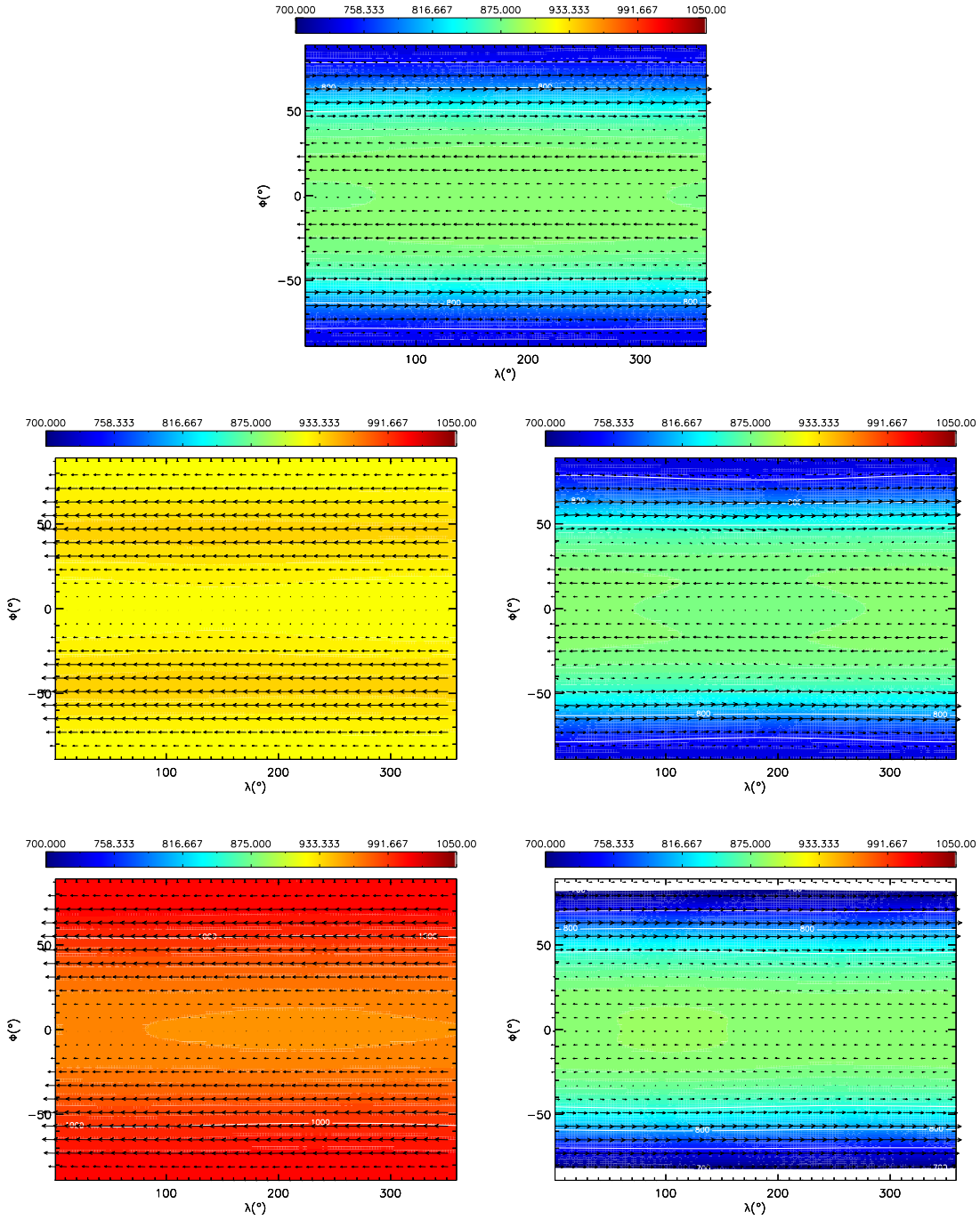

Figure 6.15: As Fig. 6.13 but at $P = 10^5$ Pa.

P–T profiles extracted from the 3D model do not significantly evolve from the intial profile for $P > 10^4$ Pa. For very high pressures ($P \gtrsim 10^6$) this is primarily because the model has not been integrated for long enough for the atmosphere to evolve at this depth where the radiative and dynamical timescales are very long. At lower pressures $P < 10^3$ Pa the P–T profiles extracted from the dayside (shown in red) are generally warmer than the initial profile whilst the nightside profiles (shown in blue) are generally cooler.

The zonal temperature gradient at the equator increases with increasing metallicity for the R1, R10 and R100 models with the largest temperature contrast being $\sim 300K$ for the R100 model, compared with < 200 K for the R1 model. There is negligible change in the P–T profiles as μ and c_p change with increasing metallicity in the D10 and D100 models.

Fig. 6.17 shows the same information but for a series of latitude points on the dayside ($\lambda = 180°$) and on the nightside ($\lambda = 0°$). Overall, we can see that for this model atmosphere across all metallicity cases, the meridional temperature gradient is generally larger than the zonal temperature gradient (compare Fig. 6.16 with Fig. 6.17). In addition, the P–T profiles essentially become zonally uniform for $P > 10^3$ Pa (Fig. 6.16) but significant meridional temperature gradients still exist at $P \sim 10^5$ Pa.

6.4.5 Emission and reflection spectra and phase curves

In this section we present the emission and reflection of the atmosphere. The top-of-atmosphere (TOA) emission/reflection as a function of wavelength and orbital phase, as seen by an observer, were produced directly from the UM using the same method as Boutle et al. [2017]. In essence, following the full integration of the UM simulations (here out to 800 days), we restart the model but using a much higher spectral resolution in the radiative transfer (500 bands instead of 32) and run over one complete orbit.

The TOA emission and reflection spectra for each model are shown in Fig. 6.18. In the shortwave region ($\lambda < 1$ μm) the planetary flux F_p is dominated by reflected stellar radiation. The planet-to-star flux ratio (F_p/F_s) varies significantly here between 10^{-8} and 10^{-5} for phase angles of 0° and 180°, respectively.

At longer wavelengths, the planetary flux F_p is dominated by thermal emission of the planetary atmosphere and the flux ratio increases with increasing wavelength. Overall, there is very little variation in the emission as a function of phase angle. This is due to the small zonal temperature gradients leading to a small change in the TOA emission as a function of longitude (and correspondingly in orbital phase angle). The model with the largest zonal temperature gradients (R100) shows only

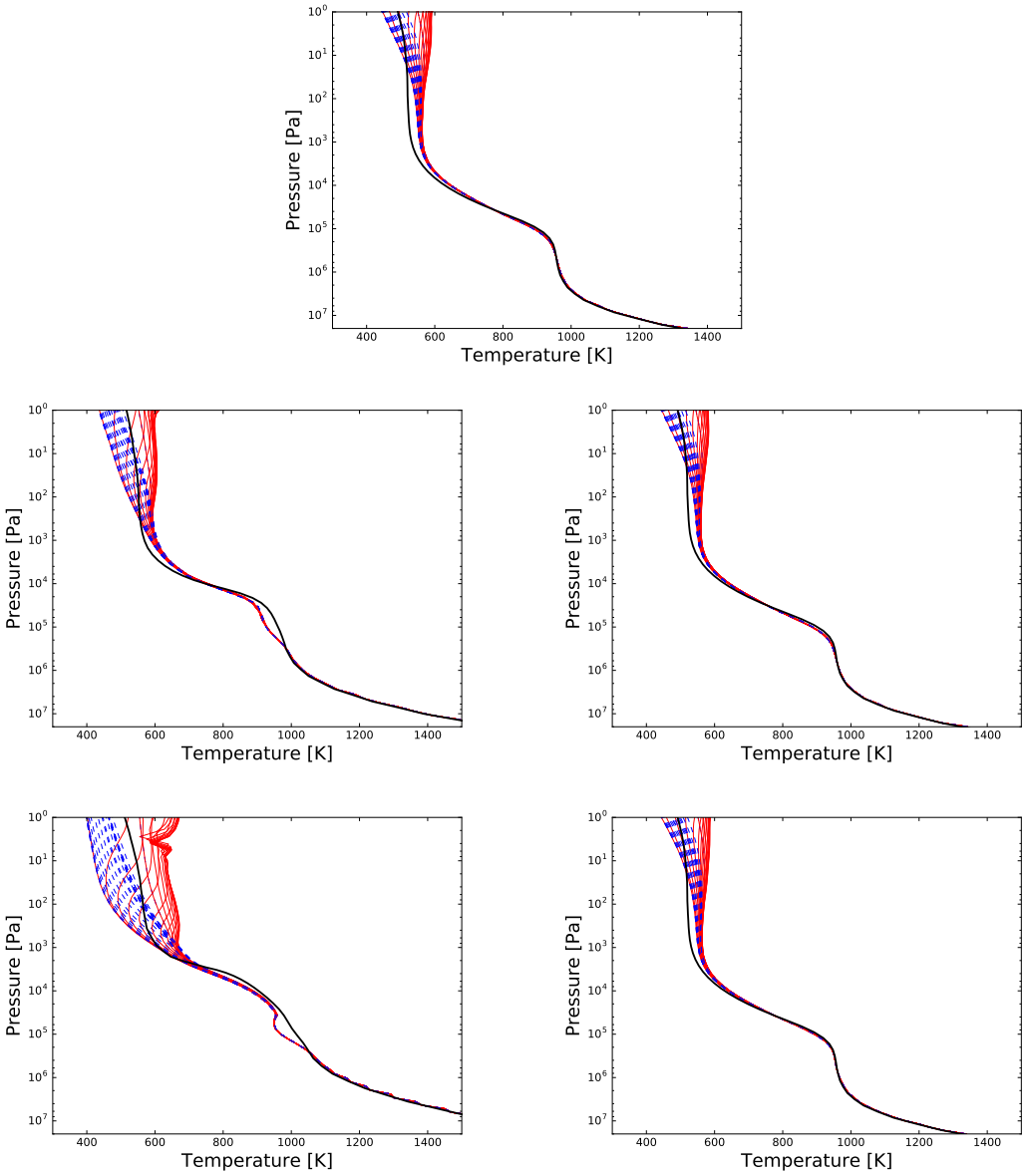

Figure 6.16: A figure showing P–T profiles extracted from the 3D simulation for the models R1 (*top*), R10 (*middle left*), D10 (*middle right*), R100 (*bottom left*) and D100 (*bottom right*) after 800 days. Here we show a series of P–T profiles for different longitude points around the equator ($\phi = 0°$). Profiles on the nightside are shown in blue dashed lines and profiles on the dayside are shown in red solid lines. The ATMO P–T profile used to initialise the UM simulation is shown in black.

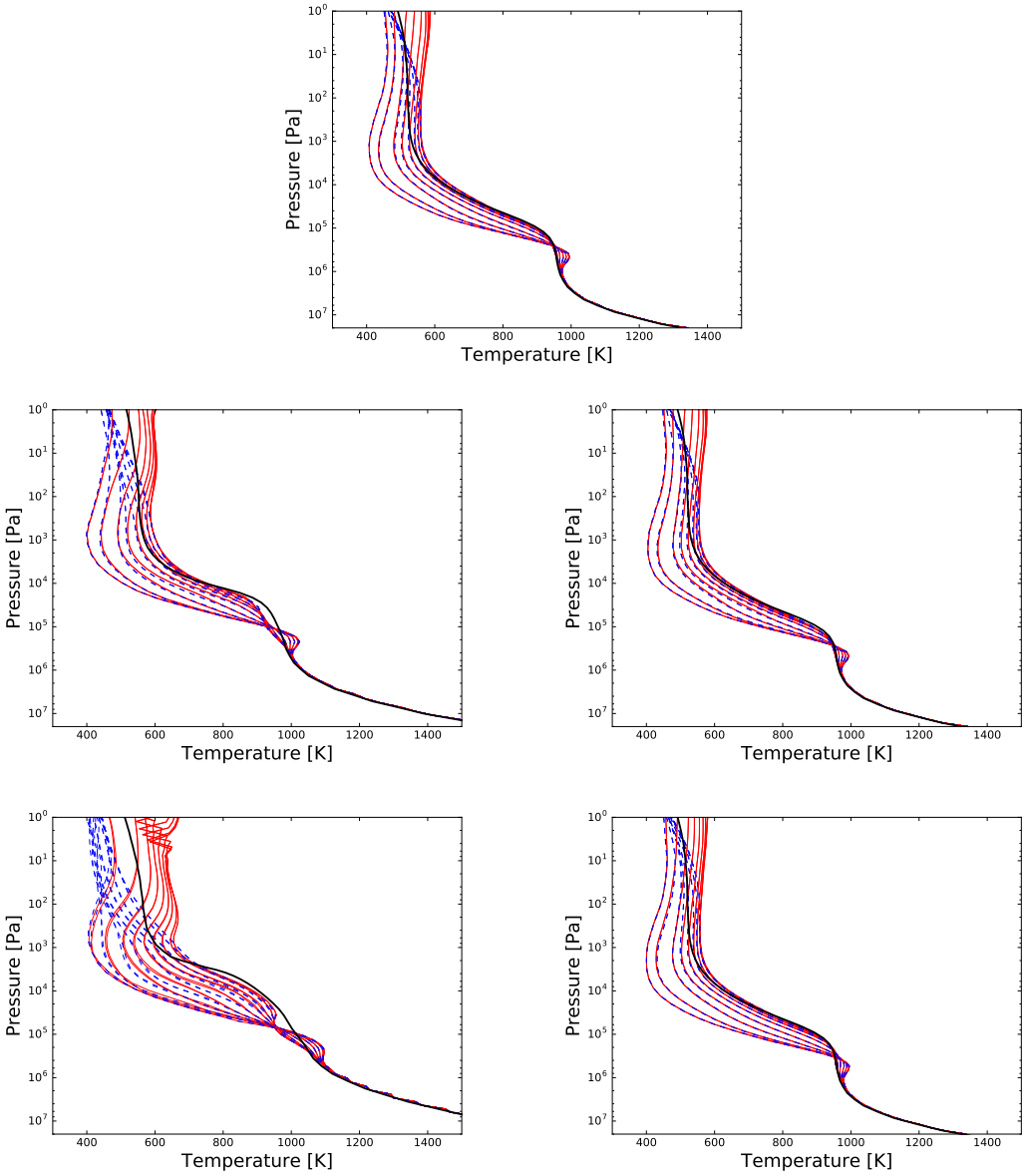

Figure 6.17: As Fig. 6.16 but for P–T profiles at a series of latitude points for $\lambda = 180°$ (red solid) on the dayside and $\lambda = 0°$ on the nightside (blue dashed).

a minor dependence on phase angle in the spectral regions 2.5-3.0 μm and 5-7 μm, with a larger flux corresponding to the phase angle where the warmer regions of the atmosphere are visible to the observer. These spectral regions correspond to water absorption features and the flux here originates from lower pressures than the spectral regions outside the water absorption features. Since the zonal temperature gradient increases with decreasing pressure, a larger variation in the spectrum with phase angle is expected here. Outside of the water absorption features, the flux originates from deeper in the atmosphere where the temperature is zonally quite uniform.

Fig. 6.19 shows the emission phase curve for each model in a series of wavelength bins. As indicated by the small variation in the emission spectra with phase angle, the phase curves are rather flat, due to the small zonal temperature gradients in these models. For the R100 model, the emission in the wavelength bands 2.50-2.94 μm and 5.56-7.14 μm does show some dependence on the phase angle (as seen earlier in the spectra, Fig. 6.18). For each case the peak in the emission is offset from the secondary eclipse (180°) by around 40°. Similar to previous work [e.g. Amundsen et al., 2016] this relates to an eastwards shift of the hot spot from the sub-stellar point, as seen in Fig. 6.13.

Overall, the emission/reflection spectra and emission phase curves show very little dependence on both the metallicity and on the orbital phase. Only for the highest metallicity model including "radiative effect" (R100) do we see some small variation in the flux ratio with phase angle, but that variation does not exceed a factor of 2.

6.5 Conclusions

In this chapter we have presented results from the first GCM simulations that couple the Met Office Unified Model to a highly flexible chemical equilibrium model that solves for the abundances by minimising the Gibbs energy of the system. In this first application we modelled the atmosphere of a super-Earth type exoplanet GJ 1214b and investigated the role of metallicity in shaping the dynamical and thermodynamical structure of the atmosphere, and subsequently examined the effect on the observable emission and reflection spectra and phase curves.

Overall we found that:

- increasing the metallicity, including the effect on the opacity, leads (generally) to a faster and deeper equatorial zonal jet, whilst the zonal winds at high latitudes decrease

- the effect of changing only the mean molecular weight and the 'dynamical'

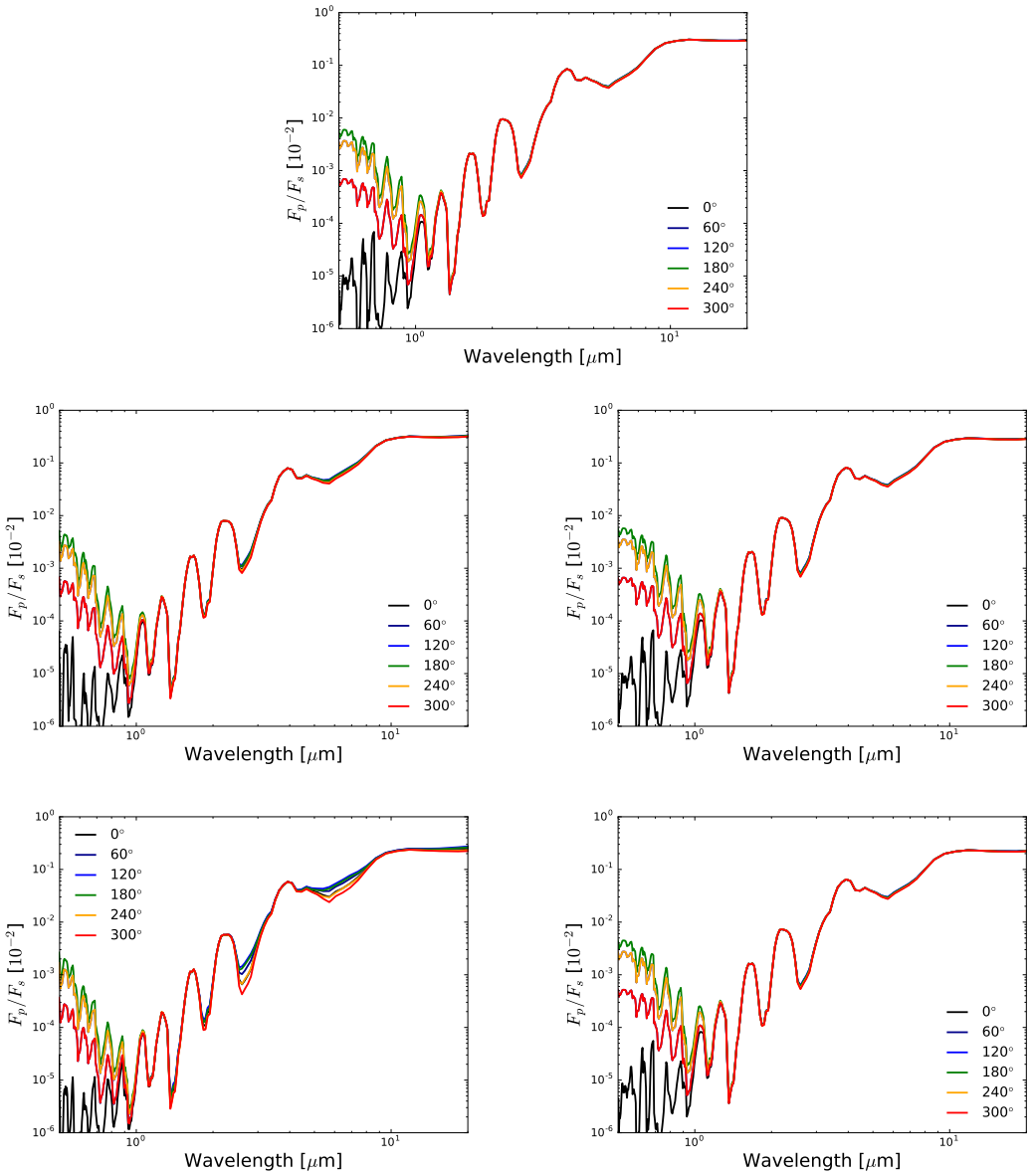

Figure 6.18: A figure showing the emission spectrum as seen at a variety of points throughout the orbit for the models R1 (*top*), R10 (*middle left*), D10 (*middle right*), R100 (*bottom left*) and D100 (*bottom right*) after 800 days. Generally the emission in the longwave region ($\lambda > 1$ μm) shows very little variation with the phase angle, indicative of the small day-night temperature contrast. At shorter wavelengths the spectrum varies significantly due to the varying amount of reflected light seen by the observer as the planet sweeps around the orbit.

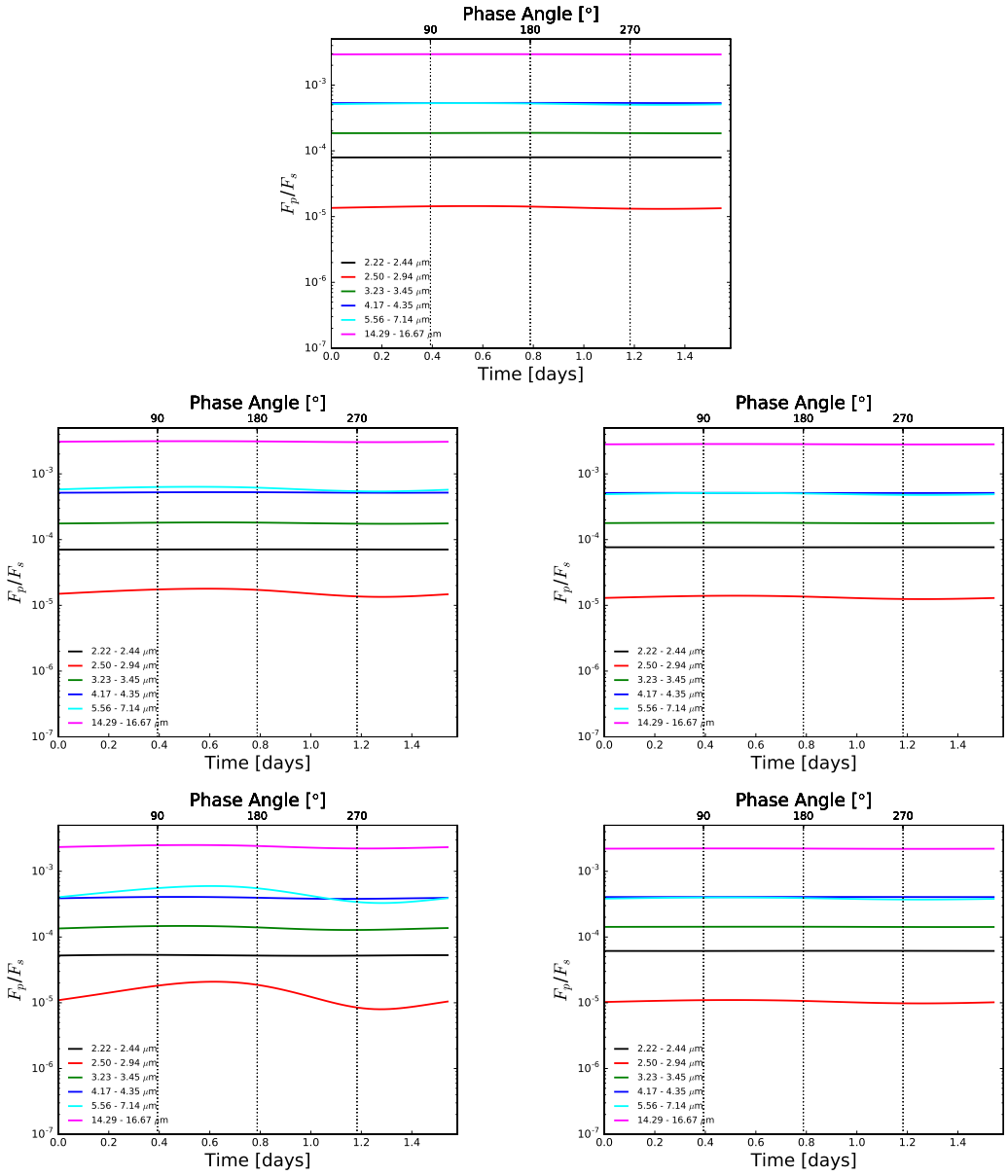

Figure 6.19: A figure showing the emission phase curves of the GJ 1214b model for a series of different wavelength bins for the models R1 (*top*), R10 (*middle left*), D10 (*middle right*), R100 (*bottom left*) and D100 (*bottom right*) after 800 days. Generally the emission in the longwave region ($\lambda > 1$ μm) shows very little variation with the phase angle, indicative of the small zonal temperature gradient.

heat capacity produces a similar trend but with a smaller overall effect

- the "radiative effect" of changing the bulk composition (opacities and radiative heat capacity) is far more important than the "dynamical effect" (mean molecular weight and dynamical heat capacity)
- the zonal temperature gradient increases as the metallicity increases, with the effect being strongest at lower pressures
- for hydrogen-dominated atmospheres with physical parameters similar to GJ 1214b the dominant horizontal temperature gradient is in the meridional direction across a wide range of pressures and over a range of metallicities
- the effect of increasing the metallicity from solar to 100× solar on the emission and reflection spectra and phase curves is not significant
- the phase curves for the models performed here are relatively flat, due to the small zonal temperature gradients
- the results here independently agree well with those of Zhang and Showman [2016], for the "dynamical effect", and with those of Lewis et al. [2010] and Kataria et al. [2014], for the "radiative effect". However they also highlight the much greater importance of the "radiative effect", compared with the "dynamical effect", which strongly controls the dynamical and thermodynamical structure.

We investigated the effect of varying the metallicity of the atmosphere between 1× and 100× solar. The choice of this parameter space was motivated by the need to retain a hydrogen-dominated atmosphere, due to current limitations of the model. As the metallicity is increased significantly further the assumption of a hydrogen-dominated atmosphere breaks down and CO_2 or H_2O become the dominant species [Moses et al., 2013a]. In this case, it is vital to include additional opacities such as collision-induced-absorption (CIA) due to species not currently included (CO_2, H_2O, etc) as well as scattering due to the relevant molecules. Line-broadening due to other species will also become important as the composition moves away from the hydrogen-dominated case [Hedges and Madhusudhan, 2016]. This presents a challenge in terms of both the availability of the data for the relevant pressures and temperatures [e.g. Fortney et al., 2016] as well as the increase in computationally expense of including additional opacities.

However, a natural next step to this project is to include the relevant additional opacity sources and extend the investigated parameter space (metallicity) beyond the hydrogen-dominated limit [e.g. Kataria et al., 2014], with a model that consistently includes these additional opacity sources.

Chapter 7

Conclusions and Perspectives

In this thesis we have improved the treatment of atmospheric chemistry in the 1D code ATMO and the exoplanet configuration of the 3D Met Office Unified Model (UM). Within the 1D models published in the literature a clear limitation has been an inconsistency between the chemical composition and the thermal structure of the atmosphere. The developments presented here address this issue and quantify the impact of bringing together these inherently linked processes.

For the 3D models, the representation of dynamics and, more recently, radiative transfer has been the focus of many of the recent developments, at the expense of chemistry. In this work a main focus has been to improve the treatment of chemistry in a 3D model to provide both more flexibility and better accuracy.

In this chapter we present our final conclusions before discussing future goals and prospects.

7.1 Conclusions

We have described in detail the approach taken to calculate both the chemical equilibrium and non-equilibrium abundances of chemical species in the 1D model ATMO. An important limitation of previous models applied to derive the non-equilibrium abundances in hot exoplanet atmospheres was an inconsistency in the treatment of the thermal structure and the chemical composition; the models used a fixed P–T profile that assumes chemical equilibrium. In this work we have coupled the radiative-convective equilibrium and chemical kinetics calculations to self-consistently calculate the non-equilibrium chemical abundances.

To quantify the effect of non-equilibrium chemistry on the P–T profile we performed simulations of two typical hot Jupiters and found shifts of up to 100 K, compared to the P–T profile assuming chemical equilibrium, when including vertical mixing. For the current model, the effect of photodissociations on the P–T profile were negligible. The evolution of the P–T profile also had a feedback

impact on the chemical abundances and we found that the quenched abundances of CH_4 and NH_3 varied significantly between the consistent and non-consistent models. In addition, performing these calculations self-consistently was found to have an important impact on the calculated emission from the model atmosphere. In the non-consistent models the emission flux was strongly affected by vertical mixing, through changes in the opacity due to quenching of species like CH_4 and NH_3. However, in the consistent model the emission flux was not significantly changed compared with the chemical equilibrium model. Ultimately, it was found that the non-consistent models do not conserve energy.

We also described the coupling of two chemistry schemes to the UM to increase both the flexibility and accuracy of the chemistry in the model, when applied to exoplanet atmospheres. The coupling of the Gibbs energy minimisation scheme allows for the calculation of the abundances of a large number of chemical species for a general elemental composition and for a large range of thermodynamic conditions.

In addition, we have described and presented early tests of a recently coupled chemical kinetics scheme that, together with existing capabilities in the UM, will allow for the effects of advection and chemical evolution to be accounted for. Ultimately, this will enable the model to be used to investigate the importance and effects of 3D non-equilibrium chemistry due to large scale advection. In this work we presented and discussed idealised tests using a simplified chemistry case to investigate the balance between the chemical and advection timescales. In cases where the chemical timescale is faster than the advection timescale the chemistry maintains chemical equilibrium. On the other hand, where the advection timescale is faster than the chemical timescale the chemistry becomes well mixed as advection dominates.

Using the coupled Gibbs energy minimisation scheme, we investigated the effect of changing the metallicity on the dynamical and thermodynamical structure of the atmosphere of a hot hydrogen-dominated exoplanet atmosphere. Several simulations, with planetary and stellar parameters of GJ 1214b, were performed with a range of metallicities. We found similar trends to previous studies: as the metallicity is increased the dynamical structure evolves from a state with large scale day-to-night flows to one that is dominated by an equatorial super-rotating jet. The dayside-nightside temperature constrast also increases with increasing metallicity. We found that the "radiative effect", the effect of changing the opacities, greatly outweighs the "dynamical effect", the effect of changing the mean molecular weight and heat capacity, as the metallicity is increased. The effect of changing the metallicity was found to have a small impact on the observables, such as the emission spectrum and phase curve.

Overall, the goals of this work have been to improve the accuracy, flexibility

and consistency of the treatment of chemistry in atmosphere models applied to hot exoplanets. Particularly in 3D models, the inclusion of chemistry has been limited due to its high computational expense. However, to tackle many of the existing questions in the field will require inclusion of chemical processes; such as understanding the role of horizontal non-equilibrium chemistry, cloud and haze formation and understanding the effect of varying elemental abundances.

7.2 Future work

The future prospects of the work presented here include new applications of existing developments as well as expanding the capabilities further.

The first application of the consistent non-equilibrium 1D model to the atmosphere of hot Jupiters only examined a small section of the known parameter space that exoplanets inhabit. Further studies would be required to test the behaviour of the system over different metallicities or elemental abundances and for atmospheres cooler than those of hot Jupiters. This work could be performed with current model.

In addition, it is important to consider that the current model may not be complete with respect to the chemical species included in the chemistry scheme or the species that are included as opacity sources. In the present work we found negligible effects due to photochemical processes on the thermal profile. However, a limitation of the model is the lack of inclusion of any photochemically produced species as sources of opacity. Therefore, the only effect of photochemistry is through reductions in the abundances of molecules that are dissociated, such as H_2O and CH_4. For example, consider a consistent photochemical model of the Earth atmosphere that did not include opacity due to photochemically produced ozone. It would be interesting to consider the various photochemical products that are formed in hot Jupiter atmospheres and to assess whether any may contribute significant opacity to the atmosphere that may be important in determining the P–T profile. Following identification of potentially significant species, further studies could be performed to quantify the effect of these photochemical products on the thermal profile and observables.

Currently, ATMO is suitable for modelling the atmospheres of gas giant objects; Brown Dwarfs, hot Jupiters, etc. Through the inclusion of a solid surface the model can relatively easily be extended to terrestrial planets. Important physical processes such as reflection and emission of radiation would be requirements. In addition, more complex surface-atmosphere exchange processes (of, e.g., moisture) could also be included to represent surface evaporation etc. The inclusion of the relevant opacity data and chemical networks that are more suitable for terrestrial planets (i.e. not hydrogen-dominated) would also be required. This additional ca-

pability will be vital in the future as the focus broadens to include terrestrial planets as well the gas giants.

The coupling of the chemical kinetics scheme to the UM was also described in this work, alongside idealised experiments using a simplified chemistry case. Clearly, these tests need to be reproduced using a more complete chemical network. Following this, the first applications will be to assess the importance of 3D non-equilibrium chemistry due to large scale advection. A first step would be to quantify the balance of the advection and chemical timescales using a full chemical network and to assess the degree of non-equilibrium chemistry expected in hot Jupiter atmospheres. Secondly, it will be important to make the radiative transfer and chemistry consistent. This can be achieved by calculating the opacity from the advected chemical tracers to include the effect of non-equilibrium chemistry on the heating rates and thermal evolution of the atmospheres. Finally, such models will be able to assess the significance of the effects of non-equilibrium chemistry on the emission phase curve of hot Jupiters.

An additional future development would be to include photochemical processes in the 3D model. This would require calculation of the photon flux in each cell of the 3D grid, using either existing radiative transfer schemes in the UM or using a more simple approach.

In conclusion, the developments presented in this thesis provide a model framework with which many of the current questions in the field can be tackled; such as the presence of clouds and haze, that first requires accurate description of the gas-phase composition, and the nightside emission flux problem of many hot Jupiters. The complimentary use of 1D and 3D models allows for the detailed investigation of physical processes as well as their effect in a more complex 3D system, respectively. The current focus has been on understanding the atmospheres of hot, highly irradiated exoplanets. However, the UM is, of course, designed to simulate the Earth atmosphere and clearly is well suited to modelling these atmosphere types.

Appendix A

Method of Lagrange Multipliers

The method of Lagrange multipliers is a mathematical method of minimising a function subject to some constraint.

Let us take the problem of minimising the function $f(x, y)$. Without any constraint we would minimise the function $f(x, y)$ by setting the derivitive to zero $\nabla f(x, y)$=0. However, if we wish to minimise the function $f(x, y)$ subject to some constraint, $g(x, y)$=0, we can introduce a new variable, the Lagrange multiplier λ, and define a new function, the Lagrange function L.

We are interested in finding the values of x and y for which $f(x, y)$ is minimised and $g(x, y) = 0$ is satisfied. We are looking for points along the contour of $g(x, y) = 0$ where f is stationary. This could be because f and g are parallel, or because f has reached an extremum at some point along the contour of $g(x, y) = 0$.

In the first instance, this means that the gradients of $f(x, y)$ and $g(x, y)$ are parallel,

$$\nabla_{x,y} f = -\lambda \nabla_{x,y} g,$$

where the Lagrange multiplier λ has been introduced, since though the direction of the gradients are equal, they are not necessarily equal in magnitude. In the second instance, where $\nabla_{x,y} f = 0$, we can set $\lambda = 0$ by choice, independent of g.

We can therefore define the Lagrange function as,

$$L(x, y, \lambda) = f(x, y) + \lambda \cdot g(x, y). \tag{A.1}$$

Now to find the minimum of $f(x, y)$ ($\nabla_{x,y} f$=0) subject to the constraint of $g(x, y)$=0, we minimise the Lagrange function

$$\nabla_{x,y,\lambda} L = 0. \tag{A.2}$$

Appendix B

Thermodynamical Data: The NASA Polynomial Coefficients

The thermodynamic properties of chemical species can convieniently be calculated for a given temperature using the NASA polynomical coefficients [McBride et al., 1993, 2002]. This library contains data on over 2000 species (gas, liquid and solid), spanning a large temperature range. The data allow the calculation of the standard heat capacity at constant pressure C_p^0, the standard enthalpy H^0, the standard entropy S^0 and the standard chemical potential μ^0.

B.1 Fourth-order polynomials

The original database [McBride et al., 1993] utilised fourth-order polynomials to represent the heat capacity, with integration constants for the calculation of the enthalpy and the entropy; leading to seven terms in total. Most of the data included in ATMO use this 7-coefficient data. The dimensionless standard heat capacity, enthalpy and entropy are calculated at any temperature using the following formulae:

$$\frac{C_p^0(T)}{R} = a_1 + a_2 T + a_3 T^2 + a_4 T^3 + a_5 T^4 \tag{B.1}$$

$$\frac{H^0(T)}{RT} = a_1 + \frac{a_2 T}{2} + \frac{a_3 T^2}{3} + \frac{a_4 T^3}{4} + \frac{a_5 T^4}{5} + \frac{b_1}{T} \tag{B.2}$$

$$\frac{S^0(T)}{R} = a_1 \ln T + a_2 T + \frac{a_3 T^2}{2} + \frac{a_4 T^3}{3} + \frac{a_5 T^4}{4} + b_2 \tag{B.3}$$

where a_i are the coefficients of the fourth-order polynomial and b_1 and b_2 are integration constants, and T is the temperature in Kelvin. The chemical potential, which is related to the enthalpy and the entropy via,

$$\frac{\mu^0(T)}{RT} = \frac{H^0(T)}{RT} - \frac{S^0(T)}{R}$$

can also be expressed directly in terms of the NASA coefficients:

$$\frac{\mu^0(T)}{RT} = a_1\left(1-\ln T\right) - \frac{a_2 T}{2} - \frac{a_3 T^2}{6} - \frac{a_4 T^3}{12} - \frac{a_5 T^4}{20} + \frac{b_1}{T} - b_2. \tag{B.4}$$

B.2 Sixth-order polynomials

An update to the database [McBride et al., 2002] saw the inclusion of additional species, as well as an extension of the data to a sixth-order polynomial format, to increase the accuracy over wider temperature ranges. With the two integration constants, this brings the new format up to nine-coefficients for each molecule.

The updated equations for the calculation of the dimensionless standard heat capacity, enthalpy, entropy and chemical potential are:

$$\frac{C_p^0(T)}{R} = a_1 T^{-2} + a_2 T^{-1} + a_3 + a_4 T + a_5 T^2 + a_6 T^3 + a_7 T^4 \tag{B.5}$$

$$\frac{H^0(T)}{RT} = -a_1 T^{-2} + a_2 \frac{\ln T}{T} + a_3 + \frac{a_4 T}{2} + \frac{a_5 T^2}{3} + \frac{a_6 T^3}{4} + \frac{a_7 T^4}{5} + \frac{b_1}{T} \tag{B.6}$$

$$\frac{S^0(T)}{R} = -a_1 T^{-2} - a_2 T^{-1} + a_3 \ln T + a_4 T + \frac{a_5 T^2}{2} + \frac{a_6 T^3}{3} + \frac{a_7 T^4}{4} + b_2 \tag{B.7}$$

$$\frac{\mu^0(T)}{RT} = -\frac{a_1 T^{-2}}{2} + \frac{a_2}{T}(1+\ln T) + a_3\left(1-\ln T\right) - \frac{a_4 T}{2} - \frac{a_5 T^2}{6} - \frac{a_6 T^3}{12} - \frac{a_7 T^4}{20} + \frac{b_1}{T} - b_2. \tag{B.8}$$

Appendix C

Thermodynamical Quantities

C.1 Enthalpy of formation

The standard enthalpy of formation, H_f^0, is the change in enthalpy when forming a chemical species from its constituent elements at the *standard state*. The standard state is defined as a pressure of 1 atm and with all of the species in their most stable form; e.g. oxygen in gas phase molecular form (O_2), and carbon in graphite.

The general formula for H_f^0 of a hypothetical molecule X is:

$$H_f^0(T)[\mathrm{X}] = H^0(T)[\mathrm{X}] - \sum_i^I H_i^0(T), \tag{C.1}$$

where $H^0(T)[\mathrm{X}]$ is the enthalpy of the molecule X at temperature T, and the sum is over the enthalpies of the consistuent elements of X, in their standard states. For example, the standard enthalpy of formation of CO is:

$$H_f^0(T)[\mathrm{CO}] = H^0(T)[\mathrm{CO}] - H^0(T)[\mathrm{C(gr)}] - \frac{1}{2}H^0(T)[\mathrm{O_2(g)}]. \tag{C.2}$$

C.2 Enthalpy of reaction

The change in enthalpy, ΔH, of any thermodynamic system is defined by

$$\Delta H = H_{\mathrm{final}} - H_{\mathrm{initial}} \tag{C.3}$$

where H_{final} and H_{initial} are the final and initial enthalpies of the system respectively.

For a chemical reaction, Hess's Law states that the enthalpy change of a reaction is only dependent on the initial and final states, and is independent of any intermediate steps or reactions. The enthalpy change of reaction is given by the

difference of the sum of the enthalpies of formation of the products to the reactants:

$$\Delta H_r^0 = \sum H_{f,\text{products}}^0 - \sum H_{f,\text{reactants}}^0. \tag{C.4}$$

A reaction with a positive enthalpy of reaction requires an input of energy to proceed, whereas if the enthalpy of reaction is negative the reaction proceeds spontaneously, releasing energy to the surroundings.

C.3 The heat capacity

The heat capacity of substance at constant pressure is defined as

$$C_P = \left(\frac{\partial H}{\partial T}\right)_P = \left(\frac{\partial Q}{\partial T}\right)_P. \tag{C.5}$$

Here we will denote the *specific* heat capacity, c_P, as the heat capacity per unit mass [J kg^{-1} K^{-1}] and the *molar* heat capacity, C_P, as the heat capacity per mole [J mol^{-1} K^{-1}]. The specific and molar heat capacities are *intensive* properties of the substance. By contrast, the *extensive* form of heat capacity C, measured in [J K^{-1}], is related to the *intensive* forms via

$$\begin{aligned} c_P &= \left(\frac{\partial C}{\partial m}\right)_P \\ C_P &= \left(\frac{\partial C}{\partial n}\right)_P \end{aligned} \tag{C.6}$$

where m is the mass of the substance, and n is the total number of moles.

C.3.1 The heat capacity of a mixture

The total enthalpy of a mixture is given by, using the notation of Gordon and McBride [1994],

$$h = \sum_j n_j H_j^0 \tag{C.7}$$

where h is the total *specific* enthalpy of the system in J kg^{-1}, n_j is the number of moles per kilogram of species j in mol kg^{-1} and H_j^0 is the *molar* enthalpy of the species j in J mol^{-1}.

Now, using the definition of the heat capacity (C.5) we find the total *specific* heat capacity of the mixture

$$c_P = \left(\frac{\partial h}{\partial T}\right)_P$$

$$c_P = \sum_j n_j \left(\frac{\partial H_j^0}{\partial T}\right)_P + \sum_j H_j^0 \left(\frac{\partial n_j}{\partial T}\right)_P$$
$$c_P = \sum_j n_j C_P^0 + \sum_j H_j^0 \left(\frac{\partial n_j}{\partial T}\right)_P \tag{C.8}$$

where C_P^0 is the *molar* standard heat capacity of the species j. It is clear that the total heat capacity of the mixture is a combination of two parts. The first term on the right in the final equation of (C.8) represents the sum of the molar heat capacities of the individual species (multiplied by the number of moles per kilogram, in this case). This component is referred to as the "frozen" heat capacity by Gordon and McBride [1994]. The second term, called the "reaction" heat capacity, contains a derivitive of the number of moles (per unit mass) with temperature. This term becomes important when the abundance of a species varies rapidly with the temperature, for instance at a pressure-temperature region where the chemistry transitions from a CO-dominated to a CH_4-dominated atmosphere, or in the region of a condensation curve.

Equation C.8 yields the specific heat capacity, the heat capacity per unit mass. The molar heat capacity can be easily obtained by multiplying by the mean molecular weight of the substance

$$C_P = \mu c_P \tag{C.9}$$

where μ is in kg mol^{-1}.

C.4 Derivation of chemical equilibrium

The defintion of chemical equilibrium as the minimum of the Gibbs energy can be derived from first principles from the first and second laws of thermodynamics.

Starting with the defintion of the Gibbs energy,

$$G = H - TS, \tag{C.10}$$

and the defintion of enthalpy,

$$H = U + PV, \tag{C.11}$$

we can write G in terms of U, P, V, T and S,

$$G = U + PV - TS. \tag{C.12}$$

Writing this in incremental form gives

$$dG = dU + PdV + VdP - TdS - SdT. \tag{C.13}$$

Using the first law of thermodynamics,

$$\delta Q = dU + PdV, \tag{C.14}$$

we can substitue for dU in Eq. (C.13) to give

$$dG = \delta Q + VdP - TdS - SdT. \tag{C.15}$$

Now we use the second law of thermodynamics,

$$dS > \frac{\delta Q}{T}, \tag{C.16}$$

and replacing for δQ in Eq. (C.15) then canceling the relevant terms and rearranging we find

$$dG < VdP - SdT. \tag{C.17}$$

If we now consider a system at constant temperature ($dT = 0$) and constant pressure ($dP = 0$) we can see that

$$dG < 0. \tag{C.18}$$

Physically this means that any isothermal and isobaric process reduces the Gibbs energy of the system and therefore, intuitively, an equilibrium state will be reached when G has reached a minimum value.

C.5 Relating the equilibrium constant with the Gibbs energy of reaction

In this section we describe the relationship between the equilibrium constant K_{eq} and the Gibbs energy of reaction $\Delta_r G$. We begin by considering the chemical equilibrium state where, as shown in Appendix C.4, we have

$$dG = 0.$$

For an example bimolecular reaction A+B↔C+D we can write the Gibbs energy of reaction as the difference between the partial Gibbs energies (or chemical

potentials) of the products and reactants

$$dG = \mu_{\mathrm{C}} + \mu_{\mathrm{D}} - \mu_{\mathrm{A}} - \mu_{\mathrm{B}} = 0. \tag{C.19}$$

For a gas, the chemical potential can be written in terms of the standard chemical potential and the partial pressure of the species

$$\mu_j = \mu_j^0 + RT \ln P_j. \tag{C.20}$$

Substituting Eq. (C.20) into Eq. (C.19) and rearranging gives

$$\begin{aligned} dG = \mu_{\mathrm{C}}^0 + \mu_{\mathrm{D}}^0 - \mu_{\mathrm{A}}^0 - \mu_{\mathrm{B}}^0 + RT \ln \frac{P_{\mathrm{C}} P_{\mathrm{D}}}{P_{\mathrm{A}} P_{\mathrm{B}}} = 0 \\ dG = \Delta_r G + RT \ln \frac{P_{\mathrm{C}} P_{\mathrm{D}}}{P_{\mathrm{A}} P_{\mathrm{B}}} = 0, \end{aligned} \tag{C.21}$$

where we have defined the Gibbs energy of reaction $\Delta_r G$ as the difference between the standard chemical potentials of the products and reactants. Using the definition of the equilibrium constant (see Section 2.4.3) and rearranging we finally obtain

$$K_{\mathrm{eq}} = \frac{P_{\mathrm{C}} P_{\mathrm{D}}}{P_{\mathrm{A}} P_{\mathrm{B}}} = \exp\left[-\frac{\Delta_r G}{RT}\right], \tag{C.22}$$

thus relating Gibbs energy of reaction with the kinetic equilibrium constant.

Appendix D

Numerical Solution of Ordinary Differential Equations

Numerical integration is required to solve ordinary (i.e. not partial) differential equations. There are many methods, with varying accuracies, stabilities and computational costs.

D.1 The Euler Method

The Euler method is the most simple of all numerical integration methods. For an example ordinary differential equation (ODE)

$$\frac{dy}{dt} = f(y,t), \tag{D.1}$$

where f is some known function dependent on y and t, with an initial condition such as $y(t = t_0) = y_0$, the solution can be advanced using

$$y_1 = y_0 + hf(y_0, t_0), \tag{D.2}$$

where h is some step size. More generally, we write:

$$y_n = y_{n-1} + hf(y_{n-1}, t_{n-1}). \tag{D.3}$$

Often, the task is to solve $f(y,t)$ for some steady-state solution (i.e. in relation to the work of this thesis, for the chemical steady state) where variation of y with t approaches zero; i.e.

$$\frac{dy}{dt} = f(y,t) < \epsilon, \tag{D.4}$$

where ϵ is some defined accuracy of the solution.

Since the iterations of the Euler method only depend on the *current* evaluation

of $f(y_{n-1}, t_{n-1})$, it is an *explicit* method. This often leads to stability problems, unless a very small step size h is employed, and the Euler method is therefore not useful in most applications.

D.2 The Backward Euler Method

One way of improving on the Euler method is to modify it to become an *implicit* method. In other words, instead of deriving the new evaluation y_n using the current state, as in (D.3), we use the value at the next iteration

$$y_n = y_{n-1} + hf(y_n, t_n). \tag{D.5}$$

The implicit Backward Euler method is found to be far more stable than the (forward) Euler method. As a consequence, typically a larger step size h can be employed in the Backward Euler method. However, since the unknown y_n now appears on both sides of equation D.5, an additional calculation must be performed on each step. Usually, an iterative Newton-Raphson method is used to evaluate y_n.

Therefore, whilst the Backward Euler method offers much greater stability and a larger step size than the Euler method, it is much more computationally demanding due to the need for an iterative procedure to determine y_n.

D.3 Linear Multistep Methods

Linear Multistep Methods (LMMs) solve for the current value y_n using the following general formula [Radhakrishnan and Hindmarsh, 1993]:

$$y_n = \sum_{j=1}^{K_1} \alpha_j y_{n-j} + h \sum_{j=0}^{K_2} \beta_j f(y_{n-j}, t_{n-j}) \tag{D.6}$$

where the coefficients α_j, β_j, K_1 and K_2 are dependent on the particular method employed. For example, $\alpha_j = \beta_j = K_1 = 1$ and $K_2 = 0$ returns the backward Euler method. In the LMM, the solution of multiple previous steps $(y_{n-j}, j = 1, 2, ...)$ are used to determine the next value y_n.

D.3.1 Backwards Differentiation Formulae

The method of Backward Differentiation Formulae (BDF) is widely used for the solution of stiff problems and is an example of a LMM. This is the method employed by the LSODE library for the solution of stiff problems. The BDF equation is determined from the general LMM formula above by setting $K_2 = 0$ and $K_1 = q$,

where q is the order of the method, yielding

$$y_n = \sum_{j=1}^{q} \alpha_j y_{n-j} + h\beta f(y_n, t_n). \tag{D.7}$$

The order q determines the number of previous iterations which are used to determine the next iteration. Generally, the order for the BDF method is limited to $q \leq 6$ due to stability issues [Gear, 1971]; however, within the LSODE library this is actually limited to $q \leq 5$ [Radhakrishnan and Hindmarsh, 1993]. The coefficients α_j and β are given by Gear [1971] depending on the order q selected.

Appendix E

Implementation of the ATMO chemistry schemes in the UM

In this appendix we decribe the coupling of the Gibbs energy minimisation scheme and chemical kinetics scheme, originally developed in ATMO, to the UM.

E.1 Coupling the Gibbs energy minimisation scheme

E.1.1 Code structure

All model developments involved in coupling the Gibbs energy minimisation scheme were performed in a branch from the trunk of the UM source code at version 10.6. The developments are currently in a branch called `vn10.6_add_idealised_gibbs_minimisation` and the branch will be submitted for inclusion in the trunk of the UM source code in the near future. All subroutines required for calculation of the equilibrium abundances are included in a new fortran module `idealised_chemistry_mod.F90`. Lines of code were then added to the existing UM subroutine `rad_ctl` (the main radiative transfer routine) to call the various subroutines in the new Fortran module.

During a UM simulation, an initialisation subroutine is called `initialise_gibbs` on the first call to `rad_ctl` which allocates several Fortran arrays and handles input of the required data: list of molecules and thermochemical data. Following this, the subroutine `gibbs_min_main` is called with 3D arrays of the pressure and temperature as arguments.

Within the subroutine `gibbs_min_main`, the code loops over the 3D grid and calls the subroutine `gibbs_minimisation_solver` for each vertical column passing the 1D arrays of temperature and pressure and returning an array of the chemical abundances along the vertical profile. During this iteration the abundances are stored in a 4D array (three spatial dimensions and another for the number of chem-

ical species) for later use by the existing UM subroutines to calculate the opacity.

E.1.2 Input and output

The inputs required by the Gibbs energy minimisation scheme are the temperature, pressure, elemental abundances, a list of the chemical species to include in the calculation and thermochemical data to compute the Gibbs energy. The temperature and pressure are calculated by the main UM model. The elemental abundances are hard-coded within the Fortran module however they can be scaled using variables that determine the metallicity (`mdh`) and the carbon to oxygen ratio (`coratio`).

The list of chemical species to include are provided as an input file in netCDF format. The thermochemical data (NASA polynomial coefficients) are also provided in an input text file. Both of these files are read in on the first main UM timestep in the subroutine `initialise_gibbs`.

A series of namelist variables have been added to control the coupled Gibbs energy minimisation scheme and these are described in Table E.1.

The output of the scheme is the mole fraction of each chemical species and the specific heat capacity of the mixture. If the Gibbs energy minimisation scheme is used (`l_gibbs_abundances = .True.`) then the mole fractions of the relevant species are provided to the radiation modules in the existing subroutine `r2_set_gas_mix_ratio`. Specifically, the radiation scheme requires the mass fractions and so we obtain this from the mole fraction using Eq. (2.1).

If the option to use the specific heat capacity calculated by the Gibbs energy minimisation scheme is selected (`l_cp_chem = .True.`) then the value is copied to the existing radiation modules in `set_thermodynamic_mod`. If the latter is not true then the global value of the heat capacity is used that is set in the main UM namelist.

E.2 Coupling the chemical kinetics scheme

E.2.1 Code structure

All developments for the coupling of the chemical kinetics were performed in a branch from the UM source code `vn10.6_add_idealised_chemical_kinetics`. These developments will ultimately be submitted for inclusion in the main trunk of the code. Note that the kinetics scheme also depends on various subroutines included in the Gibbs energy minimisation coupling developments (`vn10.6_add_gibbs_minimisation`) and so both development branches are required.

A new module (`idealised_chemical_kinetics.F90`) was added to the UM source code that contains subroutines required for the chemical kinetics scheme. An

Table E.1: A table showing the namelist variables associated with the coupled Gibbs energy minimisation scheme.

Variable	Description	Type
`l_gibbs_abundances`	Turn on/off Gibbs energy minimisation	Logical
`l_cp_chem`	Use heat capacity from chemistry to compute heating rate	Logical
`l_mdh_ramp`	Include ramp in metallicity from Solar to `mdh`	Logical
`mdh`	Metallicity factor	Real
`coratio`	Carbon to oxygen ratio	Real
`mod_gibbs`	Frequency (in number of timesteps) to calculate abundances	Integer
`fmolname`	Filename of the molecule list netCDF file	Character
`fnasapol`	Filename of the NASA polynomial coefficients	Character

additional module (`idealised_chemistry_tracers.F90`) was added that contains a subroutine that passes the chemical abundances to and from the free tracer arrays.

Similar to the Gibbs energy minimisation coupling, the code to call the new subroutines was added to the main radiative transfer subroutine `rad_ctl`. On the first timestep of the main UM model a subroutine `initialise_kinetics` is called that reads in the necessary input data (reaction lists, coefficients to compute rate constants, ...) and allocates arrays. Also on the first timestep, we call both the Gibbs energy minimisation initialisation (`initialise_gibbs`) and main subroutines (`gibbs_min_main`) to calculate the chemical equilibrium abundances in each grid cell. These are used as the initial condition for the advected chemical species and the equilibrium abundances are passed to the free tracer arrays by the subroutine `set_idealised_tracers`.

As the main UM model is integrated the advection of the free tracers is handled by the existing UM code. Periodically we call the chemical kinetics solver to integrate the continuity equation for the chemical abundances in the free tracer arrays. On a set frequency of timesteps we call again the subroutine `set_idealised_tracers` and now call the main kinetics subroutine `get_kinetics` passing the 3D temperature, pressure and current chemical abundance arrays as arguments. Within this subroutine we loop over the 3D grid and call the chemical kinetics solver subroutine for each individual vertical column and solve the continuity equation until the set maximum time (the chemical timestep). Once these kinetics calculations are complete we copy the updated abundances to the free tracer arrays and continue with the main UM model integration. The process is repeated each chemical timestep.

Table E.2: A table showing the namelist variables associated with the coupled chemical kinetics scheme.

Variable	Description	Type
`l_init_kinetics`	Initialise the kinetics scheme	Logical
`l_run_kinetics`	Run the kinetics calculation every `mod_kinetics` timesteps	Logical
`tmax_kinetics`	The maximum integration time for the kinetics solver	Real
`mod_kinetics`	Frequency (in number of timesteps) to calculate kinetics	Integer
`dir_neq`	Directory path for the chemical network text files	Character

E.2.2 Input and output

The input required by the chemical kinetics solver are the pressure, temperature, the current chemical abundances and the chemical reaction list and associated data to calculate the rate constants.

The pressure and temperature are calculated by the main UM model and are communicated to the chemical kinetics module. The current chemical abundances taken from the main UM free tracer arrays, which were initialised in the first model timestep to the chemical equilibrium values in the first model timestep. The reaction lists and associated parameters are provided as text files that are read in on the first model timestep in the subroutine `initialise_kinetics`.

A number of variables have been added to the UM namelist that control the operation of the coupled chemical kinetics scheme and are described in Table E.2.

The output is the chemical abundance of each species that has been integrated (using the continuity equation) for the prescribed chemical timestep and these are copied back to the free tracer arrays.

Bibliography

M. Agúndez, O. Venot, N. Iro, F. Selsis, F. Hersant, E. Hébrard, and M. Dobrijevic. The impact of atmospheric circulation on the chemistry of the hot Jupiter HD 209458b. A&A, 548:A73, December 2012. doi: 10.1051/0004-6361/201220365.

M. Agúndez, V. Parmentier, O. Venot, F. Hersant, and F. Selsis. Pseudo 2D chemical model of hot-Jupiter atmospheres: application to HD 209458b and HD 189733b. A&A, 564:A73, April 2014a. doi: 10.1051/0004-6361/201322895.

M. Agúndez, O. Venot, F. Selsis, and N. Iro. The Puzzling Chemical Composition of GJ 436b's Atmosphere: Influence of Tidal Heating on the Chemistry. ApJ, 781:68, February 2014b. doi: 10.1088/0004-637X/781/2/68.

F. Allard, D. Homeier, B. Freytag, and C. M. Sharp. Atmospheres From Very Low-Mass Stars to Extrasolar Planets. In C. Reylé, C. Charbonnel, and M. Schultheis, editors, *EAS Publications Series*, volume 57 of *EAS Publications Series*, pages 3–43, November 2012. doi: 10.1051/eas/1257001.

D. S. Amundsen. *Climate Simulations of Hot Jupiters: Developing and Applying an Accurate Radiation Scheme*. PhD thesis, University of Exeter, 2015.

D. S. Amundsen, I. Baraffe, P. Tremblin, J. Manners, W. Hayek, N. J. Mayne, and D. M. Acreman. Accuracy tests of radiation schemes used in hot Jupiter global circulation models. A&A, 564:A59, April 2014. doi: 10.1051/0004-6361/201323169.

D. S. Amundsen, N. J. Mayne, I. Baraffe, J. Manners, P. Tremblin, B. Drummond, C. Smith, D. M. Acreman, and D. Homeier. The UK Met Office global circulation model with a sophisticated radiation scheme applied to the hot Jupiter HD 209458b. A&A, 595:A36, October 2016. doi: 10.1051/0004-6361/201629183.

D. S. Amundsen, P. Tremblin, J. Manners, I. Baraffe, and N. J. Mayne. Treatment of overlapping gaseous absorption with the correlated-k method in hot Jupiter and brown dwarf atmosphere models. A&A, 598:A97, February 2017. doi: 10.1051/0004-6361/201629322.

G. Anglada-Escudé, P. J. Amado, J. Barnes, Z. M. Berdiñas, R. P. Butler, G. A. L. Coleman, I. de La Cueva, S. Dreizler, M. Endl, B. Giesers, S. V. Jeffers, J. S. Jenkins, H. R. A. Jones, M. Kiraga, M. Kürster, M. J. López-González, C. J. Marvin, N. Morales, J. Morin, R. P. Nelson, J. L. Ortiz, A. Ofir, S.-J. Paardekooper, A. Reiners, E. Rodríguez, C. Rodríguez-López, L. F. Sarmiento, J. P. Strachan, Y. Tsapras, M. Tuomi, and M. Zechmeister. A terrestrial planet candidate in a temperate orbit around Proxima Centauri. Nature, 536:437–440, August 2016. doi: 10.1038/nature19106.

D. Apai, M. Kasper, A. Skemer, J. R. Hanson, A.-M. Lagrange, B. A. Biller, M. Bonnefoy, E. Buenzli, and A. Vigan. High-cadence, High-contrast Imaging for Exoplanet Mapping: Observations of the HR 8799 Planets with VLT/SPHERE Satellite-spot-corrected Relative Photometry. ApJ, 820:40, March 2016. doi: 10.3847/0004-637X/820/1/40.

M. Asplund, N. Grevesse, A. J. Sauval, and P. Scott. The Chemical Composition of the Sun. ARA&A, 47:481–522, September 2009. doi: 10.1146/annurev.astro.46.060407.145222.

I. Baraffe, G. Chabrier, and T. Barman. The physical properties of extra-solar planets. *Reports on Progress in Physics*, 73(1):016901, January 2010. doi: 10.1088/0034-4885/73/1/016901.

I. Baraffe, G. Chabrier, J. Fortney, and C. Sotin. Planetary Internal Structures. *Protostars and Planets VI*, pages 763–786, 2014. doi: 10.2458/azu_uapress_9780816531240-ch033.

T. Barman. Identification of Absorption Features in an Extrasolar Planet Atmosphere. ApJL, 661:L191–L194, June 2007. doi: 10.1086/518736.

T. S. Barman, P. H. Hauschildt, and F. Allard. Phase-Dependent Properties of Extrasolar Planet Atmospheres. ApJ, 632:1132–1139, October 2005. doi: 10.1086/444349.

T. S. Barman, B. Macintosh, Q. M. Konopacky, and C. Marois. Clouds and Chemistry in the Atmosphere of Extrasolar Planet HR8799b. ApJ, 733:65, May 2011. doi: 10.1088/0004-637X/733/1/65.

T. S. Barman, Q. M. Konopacky, B. Macintosh, and C. Marois. Simultaneous Detection of Water, Methane, and Carbon Monoxide in the Atmosphere of Exoplanet HR8799b. ApJ, 804:61, May 2015. doi: 10.1088/0004-637X/804/1/61.

S. S. Barshay and J. S. Lewis. Chemical structure of the deep atmosphere of Jupiter. Icarus, 33:593–611, March 1978. doi: 10.1016/0019-1035(78)90192-6.

K. Batygin and D. J. Stevenson. Inflating Hot Jupiters with Ohmic Dissipation. ApJL, 714:L238–L243, May 2010. doi: 10.1088/2041-8205/714/2/L238.

J. L. Bean, J.-M. Désert, P. Kabath, B. Stalder, S. Seager, E. Miller-Ricci Kempton, Z. K. Berta, D. Homeier, S. Walsh, and A. Seifahrt. The Optical and Near-infrared Transmission Spectrum of the Super-Earth GJ 1214b: Further Evidence for a Metal-rich Atmosphere. ApJ, 743:92, December 2011. doi: 10.1088/0004-637X/743/1/92.

J. P. Beaulieu, D. M. Kipping, V. Batista, G. Tinetti, I. Ribas, S. Carey, J. A. Noriega-Crespo, C. A. Griffith, G. Campanella, S. Dong, J. Tennyson, R. J. Barber, P. Deroo, S. J. Fossey, D. Liang, M. R. Swain, Y. Yung, and N. Allard. Water in the atmosphere of HD 209458b from 3.6-8 μm IRAC photometric observations in primary transit. MNRAS, 409:963–974, December 2010. doi: 10.1111/j.1365-2966.2010.16516.x.

C. Beichman, B. Benneke, H. Knutson, R. Smith, P.-O. Lagage, C. Dressing, D. Latham, J. Lunine, S. Birkmann, P. Ferruit, G. Giardino, E. Kempton, S. Carey, J. Krick, P. D. Deroo, A. Mandell, M. E. Ressler, A. Shporer, M. Swain, G. Vasisht, G. Ricker, J. Bouwman, I. Crossfield, T. Greene, S. Howell, J. Christiansen, D. Ciardi, M. Clampin, M. Greenhouse, A. Sozzetti, P. Goudfrooij, D. Hines, T. Keyes, J. Lee, P. McCullough, M. Robberto, J. Stansberry, J. Valenti, M. Rieke, G. Rieke, J. Fortney, J. Bean, L. Kreidberg, D. Ehrenreich, D. Deming, L. Albert, R. Doyon, and D. Sing. Observations of Transiting Exoplanets with the James Webb Space Telescope (JWST). PASP, 126:1134, December 2014. doi: 10.1086/679566.

Z. K. Berta-Thompson, J. Irwin, D. Charbonneau, E. R. Newton, J. A. Dittmann, N. Astudillo-Defru, X. Bonfils, M. Gillon, E. Jehin, A. A. Stark, B. Stalder, F. Bouchy, X. Delfosse, T. Forveille, C. Lovis, M. Mayor, V. Neves, F. Pepe, N. C. Santos, S. Udry, and A. Wünsche. A rocky planet transiting a nearby low-mass star. Nature, 527:204–207, November 2015. doi: 10.1038/nature15762.

J.-L. Beuzit, M. Feldt, K. Dohlen, D. Mouillet, P. Puget, F. Wildi, L. Abe, J. Antichi, A. Baruffolo, P. Baudoz, A. Boccaletti, M. Carbillet, J. Charton, R. Claudi, M. Downing, C. Fabron, P. Feautrier, E. Fedrigo, T. Fusco, J.-L. Gach, R. Gratton, T. Henning, N. Hubin, F. Joos, M. Kasper, M. Langlois, R. Lenzen, C. Moutou, A. Pavlov, C. Petit, J. Pragt, P. Rabou, F. Rigal, R. Roelfsema, G. Rousset, M. Saisse, H.-M. Schmid, E. Stadler, C. Thalmann, M. Turatto, S. Udry, F. Vakili, and R. Waters. SPHERE: a 'Planet Finder' instrument for the VLT. In *Ground-based and Airborne Instrumentation for Astronomy II*, volume 7014 of Proc. SPIE, page 701418, July 2008. doi: 10.1117/12.790120.

B. Bézard, E. Lellouch, D. Strobel, J.-P. Maillard, and P. Drossart. Carbon Monoxide on Jupiter: Evidence for Both Internal and External Sources. Icarus, 159: 95–111, September 2002. doi: 10.1006/icar.2002.6917.

J. L. Birkby, R. J. de Kok, M. Brogi, E. J. W. de Mooij, H. Schwarz, S. Albrecht, and I. A. G. Snellen. Detection of water absorption in the day side atmosphere of HD 189733 b using ground-based high-resolution spectroscopy at 3.2 μm. MNRAS, 436:L35–L39, November 2013. doi: 10.1093/mnrasl/slt107.

J. Blecic, J. Harrington, and M. O. Bowman. TEA: A Code for Calculating Thermochemical Equilibrium Abundances. *ArXiv e-prints*, May 2015.

M. Bonnefoy, A. Boccaletti, A.-M. Lagrange, F. Allard, C. Mordasini, H. Beust, G. Chauvin, J. H. V. Girard, D. Homeier, D. Apai, S. Lacour, and D. Rouan. The near-infrared spectral energy distribution of β Pictoris b. A&A, 555:A107, July 2013. doi: 10.1051/0004-6361/201220838.

W. J. Borucki, D. Koch, G. Basri, N. Batalha, T. Brown, D. Caldwell, J. Caldwell, J. Christensen-Dalsgaard, W. D. Cochran, E. DeVore, E. W. Dunham, A. K. Dupree, T. N. Gautier, J. C. Geary, R. Gilliland, A. Gould, S. B. Howell, J. M. Jenkins, Y. Kondo, D. W. Latham, G. W. Marcy, S. Meibom, H. Kjeldsen, J. J. Lissauer, D. G. Monet, D. Morrison, D. Sasselov, J. Tarter, A. Boss, D. Brownlee, T. Owen, D. Buzasi, D. Charbonneau, L. Doyle, J. Fortney, E. B. Ford, M. J. Holman, S. Seager, J. H. Steffen, W. F. Welsh, J. Rowe, H. Anderson, L. Buchhave, D. Ciardi, L. Walkowicz, W. Sherry, E. Horch, H. Isaacson, M. E. Everett, D. Fischer, G. Torres, J. A. Johnson, M. Endl, P. MacQueen, S. T. Bryson, J. Dotson, M. Haas, J. Kolodziejczak, J. Van Cleve, H. Chandrasekaran, J. D. Twicken, E. V. Quintana, B. D. Clarke, C. Allen, J. Li, H. Wu, P. Tenenbaum, E. Verner, F. Bruhweiler, J. Barnes, and A. Prsa. Kepler Planet-Detection Mission: Introduction and First Results. *Science*, 327:977, February 2010. doi: 10.1126/science.1185402.

F. Bouchy, C. Moutou, D. Queloz, and the CoRoT Exoplanet Science Team. Radial velocity follow-up for confirmation and characterization of transiting exoplanets. *ArXiv e-prints*, February 2009.

I. A. Boutle, N. J. Mayne, B. Drummond, J. Manners, J. Goyal, F. H. Lambert, D. M. Acreman, and P. D. Earnshaw. Exploring the climate of Proxima B with the Met Office Unified Model. *ArXiv e-prints*, February 2017.

M. Brogi, I. A. G. Snellen, R. J. de Kok, S. Albrecht, J. Birkby, and E. J. W. de Mooij. The signature of orbital motion from the dayside of the planet τ Boötis b. Nature, 486:502–504, June 2012. doi: 10.1038/nature11161.

M. Brogi, R. J. de Kok, S. Albrecht, I. A. G. Snellen, J. L. Birkby, and H. Schwarz. Rotation and Winds of Exoplanet HD 189733 b Measured with High-dispersion Transmission Spectroscopy. ApJ, 817:106, February 2016. doi: 10.3847/0004-637X/817/2/106.

T. M. Brown. Transmission Spectra as Diagnostics of Extrasolar Giant Planet Atmospheres. ApJ, 553:1006–1026, June 2001. doi: 10.1086/320950.

A. Burrows and C. M. Sharp. Chemical Equilibrium Abundances in Brown Dwarf and Extrasolar Giant Planet Atmospheres. ApJ, 512:843–863, February 1999. doi: 10.1086/306811.

A. Burrows, I. Hubeny, W. B. Hubbard, D. Sudarsky, and J. J. Fortney. Theoretical Radii of Transiting Giant Planets: The Case of OGLE-TR-56b. ApJL, 610:L53–L56, July 2004. doi: 10.1086/423173.

A. Burrows, D. Sudarsky, and I. Hubeny. Theory for the Secondary Eclipse Fluxes, Spectra, Atmospheres, and Light Curves of Transiting Extrasolar Giant Planets. ApJ, 650:1140–1149, October 2006. doi: 10.1086/507269.

A. Burrows, I. Hubeny, J. Budaj, and W. B. Hubbard. Possible Solutions to the Radius Anomalies of Transiting Giant Planets. ApJ, 661:502–514, May 2007. doi: 10.1086/514326.

A. Burrows, E. Rauscher, D. S. Spiegel, and K. Menou. Photometric and Spectral Signatures of Three-dimensional Models of Transiting Giant Exoplanets. ApJ, 719:341–350, August 2010. doi: 10.1088/0004-637X/719/1/341.

E. Caffau, H.-G. Ludwig, M. Steffen, B. Freytag, and P. Bonifacio. Solar Chemical Abundances Determined with a CO5BOLD 3D Model Atmosphere. Sol. Phys., 268:255–269, February 2011. doi: 10.1007/s11207-010-9541-4.

J. A. Carter, J. N. Winn, M. J. Holman, D. Fabrycky, Z. K. Berta, C. J. Burke, and P. Nutzman. The Transit Light Curve Project. XIII. Sixteen Transits of the Super-Earth GJ 1214b. ApJ, 730:82, April 2011. doi: 10.1088/0004-637X/730/2/82.

G. Chabrier and I. Baraffe. Heat Transport in Giant (Exo)planets: A New Perspective. ApJL, 661:L81–L84, May 2007. doi: 10.1086/518473.

D. Charbonneau, T. M. Brown, D. W. Latham, and M. Mayor. Detection of Planetary Transits Across a Sun-like Star. ApJL, 529:L45–L48, January 2000. doi: 10.1086/312457.

D. Charbonneau, T. M. Brown, R. W. Noyes, and R. L. Gilliland. Detection of an Extrasolar Planet Atmosphere. ApJ, 568:377–384, March 2002. doi: 10.1086/338770.

D. Charbonneau, L. E. Allen, S. T. Megeath, G. Torres, R. Alonso, T. M. Brown, R. L. Gilliland, D. W. Latham, G. Mandushev, F. T. O'Donovan, and A. Sozzetti. Detection of Thermal Emission from an Extrasolar Planet. ApJ, 626:523–529, June 2005. doi: 10.1086/429991.

C. S. Cooper and A. P. Showman. Dynamics and Disequilibrium Carbon Chemistry in Hot Jupiter Atmospheres, with Application to HD 209458b. ApJ, 649:1048–1063, October 2006. doi: 10.1086/506312.

N. B. Cowan and E. Agol. Inverting Phase Functions to Map Exoplanets. ApJL, 678:L129, May 2008. doi: 10.1086/588553.

A. N. Cox. *Allen's astrophysical quantities*. 2000.

T. Currie, A. Burrows, Y. Itoh, S. Matsumura, M. Fukagawa, D. Apai, N. Madhusudhan, P. M. Hinz, T. J. Rodigas, M. Kasper, T.-S. Pyo, and S. Ogino. A Combined Subaru/VLT/MMT 1-5 μm Study of Planets Orbiting HR 8799: Implications for Atmospheric Properties, Masses, and Formation. ApJ, 729:128, March 2011. doi: 10.1088/0004-637X/729/2/128.

T. Davies, M. J. P. Cullen, A. J. Malcolm, M. H. Mawson, A. Staniforth, A. A. White, and N. Wood. A new dynamical core for the met office's global and regional modelling of the atmosphere. *Quarterly Journal of the Royal Meteorological Society*, 131(608):1759–1782, 2005. ISSN 1477-870X. doi: 10.1256/qj.04.101. URL `http://dx.doi.org/10.1256/qj.04.101`.

D. Deming, J. Harrington, S. Seager, and L. J. Richardson. Strong Infrared Emission from the Extrasolar Planet HD 189733b. ApJ, 644:560–564, June 2006. doi: 10.1086/503358.

D. Deming, A. Wilkins, P. McCullough, A. Burrows, J. J. Fortney, E. Agol, I. Dobbs-Dixon, N. Madhusudhan, N. Crouzet, J.-M. Desert, R. L. Gilliland, K. Haynes, H. A. Knutson, M. Line, Z. Magic, A. M. Mandell, S. Ranjan, D. Charbonneau, M. Clampin, S. Seager, and A. P. Showman. Infrared Transmission Spectroscopy of the Exoplanets HD 209458b and XO-1b Using the Wide Field Camera-3 on the Hubble Space Telescope. ApJ, 774:95, September 2013. doi: 10.1088/0004-637X/774/2/95.

H. Diamond-Lowe, K. B. Stevenson, J. L. Bean, M. R. Line, and J. J. Fortney. New Analysis Indicates No Thermal Inversion in the Atmosphere of HD 209458b. ApJ, 796:66, November 2014. doi: 10.1088/0004-637X/796/1/66.

I. Dobbs-Dixon and E. Agol. Three-dimensional radiative-hydrodynamical simulations of the highly irradiated short-period exoplanet HD 189733b. MNRAS, 435: 3159–3168, November 2013. doi: 10.1093/mnras/stt1509.

I. Dobbs-Dixon and D. N. C. Lin. Atmospheric Dynamics of Short-Period Extrasolar Gas Giant Planets. I. Dependence of Nightside Temperature on Opacity. ApJ, 673:513-525, January 2008. doi: 10.1086/523786.

B. Drummond, P. Tremblin, I. Baraffe, D. S. Amundsen, N. J. Mayne, O. Venot, and J. Goyal. The effects of consistent chemical kinetics calculations on the pressure-temperature profiles and emission spectra of hot Jupiters. A&A, 594:A69, October 2016. doi: 10.1051/0004-6361/201628799.

J. M. Edwards and A. Slingo. Studies with a flexible new radiation code. i: Choosing a configuration for a large-scale model. *Quarterly Journal of the Royal Meteorological Society*, 122(531):689–719, 1996. ISSN 1477-870X. doi: 10.1002/qj.49712253107. URL `http://dx.doi.org/10.1002/qj.49712253107`.

Janusz Eluszkiewicz, Richard S. Hemler, Jerry D. Mahlman, Lori Bruhwiler, and Lawrence L. Takacs. Sensitivity of age-of-air calculations to the choice of advection scheme. *Journal of the Atmospheric Sciences*, 57(19):3185–3201, 2000. doi: 10.1175/1520-0469(2000)057¡3185:SOAOAC¿2.0.CO;2. URL `http://dx.doi.org/10.1175/1520-0469(2000)057<3185:SOAOAC>2.0.CO;2`.

T. M. Evans, S. Aigrain, N. Gibson, J. K. Barstow, D. S. Amundsen, P. Tremblin, and P. Mourier. A uniform analysis of HD 209458b Spitzer/IRAC light curves with Gaussian process models. MNRAS, 451:680–694, July 2015. doi: 10.1093/mnras/stv910.

T. M. Evans, D. K. Sing, H. R. Wakeford, N. Nikolov, G. E. Ballester, B. Drummond, T. Kataria, N. P. Gibson, D. S. Amundsen, and J. Spake. Detection of H_2O and Evidence for TiO/VO in an Ultra-hot Exoplanet Atmosphere. ApJL, 822:L4, May 2016. doi: 10.3847/2041-8205/822/1/L4.

B. Fegley, Jr. and K. Lodders. Chemical models of the deep atmospheres of Jupiter and Saturn. Icarus, 110:117–154, July 1994. doi: 10.1006/icar.1994.1111.

J. J. Fortney, M. S. Marley, K. Lodders, D. Saumon, and R. Freedman. Comparative Planetary Atmospheres: Models of TrES-1 and HD 209458b. ApJL, 627:L69–L72, July 2005. doi: 10.1086/431952.

J. J. Fortney, C. S. Cooper, A. P. Showman, M. S. Marley, and R. S. Freedman. The Influence of Atmospheric Dynamics on the Infrared Spectra and Light Curves of Hot Jupiters. ApJ, 652:746–757, November 2006. doi: 10.1086/508442.

J. J. Fortney, K. Lodders, M. S. Marley, and R. S. Freedman. A Unified Theory for the Atmospheres of the Hot and Very Hot Jupiters: Two Classes of Irradiated Atmospheres. ApJ, 678:1419-1435, May 2008. doi: 10.1086/528370.

J. J. Fortney, M. Shabram, A. P. Showman, Y. Lian, R. S. Freedman, M. S. Marley, and N. K. Lewis. Transmission Spectra of Three-Dimensional Hot Jupiter Model Atmospheres. ApJ, 709:1396–1406, February 2010. doi: 10.1088/0004-637X/709/2/1396.

J. J. Fortney, T. D. Robinson, S. Domagal-Goldman, D. Skålid Amundsen, M. Brogi, M. Claire, D. Crisp, E. Hebrard, H. Imanaka, R. de Kok, M. S. Marley, D. Teal, T. Barman, P. Bernath, A. Burrows, D. Charbonneau, R. S. Freedman, D. Gelino, C. Helling, K. Heng, A. G. Jensen, S. Kane, E. M.-R. Kempton, R. K. Kopparapu, N. K. Lewis, M. Lopez-Morales, J. Lyons, W. Lyra, V. Meadows, J. Moses, R. Pierrehumbert, O. Venot, S. X. Wang, and J. T. Wright. The Need for Laboratory Work to Aid in The Understanding of Exoplanetary Atmospheres. *ArXiv e-prints*, February 2016.

L. Fossati, V. Bourrier, D. Ehrenreich, C. A. Haswell, K. G. Kislyakova, H. Lammer, A. Lecavelier des Etangs, Y. Alibert, T. R. Ayres, G. E. Ballester, J. Barnes, D. V. Bisikalo, A. Collier, Cameron, S. Czesla, J.-M. Desert, K. France, M. Guedel, E. Guenther, C. Helling, K. Heng, M. Homstrom, L. Kaltenegger, T. Koskinen, A. F. Lanza, J. L. Linsky, C. Mordasini, I. Pagano, D. Pollacco, H. Rauer, A. Reiners, M. Salz, P. C. Schneider, V. I. Shematovich, D. Staab, A. A. Vidotto, P. J. Wheatley, B. E. Wood, and R. V. Yelle. Characterising exoplanets and their environment with UV transmission spectroscopy. *ArXiv e-prints*, March 2015.

C.W. Gear. *Numerical Initial Value Problems in Ordinary Differential Equations*. Prentice Hall PTR Upper Saddle River, NJ, USA, 1971.

M. Gillon, A. H. M. J. Triaud, B.-O. Demory, E. Jehin, E. Agol, K. M. Deck, S. M. Lederer, J. de Wit, A. Burdanov, J. G. Ingalls, E. Bolmont, J. Leconte, S. N. Raymond, F. Selsis, M. Turbet, K. Barkaoui, A. Burgasser, M. R. Burleigh, S. J. Carey, A. Chaushev, C. M. Copperwheat, L. Delrez, C. S. Fernandes, D. L. Holdsworth, E. J. Kotze, V. Van Grootel, Y. Almleaky, Z. Benkhaldoun, P. Magain, and D. Queloz. Seven temperate terrestrial planets around the nearby ultracool dwarf star TRAPPIST-1. Nature, 542:456–460, February 2017. doi: 10.1038/nature21360.

G. R. Gladstone, M. Allen, and Y. L. Yung. Hydrocarbon Photochemistry in the Upper Atmosphere of Jupiter. Icarus, 119:1–52, January 1996. doi: 10.1006/icar.1996.0001.

R. Goody, R. West, L. Chen, and D. Crisp. The correlated-k method for radiation calculations in nonhomogeneous atmospheres. J. Quant. Spec. Radiat. Transf., 42:539–550, December 1989. doi: 10.1016/0022-4073(89)90044-7.

S. Gordon and B. J. McBride. Computer program for calculation of complex chemical equilibrium compositions and applications. *NASA Reference Publication*, 1311, 1994.

T. P. Greene, M. R. Line, C. Montero, J. J. Fortney, J. Lustig-Yaeger, and K. Luther. Characterizing Transiting Exoplanet Atmospheres with JWST. ApJ, 817:17, January 2016. doi: 10.3847/0004-637X/817/1/17.

C. A. Griffith, R. V. Yelle, and M. S. Marley. The Dusty Atmosphere of the Brown Dwarf Gliese 229B. *Science*, 282:2063, December 1998. doi: 10.1126/science.282.5396.2063.

T. Guillot, A. Burrows, W. B. Hubbard, J. I. Lunine, and D. Saumon. Giant Planets at Small Orbital Distances. ApJL, 459:L35, March 1996. doi: 10.1086/309935.

B Gustafsson, B Edvardsson, K Eriksson, U G Jørgensen, Å Nordlund, and B Plez. A grid of MARCS model atmospheres for late-type stars. I. Methods and general properties. *A&A*, 486(3):951–970, August 2008.

J. Harrington, B. M. Hansen, S. H. Luszcz, S. Seager, D. Deming, K. Menou, J. Y.-K. Cho, and L. J. Richardson. The Phase-Dependent Infrared Brightness of the Extrasolar Planet Upsi Andromedae b. *Science*, 314:623–626, October 2006. doi: 10.1126/science.1133904.

K. Haynes, A. M. Mandell, N. Madhusudhan, D. Deming, and H. Knutson. Spectroscopic Evidence for a Temperature Inversion in the Dayside Atmosphere of Hot Jupiter WASP-33b. ApJ, 806:146, June 2015. doi: 10.1088/0004-637X/806/2/146.

C. Hedges and N. Madhusudhan. Effect of pressure broadening on molecular absorption cross sections in exoplanetary atmospheres. MNRAS, 458:1427–1449, May 2016. doi: 10.1093/mnras/stw278.

K. Heng and S.-M. Tsai. Analytical Models of Exoplanetary Atmospheres. III. Gaseous C-H-O-N Chemistry with 9 Molecules. *ArXiv e-prints*, March 2016.

K. Heng, K. Menou, and P. J. Phillipps. Atmospheric circulation of tidally locked exoplanets: a suite of benchmark tests for dynamical solvers. MNRAS, 413:2380–2402, June 2011. doi: 10.1111/j.1365-2966.2011.18315.x.

A.C. Hindmarsh. Odepack, a sytematized collection of ode solvers. *Scientific Computing*, 1983.

A. W. Howard, R. Sanchis-Ojeda, G. W. Marcy, J. A. Johnson, J. N. Winn, H. Isaacson, D. A. Fischer, B. J. Fulton, E. Sinukoff, and J. J. Fortney. A rocky composition for an Earth-sized exoplanet. Nature, 503:381–384, November 2013. doi: 10.1038/nature12767.

I. Hubeny and A. Burrows. A Systematic Study of Departures from Chemical Equilibrium in the Atmospheres of Substellar Mass Objects. ApJ, 669:1248–1261, November 2007. doi: 10.1086/522107.

N. Iro, B. Bézard, and T. Guillot. A time-dependent radiative model of HD 209458b. A&A, 436:719–727, June 2005. doi: 10.1051/0004-6361:20048344.

P. G. J. Irwin, N. A. Teanby, R. de Kok, L. N. Fletcher, C. J. A. Howett, C. C. C. Tsang, C. F. Wilson, S. B. Calcutt, C. A. Nixon, and P. D. Parrish. The NEMESIS planetary atmosphere radiative transfer and retrieval tool. J. Quant. Spec. Radiat. Transf., 109:1136–1150, April 2008. doi: 10.1016/j.jqsrt.2007.11.006.

I. S. A. Isaksen, K. H. Midtbo, J. Sunde, and P. J. Crutzen. A simplified method to include molecular scattering and reflection in calculations of photon fluxes and photodissociation rates. *Geophysica Norvegica*, 31:11–26, 1977.

M. Janson, T. D. Brandt, M. Kuzuhara, D. S. Spiegel, C. Thalmann, T. Currie, M. Bonnefoy, N. Zimmerman, S. Sorahana, T. Kotani, J. Schlieder, J. Hashimoto, T. Kudo, N. Kusakabe, L. Abe, W. Brandner, J. C. Carson, S. Egner, M. Feldt, M. Goto, C. A. Grady, O. Guyon, Y. Hayano, M. Hayashi, S. Hayashi, T. Henning, K. W. Hodapp, M. Ishii, M. Iye, R. Kandori, G. R. Knapp, J. Kwon, T. Matsuo, M. W. McElwain, K. Mede, S. Miyama, J.-I. Morino, A. Moro-Martín, T. Nakagawa, T. Nishimura, T.-S. Pyo, E. Serabyn, T. Suenaga, H. Suto, R. Suzuki, Y. Takahashi, M. Takami, N. Takato, H. Terada, D. Tomono, E. L. Turner, M. Watanabe, J. Wisniewski, T. Yamada, H. Takami, T. Usuda, and M. Tamura. Direct Imaging Detection of Methane in the Atmosphere of GJ 504 b. ApJL, 778: L4, November 2013. doi: 10.1088/2041-8205/778/1/L4.

P. Kalas, J. R. Graham, E. Chiang, M. P. Fitzgerald, M. Clampin, E. S. Kite, K. Stapelfeldt, C. Marois, and J. Krist. Optical Images of an Exosolar Planet 25 Light-Years from Earth. *Science*, 322:1345, November 2008. doi: 10.1126/science.1166609.

J. A. Kammer, H. A. Knutson, M. R. Line, J. J. Fortney, D. Deming, A. Burrows, N. B. Cowan, A. H. M. J. Triaud, E. Agol, J.-M. Desert, B. J. Fulton, A. W. Howard, G. P. Laughlin, N. K. Lewis, C. V. Morley, J. I. Moses, A. P. Showman, and K. O. Todorov. Spitzer Secondary Eclipse Observations of Five Cool Gas

Giant Planets and Empirical Trends in Cool Planet Emission Spectra. ApJ, 810: 118, September 2015. doi: 10.1088/0004-637X/810/2/118.

J. F. Kasting. Bolide impacts and the oxidation state of carbon in the earth's early atmosphere. *Origins of Life and Evolution of the Biosphere*, 20:199–231, May 1990. doi: 10.1007/BF01808105.

J. F. Kasting, K. J. Zahnle, J. P. Pinto, and A. T. Young. Sulfur, ultraviolet radiation, and the early evolution of life. *Origins of Life and Evolution of the Biosphere*, 19:252–253, May 1989. doi: 10.1007/BF02388836.

T. Kataria, A. P. Showman, J. J. Fortney, M. S. Marley, and R. S. Freedman. The Atmospheric Circulation of the Super Earth GJ 1214b: Dependence on Composition and Metallicity. ApJ, 785:92, April 2014. doi: 10.1088/0004-637X/785/2/92.

T. Kataria, D. K. Sing, N. K. Lewis, C. Visscher, A. P. Showman, J. J. Fortney, and M. S. Marley. The Atmospheric Circulation of a Nine-hot-Jupiter Sample: Probing Circulation and Chemistry over a Wide Phase Space. ApJ, 821:9, April 2016. doi: 10.3847/0004-637X/821/1/9.

H. A. Knutson, D. Charbonneau, L. E. Allen, J. J. Fortney, E. Agol, N. B. Cowan, A. P. Showman, C. S. Cooper, and S. T. Megeath. A map of the day-night contrast of the extrasolar planet HD 189733b. Nature, 447:183–186, May 2007a. doi: 10.1038/nature05782.

H. A. Knutson, D. Charbonneau, R. W. Noyes, T. M. Brown, and R. L. Gilliland. Using Stellar Limb-Darkening to Refine the Properties of HD 209458b. ApJ, 655: 564–575, January 2007b. doi: 10.1086/510111.

H. A. Knutson, D. Charbonneau, L. E. Allen, A. Burrows, and S. T. Megeath. The 3.6-8.0 μm Broadband Emission Spectrum of HD 209458b: Evidence for an Atmospheric Temperature Inversion. ApJ, 673:526-531, January 2008. doi: 10.1086/523894.

H. A. Knutson, D. Charbonneau, N. B. Cowan, J. J. Fortney, A. P. Showman, E. Agol, and G. W. Henry. The 8 μm Phase Variation of the Hot Saturn HD 149026b. ApJ, 703:769–784, September 2009a. doi: 10.1088/0004-637X/703/1/769.

H. A. Knutson, D. Charbonneau, N. B. Cowan, J. J. Fortney, A. P. Showman, E. Agol, G. W. Henry, M. E. Everett, and L. E. Allen. Multiwavelength Constraints on the Day-Night Circulation Patterns of HD 189733b. ApJ, 690:822–836, January 2009b. doi: 10.1088/0004-637X/690/1/822.

H. A. Knutson, N. Madhusudhan, N. B. Cowan, J. L. Christiansen, E. Agol, D. Deming, J.-M. Désert, D. Charbonneau, G. W. Henry, D. Homeier, J. Langton, G. Laughlin, and S. Seager. A Spitzer Transmission Spectrum for the Exoplanet GJ 436b, Evidence for Stellar Variability, and Constraints on Dayside Flux Variations. ApJ, 735:27, July 2011. doi: 10.1088/0004-637X/735/1/27.

H. A. Knutson, B. Benneke, D. Deming, and D. Homeier. A featureless transmission spectrum for the Neptune-mass exoplanet GJ436b. Nature, 505:66–68, January 2014. doi: 10.1038/nature12887.

Q. M. Konopacky, T. S. Barman, B. A. Macintosh, and C. Marois. Detection of Carbon Monoxide and Water Absorption Lines in an Exoplanet Atmosphere. *Science*, 339:1398–1401, March 2013. doi: 10.1126/science.1232003.

R. k. Kopparapu, J. F. Kasting, and K. J. Zahnle. A Photochemical Model for the Carbon-rich Planet WASP-12b. ApJ, 745:77, January 2012. doi: 10.1088/0004-637X/745/1/77.

T. T. Koskinen, M. J. Harris, R. V. Yelle, and P. Lavvas. The escape of heavy atoms from the ionosphere of HD209458b. I. A photochemical-dynamical model of the thermosphere. Icarus, 226:1678–1694, November 2013. doi: 10.1016/j.icarus.2012.09.027.

L. Kreidberg, J. L. Bean, J.-M. Désert, B. Benneke, D. Deming, K. B. Stevenson, S. Seager, Z. Berta-Thompson, A. Seifahrt, and D. Homeier. Clouds in the atmosphere of the super-Earth exoplanet GJ1214b. Nature, 505:69–72, January 2014. doi: 10.1038/nature12888.

A. A. Lacis and V. Oinas. A description of the correlated-k distribution method for modelling nongray gaseous absorption, thermal emission, and multiple scattering in vertically inhomogeneous atmospheres. J. Geophys. Res., 96:9027–9064, May 1991. doi: 10.1029/90JD01945.

G. Lee, I. Dobbs-Dixon, C. Helling, K. Bognar, and P. Woitke. Dynamic mineral clouds on HD 189733b. I. 3D RHD with kinetic, non-equilibrium cloud formation. A&A, 594:A48, October 2016. doi: 10.1051/0004-6361/201628606.

N. K. Lewis, A. P. Showman, J. J. Fortney, M. S. Marley, R. S. Freedman, and K. Lodders. Atmospheric Circulation of Eccentric Hot Neptune GJ436b. ApJ, 720:344–356, September 2010. doi: 10.1088/0004-637X/720/1/344.

M.-C. Liang, C. D. Parkinson, A. Y.-T. Lee, Y. L. Yung, and S. Seager. Source of Atomic Hydrogen in the Atmosphere of HD 209458b. ApJL, 596:L247–L250, October 2003. doi: 10.1086/379314.

M. R. Line, M. C. Liang, and Y. L. Yung. High-temperature Photochemistry in the Atmosphere of HD 189733b. ApJ, 717:496–502, July 2010. doi: 10.1088/0004-637X/717/1/496.

M. R. Line, G. Vasisht, P. Chen, D. Angerhausen, and Y. L. Yung. Thermochemical and Photochemical Kinetics in Cooler Hydrogen-dominated Extrasolar Planets: A Methane-poor GJ436b? ApJ, 738:32, September 2011. doi: 10.1088/0004-637X/738/1/32.

A. C. Lockwood, J. A. Johnson, C. F. Bender, J. S. Carr, T. Barman, A. J. W. Richert, and G. A. Blake. Near-IR Direct Detection of Water Vapor in Tau Boötis b. ApJL, 783:L29, March 2014. doi: 10.1088/2041-8205/783/2/L29.

K. Lodders. Alkali Element Chemistry in Cool Dwarf Atmospheres. ApJ, 519: 793–801, July 1999. doi: 10.1086/307387.

K. Lodders and B. Fegley. Atmospheric Chemistry in Giant Planets, Brown Dwarfs, and Low-Mass Dwarf Stars. I. Carbon, Nitrogen, and Oxygen. Icarus, 155:393–424, February 2002. doi: 10.1006/icar.2001.6740.

K. Lodders, H. Palme, and H.-P. Gail. Abundances of the Elements in the Solar System. *Landolt Börnstein*, 2009.

C. Lovis, I. Snellen, D. Mouillet, F. Pepe, F. Wildi, N. Astudillo-Defru, J.-L. Beuzit, X. Bonfils, A. Cheetham, U. Conod, X. Delfosse, D. Ehrenreich, P. Figueira, T. Forveille, J. H. C. Martins, S. P. Quanz, N. C. Santos, H.-M. Schmid, D. Ségransan, and S. Udry. Atmospheric characterization of Proxima b by coupling the SPHERE high-contrast imager to the ESPRESSO spectrograph. A&A, 599:A16, February 2017. doi: 10.1051/0004-6361/201629682.

B. Macintosh, J. Graham, D. Palmer, R. Doyon, D. Gavel, J. Larkin, B. Oppenheimer, L. Saddlemyer, J. K. Wallace, B. Bauman, J. Evans, D. Erikson, K. Morzinski, D. Phillion, L. Poyneer, A. Sivaramakrishnan, R. Soummer, S. Thibault, and J.-P. Veran. The Gemini Planet Imager. In *Society of Photo-Optical Instrumentation Engineers (SPIE) Conference Series*, volume 6272 of Proc. SPIE, page 62720L, June 2006. doi: 10.1117/12.672430.

B. Macintosh, J. R. Graham, P. Ingraham, Q. Konopacky, C. Marois, M. Perrin, L. Poyneer, B. Bauman, T. Barman, A. S. Burrows, A. Cardwell, J. Chilcote, R. J. De Rosa, D. Dillon, R. Doyon, J. Dunn, D. Erikson, M. P. Fitzgerald, D. Gavel, S. Goodsell, M. Hartung, P. Hibon, P. Kalas, J. Larkin, J. Maire, F. Marchis, M. S.

Marley, J. McBride, M. Millar-Blanchaer, K. Morzinski, A. Norton, B. R. Oppenheimer, D. Palmer, J. Patience, L. Pueyo, F. Rantakyro, N. Sadakuni, L. Saddlemyer, D. Savransky, A. Serio, R. Soummer, A. Sivaramakrishnan, I. Song, S. Thomas, J. K. Wallace, S. Wiktorowicz, and S. Wolff. First light of the Gemini Planet Imager. *Proceedings of the National Academy of Science*, 111:12661–12666, September 2014. doi: 10.1073/pnas.1304215111.

B. Macintosh, J. R. Graham, T. Barman, R. J. De Rosa, Q. Konopacky, M. S. Marley, C. Marois, E. L. Nielsen, L. Pueyo, A. Rajan, J. Rameau, D. Saumon, J. J. Wang, J. Patience, M. Ammons, P. Arriaga, E. Artigau, S. Beckwith, J. Brewster, S. Bruzzone, J. Bulger, B. Burningham, A. S. Burrows, C. Chen, E. Chiang, J. K. Chilcote, R. I. Dawson, R. Dong, R. Doyon, Z. H. Draper, G. Duchêne, T. M. Esposito, D. Fabrycky, M. P. Fitzgerald, K. B. Follette, J. J. Fortney, B. Gerard, S. Goodsell, A. Z. Greenbaum, P. Hibon, S. Hinkley, T. H. Cotten, L.-W. Hung, P. Ingraham, M. Johnson-Groh, P. Kalas, D. Lafreniere, J. E. Larkin, J. Lee, M. Line, D. Long, J. Maire, F. Marchis, B. C. Matthews, C. E. Max, S. Metchev, M. A. Millar-Blanchaer, T. Mittal, C. V. Morley, K. M. Morzinski, R. Murray-Clay, R. Oppenheimer, D. W. Palmer, R. Patel, M. D. Perrin, L. A. Poyneer, R. R. Rafikov, F. T. Rantakyrö, E. L. Rice, P. Rojo, A. R. Rudy, J.-B. Ruffio, M. T. Ruiz, N. Sadakuni, L. Saddlemyer, M. Salama, D. Savransky, A. C. Schneider, A. Sivaramakrishnan, I. Song, R. Soummer, S. Thomas, G. Vasisht, J. K. Wallace, K. Ward-Duong, S. J. Wiktorowicz, S. G. Wolff, and B. Zuckerman. Discovery and spectroscopy of the young jovian planet 51 Eri b with the Gemini Planet Imager. *Science*, 350:64–67, October 2015. doi: 10.1126/science.aac5891.

N. Madhusudhan. C/O Ratio as a Dimension for Characterizing Exoplanetary Atmospheres. ApJ, 758:36, October 2012. doi: 10.1088/0004-637X/758/1/36.

N. Madhusudhan and S. Redfield. Optimal measures for characterizing water-rich super-Earths. *International Journal of Astrobiology*, 14:177–189, April 2015. doi: 10.1017/S1473550414000421.

N. Madhusudhan and S. Seager. A Temperature and Abundance Retrieval Method for Exoplanet Atmospheres. ApJ, 707:24–39, December 2009. doi: 10.1088/0004-637X/707/1/24.

N. Madhusudhan and S. Seager. High Metallicity and Non-equilibrium Chemistry in the Dayside Atmosphere of hot-Neptune GJ 436b. ApJ, 729:41, March 2011. doi: 10.1088/0004-637X/729/1/41.

N. Madhusudhan, A. Burrows, and T. Currie. Model Atmospheres for Massive Gas Giants with Thick Clouds: Application to the HR 8799 Planets and Pre-

dictions for Future Detections. ApJ, 737:34, August 2011a. doi: 10.1088/0004-637X/737/1/34.

N. Madhusudhan, J. Harrington, K. B. Stevenson, S. Nymeyer, C. J. Campo, P. J. Wheatley, D. Deming, J. Blecic, R. A. Hardy, N. B. Lust, D. R. Anderson, A. Collier-Cameron, C. B. T. Britt, W. C. Bowman, L. Hebb, C. Hellier, P. F. L. Maxted, D. Pollacco, and R. G. West. A high C/O ratio and weak thermal inversion in the atmosphere of exoplanet WASP-12b. Nature, 469:64–67, January 2011b. doi: 10.1038/nature09602.

N. Madhusudhan, N. Crouzet, P. R. McCullough, D. Deming, and C. Hedges. H_2O Abundances in the Atmospheres of Three Hot Jupiters. ApJL, 791:L9, August 2014a. doi: 10.1088/2041-8205/791/1/L9.

N. Madhusudhan, H. Knutson, J. J. Fortney, and T. Barman. Exoplanetary Atmospheres. *Protostars and Planets VI*, pages 739–762, 2014b. doi: 10.2458/azu_uapress_9780816531240-ch032.

N. Madhusudhan, M. Agúndez, J. I. Moses, and Y. Hu. Exoplanetary Atmospheres: Chemistry, Formation Conditions, and Habitability. Space Sci. Rev., 205:285–348, December 2016. doi: 10.1007/s11214-016-0254-3.

M. S. Marley. Atmospheres of Giant Planets from Neptune to Gliese 229B. *ArXiv Astrophysics e-prints*, June 1997.

N. J. Mayne, I. Baraffe, D. M. Acreman, C. Smith, M. K. Browning, D. Skålid Amundsen, N. Wood, J. Thuburn, and D. R. Jackson. The unified model, a fully-compressible, non-hydrostatic, deep atmosphere global circulation model, applied to hot Jupiters. ENDGame for a HD 209458b test case. A&A, 561:A1, January 2014a. doi: 10.1051/0004-6361/201322174.

N. J. Mayne, I. Baraffe, D. M. Acreman, C. Smith, N. Wood, D. S. Amundsen, J. Thuburn, and D. R. Jackson. Using the UM dynamical cores to reproduce idealised 3-D flows. *Geoscientific Model Development*, 7:3059–3087, December 2014b. doi: 10.5194/gmd-7-3059-2014.

M. Mayor and D. Queloz. A Jupiter-mass companion to a solar-type star. Nature, 378:355–359, November 1995. doi: 10.1038/378355a0.

R. Mbarek and E. M.-R. Kempton. Clouds in Super-Earth Atmospheres: Chemical Equilibrium Calculations. ApJ, 827:121, August 2016. doi: 10.3847/0004-637X/827/2/121.

B. J. McBride, S. Gordon, and M. A. Reno. Coefficients for calculating thermodynamic and transport properties of individual species. *NASA Technical Memorandum*, 4513, 1993.

B. J. McBride, M. J. Zehe, and S. Gordon. Nasa glenn coefficients for calculating thermodynamic properties of individual species. *NASA/TP*, 2002-211556, 2002.

J. McCormac, D. Pollacco, P. J. Wheatley, R. G. West, S. Walker, J. Bento, I. Skillen, F. Faedi, M. R. Burleigh, S. L. Casewell, B. Chazelas, L. Genolet, N. P. Gibson, M. R. Goad, K. A. Lawrie, R. Ryans, I. Todd, S. Udry, and C. A. Watson. The Next Generation Transit Survey - Prototyping Phase. PASP, 129 (2):025002, February 2017. doi: 10.1088/1538-3873/129/972/025002.

K. Menou and E. Rauscher. Atmospheric Circulation of Hot Jupiters: A Shallow Three-Dimensional Model. ApJ, 700:887–897, July 2009. doi: 10.1088/0004-637X/700/1/887.

Diane V. Michelangeli, Mark Allen, Yuk L. Yung, Run-Lie Shia, David Crisp, and Janusz Eluszkiewicz. Enhancement of atmospheric radiation by an aerosol layer. *Journal of Geophysical Research: Atmospheres*, 97(D1):865–874, 1992. ISSN 2156-2202. doi: 10.1029/91JD01308. URL `http://dx.doi.org/10.1029/91JD01308`.

Y. Miguel and L. Kaltenegger. Exploring Atmospheres of Hot Mini-Neptunes and Extrasolar Giant Planets Orbiting Different Stars with Application to HD 97658b, WASP-12b, CoRoT-2b, XO-1b, and HD 189733b. ApJ, 780:166, January 2014. doi: 10.1088/0004-637X/780/2/166.

T. Mizuki, T. Yamada, J. C. Carson, M. Kuzuhara, T. Nakagawa, J. Nishikawa, M. L. Sitko, T. Kudo, N. Kusakabe, J. Hashimoto, L. Abe, W. Brander, T. D. Brandt, S. Egner, M. Feldt, M. Goto, C. A. Grady, O. Guyon, Y. Hayano, M. Hayashi, S. S. Hayashi, T. Henning, K. W. Hodapp, M. Ishii, M. Iye, M. Janson, R. Kandori, G. R. Knapp, J. Kwon, T. Matsuo, M. W. McElwain, S. Miyama, J. Morino, A. Moro-Martin, T. Nishimura, T. Pyo, E. Serabyn, T. Suenaga, H. Suto, R. Suzuki, Y. H. Takahashi, M. Takami, N. Takato, H. Terada, C. Thalmann, E. L. Turner, M. Watanabe, J. Wisniewski, H. Takami, T. Usuda, and M. Tamura. High-contrast imaging of ϵ Eridani with ground-based instruments. A&A, 595:A79, November 2016. doi: 10.1051/0004-6361/201628544.

J. I. Moses, E. Lellouch, B. Bézard, G. R. Gladstone, H. Feuchtgruber, and M. Allen. Photochemistry of Saturn's Atmosphere. II. Effects of an Influx of External Oxygen. Icarus, 145:166–202, May 2000. doi: 10.1006/icar.1999.6320.

J. I. Moses, C. Visscher, J. J. Fortney, A. P. Showman, N. K. Lewis, C. A. Griffith, S. J. Klippenstein, M. Shabram, A. J. Friedson, M. S. Marley, and R. S. Freedman. Disequilibrium Carbon, Oxygen, and Nitrogen Chemistry in the Atmospheres of HD 189733b and HD 209458b. ApJ, 737:15, August 2011. doi: 10.1088/0004-637X/737/1/15.

J. I. Moses, M. R. Line, C. Visscher, M. R. Richardson, N. Nettelmann, J. J. Fortney, T. S. Barman, K. B. Stevenson, and N. Madhusudhan. Compositional Diversity in the Atmospheres of Hot Neptunes, with Application to GJ 436b. ApJ, 777:34, November 2013a. doi: 10.1088/0004-637X/777/1/34.

J. I. Moses, N. Madhusudhan, C. Visscher, and R. S. Freedman. Chemical Consequences of the C/O Ratio on Hot Jupiters: Examples from WASP-12b, CoRoT-2b, XO-1b, and HD 189733b. ApJ, 763:25, January 2013b. doi: 10.1088/0004-637X/763/1/25.

H. B. Niemann, S. K. Atreya, G. R. Carignan, T. M. Donahue, J. A. Haberman, D. N. Harpold, R. E. Hartle, D. M. Hunten, W. T. Kasprzak, P. R. Mahaffy, T. C. Owen, and S. H. Way. The composition of the Jovian atmosphere as determined by the Galileo probe mass spectrometer. J. Geophys. Res., 103:22831–22846, September 1998. doi: 10.1029/98JE01050.

N. Nikolov, D. K. Sing, N. P. Gibson, J. J. Fortney, T. M. Evans, J. K. Barstow, T. Kataria, and P. A. Wilson. VLT FORS2 Comparative Transmission Spectroscopy: Detection of Na in the Atmosphere of WASP-39b from the Ground. ApJ, 832:191, December 2016. doi: 10.3847/0004-637X/832/2/191.

B. R. Oppenheimer, C. Baranec, C. Beichman, D. Brenner, R. Burruss, E. Cady, J. R. Crepp, R. Dekany, R. Fergus, D. Hale, L. Hillenbrand, S. Hinkley, D. W. Hogg, D. King, E. R. Ligon, T. Lockhart, R. Nilsson, I. R. Parry, L. Pueyo, E. Rice, J. E. Roberts, L. C. Roberts, Jr., M. Shao, A. Sivaramakrishnan, R. Soummer, T. Truong, G. Vasisht, A. Veicht, F. Vescelus, J. K. Wallace, C. Zhai, and N. Zimmerman. Reconnaissance of the HR 8799 Exosolar System. I. Near-infrared Spectroscopy. ApJ, 768:24, May 2013. doi: 10.1088/0004-637X/768/1/24.

V. Parmentier, A. P. Showman, and Y. Lian. 3D mixing in hot Jupiters atmospheres. I. Application to the day/night cold trap in HD 209458b. A&A, 558:A91, October 2013. doi: 10.1051/0004-6361/201321132.

F. Pepe, A. C. Cameron, D. W. Latham, E. Molinari, S. Udry, A. S. Bonomo, L. A. Buchhave, D. Charbonneau, R. Cosentino, C. D. Dressing, X. Dumusque, P. Figueira, A. F. M. Fiorenzano, S. Gettel, A. Harutyunyan, R. D. Haywood,

K. Horne, M. Lopez-Morales, C. Lovis, L. Malavolta, M. Mayor, G. Micela, F. Motalebi, V. Nascimbeni, D. Phillips, G. Piotto, D. Pollacco, D. Queloz, K. Rice, D. Sasselov, D. Ségransan, A. Sozzetti, A. Szentgyorgyi, and C. A. Watson. An Earth-sized planet with an Earth-like density. Nature, 503:377–380, November 2013. doi: 10.1038/nature12768.

Bruce. E. Poling, John. M. Prausnitz, and John. P. O'Connell. *The Properties of Gases and Liquids: Fifth Edition*. McGraw-Hill, 2001.

D. L. Pollacco, I. Skillen, A. Collier Cameron, D. J. Christian, C. Hellier, J. Irwin, T. A. Lister, R. A. Street, R. G. West, D. R. Anderson, W. I. Clarkson, H. Deeg, B. Enoch, A. Evans, A. Fitzsimmons, C. A. Haswell, S. Hodgkin, K. Horne, S. R. Kane, F. P. Keenan, P. F. L. Maxted, A. J. Norton, J. Osborne, N. R. Parley, R. S. I. Ryans, B. Smalley, P. J. Wheatley, and D. M. Wilson. The WASP Project and the SuperWASP Cameras. PASP, 118:1407–1418, October 2006. doi: 10.1086/508556.

F. Pont, H. Knutson, R. L. Gilliland, C. Moutou, and D. Charbonneau. Detection of atmospheric haze on an extrasolar planet: the 0.55-1.05 μm transmission spectrum of HD 189733b with the HubbleSpaceTelescope. MNRAS, 385:109–118, March 2008. doi: 10.1111/j.1365-2966.2008.12852.x.

K. Radhakrishnan and A. Hindmarsh. Description and Use of LSODE, the Livermore Solver for Ordinary Differential Equations. Technical report, LLNL report UCRL-ID-113855, 1993.

E. Rauscher and K. Menou. The Role of Drag in the Energetics of Strongly Forced Exoplanet Atmospheres. ApJ, 745:78, January 2012a. doi: 10.1088/0004-637X/745/1/78.

E. Rauscher and K. Menou. A General Circulation Model for Gaseous Exoplanets with Double-gray Radiative Transfer. ApJ, 750:96, May 2012b. doi: 10.1088/0004-637X/750/2/96.

G. R. Ricker, J. N. Winn, R. Vanderspek, D. W. Latham, G. Á. Bakos, J. L. Bean, Z. K. Berta-Thompson, T. M. Brown, L. Buchhave, N. R. Butler, R. P. Butler, W. J. Chaplin, D. Charbonneau, J. Christensen-Dalsgaard, M. Clampin, D. Deming, J. Doty, N. De Lee, C. Dressing, E. W. Dunham, M. Endl, F. Fressin, J. Ge, T. Henning, M. J. Holman, A. W. Howard, S. Ida, J. M. Jenkins, G. Jernigan, J. A. Johnson, L. Kaltenegger, N. Kawai, H. Kjeldsen, G. Laughlin, A. M. Levine, D. Lin, J. J. Lissauer, P. MacQueen, G. Marcy, P. R. McCullough, T. D. Morton, N. Narita, M. Paegert, E. Palle, F. Pepe, J. Pepper, A. Quirrenbach, S. A.

Rinehart, D. Sasselov, B. Sato, S. Seager, A. Sozzetti, K. G. Stassun, P. Sullivan, A. Szentgyorgyi, G. Torres, S. Udry, and J. Villasenor. Transiting Exoplanet Survey Satellite (TESS). *Journal of Astronomical Telescopes, Instruments, and Systems*, 1(1):014003, January 2015. doi: 10.1117/1.JATIS.1.1.014003.

P. B. Rimmer and C. Helling. A Chemical Kinetics Network for Lightning and Life in Planetary Atmospheres. ApJS, 224:9, May 2016. doi: 10.3847/0067-0049/224/1/9.

F. Rodler, M. Lopez-Morales, and I. Ribas. Weighing the Non-transiting Hot Jupiter τ Boo b. ApJL, 753:L25, July 2012. doi: 10.1088/2041-8205/753/1/L25.

J. C. Rogers, D. Apai, M. López-Morales, D. K. Sing, and A. Burrows. Ks-Band Detection of Thermal Emission and Color Constraints to CoRoT-1b: A Low-Albedo Planet with Inefficient Atmospheric Energy Redistribution and a Temperature Inversion. ApJ, 707:1707-1716, December 2009. doi: 10.1088/0004-637X/707/2/1707.

H. Schwarz, M. Brogi, R. de Kok, J. Birkby, and I. Snellen. Evidence against a strong thermal inversion in HD 209458b from high-dispersion spectroscopy. A&A, 576: A111, April 2015. doi: 10.1051/0004-6361/201425170.

S. E. Schwarz and P. Warneck. Units for Use in Atmospheric Chemistry. *Pure & Appl. Chem.*, 67:1377–406, 1995.

S. Seager and D. D. Sasselov. Theoretical Transmission Spectra during Extrasolar Giant Planet Transits. ApJ, 537:916–921, July 2000. doi: 10.1086/309088.

S. Seager, L. J. Richardson, B. M. S. Hansen, K. Menou, J. Y.-K. Cho, and D. Deming. On the Dayside Thermal Emission of Hot Jupiters. ApJ, 632:1122–1131, October 2005. doi: 10.1086/444411.

A. P. Showman and T. Guillot. Atmospheric circulation and tides of "51 Pegasus b-like" planets. A&A, 385:166–180, April 2002. doi: 10.1051/0004-6361:20020101.

A. P. Showman, J. J. Fortney, Y. Lian, M. S. Marley, R. S. Freedman, H. A. Knutson, and D. Charbonneau. Atmospheric Circulation of Hot Jupiters: Coupled Radiative-Dynamical General Circulation Model Simulations of HD 189733b and HD 209458b. ApJ, 699:564–584, July 2009. doi: 10.1088/0004-637X/699/1/564.

D. K. Sing, A. Vidal-Madjar, J.-M. Désert, A. Lecavelier des Etangs, and G. Ballester. Hubble Space Telescope STIS Optical Transit Transmission Spectra of the Hot Jupiter HD 209458b. ApJ, 686:658-666, October 2008. doi: 10.1086/590075.

D. K. Sing, A. Lecavelier des Etangs, J. J. Fortney, A. S. Burrows, F. Pont, H. R. Wakeford, G. E. Ballester, N. Nikolov, G. W. Henry, S. Aigrain, D. Deming, T. M. Evans, N. P. Gibson, C. M. Huitson, H. Knutson, A. P. Showman, A. Vidal-Madjar, P. A. Wilson, M. H. Williamson, and K. Zahnle. HST hot-Jupiter transmission spectral survey: evidence for aerosols and lack of TiO in the atmosphere of WASP-12b. MNRAS, 436:2956–2973, December 2013. doi: 10.1093/mnras/stt1782.

D. K. Sing, J. J. Fortney, N. Nikolov, H. R. Wakeford, T. Kataria, T. M. Evans, S. Aigrain, G. E. Ballester, A. S. Burrows, D. Deming, J.-M. Désert, N. P. Gibson, G. W. Henry, C. M. Huitson, H. A. Knutson, A. L. D. Etangs, F. Pont, A. P. Showman, A. Vidal-Madjar, M. H. Williamson, and P. A. Wilson. A continuum from clear to cloudy hot-Jupiter exoplanets without primordial water depletion. Nature, 529:59–62, January 2016. doi: 10.1038/nature16068.

I. Snellen, R. de Kok, J. L. Birkby, B. Brandl, M. Brogi, C. Keller, M. Kenworthy, H. Schwarz, and R. Stuik. Combining high-dispersion spectroscopy with high contrast imaging: Probing rocky planets around our nearest neighbors. A&A, 576:A59, April 2015. doi: 10.1051/0004-6361/201425018.

I. A. G. Snellen, R. J. de Kok, E. J. W. de Mooij, and S. Albrecht. The orbital motion, absolute mass and high-altitude winds of exoplanet HD209458b. Nature, 465:1049–1051, June 2010. doi: 10.1038/nature09111.

I. A. G. Snellen, R. J. de Kok, R. le Poole, M. Brogi, and J. Birkby. Finding Extraterrestrial Life Using Ground-based High-dispersion Spectroscopy. ApJ, 764:182, February 2013. doi: 10.1088/0004-637X/764/2/182.

J. Southworth. Homogeneous studies of transiting extrasolar planets - III. Additional planets and stellar models. MNRAS, 408:1689–1713, November 2010. doi: 10.1111/j.1365-2966.2010.17231.x.

G E Thomas and K Stammes. *Radiative Transfer in the Atmosphere and Ocean*. Cambridge University Press, November 1999.

H. T. Thrastarson and J. Y. Cho. Effects of Initial Flow on Close-in Planet Atmospheric Circulation. ApJ, 716:144–153, June 2010. doi: 10.1088/0004-637X/716/1/144.

P. Tremblin, D. S. Amundsen, P. Mourier, I. Baraffe, G. Chabrier, B. Drummond, D. Homeier, and O. Venot. Fingering Convection and Cloudless Models for Cool Brown Dwarf Atmospheres. ApJL, 804:L17, May 2015. doi: 10.1088/2041-8205/804/1/L17.

P. Tremblin, D. S. Amundsen, G. Chabrier, I. Baraffe, B. Drummond, S. Hinkley, P. Mourier, and O. Venot. Cloudless Atmospheres for L/T Dwarfs and Extrasolar Giant Planets. ApJL, 817:L19, February 2016. doi: 10.3847/2041-8205/817/2/L19.

S.-M. Tsai, J. R. Lyons, L. Grosheintz, P. B. Rimmer, D. Kitzmann, and K. Heng. VULCAN: An Open-source, Validated Chemical Kinetics Python Code for Exoplanetary Atmospheres. ApJS, 228:20, February 2017. doi: 10.3847/1538-4365/228/2/20.

M. Turbet, J. Leconte, F. Selsis, E. Bolmont, F. Forget, I. Ribas, S. N. Raymond, and G. Anglada-Escudé. The habitability of Proxima Centauri b. II. Possible climates and observability. A&A, 596:A112, December 2016. doi: 10.1051/0004-6361/201629577.

S. Udry, D. Fischer, and D. Queloz. A Decade of Radial-Velocity Discoveries in the Exoplanet Domain. *Protostars and Planets V*, pages 685–699, 2007.

O. Venot, E. Hébrard, M. Agúndez, M. Dobrijevic, F. Selsis, F. Hersant, N. Iro, and R. Bounaceur. A chemical model for the atmosphere of hot Jupiters. A&A, 546: A43, October 2012. doi: 10.1051/0004-6361/201219310.

O. Venot, N. Fray, Y. Bénilan, M.-C. Gazeau, E. Hébrard, G. Larcher, M. Schwell, M. Dobrijevic, and F. Selsis. High-temperature measurements of VUV-absorption cross sections of CO_2 and their application to exoplanets. A&A, 551:A131, March 2013. doi: 10.1051/0004-6361/201220945.

O. Venot, M. Agúndez, F. Selsis, M. Tessenyi, and N. Iro. The atmospheric chemistry of the warm Neptune GJ 3470b: Influence of metallicity and temperature on the CH_4/CO ratio. A&A, 562:A51, February 2014. doi: 10.1051/0004-6361/201322485.

O. Venot, E. Hébrard, M. Agúndez, L. Decin, and R. Bounaceur. New chemical scheme for studying carbon-rich exoplanet atmospheres. A&A, 577:A33, May 2015. doi: 10.1051/0004-6361/201425311.

O. Venot, M. Rocchetto, S. Carl, A. Roshni Hashim, and L. Decin. Influence of Stellar Flares on the Chemical Composition of Exoplanets and Spectra. ApJ, 830:77, October 2016. doi: 10.3847/0004-637X/830/2/77.

Olivia Venot. *Photochimie des exoplantes chaudes : modlisations et expriences*. PhD thesis, LUNIVERSIT DE BORDEAUX, 2012.

A. Vigan, M. Bonnefoy, C. Ginski, H. Beust, R. Galicher, M. Janson, J.-L. Baudino, E. Buenzli, J. Hagelberg, V. D'Orazi, S. Desidera, A.-L. Maire, R. Gratton, J.-F. Sauvage, G. Chauvin, C. Thalmann, L. Malo, G. Salter, A. Zurlo, J. Antichi, A. Baruffolo, P. Baudoz, P. Blanchard, A. Boccaletti, J.-L. Beuzit, M. Carle, R. Claudi, A. Costille, A. Delboulbé, K. Dohlen, C. Dominik, M. Feldt, T. Fusco, L. Gluck, J. Girard, E. Giro, C. Gry, T. Henning, N. Hubin, E. Hugot, M. Jaquet, M. Kasper, A.-M. Lagrange, M. Langlois, D. Le Mignant, M. Llored, F. Madec, P. Martinez, D. Mawet, D. Mesa, J. Milli, D. Mouillet, T. Moulin, C. Moutou, A. Origné, A. Pavlov, D. Perret, C. Petit, J. Pragt, P. Puget, P. Rabou, S. Rochat, R. Roelfsema, B. Salasnich, H.-M. Schmid, A. Sevin, R. Siebenmorgen, A. Smette, E. Stadler, M. Suarez, M. Turatto, S. Udry, F. Vakili, Z. Wahhaj, L. Weber, and F. Wildi. First light of the VLT planet finder SPHERE. I. Detection and characterization of the substellar companion GJ 758 B. A&A, 587:A55, March 2016. doi: 10.1051/0004-6361/201526465.

C. Visscher and J. I. Moses. Quenching of Carbon Monoxide and Methane in the Atmospheres of Cool Brown Dwarfs and Hot Jupiters. ApJ, 738:72, September 2011. doi: 10.1088/0004-637X/738/1/72.

I. P. Waldmann, G. Tinetti, M. Rocchetto, E. J. Barton, S. N. Yurchenko, and J. Tennyson. Tau-REx I: A Next Generation Retrieval Code for Exoplanetary Atmospheres. ApJ, 802:107, April 2015. doi: 10.1088/0004-637X/802/2/107.

R.P. Wayne. *Chemistry of Atmospheres*. Oxford Science Publications, Oxford University Press, New York, 2nd edition, 1991.

J. C. Wheeler, C. Sneden, and J. W. Truran, Jr. Abundance ratios as a function of metallicity. ARA&A, 27:279–349, 1989. doi: 10.1146/annurev.aa.27.090189.001431.

A. A. White, B. J. Hoskins, I. Roulstone, and A. Staniforth. Consistent approximate models of the global atmosphere: shallow, deep, hydrostatic, quasi-hydrostatic and non-hydrostatic. *Quarterly Journal of the Royal Meteorological Society*, 131(609):2081–2107, 2005. ISSN 1477-870X. doi: 10.1256/qj.04.49. URL `http://dx.doi.org/10.1256/qj.04.49`.

A. Wolszczan and D. A. Frail. A planetary system around the millisecond pulsar PSR1257 + 12. Nature, 355:145–147, January 1992. doi: 10.1038/355145a0.

I. Wong, H. A. Knutson, T. Kataria, N. K. Lewis, A. Burrows, J. J. Fortney, J. Schwartz, A. Shporer, E. Agol, N. B. Cowan, D. Deming, J.-M. Désert, B. J. Fulton, A. W. Howard, J. Langton, G. Laughlin, A. P. Showman, and K. Todorov. 3.6

and 4.5 μm Spitzer Phase Curves of the Highly Irradiated Hot Jupiters WASP-19b and HAT-P-7b. ApJ, 823:122, June 2016. doi: 10.3847/0004-637X/823/2/122.

Nigel Wood, Andrew Staniforth, Andy White, Thomas Allen, Michail Diamantakis, Markus Gross, Thomas Melvin, Chris Smith, Simon Vosper, Mohamed Zerroukat, and John Thuburn. An inherently mass-conserving semi-implicit semi-lagrangian discretization of the deep-atmosphere global non-hydrostatic equations. *Quarterly Journal of the Royal Meteorological Society*, 140(682):1505–1520, 2014. ISSN 1477-870X. doi: 10.1002/qj.2235. URL `http://dx.doi.org/10.1002/qj.2235`.

R. V. Yelle. Aeronomy of extra-solar giant planets at small orbital distances. Icarus, 170:167–179, July 2004. doi: 10.1016/j.icarus.2004.02.008.

Y. L. Yung and W. B. DeMore. *Photochemistry of Planetary Atmospheres*. Oxford University Press, 1999.

K. Zahnle, M. Claire, and D. Catling. The loss of mass-independent fractionation in sulfur due to a palaeoproterozoic collapse of atmospheric methane. *Geobiology*, 4 (4):271–283, 2006. ISSN 1472-4669. doi: 10.1111/j.1472-4669.2006.00085.x. URL `http://dx.doi.org/10.1111/j.1472-4669.2006.00085.x`.

K. Zahnle, M. S. Marley, R. S. Freedman, K. Lodders, and J. J. Fortney. Atmospheric Sulfur Photochemistry on Hot Jupiters. ApJL, 701:L20–L24, August 2009. doi: 10.1088/0004-637X/701/1/L20.

K. Zahnle, M. S. Marley, C. V. Morley, and J. I. Moses. Photolytic Hazes in the Atmosphere of 51 Eri b. ApJ, 824:137, June 2016. doi: 10.3847/0004-637X/824/2/137.

K. J. Zahnle and M. S. Marley. Methane, Carbon Monoxide, and Ammonia in Brown Dwarfs and Self-Luminous Giant Planets. ApJ, 797:41, December 2014. doi: 10.1088/0004-637X/797/1/41.

R. T. Zellem, C. A. Griffith, P. Deroo, M. R. Swain, and I. P. Waldmann. The Ground-based H-, K-, and L-band Absolute Emission Spectra of HD 209458b. ApJ, 796:48, November 2014a. doi: 10.1088/0004-637X/796/1/48.

R. T. Zellem, N. K. Lewis, H. A. Knutson, C. A. Griffith, A. P. Showman, J. J. Fortney, N. B. Cowan, E. Agol, A. Burrows, D. Charbonneau, D. Deming, G. Laughlin, and J. Langton. The 4.5 μm Full-orbit Phase Curve of the Hot Jupiter HD 209458b. ApJ, 790:53, July 2014b. doi: 10.1088/0004-637X/790/1/53.

X. Zhang and A. P. Showman. Effects of Bulk Composition on The Atmospheric Dynamics on Close-in Exoplanets. *ArXiv e-prints*, July 2016.

Glossary

A Pre-exponential factor [$\mathrm{cm^3\ s^{-1}}$]

A' Modified pre-exponential factor [$\mathrm{cm^3\ s^{-1}}$]

A_i Elemental abundances normalised to 10^{12} atoms of hydrogen [-]

B_i Number fraction of atoms of element i in a mixture [-]

C_p Molar heat capacity [$\mathrm{J\ K^{-1}\ mol^{-1}}$]

D_j Molecular diffusion coefficient of species j [$\mathrm{cm^2\ s^{-1}}$]

E_a Activation energy [$\mathrm{J\ mol^{-1}}$]

F Photon flux [photon $\mathrm{cm^{-2}\ s^{-1}}$]

G Gibbs energy [J]

H Enthalpy [J]

H_a Scale height of the atmosphere [m]

H_j Scale height of the species j [m]

J Number of gas and condensed phase species in the mixture

J Photodissociation rate [$\mathrm{s^{-1}}$]

J^* Photon absorption rate [$\mathrm{s^{-1}}$]

J_g Number of gas phase species in the mixture

K_P Equilibrium constant in terms of partial pressures P_j [-]

K_eq Equilibrium constant in terms of number density n_j [-]

K_{zz} Eddy diffusion coefficient [$\mathrm{cm^2\ s^{-1}}$]

L_j Chemical loss term of species j [$\mathrm{cm^{-3}\ s^{-1}}$]

M Mass [kg]

M_J Jovian mass [kg]

M_i Total mass of element i in a mixture [kg]

M_p Mass of the planet [kg]

M_p^* Apparent mass of the planet [kg]

N Number of moles in the mixture [mol]

N_i^{atoms} Number of atoms of element i [-]

N_j Number of moles of species j [mol]

P Pressure [Pa or dyn cm^{-2} or bar]

P_0 Reference pressure [Pa]

P_j Chemical production term of species j [cm^{-3} s^{-1}]

P_j Partial pressure of species j [Pa or dyn cm^{-2} or bar]

Q Heating rate [K s^{-1}]

R Molar gas constant [J K^{-1} mol^{-1}]

R^* Rate of reaction [cm^{-3} s^{-1}]

R_f^* Rate of the forward reaction [cm^{-3} s^{-1}]

R_r^* Rate of the reverse reaction [cm^{-3} s^{-1}]

R_J Jovian radius [m]

R_p Radius of the planet [m]

R_s Radius of the star [m]

S Entropy [J K^{-1}]

T Temperature [K]

T_{eff} Effective temperature [K]

$X^{\text{C/O}}$ Carbon to oxygen ratio [-]

Z Metallicity by mass fraction [-]

[M/H] Metallicity by number fraction [-]

$\Delta_r G^0$ Standard Gibbs energy of reaction [J mol^{-1}]

$\Delta_r H^0$ Standard enthalpy of reaction [J mol^{-1}]

$\Delta_r S^0$ Standard entropy of reaction [J mol^{-1} K^{-1}]

Δt_{chem} Chemical timestep [s]

Δt_{dyn} Dynamical timestep [s]

Δt_{rad} Radiative timestep [s]

Φ_j Flux of particles [cm^{-2} s^{-1}]

Π Exner pressure [-]

α Absorption coefficient per unit mass [cm^2 kg^{-1}]

α_j^{th} Thermal diffusion parameter of the species j [-]

α_j Absorption cross section of species j [cm^2]

$\bar{R}$ Specific gas constant [J K^{-1} mol^{-1}]

λ Wavelength [m]

λ_i Lagrange multiplier

μ Mean molar mass [g mol^{-1}]

μ_j Chemical potential of species j [J mol^{-1}]

μ_j^0 Standard chemical potential of species j [J mol^{-1}]

π_i Lagrange multiplier over RT (λ_i/RT)

ρ Mass density [kg m^{-3}]

σ Absorption cross section [m^2]

σ^{RAY} Rayleigh scattering cross section of species j [m^2]

σ^{RAY} Rayleigh scattering coefficient per unit mass [cm^2 kg^{-1}]

σ_{col} Cross section of collisions [cm^2]

τ_{adv} Advection timescale [s]

τ_{chem} Chemical timescale [s]

θ Potential temperature [K]

a Semi-major axis [AU]

a_{ij} Number of atoms of element i in a molecule of j

c_p Specific heat capacity [J K^{-1} kg^{-1}]

f_j Mole fraction of species j [-]

f_{P-T} Frequency to recalculate the P–T profile

g Height dependent gravity [m s^{-2}]

g_p Surface gravity [m s^{-2}]

h Planck constant [J s]

i Orbital inclination [°]

k Bimolecular rate constant [cm^3 s^{-1}]

k_0 Three-body rate constant in low pressure limit [cm^6 s^{-1}]

k_f Bimolecular forward rate constant [cm^3 s^{-1}]

k_r Bimolecular reverse rate constant [cm^3 s^{-1}]

k_∞ Three-body rate constant in high pressure limit [cm^6 s^{-1}]

k_{B} Boltzmann constant [J K^{-1}]

k_{Troe} Three-body rate constant from Troe formalism [cm^6 s^{-1}]

k_{col} Rate of collisions [cm^3 s^{-1}]

m_j Molar mass of species j [g mol^{-1}]

n Number density of the mixture [cm^{-3} or m^{-3}]

n_j Number density of species j [cm^{-3} or m^{-3}]

q_j Mole mixing ratio of species j [-]

sc Stellar constant [W m^{-2}]

t Time [s]

u Zonal wind velocity [m s^{-1}]

v Meridional wind velocity [m s^{-1}]

w Vertical wind velocity [m s^{-1}]

w_j Mass fraction of species j [-]

z Altitude [m]